PB91-181818

Feasibility of Hydraulic Fracturing of Soil to Improve Remedial Actions

Cincinnati Univ., OH

Prepared for:

Environmental Protection Agency, Cincinnati, OH

Apr 91

U.S. Department of Commerce
National Technical Information Service
NTIS

PB91-181818

EPA/600/2-91/012
April 1991

FEASIBILITY OF HYDRAULIC FRACTURING OF SOIL TO IMPROVE REMEDIAL ACTIONS

by

L. C. Murdoch, G. Losonsky, P. Cluxton,
B. Patterson, I. Klich, B. Braswell

Center Hill Research Facility
University of Cincinnati
Cincinnati, Ohio 45224

Contract 68-03-3379
Work Assignment No. 8

Project Officer
Michael H. Roulier
Risk Reduction Enginnering Laboratory
Cincinnati, Ohio 45268

RISK REDUCTION ENGINNERING LABORATORY
OFFICE OF RESEARCH AND DEVELOPMENT
U.S. ENVIRONMENTAL PROTECTION AGENCY
CINCINNATI, OHIO 45268

REPRODUCED BY
U.S. DEPARTMENT OF COMMERCE
NATIONAL TECHNICAL
INFORMATION SERVICE
SPRINGFIELD, VA 22161

TECHNICAL REPORT DATA

(Please read Instructions on the reverse before completi-

1. REPORT NO. EPA/600/2-91/012

2.

3. PB91-181818

4. TITLE AND SUBTITLE
Feasibility of Hydraulic Fracturing of Soil to Improve Remedial Actions

5. REPORT DATE April 1991

6. PERFORMING ORGANIZATION CODE

7. AUTHOR(S)
L.C. Murdoch, G. Losonsky, P. Cluxton, B. Patterson, I. Klich, and B. Braswell

8. PERFORMING ORGANIZATION REPORT NO.

9. PERFORMING ORGANIZATION NAME AND ADDRESS
University of Cincinnati
Center Hill Research Facility
5995 Center Hill Road
Cincinnati, OH 45224

10. PROGRAM ELEMENT NO. TEJY1A

11. CONTRACT/GRANT NO. 68-03-3379

12. SPONSORING AGENCY NAME AND ADDRESS
Risk Reduction Engineering Laboratory
Office of Research and Development
U.S. Environmental Protection Agency
Cincinnati, OH 45268

13. TYPE OF REPORT AND PERIOD COVERED Complete

14. SPONSORING AGENCY CODE EPA/600/14

15. SUPPLEMENTARY NOTES
Project Officer: Michael H. Roulier (513) 569-7796 or FTS 684-7796

16. ABSTRACT

Hydraulic fracturing, a method of increasing fluid flow within the subsurface, should improve the effectiveness of several remedial techniques, including pump and treat, vapor extraction, bio-remediation, and soil-flushing. The technique is widely used to increase the yields of oil wells, but is untested under conditions typical of contaminated sites.

The project consisted of laboratory experiments, where hydraulic fractures were created in a triaxial pressure cell, and two field tests, where fractures were created at shallow depths in soil. The lab tests showed that hydraulic fractures are readily created in clayey silt, even when it is saturated and loosely-consolidated. Many of the lab observations can be explained using parameters and analyses based on linear elastic fracture mechanics.

Following the field tests, the vicinity of the boreholes was excavated to reveal details of the hydraulic fractures. Maximum lengths of the fractures, as measured from the borehold to the leading edge, averaged 4.0 m, and the average area was 19 m^2. Maximum thickness of sand ranged from 2 to 20 mm, averaging 11 mm. As many as four fractures were created from a single borehold, stacked one over the other at vertical spacing of 15 to 30 cm.

17. KEY WORDS AND DOCUMENT ANALYSIS

a. DESCRIPTORS	b. IDENTIFIERS/OPEN ENDED TERMS	c. COSATI Field/Group

18. DISTRIBUTION STATEMENT
RELEASE TO PUBLIC

19. SECURITY CLASS *(This Report)* UNCLASSIFIED

20. SECURITY CLASS *(This page)* UNCLASSIFIED

21. NO. OF PAGES 307

22. PRICE

EPA Form 2220-1 (Rev. 4-77) PREVIOUS EDITION IS OBSOLETE

NOTICE

The information in this document has been funded by the United States Environmental Protection Agency under Contract 68-03-3379 to the University of Cincinnati. It has been subjected to the Agency's peer and administrative review, and it has been approved for publication as an EPA document. Mention of trade names or commercial products does not constitute endorsement or recommendation for use.

FOREWORD

Today's rapidly developing and changing technologies and industrial products and practices frequently carry with them the increased generation of materials that, if improperly dealt with, can threaten both public health and the environment. The U.S. Environmental Protection Agency is charged by Congress with protecting the Nation's land, air and water resources. Under a mandate of national environmental laws, the Agency strives to formulate and implement actions leading to a compatible balance between human activities and the ability of natural systems to support and nurture life. These laws direct the EPA to perform research to define our environmental problems, measure the impacts, and search for solutions.

The Risk Reduction Engineering Laboratory is responsible for planning, implementing, and managing of research, development, and demonstration programs to provide an authoritative, defensible engineering basis in support of the policies, programs, and regulations of the EPA with respect to drinking water, wastewater, pesticides, toxic substances, solid and hazardous wastes, and Superfund-related activities. This publication is one of the products of that research and provides a vital communication link between the researcher and the user community.

This study was undertaken to determine if hydraulic fracturing, a method of increasing fluid flow in subsurface soils, could improve the effectiveness of several remedial action techniques at sites contaminated by hazardous wastes.

E. Timothy Oppelt, Director

Risk Reduction Engineering Laboratory

ABSTRACT

Hydraulic fracturing, a method of increasing fluid flow within the subsurface, should improve the effectiveness of several remedial techniques, including pump and treat, vapor extraction, bio-remediation, and soil-flushing. The technique is widely used to increase the yields of oil wells, but it is untested under conditions typical of contaminated sites.

The project consisted of laboratory experiments, where hydraulic fractures were created in a triaxial pressure cell, and two field tests, where fractures were created at shallow depths in soil. The laboratory tests showed that hydraulic fractures are readily created in clayey silt, even when it was saturated and loosely-consolidated. Many of the laboratory observations can be explained using parameters and analyses based on linear elastic fracture mechanics.

Field tests were conducted during the summers of 1988 and 1989 at sites underlain by Pleistocene glacial till. During the 1988 test, hydraulic fractures were successfully created from cemented casing at depths of 2 to 4 m using equipment designed for fracturing oil wells. The tests were limited to creating one fracture per well, and they were hindered by the large oil-field equipment, which was difficult to control because it was designed to operate under flow rates and pressures much greater than those used during the test. Many of the fractures created in 1988 closed completely because they were barren of proppant, a condition that apparently resulted from insufficient control.

For the 1989 test, a new method of setting casing was designed, and pumps and blenders designed for injection grouting were used. Casing was set by inserting a drill rod tipped with a conical point and driving the assembly into the ground. The rod and point were retracted and a water jet was inserted to cut a disk-shaped notch beneath the casing. A hydraulic fracture was nucleated at the notch by injecting gel and sand into the casing. Following fracturing, the rod and point were inserted and the assembly was driven to a greater depth, where the process was repeated.

Following the tests, the vicinity of the boreholes was excavated to reveal details of the hydraulic fractures. In general, they were slightly elongate (aspect of 2:3) in plan view, and they were highly asymmetric with respect to their parent borehole; in each case there was a preferred direction of propagation. The fractures created in 1988 climbed gently and vented to the ground surface, whereas the ones created in 1989 were nearly flat-lying, and few of them vented. Maximum lengths of the fractures in 1989, as measured from the borehole to the leading edge, averaged 4.0 m, and the average area was 19 m^2. Maximum thickness of sand in individual fractures ranged from 2 to 20 mm, averaging 11 mm. As many as four fractures were created from a single borehole, stacked one over the other at vertical spacings of 15 to 30 cm.

Four monitoring methods were evaluated: injection pressure, surface uplift, surface tilt, and electrical resistivity. Results indicate that it should be feasible to monitor the growth of hydraulic fractures at shallow depths.

It is feasible to create hydraulic fractures at shallow depths in unlithified sediment, and we recommend that this technology be tested during the remediation of contaminated sites.

CONTENTS

Foreword iii
Abstract iv
Figures vii
Tables. x
Acknowledgment xi

Introduction 1
  Statement of the problem 2
  Approach 3
  Major Conclusions 4
  Laboratory Studies: Summary of Results 4
  Field Studies: Summary of Results 6
  Recommendations 8

1: Potential Remedial Applications and Previous Investigations of Hydraulic Fracturing 6
  Assessment of Potential Applications 6
  Previous Studies of Hydraulic Fracturing 18

2: Observations During Laboratoty Experiments 33
  Experimental Design 33
  Appearance of a Hydraulic Fracture in Center Hill Clay 43
  Records of Driving Pressure 54
  Summary and Discussion 63

3: Analysis of Hydraulic Fracturing of Soil 67
  Predicting the Onset of Hydraulic Fracturing 68
  Propagation of a Hydraulic Fracture in Soil 75
  Data Quality 116
  Discussion 120

4: Setting and Design of the Field Test - 1988 122
  Site Characteristics 122
  Boreholes 132
  Method of Fracturing 137

5: Hydraulic Fractures Created During the Field Test 141
  Forms of the Hydraulic Fractures 142
  Dimensions of Hydraulic Fractures 160
  Direction of Propagation 161
  Summary: An Idealized Hydraulic Fracture 163
  Discussion: Development of the Idealized Fracture 165

6: Setting and Design of the Field Test -- 1989 170
  Quality Assurance and Control 170
  Site Characteristics 170
  Method of Fracturing 172

7: Hydraulic Fractures Created During the Field Test -- 1989 181
 Quality Assurance and Control 181
 Forms of the Hydraulic Fractures 181
 Dimensions of the Hydraulic Fractures 204
 Thickness Profiles of the Hydraulic Fractures 205
 Direction of Propagation 205
 Discussion 205

8: Monitoring Hydraulic Fractures 214
 Injection Pressure 214
 Surface Tilt 229
 Surface Uplift 239
 Electrical Resistivity 243
 Discussion 257

9: Summary and Conclusions 258
 Potential Applications 258
 Laboratory Studies: Summary of Results 259
 Field Studies: Summary of Results 261

References 265
Appendix : Records of Pressure, Volume, Surface Displacement, and Surface Tilt From 1988 Field Tests 282

FIGURES

Number Page

1.1. Production rate of an oil well in North Texas as a function of time 9
1.2. Rates of inflow into boreholes in till 11
1.3. Recovery capacity of a flat-lying, circular fracture in a confined aquifer 17
2.1. Apparatus used for hydraulic fracturing experiments 35
2.2. Cut-away sketch of hydraulic fracturing cell 36
2.3. Grain-size distribution of soils used in the laboratory experiments 39
2.4. Bulk density as a function of moisture content from Proctor tests and fracture tests 40
2.5. Photograph and sketch of the surface of a hydraulic fracture 44
2.6. Sketches of surfaces of three hydraulic fractures of various lengths 46
2.7. Idealized diagram of the leading edge and propagation paths 47
2.8. Idealized configurations of commonly-occurring fracture lobes 49
2.9. Leading edge of a hydraulic fracture 52
2.10. Length of undyed zone as functions of dyed length and moisture content 53
2.11. Records of driving pressure as a function of time 55
2.12. Idealized record of driving pressure as a function of time 58
2.13. Records of injection pressure as a function of time for samples of various moisture contents 60
2.14. Records of injection pressure as a function of time using various lengths of starter slots 66
2.15. Idealized cross-section of a hydraulic fracture in a laboratory sample 70
3.1. Critical stress intensity as a function of half-length of starter slot 73
3.2. Critical stress intensity as functions of moisture content and duration of consolidation 77
3.3. Conceptual model of growth of an idealized hydraulic fracture in laboratory samples 80
3.4. Geometry used in analyses 84
3.5. Velocities of fluid within a fracture and of the fracture tip 91
3.6. Normalized length of unwetted tip with respect to length of etted fracture 93
3.7. Normalized driving pressure, aperture, and half-length as functions of time predicted by analyses 95
3.7a. Average propagation velocities from laboratory experiments 96
3.8. Driving pressure and apertures as functions of length, during inflation and propagation. The x symbol marks the end of the fracture 98
3.9. Loading conditions used to develop analytical model 102
3.10. The effect of m on dimensionless driving pressure, half-length and aperture 104

Number Page

3.15. Records of driving pressure as a function of time from experiments and from analytical solution for samples of various moisture contents 110
3.16. Records of driving pressure as a function of time from experiments and from analytical solution for samples that differ only in the length of their starter slot 111
3.17. The ratio of wetted to total length of a fracture as a function of confining stress. Data from Medlin and Masse (1984) 117
3.18. Variation in exponents in eq. (3.40) as functions of confining stress 118
4.1. Topography and locations of boreholes, vents, and hydraulic fracturing equipment at the ELDA test site 123
4.2. Geology of the ELDA test site 124
4.3. Stratigraphic section from the vicinity of the ELDA test site 125
4.4. Method of creating small hydraulic fracture to measure the least horizontal confining stress 128
4.5. Injection pressure as a function of time during laboratory experiments (a), and using field apparatus (b) 130
4.6. Grain size distributions in samples of ELDA Till 133
4.7. A borehole used to create hydraulic fractures 136
5.1. Hydraulic fractures HF5, HF6, and HF7. Structural contours are on the fracture surfaces 144
5.2. Trace of hydraulic fractures HF5 and HF6 146
5.3 Trace of hydraulic fracture HF6 147
5.4 Trace of hydraulic fracture HF7 148
5.5. Hydraulic fracture HF9 150
5.6. Trace of hydraulic fracture HF9 151
5.7. Hydraulic fractures HF10 and HF11 152
5.8. Hydraulic fracture HF12 154
5.9. Geology and trace of hydraulic fracture HF12 155
5.10. Hydraulic fracture HF13 157
5.11. Outline of HF13 showing area where fracture cuts a bed of upwardly-grading gravel, sand and silt 158
5.12. Trace of hydraulic fracture HF13 159
5.13. Outlines of hydraulic fractures and locations of a backhoe at the time of fracturing 162
5.14. Idealized hydraulic fracture created at the ELDA test site 166
6.1. Scheme for hydraulic fracturing operation performed during the 1989 field test 173
6.2. Fracturing lance, used to prepare boreholes for hydraulic fracturing during the 1989 field test 177
6.3. Five steps of hydraulic fracturing 178
7.1. Map of ELDA landfill site 182
7.2. Fracture map of trenches B and C 184
7.3. Fracture map of trenches D, E and F 185
7.4. Fracture map of trenches G, H and I 186
7.5. Cross section B-B' 188
7.6. Cross section C-C' 188
7.7. Cross section D-D' 189

Number Page

7.8. Cross section E-E' 189
7.9. Cross section F-F' 189
7.10. Cross section G-G' 190
7.11. Cross section H-H' 190
7.12. Map of east wall of trench B 191
7.13. Map of east wall of trench C 192
7.14. Map of east wall of trench D 193
7.15. Map of east wall of trench E 194
7.16. Map of east wall of trench F 195
7.17. Map of east wall of trench G 196
7.18. Map of east wall of trench H 197
7.19. Map of north wall of trench I 198
7.20. Fracture thickness for EL6F1, EL6F2 and EL6F3 206
7.21. Fracture thickness for EL7F1 and EL7F2 207
7.22. Fracture thickness for EL3F1 and EL3F2 208
7.23. Fracture thickness for EL1F1 and EL1F2 209
7.24. Fracture thickness for EL2F1 and EL2F2 210
7.25. Fracture thickness for EL4F1, EL4F2, EL4F3 and EL4F4 211
7.26. Fracture thickness for EL5F1, EL5F2 and EL5F3 212
8.1. Pressure records from fracturing tests during 1989 215
8.2. Tiltmeter array from 1989 tests 231
8.3. Tilt as a function of time 232
8.4. Hydraulic fracture and surface tilt interpretation of HF5 235
8.5. Hydraulic fracture and surface tilt interpretation of HF6 237
8.6. Hydraulic fracture and surface tilt interpretation of HF7 238
8.7. Thickness and uplift contours for EL6F2 and EL6F3 240
8.8. Thickness and uplift contours for EL7F1 241
8.9. Thickness and uplift contours for EL7F2 244
8.10. Thickness and uplift contours for EL5F1, EL5F2, EL5F3 and L5F4 245
8.11. Apparent resistivity contour map on borehole 4, following fracture H4 248
8.12. Apparent resistivity contour map on borehole 6, following fracture H4 249
8.13. Apparent resistivity contour map on borehole 5, following fracture H4 and H5 250
8.14. Apparent resistivity contour map on borehole 4, following fracture H5 251
8.15. Apparent resistivity contour map on borehole 4, following fractures H4, H5 and H7 252
8.16. Apparent resistivity contour map on borehole 7, following fractures H4, H5, and H7 253
8.17. Apparent resistivity contour map on borehole 4, following fractures H6 254
8.18. Apparent resistivity contour map on borehole 6, following fracture H6 255
8.19. Summary of apparent resistivity changes relative to borehole 4 resulting from H4, H5, H6 and H7 256

TABLES

Number Page

1.1. Production rates before and after hydraulic fracture 7
1.2. Inflow rates into glacial till 13
1.3. Some possible constants in Eq. (1.9) 27
2.1. Characteristics of soils used in the study 38
3.1. Parameters used in numerical analyses 89
3.2. Parameters used in analyses shown in figures 112
3.3. Exponents from various analytical solutions 114
3.4. Comparison of constants 115
3.5. Accuracy of laboratory measurements 119
4.1. Conditions of boreholes prior to testing 127
4.2. Saturated hydraulic conductivities of till 131
4.3. Physical characteristics of silty-clay till 132
4.4. Summary of data from field tests 139
5.1. Dimensions and dips of hydraulic fractures 160
5.2. Azimuths of features of hydraulic fractures 163
7.1. Fracture size 183
7.2. Fracture thickness 200
7.3. Proppant concentration 202
7.4. Flow parameters 203
8.1. Actual and predicted orientations of fractures 234

ACKNOWLEDGMENTS

The efforts of Doug Ammon, formerly of the USEPA, who initially recognized the potential of hydraulic fracturing, and the continued support of Herb Pahren and Mike Roulier of the USEPA have been essential to the success of this project. Reviews by Herb Pahren, Robert Hartley and Ken Dotson improved the quality of this report. John Stark, manager of the ELDA Landfill, gave us permission to conduct the 1988 and 1989 field tests on property owned by ELDA. Tom Busek, president of the Goettle Construction Company, gave us permission to conduct tests during 1989 on property owned by Goettle Construction. Don Steirman, professor of geophysics at the Univerisity of Toledo, and his assistants conducted the resistivity surveys during the 1988 field tests. Gary Holzhausen and Howard Egan of Applied Geomechanics, Santa Cruz, CA, supplied us with tiltmeters and they analyzed the tilt signals obtained during the 1988 field tests. Mark Roberts and his field crew from Halliburton Services created the hydraulic fractures during the 1988 tests.

Space limitations prevent us from acknowledging individually a number of colleagues and associates who contributed to this project. Their efforts have been greatly appreciated.

INTRODUCTION

The recovery of hazardous chemicals from contaminated ground is often difficult and sometimes impossible using established techniques, so earth scientists have begun to turn to related fields for innovative ideas. In petroleum engineering, the problem of recovering hydrocarbons from reservoirs is closely analogous to the problem of recovering contaminants from aquifers. A wide range of techniques has been developed to enhance the recovery of oil from reservoirs, and one of the most effective is hydraulic fracturing. This research was motivated by the possibility of using hydraulic fractures to improve the remediation of contaminated ground.

The basic process of hydraulic fracturing, as it is used in the petroleum industry, begins with the injection of fluid into a well until the pressure of the fluid exceeds a critical value and a fracture is nucleated. A granular material, which is usually sand and is termed a *proppant*, is pumped into the fracture as it grows away from the well. Transport of the proppant is facilitated by using a viscous fluid, usually a gel formed from guar gum and water, to carry the proppant grains into the fracture. After pumping, proppant holds the fracture open while the viscous gel breaks down into a thin fluid. The thinned gel is then pumped out of the fracture, creating a permeable channelway suitable for either the delivery or recovery of liquid or vapor. As a result of hydraulic fracturing the flow rates of oil wells commonly increase by factors of 1.5 to 8 (e.g. Howard and Fast, 1970). In some cases where oil or gas is present in an adjacent formation but initially undetectable in a well, hydraulic fracturing can dramatically increase the yield and make the well an economic producer, according to Howard and Fast (1970).

STATEMENT OF THE PROBLEM

Experience from oil wells suggests that hydraulic fracturing could increase flow rates from wells used to recover ground water contaminants. However, to realize this increase hydraulic fractures would have to be created and filled with sand under conditions of contaminated regions. Oil reservoirs are typically deeper and are composed of different materials than contaminated regions, so the applicability of fracturing methods used by petroleum engineers is unknown. Contaminants commonly occur in soils[1] that are weaker and more compliant than limestone or sandstone typical of reservoirs. Effects of soil properties on hydraulic fractures are difficult to anticipate based on the results of previous studies of hydraulic fractures in rock. Moreover, most contaminants occur at shallow depths (several meters to several tens of meters), so intersecting the ground surface and venting could severely limit the length, and thus the performance of the fracture. Hydraulic fractures virtually never vent when they are created in oil reservoirs, which are several hundred to several thousand meters deep, so the practical problem of creating fractures at shallow depths has yet to be addressed.

Previous investigations of hydraulic fracturing of soil have focused on methods of preventing fracture initiation, largely ignoring the problems cited above. As a result, little is known about both the basic problem of the mechanical behavior of hydraulic fracture propagation in soil, and the applied problem of creating useful, proppant-filled hydraulic fractures at shallow depths.

---

[1] The term *soil* is used in this work to mean an unlithified, or uncemented sediment

APPROACH

The approach of this research was to adapt methods proven for hydraulic fracturing of rock to applications of hydraulic fracturing of soil. Laboratory experiments were conducted by creating hydraulic fractures in rectangular samples of remolded clayey-silt confined in a triaxial pressure cell. Results of those experiments were analyzed using methods of linear elastic fracture mechanics, a branch of elasticity theory that is widely used to analyze hydraulic fractures in rock.

Two sets of field experiments were performed by creating hydraulic fractures in Pleistocene glacial drift at depths of between two and four meters. The first set was conducted during June 1988 in collaboration with a subcontractor, who used equipment designed to create hydraulic fractures from oil wells; whereas the second set was conducted during June and July 1989 by investigators from the Center Hill Facility, who used equipment that was either rented or designed for the project. Hydraulic fractures were successfully created during the field tests, and then they were exposed on the walls of trenches dug with a backhoe. Detailed descriptions of exposures document the geometries of the fractures, highlighting the potential that this process should have in remediation of contaminated soil.

MAJOR CONCLUSIONS

The project consisted of studies in the laboratory and in the field, as well as an investigation of possible applications and a review of previous work. Most remedial systems requiring fluid flow either into or out of the subsurface could benefit from hydraulic fracturing. Pump and treat systems are obvious candidates because they employ procedures resembling those used in petroleum recovery, where the benefits of hydraulic fractures are without question. The yields of vapor-producing wells, such as those recovering natural gas or steam, are improved by hydraulic fracturing, so by analogy we expect that vapor extraction systems could benefit from this technology. Similarly, hydraulic fracturing could be used in conjunction with steam stripping--a process developed to improve yields of oil wells and currently being tested under remedial conditions. Horizontal, sheet-like hydraulic fractures placed below a contaminated region could be used as gravity drains to intercept the leachate from soil flushing systems (Murdoch and others, 1987), improving the effectivness of that remedial action. Bio-remediation systems stand to benefit in particular because either nutrients for microorganisms, or the microorganisms themselves, could potentially be delivered as fine-grained solids in hydraulic fractures.

Laboratory Studies: Summary of Results

1. Hydraulic fracturing in the Center Hill clay (a type CL clayey silt) can be predicted using methods of linear elastic fracture mechanics, according to both empirical evaluation and estimates of the size of the crack tip process zone. Many published methods of analyzing hydraulic fracturing in rock,

which are based on linear elastic fracture mechanics, can be used to analyze applications in soil, with appropriate modifications for boundary conditions (e.g. ground surface), material properties (e.g. elastic constants, leakoff parameters), and state of stress encountered at shallow depths.

2. The appearance of hydraulic fractures in silt, and clayey silt resemble published descriptions of hydraulic fractures in rock created during laboratory experiments. Details of the fracturing process are sensitive to moisture content of the soil; moisture affects the appearance of the fracture tip, the magnitude of driving pressure required to initiate fracturing, and the form of the pressure record during propagation of the fracture. Changes in all those factors with changes in moisture content are particularly large when moisture conditions are near the plastic limit of the soil.

3. The critical stress intensity factor can adequately predict the pressure required to initiate hydraulic fracturing of soil. It is independent of the length of starter slot (or pre-existing fractures), for the slot lengths used in this study, and it predicts the driving pressure at the onset of fracturing to within 10 percent, on average. It was more accurate for samples whose moisture contents (moisture content = wt. water/wt. solid) exceeded 21% and less accurate for drier samples.

4. The value of the critical stress intensity is highly sensitive to moisture content, decreasing sharply from roughly 200 kPa $cm^{1/2}$ to 30 kPa $cm^{1/2}$ as moisture content increased by a few percent in the range of the plastic limit. Critical stress intensity goes to zero for samples of Center Hill clay greater than 32% moisture, although hydraulic fractures are readily created under those moisture conditions.

5. Theoretical analyses based on linear elastic fracture mechanics and linear viscous fluid mechanics explain many of the details of the laboratory experiments, including the development of an unwetted tip, the average propagation velocity, changes in the form of the pressure record with changes in slot length or moisture content.

Field Studies: Summary of Conclusions

1. Hydraulic fractures of useful size were created and propped with sand at shallow depths in glacial drift during field tests in 1988 and 1989.

2. A technique was developed that consistently produced hydraulic fractures propped with sand in glacial drift. The technique uses a unit, which is readily available for injection grouting, to inject a slurry of sand and cross-linked guar gum. To create a fracture, an apparatus composed of an outer casing and an inner rod was driven out through the bottom of a hollow-stem auger. The inner rod was removed and a water jet was used to cut a disk-shaped slot in soil enveloping the casing. Slurry was injected into the casing with a positive displacement pump, nucleating a hydraulic fracture at the slot.

3. Hydraulic fractures created during the 1989 test were nearly flat-lying; their steepest dip was 5°. In plan view, they were slightly elongate with aspect

ratios of 2:3, and they were highly asymetric with respect to their parent boreholes. They were created at depths ranging from 1 to 4 m, and the shapes and sizes of fractures created at depths between 1 and 2 m are known in detail from excavations. The dimensions are as follows: maximum distance from the borehole ranged from 0.8 to 7.2 m, and averaged 4.0 m. Areas covered by the fractures ranged from 0.8 to 36.7 m^2, and averaged 19.2 m^2. All the fractures contained sand, ranging in maximum thickness from 2 to 20 mm, and the average maximum thickness was 11 mm.

4. The fracturing apparatus facilitates the creation of multiple fractures from a single borehole. Stacks of flat-lying fractures with vertical spacings from 15 to 30 cm were created with the device.

5. The fractures were highly asymetric with respect to their parent borehole; that is there was always a preferred direction of propagation. This direction was related to loading at the ground surface, with the fracture either growing away from a backhoe parked next to the borehole, or growing in the direction of maximum slope. This indicates that topography, or surface loading (e.g. vehicles, buildings), will affect the direction of propagation of shallow hydraulic fractures.

6. Pressure records, surface uplift, and surface tilt all are available methods of monitoring hydraulic fractures at shallow depths. Electrical resistivity shows promise, although further research is required before that method is a practical monitoring tool.

7. The results of hydraulic fracturing at a site that is underalin by normally consolidated soil or fill are expected to differ markedly from the results described here. Further, during this study fractures were created in unweathered material, so the effects of creating hydraulic fractures in weathered material is unknown.

RECOMMENDATIONS

The principal recommendation is to expedite further investigation of field applications. The results of this study indicate that hydraulic fracturing potentially offers important improvements in the effectiveness of in situ remedial technologies, particularly at sites underlain by overconsolidated soil or bedrock, and our recommendation is to develop techniques necessary to assess this potential.

Specifically, we recommend the following:

1. Hydraulic fracturing should be tested during the remediation of several contaminated sites. Those field tests should assess the impact that hydraulic fracturing has on several different remedial technologies (e.g. pump and treat, vapor extraction, soil flushing, bio-remediation). They should also assess the impact of site conditions (e.g. geology, state of stress, depth of contamination, etc.).

2. Design and construct equipment intended to create hydraulic fractures at shallow depths. Equipment should be a compromise between the powerful and sophisticated rig used during the 1988 test (which lacked the required control), and the modest and simple unit used during the 1989 test (which lacked the required power and resiliency).

3. This study focused on creating hydraulic fractures in overconsolidated drift, and the results of hydraulic fracturing in normally consolidated material may differ markedly from the results reported here. We recommend that future studies develop methods of creating hydraulic fractures at shallow depths in normally consolidated soil, where in situ stresses will favor vertical fractures that are highly susceptible to venting.

4. Develop techniques of delivering nutrients and microorganisms used for bioremediation.

5. Design methods of completing and developing ground water wells intersecting hydraulic fractures.

6. Adapt or develop analyses to a.) determine treatment parameters from pressure records (e.g. Nolte and Smith, 1981, 1987; Nolte, 1988); b.) predict the size, shape and orientation of hydraulic fractures at shallow depths, particularly considering effects of topography; c.) optimize the position and dimensions of hydraulic fractures based on predictions of the transport of contaminants in the vicinity of the fractures.

SECTION ONE

POTENTIAL REMEDIAL APPLICATIONS AND PREVIOUS INVESTIGATIONS

The final decision on the use of hydraulic fractures during remediation of contaminated soilwill depend on whether the benefits they produce outweigh the effort of creating them. Most of the following report deals with the processes and problems of creating hydraulic fractures in soil, but it seems prudent at this point to review some of the potential applications and estimate the order of benefits that can be expected. Here we will assume that fractures of useful size can be created and filled with a permeable proppant.

ASSESSMENT OF POTENTIAL APPLICATIONS

Most remedial systems that require fluid flow either into or out of the subsurface could benefit from the effects expected to accompany hydraulic fracturing. Pump and treat systems are obvious candidates, as are systems involving vapor extraction, soil flushing, or steam stripping. Hydraulic fractures offer the novel possibility of delivering solid material, formed into granules and mixed with proppant, to the subsurface. Nutrients for microorganisms, or the microorganisms designed for bio-remediation themselves, could be delivered as solid grains to contaminated regions.

Filling a hydraulic fracture with material of low permeability, such as a bentonite-rich soil or grout, was proposed by Huck and others (1980) as a method of isolating contaminated material. This proposal has been investigated experimentally in the laboratory (Brunsing and Henderson, 1984), and tested in the field at a site near Whitehouse, Florida (Brunsing, 1987). The ability to place a flow barrier beneath a contaminated region without removing overburden is the principal advantage of this application. The principal drawback lies in the inability to verify continuity of a low permeability layer. Breaking into segments is a property of hydraulic fractures that seems to be inevitable. That property, combined with the presence of objects such as tree roots, will cause discontinuities in the fracture-filling that would be impossible to predict and difficult to detect using current methods. It is feasible that hydraulic fractures filled with grout could act as short-term barriers, or impediments to flow, but the likelihood of undetectable discontinuities inhibits their use as long-term barriers.

Increasing the rate of flow from a well is expected to be the most widespread application of hydraulic fracturing in remediation. The magnitude of increase will be site-specific, but a general estimate of what to expect can be obtained from the results of related applications and from theoretical analyses.

Records of oil production are irrefutable testimony of the benefits of hydraulic fracturing, and ratios of production rates are a suitable yardstick with which to measure those benefits. According to data from several dozen oil wells (Howard and Fast, 1970; Table 1.1), production ratios (production rate after fracture/initial rate) are at least 1.5 and range up to very large values. In general, the ratios range from 1.5 to roughly 10 for wells that were producing before fracturing, and the ratios are very large for wells showing negligible production prior to fracturing.

		RATE OF OIL PRODUCTION in Barrels of Oil per Day		
STATE	FORMATION	Before frx	After frx	Ratio (after/before)
Alaska	Kenai sand	1128	1584	1.4
Calif.	Stephans sand	20	120	6.0
	Vaqueros sand	10	70	7.0
Canada	Beaverhill ls.	0	75	-
	Cardium sand	50	204	4.1
	Villenuve quartz	0	4*	-
Colorado	Weber sand	20	110	5.5
Illinois	Cypress sand	4	35	8.7
	McCloskey ls.	4	50	12.5
Kansas	Arbuckle ls.	10	40	4.0
	Herrington ls.	670*	2050*	3.1
	Kansas City ls.	6	30	5.0
Louisiana	Annona Chalk	5	20	4.0
	Hackberry sand	30	115	3.0
	Marguilana sand	15	104	6.9
Michigan	Richfield ls.	22	150	6.8
New Mex.	Grayburg ls.	15	110	7.3
	San Andres ls.	20	60	3.0
	Mesa Verde	490*	5000*	10.2
N.Dakota	Madison ls.	111	295	2.6
Ohio	Berea sand	0	60	-
Oklahoma	Bartlesville sand	25	275	11.0
	Basal sand	80	350	4.4
	Granite wash	120	550	4.6
	Mississippi ls.	trace	168	-
	Pennsylvanian	130	475	3.6
Penn.	Bradford sand	6	55	9.1
Texas	Brown dolomite	6	65	10.8
	Camerina sand	26	230	8.8
	Canyon limestone	50	130	2.6
	Reklaw sand	72	113	1.6
	Strawn sand	10	35	3.5
	Wilcox sand	15*	1100*	73.0
West Va.	Benson sand	3.5*	66.1*	18.9
Wyoming	Dakota sand	25	125	5.0
	Frontier sand	16	70	4.4
	Madison limestone	473	715	1.5
	Phosphoria ls.	1050*	3050*	2.9
	Tensleep saand	20	65	3.2

* units of (Mcubic ft./day)

Table 1.1 Data describing the production rates from oil wells before and after hydraulic fracturing. From Howard and Fast (1970).

Production rates, from either fractured or unfractured wells, typically decrease as a function of time due to depletion of the reservoir, clogging of pores, or other processes. Behaviors of fractured wells through time were characterized by Howard and Fast (1970) in their classic monograph,

> "The effect of [hydraulic] fracturing on both short and long term well productivity has been studied by many investigators, most of whom conclude that, regardless of the kind of treatment, four basic patterns of production behavior have been observed.
>
> *Type A*: Sustained increase in well production accompanied by a flattening of the production decline curve following treatment.
>
> *Type B*: Sustained increase in production with the well's highest rate of production after the treatment declining essentially at the same rate established before treatment.
>
> *Type C*: Transitory increase in production lasting from a few months to several months, after which the well continues to follow the production decline trend observed prior to treatment.
>
> *Type D*: No increase in production, with the well continuing to follow its established, normal production history.
>
> In no case did a treatment have a discernibly detrimental effect on the production performance of the well."

In one example of a Type A or B result (Fig. 1.1), the production rate at a well in North Texas increased by a factor of four, from 20 to 80 barrels of oil per day (bopd), and then gradually decreased to 30 bopd over the subsequent seven months. Interestingly, a second hydraulic fracturing job increased the production rate to 80 bopd (Fig. 1.1).

Yields of water wells are also increased by hydraulic fracturing (e.g. review by Smith, 1989). Thirty years ago Koenig (1960) examined data from wells used for waterflooding or waste disposal and reported that 78 percent of those wells showed an increase in yield following hydraulic fracturing. The ratio of yields ranged up to 100, with a median of 5.0. More recently, Stewart (1974, 1978) observed increases in yields from water wells drilled in granite or schist formations in New Hampshire. Yields of one well reported by Stewart increased from 0.30 to 1.82 l/s, (ratio of 6.0), and at another well yields increased from 0.26 to 1.14 l/s (ratio of 4.4). A particularly impressive increase in yield of 22 to 25 times is described by Mony (1989), who cites a water well drilled in gneiss that yielded 0.0077 l/s prior to fracturing and 0.16 to 0.19 l/s after fracturing. Waltz and Decker (1981) used hydraulic fracturing to stimulate wells in crystalline rock in Colorado and reported ratios of yields of 1.5 to 2.0. Williamson and Woolley (1980) created hydraulic fractures from water wells penetrating igneous or metamorphic rocks in Australia, and cited improvements in specific yield by factors of 5.0 to 6.0. Several other authors (Hurlburt, 1989; Waltz, 1988; Baski, 1987; Macaulay, 1987) have recently claimed that hydraulic fracturing of water wells consistently results in increased yields that are economically significant.

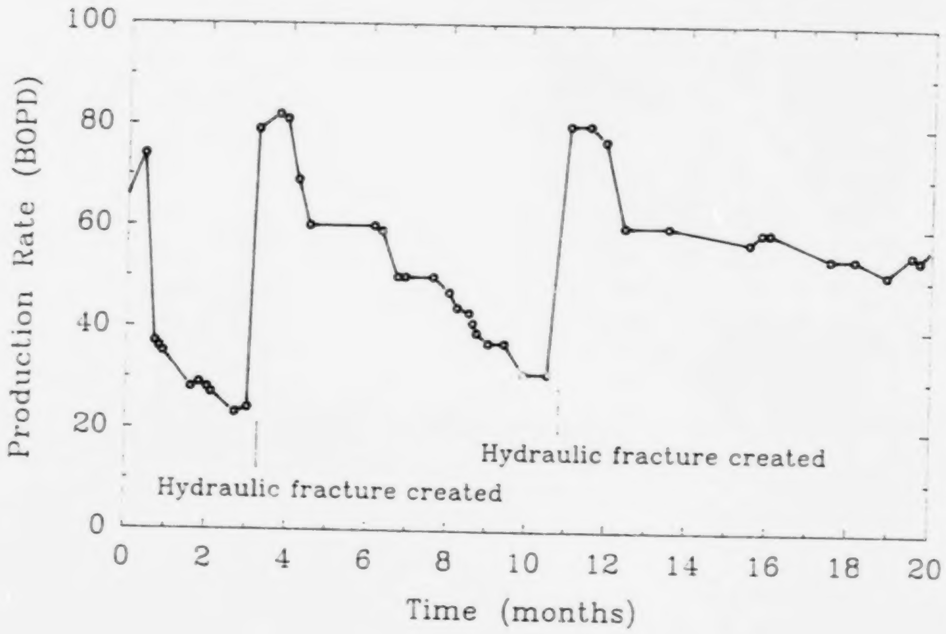

Figure 1.1. Production rate of an oil well in North Texas as a function of time.

Rates of inflow into wells used for waste disposal (Stow and others, 1985; Wolff and others, 1975; De Laguna, 1966 a and b), or as infiltration galleries are increased by hydraulic fracturing. Rates of inflow were measured as part of this project from five open boreholes intersecting sand-filled hydraulic fractures created in unsaturated glacial drift. The fractures were flat-lying, typically 1 cm in maximum thickness and as much as 8 m in maximum dimension.

For comparison, inflow rates were measured from three similar boreholes penetrating unfractured drift. Boreholes intersecting hydraulic fractures are EL2, EL5, EL6, EL7, whereas those in unfractured ground are TB1, TB2, TB3.

All boreholes were 5 cm in diameter and 2 m deep. Tests were conducted using Guelph Borehole Permeameter, manufactured by SoilMoisture Inc., Santa Barbara, Ca. The permeameter enabled us to measure flow rates while maintaining a constant water depth of one meter above the bottom of the borehole.

Rate of inflow into unfractured boreholes diminished slightly with volume, approaching steady-state rates after one to three liters. The steady-state rates were between 0.04 and 0.07 l/min, depending on the well, and the average rate was 0.055 l/min.

The rate of inflow into the wells intersecting hydraulic fractures also diminished with time, but larger volumes, as much as several tens of liters, were required to achieve steady-state. Initially, inflow rates were as rapid as 2 to 3 l/min, the upper limit that could be supplied by the permeameter. The rates diminished with volume, but they were greater than those of the unfractured wells even after large volumes. For example, the rate of inflow was roughly 0.4 l/min after 200 liters of water flowed into EL7, and the rate was 0.175 after 350 liters flowed into EL4. Steady inflow into the fracture wells occurred at 0.30 l/min.

In the works cited above, effects of a hydraulic fracture were illustrated using the ratio of flow after fracturing to flow prior to fracturing. The method used to create the hydraulic fractures precluded measuring inflow at a well before it was fractured. The average inflow into an unfractured well in the vicinity of a fractured well will be used to determine the ratios (Table 1.2). Values range from 3.1 to 9.0 for steady-state conditions, and they are typically several times greater than that for unsteady state (Fig. 1.2).

Inflow into the boreholes that intersect fractures probably would have been greater if screen and gravel packing was used to prevent collapse. The boreholes filled with mud to depths of several dm while they contained water during inflow testing. Nevertheless, the data do suggest that hydraulic fractures in unsaturated ground could provide marked improvements to remedial systems based on soil flushing.

Wells used for purposes ranging from delivery of water in unsaturated soil to recovery of oil in reservoirs have shown strikingly similar responses after hydraulic fracturing -- their yield is consistently increased, and the magnitude of increase ranges up to several orders of magnitude or more. Typically, the ratio of yields is roughly 1.5 to 8 or 10 for wells that are producing prior to fracturing, but it can be greater than 10 for wells that are initially poor producers.

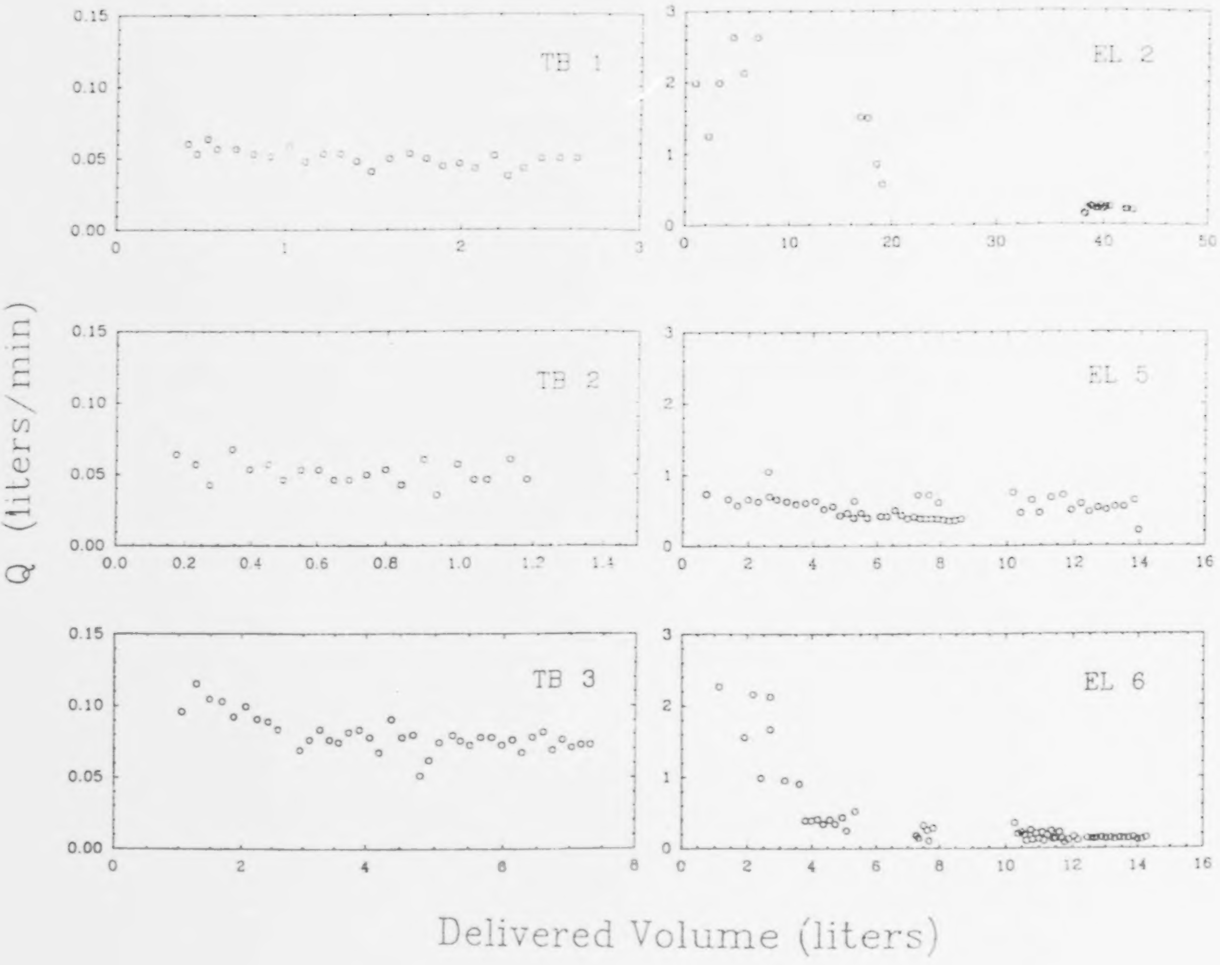

Figure 1.2 Rates of inflow into boreholes in till. TB1,TB2,TB3, are test borings, whereas EL2 through EL7 are borings intersecting hydraulic fractures.

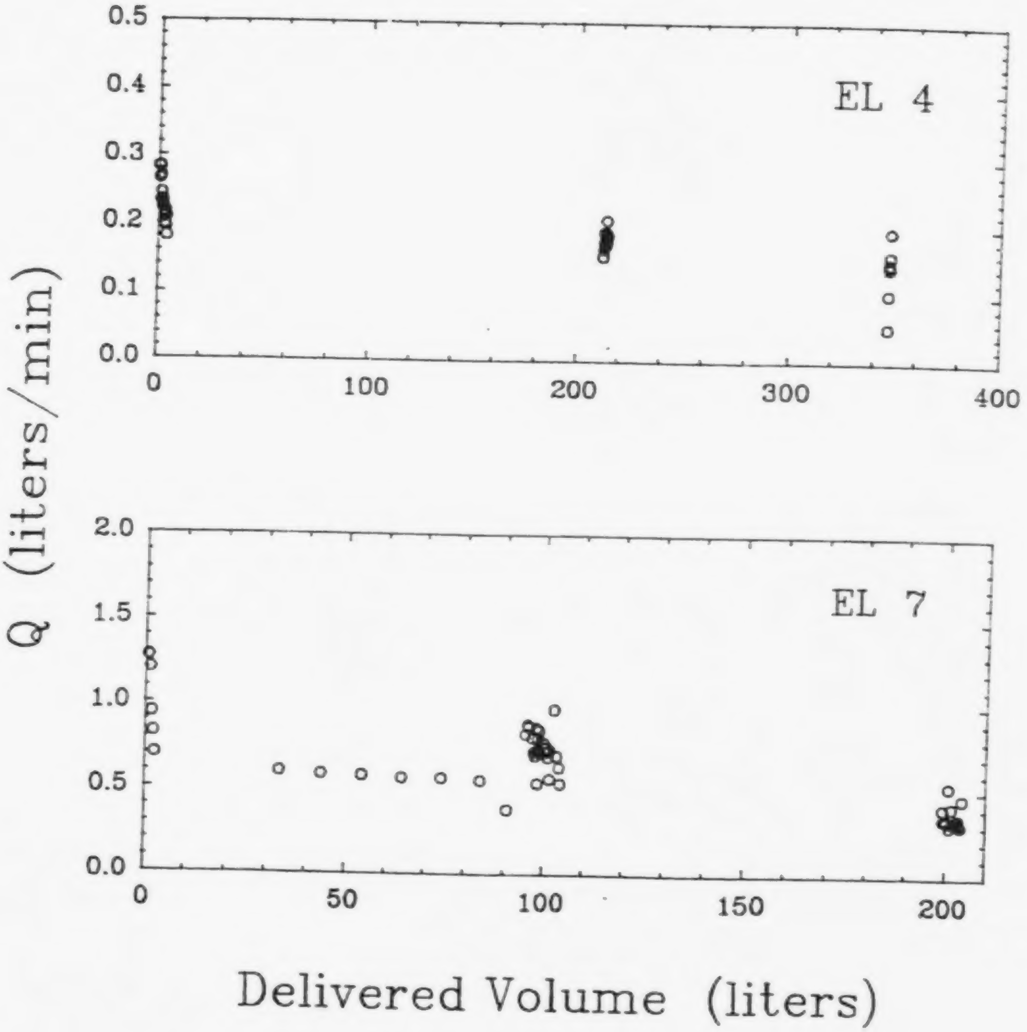

Figure 1.2 (continued).

TABLE 1.2 INFLOW RATES INTO SILTY CLAY

Borehole	Steady inflow l/min	Average	Ratio
TB1	0.04		
TB2	0.05		
TB3	0.075	0.055	
EL2	0.20		3.6
EL4	0.175		3.1
EL5	0.50		9.0
EL6	0.20		3.6
EL7	0.40	0.30	7.3

Predicting Flow to Wells That Intersect Fractures

Early schemes of predicting flow to wells that intersect hydraulic fractures were based on empirical studies, electrical analogs, and simple theory. Results were obtained for fractures that were either vertical and rectangular in shape (Prats, 1961, McGuire and Sikora, 1960; Dyes and others, 1958; van Poolen and others, 1958), or horizontal and circular in shape (Landrum and Crawford, 1961; Hartsock and Warren, 1961; Morrisson and Henderson, 1960). Today, those schemes are important for simple calculations, but more sophisticated numerical models (Gringarten, 1982; Cinco-Ley and others, 1981, 1978) are available for detailed analyses.

Many of the available analyses can be used to obtain the specific yield of a well intersecting a hydraulic fracture, which when divided by the specific yield of the well without a fracture results in a dimensionless measure of the improvement of the well. This ratio will be termed the recovery capacity J in the following pages. Recovery capacity in general depends on conditions of the fracture, such as its size, shape, aperture, location, and permeability of proppant, and on conditions of the reservoir or aquifer, such as its permeability, dimension, and the location of the well within it.

Two analyses will provide useful insights: one that shows the importance of fracture length, relative transmissivity, and radius of influence at steady-state, and another that shows the importance of fracture length as a function of time. Prats (1961) analyzed the effect of a vertical fracture of finite permeability k_f and thickness d in a confined aquifer bounded laterally by surfaces of constant pressure. Relative transmissivity T_r is defined by Prats (1961) as

$$T_r = 2k_f d/\pi k_s a \qquad (1.1)$$

where k_s is the permeability of enveloping soil or rock, a is fracture half-length. Prats describes T_r as the ratio of the ability of fluid to travel along the fracture to the ability of fluid to travel through the enveloping material and reach the fracture. The flow at the fracture increases with relative transmissivity for values of T_r between 0 and 1.0. For values of T_r greater than 1.0, however, the effect of T_r is negligible (Prats, 1961) and the fracture behaves at steady-state as if its permeability were infinite. This result is important because it indicates that in many field cases the permeability of a propped hydraulic fracture can be assumed to be essentially infinite, thereby avoiding analytical difficulties associated with fractures of finite permeability.

Assuming that the relative transmissivity is essentially infinite, the steady-state recovery capacity is

$$J = ln(r_e/r_w)/ln(r_e/(L/4)) \tag{1.2}$$

in which r_w is the actual radius of the well, and r_e is the effective radius of the area drained by the well, and L is the total fracture length. In a field of regularly-spaced wells, for example, the effective radius is roughly half the spacing between wells.

According to eq. (1.2) the steady-state behavior of the fracture is the same as that of a well whose radius is equivalent to $L/4$. A vertical fracture 10 m long would behave as a well 2.5 m in radius, so that the equivalent radius of a fracture can be much larger than most wells.

Recovery capacity certainly increases with fracture length, but its magnitude depends on the ratio of fracture length to effective radius. According to this analysis, the recovery capacity will be greatest when the fracture extends across the area drained by the well. Assuming $L = 2r_e$, the maximum J is

$$J_{smax} = 1.44\, ln(L/2r_w) \tag{1.3}$$

For example, 2.3 is the maximum recovery capacity of a fracture 10 times as long as the radius of the unfractured well, whereas the value increases to 5.6 for a fracture 100 times the well radius, according to this analysis.

As the effective radius increases, the steady-state recovery capacity decreases and approaches unity. For a single well in a large aquifer, therefore, the steady-state yield from a fractured well will approach that of one from an unfractured well. This conclusion is misleading, however, because it ignores potential increases in yields during the transient period of recovery before steady-state is achieved.

Recovery capacity is typically greatest shortly after fracturing and then it decreases with time, as shown in Figure 1.1 for example. A solution to the transient recovery capacity can be obtained in analytical form from dimensionless drawdown functions for a well and for a fracture. Dimensionless drawdown S_{aw} of a vertical well in a confined aquifer of thickness h is obtained by assuming the well behaves as a line sink (Ramey, 1967), so

$$2\pi\, hKp/Q = s_{dw}(1/t_{dw}) \tag{1.4}$$

where

$$t_{dw} = 4tKh/Sr^2 \tag{1.5}$$

and K and S are the hydraulic conductivity and the storage coefficient of the aquifer, respectively; t is the time of pumping, p, Q, and r are the drawdown, pumping rate and radius of the well, respectively. The drawdown function $s_{dw}(1/t_{dW})$ is an exponential integral given by Ramey, 1967 and polynomial approximations of the integral are in Abramowitz and Stegun (1964).

Hydraulic fractures are commonly idealized as planar sinks in flow problems because analytical solutions to several relevant geometries are available. Solutions to dimensionless drawdowns due to planar sinks can be reduced to forms similar to those for a line sink

$$2\pi hKp/Q = s_{df}(t_{df}) \tag{1.6a}$$

where

$$t_{df} = t_{dw}/n \tag{1.6b}$$

and

$$n = (2a/r)^2 \tag{1.6c}$$

in which a is a characteristic length, such as the radius of a circular sink (fracture). Drawdown functions s_{df} have been published for an envelope-shaped vertical fracture (Gringarten, and others, 1974), a circular horizontal fracture (Gringarten and Ramey, 1974), and functions for other shapes can be determined using methods given by Gringarten and Ramey (1973).

Solving eqs. (1.4) and (1.6) for recovery capacity leads to

$$J(t_{df}) = Q_f\, p_w/p_f Q_r = s_{dw}(1/nt_{df})/s_{df}(t_{df}) \tag{1.7}$$

where the drawdown function used for $s_{df}(t_{df})$ depends on the geometry of the problem. Accordingly, in this formulation improvements in recovery indicated by $J > 1.0$ are a result only of the difference in geometry between a sheet-like fracture and a line-like well.

Many hydraulic fractures created at shallow depths (less than roughly 300 m) are flat-lying and roughly equant, a geometry that can be approximated by a planar sink that is flat-lying and shaped like a circular disk. The drawdown function for a fracture of that geometry in a confined aquifer (e.g. Gringarten and Ramey, 1974;

eqs. 51 and 53) was used in eq. (1.7) to produce Figure 1.3. The ratio of aquifer thickness T to well radius r was held constant and equal to 250, and the fracture was assumed to be at mid-height in the aquifer ($z/T = 0.5$ where z is the height of the fracture above the bottom of the aquifer). Recovery capacity was determined as a function of time for ratios of a/r between 50 and 1000. The radius of the fracture equals the aquifer thickness when a/r equals 250, and it is four times the aquifer thickness when a/r equals 1000. Although the dimensionless form is valuable for many applications, a reference value of t_{df} may be helpful in some cases: if $K = 10^{-4}$ cm/sec, $S = 0.001$, $a = 10$ m, $T = 11.6$ m; then $t_{df} \times 10 = t$ in days.

Results of the analysis indicate that the recovery capacity at any given time increases with relative fracture length. Recovery capacity is roughly unity when $a/r = 50$, indicating that the recovery from a fracture 50 times the radius of a well will be similar to that of an unfractured well. As the ratio a/r increases to 1000, the value of J increases to 8.0, and even greater values of J are obtained for earlier times or longer fractures.

Magnitudes of J diminish with time because geometric advantages of a planar sink decrease compared with those of a line sink as water is removed from regions at increasingly greater distances from the sinks. Even at relatively large values of t_{df}, however, the recovery capacity is significantly greater than 1.0 (Fig. 1.3), indicating that the fracture is performing better than the well. The performance of the fracture would be even better if we assumed that the well draining the fracture was screened for the full thickness of the aquifer, which is a reasonable assumption for most applications. That case can be approximated by adding 1.0 to the right hand side of eq. (1.7), or to values of J shown in Figure 1.3.

Summary

In the previous section we have seen that hydraulic fracturing increases the yields (or inflow rates) of oil and gas wells, water wells, and infiltration wells. The magnitude of increase is consistently between 1.5 and 5 times, routinely as much as 10 times, and in some cases much more than 10 times. In general, hydraulic fracturing offers the greatest relative increase to wells which show poor yields prior to fracturing. Of course, if the initial yield of a recovery well is extremely low, even the improvement offered by hydraulic fracturing may be insufficient to make recovery a viable remedial solution. That judgement will depend on analyses of costs, which exceed the scope of this investigation.

Observations indicate that yields of fractured wells diminish with time, just as they do at unfractured wells. The relative improvement of the well diminishes following fracturing, but the effect of the fracture can be important even after many months or longer. In some cases, wells can be re-stimulated and their yields increased creating another hydraulic fracture.

A simple theoretical analysis, based on the difference in shape between plane and line sinks, predicts improvements in specific yield that are similar, both in magnitude and behavior with time, to improvements observed in the field. It follows that improvements in yield result principally from the geometric effects of the fractures.

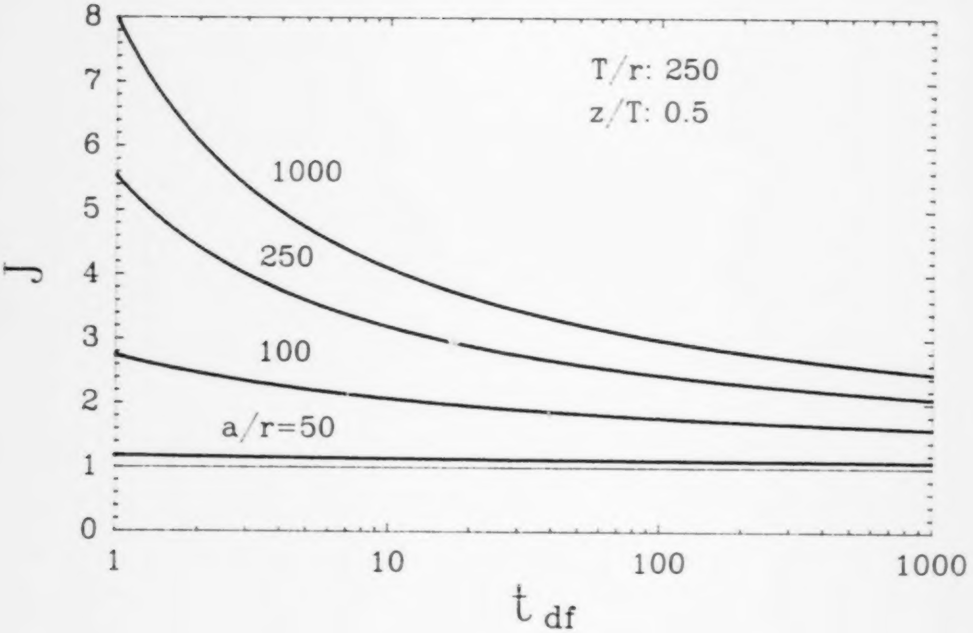

Figure 1.3. Recovery capacity of a flat-lying, circular fracture in a confined aquifer.

We conclude that the magnitude of increase in yields of contaminant recovery wells will be similar to that of wells used to recover oil, natural gas, or water from rock. Hydraulic fractures are expected to increase the yields of recovery wells in soil or rock by several times, or perhaps up to an order of magnitude. Detailed predictions of the effects of hydraulic fractures at a particular site will require more sophisticated analyses, but the general magnitude of the improvement in yield predicted by the data and analyses described above justifies further investigation into this process.

PREVIOUS STUDIES OF HYDRAULIC FRACTURING

To some investigators hydraulic fracturing is a blessing, to others it is a curse. This difference is driven by the effect of fracturing on particular processes, and it has resulted in two different research goals. When hydraulic fracturing produces useful results, such as increasing the yield of a well, providing a measure of in situ stress, or generating insight into geologic process, investigators generally focus on predicting the characteristics of a fracture (e.g. size, shape, orientation). When hydraulic fracturing causes problems, such as collapsing a dam, compromising a permeability test, or bleeding off grout or waste from a borehole, however, investigators generally focus on predicting, and thus preventing, initiation. To the latter group, the characteristics of hydraulic fractures are of little interest.

A thorough review of the vast body of published work related to hydraulic fracturing would fill several volumes, so the following section is intended only as a brief overview. Other reviews relevant to the present work have been published by Cleary (1988), Mendelsohn (1984), Veatch (1983 a and b), Geertsma and Haafkens (1979). The classic SPE monograph on hydraulic fracturing by Howard and Fast (1970) is a valuable source, and a revision of that monograph will be published in the near future.

The Hydraulic Fracture as a Tool

As early as the mid-1930s it was widely recognized by workers in the petroleum industry that pressurizing a well could fracture the enveloping formation (Yuster and Calhoun, 1945). The first use of proppants to hold fractures open, however, was the key to developing a technique of widespread importance. The first description of the creation of propped fractures is generally attributed to Clark (1949), who outlined a process that closely resembles the ones used today. Clark claimed that hydraulic fractures had been created at 32 wells when his paper was submitted for publication in 1948. Several years later in 1953, a patent of the hydraulic fracturing method was reissued to R.F. Ferris, a colleague of Clark (Howard and Fast, 1970).

During the 20 years following Clark's paper the application of hydraulic fracturing to oil and gas wells became routine, and by 1968 the technique had been used at roughly 500,000 wells (Howard and Fast, 1970). Success rates, indicated by an increased yield after fracturing, were between 75 and 80 percent during the early years, but they increased to nearly 90 percent by the late 1960s, according to Howard and Fast (1970).

Typical fracturing operations pumped volumes on the order of several thousand to several tens of thousands of gallons prior to 1970, but in the following years the sizes of fracturing jobs increased to a million gallons or more. These so-called massive hydraulic fractures opened oil reserves that could not be economically produced using previous methods. Costs involved with creating massive hydraulic fractures spurred the modern era of research into methods, materials, analyses and designs of hydraulic fracturing.

Petroleum companies are the primary users of hydraulic fractures, but they are by no means the only ones. The generation of thermal energy from hot dry rocks is a technology that makes use of hydraulic fractures to create flow paths in basement rock. In principle, two wells drilled into hot rock are linked together by one or more hydraulic fractures (e.g. Murphy, 1982; Ernst, 1980). Cold water is injected into one well, it flows through the hydraulic fractures and is heated by the wall rocks, and then is recovered at the other well where it is used to drive turbines for electrical power. This application was successfully implemented in a small-scale test at Fenton Hill, New Mexico, where two wells 2.75 km in depth were connected by a fracture 0.3 km in height (Kerr, 1987; Murphy, 1982). The hydraulic fracture acted as a heat exchange producing 3 megawatts of power. A second phase of that project, intended to create larger fractures and produce more power, encountered difficulties. Two boreholes were drilled to depths of 4.6 km, but hydraulic fractures created at one well failed to intersect the neighboring well, presumably injection resulted in slippage along many natural joints rather than dilation of a single fracture (Kerr, 1987). In a related project in Cornwall, England, investigators used gel to open natural fractures, successfully creating a circulation loop between two wells. This project was producing 5 megawatts of thermal power after two years of operation (Kerr, 1987). Similar projects involving the circulation of water through hydraulic fractures linking two boreholes have been evaluated in France (Cornet and others, 1982), and Germany (Rummel and Kappelmeyer, 1982).

Proppant was omitted from fractures created during the projects cited above, because thermal breakdown of the guar gum-based gel used to transport proppant could cause sand to plug the well casing during fracturing. A modified gel, intended for use at high temperatures, was employed by Nakatsuka and others (1982), who created hydraulic fractures used to recover wet steam at the Nigorikawa geothermal field in Japan. They injected as much as 81 metric tons of sand per fracture, and increased the yields of steam or hot water by factors as great as 2.3.

Water wells can be stimulated by hydraulic fracturing, as indicated by data cited in a previous section. Most of the applications are to water wells in igneous or metamorphic rock, where the natural permeability is low and the wells are initially nearly dry (Hurlburt, 1989; Waltz, 1988; Baski, 1987; Macaulay, 1987; Williamson and Wooley, 1980; Stewart, 1974, 1978). The use of proppant in hydraulic fractures at water wells is unnecessary in many cases because sufficient yields can often be achieved using water alone (Smith, 1989; Baski, 1987; Williamson and Woolley, 1980). Presumably this occurs because fractures in hard rock can be held open by asperities on fracture surfaces (Paillet, 1985; Detournay, 1979). Omitting proppant from a fracture eliminates the need for a blender and a sand supply, considerably reducing the expense of the fracturing operation.

Several other industries that use wells to gain access to the subsurface have applied hydraulic fracturing. The mining industry, for example, extracts soluble minerals such as halite, sylvite, sulfur, or uraninite by circulating fluids through natural ore deposits. Solution mining operations commonly employ two wells, one to produce and another to inject fluid. Hydraulic fractures are used to increase the flow rate between the two wells, in a design similar to that of geothermal energy operations (Haimson and Stahl, 1970).

Various industries have disposed of wastes by injecting them into hydraulic fractures. In 1958, injecting radioactive waste into hydraulic fractures was first considered by the Atomic Energy Commision as a means of disposal (De Laguna, 1966). This application was evaluated for 20 years at the Oak Ridge National Laboratory (Stow and others, 1985), where radionuclides were mixed with cement-based grout and injected into a shale formation. The grout formed nearly flat-lying hydraulic fractures roughly 300m below the ground surface (Stowe and others, 1985; Holzhausen and others, 1985 a and b; De Laguna, 1966).

Deep well injection is a popular technique of waste disposal that can either benefit or suffer from hydraulic fracturing. On one hand, hydraulic fracturing during deep well injection will increase the rate of injection (Bouwer, 1978) and thereby reduce the cost of disposal. On the other hand, hydraulic fractures can propagate upward from the bottom of the disposal well, cutting through low permeability formations intended to isolate the waste and possibly contaminating overlying aquifers (Wolff and others, 1975).

The state of stress in the earth's crust is a central topic of interest to investigators of tectonics, structural geology, earthquake prediction, mining, well stimulation, soil or rock mechanics, and related disciplines. Hydraulic fracturing has been used by those scientists since the early 1960s, when Scheidegger (1960, 1965), Kehle (1964), and Fairhurst (1964) proposed that the pressure required to initiate a hydraulic fracture from a well bore was related to the magnitude of in situ stress. Their method idealizes a wellbore as a pressurized cavity and assumes that hydraulic fracturing occurs when the magnitude of tensile stress in the wall of the cavity exceeds the tensile strength *S* of the formation. Assuming the wellbore is a long cylindrical cavity in a porous formation, the maximum horizontal compressive stress is given by

$$s_{\mathrm{Hmax}} = S + 3s_{\mathrm{Hmin}} - p_w - p_o \qquad (1.8)$$

in which p_w is the pressure in the wellbore at the onset of fracturing, s_{Hmin} is the minimum horizontal compressive stress, and p_o is the pressure of pore-fluid in the formation.

To solve eq. (1.8), tensile strength *S* is determined by testing core samples and the pressures p_o, p_w are obtained from transducer measurements before and during fracturing. The minimum confining stress $_{\mathrm{Hmin}}$ is generally equated to the wellbore pressure at the instant the fracture closes shut after pumping has ceased (termed the instantaneous shut-in pressure, or ISIP). Kehle (1964) presents an eloquent argument supporting the use of the ISIP in determining $_{Hmin}$ Most investigators agree that the ISIP is marked by a subtle change in slope of the pressure record after pumping has ceased, but there are a variety of methods of estimating this pressure (e.g. Aamodt and Kuriyagawa, 1982; McLennan and Roegiers, 1982; Gronseth, 1979; Nolte, 1979; Bjerrum and Anderson, 1972). The methods of Nolte and Smith (Nolte, 1979, 1982; Nolte and Smith, 1981; Smith, 1981; Nolte and Smith; 1987) are particularly robust, yielding not only $_{Hmin}$but leakoff coefficients, proppant schedules, and other parameters used to design hydraulic fracture treatments.

Flaws in the walls of boreholes, either natural fractures or cracks created during drilling or perforating a well, will nucleate hydraulic fractures and cause errors in in situ stress measurements if they are overlooked (Warpinski, 1983). Abou-Sayed and others (1978) present theoretical analyses based on linear elastic fracture mechanics that account for pre-existing cracks in a borehole during in situ stress measurement. Their analysis requires knowing the size and shape of pre-existing fractures intersecting the borehole, information that is generally difficult to obtain for naturally-occurring fractures. This difficulty is avoided by deliberately cutting a notch of known dimension in the wall of the borehole to dominate the effects of natural fractures.

Geologists have recognized natural features that formed by processes closely resembling hydraulic fracturing. The features are tabular in form and they are filled by materials that differ in composition or texture from enveloping material. Igneous sheet intrusions (Pollard, 1978), clastic dikes (Shoji and Takenouchi, 1982), hydrothermal breccia dikes (Bryant, 1968; Farmin, 1934), and some mineralized veins (Kesler and others, 1981; Anderson, 1974; Phillips, 1972 and 1973) are interpreted as resulting from natural processes related to hydraulic fracturing. High pore pressures induced by seismic shocks accompanying earthquakes (Holzer and others, 1989) can fracture overlying sediments and erupt at the ground surface as sand blows, or sand boils (Shoji and Takenouchi, 1982).

Studies of those natural features have certainly benefited from research conducted by the petroleum industry, but it has by no means been a one-way street. Natural analogs to hydraulic fractures can be studied directly where they are exposed at the ground surface, a luxury seldom afforded investigators in the petroleum industry. Much of what is known about the details of large-scale fractures has been derived from studies of exposures of igneous dikes and sills. In their argument for the state of stress as a fundamental control of the orientation of hydraulic fractures, for example, Hubbert and Willis (1957) first noted the mechanical similarity between dikes and hydraulic fractures. Then they cited the similarity between the pattern of dikes at Spanish Peaks, Colorado, and the pattern of principal stresses calculated by Ode (1957). Later, Pollard (1978, 1973) and Polard and others (1975) showed that dikes and sills are tabular in gross form, but are discontinuous in detail. The discontinuities are particularly well-developed near leading edges, where they appear as segments, or elongate lobes. Pollard (1978) argues, by analogy, that hydraulic fractures should also be discontinuous, and his argument is supported by later theoretical analyses (Pollard and others, 1982) showing how a fracture could break into segments in response to small fluctuations in the in situ state of stress. This insight is significant because it suggests that hydraulic fractures filled with grout and used as barriers to flow (Huck and others, 1980; Brunsing, 1987) could be plagued by imperfections that compromise the integrity of the barrier. Furthermore, the performance of fractures filled with sand and used as drains could be reduced if some of the sand is isolated in discontinuous lobes (Pollard, 1978).

Experiments

Experiments conducted in the laboratory or the field have contributed to useful applications of hydraulic fracturing. Laboratory experiments are designed either to measure material properties, to test theories, or to illustrate effects of processes that are difficult to analyze theoretically. Fracture toughness[2] is a material property, which was introduced to predict fracture in metals (Irwin, 1957), but has been applied the prediction of fracture in rock as well. Traditionally, fracture toughness has been ignored (set to zero) because the energy required to overcome viscous forces in large fractures is several orders of magnitude greater than the energy required to overcome material toughness (Cleary, 1980a). Recently, however, it has been recognized that fracture toughness can affect aperture and shape in cross-section (Spence and Turcotte, 1985; Nilson and Griffiths, 1986; Abe and others, 1976), and that natural variations in toughness can affect the shape of the leading edge of a hydraulic fracture (Thiercelin and others, 1989).

Methods of measuring fracture toughness of rock differ widely in specimen geometry and type of loading, but they all have one feature in common: the use of a large notch, or starter slot, cut in the sample. The starter slot nucleates failure at a pre-existing fracture of known dimension, thereby avoiding the problem of characterizing effects of naturally-occurring cracks or flaws. Some methods are adaptations of ASTM techniques, which apply external loads to measure fracture toughness of metal specimens (Klepaczko and others, 1984; Ouchterlony, 1982; Cleary, 1978b; Schmidt, 1977), whereas others are patterned after the hydraulic fracturing process and inject fluid to measure fracture toughness (Clifton and others, 1976; Abou-Sayed, 1977).

Early theories (e.g. Haimson and Fairhurst 1967; Kehle, 1964; Harrison and others, 1954) predicted that hydraulic fracturing would initiate when the circumferential stress on the wall of a borehole exceeded the tensile strength of the formation. This theory was tested by Haimson and Fairhurst (1969) by injecting fluid into cylindrical samples of hydrostone, a gypsum cement exhibiting properties similar to natural rock. They observed that during injection the fluid pressure increased and then abruptly decreased, and they assumed that fracturing, or *breakdown*, initiated at the maximum pressure. According to the elastic solution of Haimson and Fairhurst (1967), breakdown pressure increases linearly with confining pressure, but both the slope and intercept of breakdown as a function of confining pressure decrease if injection fluid penetrates the sample prior to fracturing.

---

[2] The term *fracture toughness* is used in this work only as a nominal criterion of measuring resistance to fracturing, without any implication to specific criteria, such as the critical stress intensity factor, critical strain energy release rate, *J* integral (Lawn and Wilshaw, 1975), or the fracturability index (Daneshy, 1976b).

Results of their experiments (as well as those of early studies by Harrison and others, 1954; and Scott and others, 1953) showed that fluid penetration reduces the breakdown pressure, similar to the theoretical results. In detail, results of the elastic theory predicted slightly less breakdown pressures than were actually observed by Haimson and Fairhurst (1969), a difference they attributed to plastic deformation in the walls of the borehole that was omitted by their analysis. Medlin and Masse (1979) performed similar experiments. Their results show that the elastic theory predicts breakdown pressures at relatively low confining stress, but tends to overestimate breakdown when confining pressures exceed some critical value, which depends on rock type. Medlin and Masse (1979) attribute this deviation to plastic deformation induced by the confining stresses, and they offer a modified theoretical analysis that is consistent with their results.

Haimson and Fairhurst (1969) also reported that the breakdown depended on the rate of pressurization; it increased as the rate increased. Zoback and others (1977) offered an explanation by using an increase in acoustic emissions (AE), rather than a change in slope of the pressure record, to indicate the onset of fracturing. According to Zoback and others (1977), during relatively low rates of pressurization an increase in AE occurred at the same time as the breakdown pressure. As the rate of pressurization increased, the pressure of fracturing (as indicated by AE) remained roughly constant, although the breakdown, or maximum pressure increased dramatically.

Theoretical analyses of fracture propagation have been tested in the laboratory since the first analyses were proposed. Harrison and others (1954) created hydraulic fractures in photoelastic gelatin to verify an analysis of hydraulic fracturing based on elasticity theory and originally published by Sneddon (1946). Fractures they created experimentally had ratios of length to width that were similar to those predicted by the simple theory (Harrison and others, 1954; fig, 6). Moreover, photographs of the experiments revealed fractures that were elliptical in cross-section, the shape predicted by Sneddon's theory. More recently, Medlin and Masse (1984) created fractures in rectangular blocks fitted with ultrasonic transducers to sense the fracture during propagation. Their results show that the injection fluid lags slightly behind the leading edge, resulting in an unwetted zone at the tip of the hydraulic fracture. The existence of an unwetted tip was long suspected on theoretical grounds (Khristianovich and Zheltov, 1955; Barenblatt, 1962). Rates of growth, dilation, and the pressure record during fracturing in the experiments were shown to be consistent with two-dimensional, plane-strain theories of fracture propagation (e.g. Khristianovich and Zheltov, 1955; Geerstma and de Klerk, 1969; Spence and Turcotte, 1985).

The orientation of hydraulic fractures normal to the least principal stress is a result obtained nearly universally, from the early studies of Hubbert and Willis (1957), or Haimson and Fairhurst (1969) to the more recent work of Hanson and others (1979), and Medlin and Masse (1979). Daneshy (1973) showed that the local state of stress induced by a cylindrical borehole can cause the initial orientation of a hydraulic fracture to differ from that favored by far-field conditions. In most of Daneshy's experiments, fractures contained the axis of the borehole where they were adjacent to the hole, but the fractures curved or twisted out of their original plane until they were normal to the direction of least far-field compression at some distance from the hole. Similar results were obtained by Medlin and Masse (1979), who report that the initial orientation of fractures would contain the axis of the borehole and ignore the presence of shallow notches cut in the wall of the hole at orientations favorable to the far-field conditions. Deeper notches overcame the effects of the borehole, nucleating hydraulic fractures in the plane of the notch instead of parallel to the axis of the borehole. The results of those studies are important to field applications, such as the tests described in later chapters, where horizontal fractures are created from vertical boreholes.

Model studies have contributed to the understanding of how hydraulic fractures behave at interfaces between different materials. This behavior is important to applications in the petroleum industry where vertical fractures can be contained within a thin formation by overlying and underlying units that inhibit propagation. Daneshy (1976) describes results of some of the first experiments where hydraulic fractures were created in layered media in the laboratory. He found that the shear strength of the interface was important, with hydraulic fractures cutting across well-bonded interfaces but unable to cut across poorly-bonded ones. Anderson (1979) confirmed this result, presenting qualitative evidence that it is the relative tensile strengths of the materials on either side of the interface, as well as the shear strength and normal loading on the interface itself that determine whether a fracture will cross an interface. Other experiments describing the behavior of a hydraulic fracture approaching an interface are described by Papadapolous and others (1983), Biot and others (1983), Hanson and others (1978 a and b, 1979), and Pollard (1973).

The distribution of in situ stresses play an important role in the forms of hydraulic fractures, according to the results of several laboratory investigations. Warpinski and others (1982) designed a test cell that allowed the radial load on a cylindrical rock sample (20 cm in diameter and 20 cm long) to be varied along the axis of the cylinder. Hydraulic fractures were created in homogeneous samples where radial loads at the ends of the cylindrical axis were 2.0 to 2.75 MPa greater than loads at the center of the axis. They found that a stress contrast of that magnitude alone was sufficient to inhibit growth of a hydraulic fracture out of the zone of diminished confining stress. Similar results were obtained by Ahmed and others (1983), who created fractures in large (1.0 m on a side) blocks of cement grout to reduce effects of exterior boundaries.

The experiments cited above were conducted to examine effects of nucleation and growth; other experiments address processes occurring after a fracture has been created. Of particular interest are processes that could cause a reduction in permeability of the fracture, either by embedment, or crushing of proppant grains (Howard and Fast, 1970). A propped fracture may tend to close if the normal stress on the fracture is great relative to the strength of the formation, leading to embedment of the proppant grains. Results from experimental studies using either chalk or diatomite (Hartley and Bosma, 1985; Strubhar and others, 1984; Strickland, 1985) indicate that embedment is limited to roughly one-half a grain diameter. Permeability is seriously reduced by embedment when the proppant layer is one to two grains thick, but it is only moderately reduced when the proppant is three grains thick, and fracture permeability is unaffected when proppant is greater than five grains thick (Hartley and Bosma, 1985). Studies of embedment of proppant grains into soil have not been published.

Proppant crushing can occur when the confining stress on the wall of the fracture exceeds the strength of the proppant particles. According to results of experiments reported in Howard and Fast (1970), for example, quartz sand can be crushed at pressures equivalent to depths of two km. At greater depths a high strength proppant, such as aluminum oxide, is generally recommended. Crushing of quartz sand should be of no concern to the relatively shallow applications of remediation.

Experimental investigations of hydraulic fracturing are by no means limited to the laboratory. Field experiments of most of the applications described in the previous section have been conducted to test new ideas or verify new theories. In most field experiments, data are obtained from wells intersecting the fractures, but in a few experiments data has been obtained from the fractures themselves. The pioneering paper by Clark (1949) begins with a description of a shallow hydraulic fracture exposed by excavation. A photograph of the excavation showing a wellbore intersecting a horizontal fracture propped with sand provided Clark with irrefutable evidence that fractures could be created using the process he describes.

An extensive suite of field experiments were conducted at the DOE Nevada Test Site, where hydraulic fractures were created in ash-fall volcanic tuff and excavated using mining procedures (Northrop and others, 1978). The objectives of this program were to evaluate proppant distribution, examine characteristics of a fracture intersecting an interface between different formations, evaluate results of small-volume fractures as a tool for measuring in situ stress, and compare the size and geometry of actual fractures to those predicted by theory. Results are described by Warpinski (1983), Northrop and others (1978), Tyler and Vollendorf (1975), and references cited therein.

Analyses

Hydraulic fracturing was proven as a technique of increasing the yields of oil wells long before the physics of the process were understood. As the cost of the fracturing operation increased, however, it became clear that analyses predicting fracture geometry (size, shape, orientation) could be used to maximize recovery performance and minimize expenses. Khristianovich and Zheltov (1955) recognized that the basic physics of hydraulic fracturing involves two processes: the flow of liquid within the fracture, and the dilation of the fracture walls due to deformation of enveloping material. The processes are coupled, though, in that the pressure distribution resulting from viscous losses during flow is strongly dependent on the fracture aperture, but the aperture depends on the amount of dilation caused by the pressure distribution. Dilation of the fracture resulting from material deformation is calculated, with few exceptions, using elastic, or poro-elastic theory. One of the exceptions, a study by Medlin and Masse (1982), showed that effects of plastic deformation during fracturing are detectable in the laboratory, but are undetectable in field applications of hydraulic fracturing in sedimentary rock. Effects of plastic deformation are generally ignored. Fluid flow within the fracture is commonly assumed to be laminar and governed by a linear viscous behavior. Many fracturing fluids are thixotropic, so nonlinear flow laws have been incorporated into solutions of hydraulic fracture propagation (Pascal, 1986).

Two-dimensional analytical solutions to the problem of a linear viscous fluid driving a fracture in an elastic medium have been derived that yield length, aperture, and driving pressure as functions of time for the following geometries:

1.) Vertical, circular (Perkins and Kern, 1961; Geerstma and de Klerk, 1969 Abe and others, 1976);

2.) Horizontal, circular (Perkins and Kern, 1961);

3.) Vertical, rectangular with large ratio of length to height (Perkins and Kern, 1961; Nordgren, 1972);

4.) Vertical, rectangular with small ratio of length to height (Khristianovich and Zheltov, 1955; Geerstma and de Klerk, 1969; Geerstma and Haafkens, 1979; Nilson, 1981; Spence and Turcotte, 1985; Nilson, 1986; Nilson and Giffiths, 1986) .

Analytical solutions show that the growth of an idealized hydraulic fracture, that is the characteristic length (half-length or radius), *L*, aperture, *A*, and fluid pressure, *P*, as functions of time, *t*, can be expressed as simple power functions

$$L = C_1 t^b \tag{1.9a}$$

$$A = C_2 t^c \tag{1.9b}$$

$$P = C_3 t^d \tag{1.9c}$$

assuming loss of the injected fluid by flow through the walls of the fractures, or *leakoff*, is negligible. The constants C_1, C_2, C_3 depend on details of each solution (e.g. references cited above), but in general they depend on properties of the injection system and the material containing the fracture. The superscripts *b*, *c*, and *d*, are constants that depend on fracture geometry (Table 1.3). The lengths and apertures of both types of vertical fractures, for example, are predicted to growth faster than those of the circular fractures.

It may be possible to detect the mode of growth of a fracture using Table 1.3. A horizontal, circular fracture is expected to grow by increasing its radius and compressing adjacent material early in its propagation history, and thus behave as Case A. With continued pumping, however, the fracture could cease to grow radially and increase in volume by lifting its overburden (Case B, Table 1.3), either because of a mechanical advantage achieved with increasing radius (Pollard, 1973) or because leakoff near the tip increases the sand concentration preventing flow. In either case, the change in mode of growth could be detected because the pressures would begin to increase approaching a slope of unity for Case B in Table 1.3. Similar applications of principles derived from analytical solutions of vertical fractures have been described by Nolte and Smith (1981; 1987).

TABLE 1.3. SOME POSSIBLE CONSTANTS IN EQ. (1.9)

Geometry	b	c	d
Circular			
Case A[*]	2/5	1/5	-1/5
Case B[**]	0	1	1
Vertical, Rectangular			
small L/H	2/3	1/3	-1/3
large L/H	4/5	1/5	1/5

---

[*] Vertical fracture, or deep horizontal fracture. Assumes dilation only by elastic deformation of adjacent material.

[**] Shallow, horizontal fracture. Assumes volumetric growth only by lifting overburden, no radial growth.

Analytical solutions require that the fracture geometry is known, and that it is a simple geometric shape. Furthermore, details of the fracturing procedure, such as effects of nonlinear fluid rheologies, transport of proppant grains, leakoff, back stress, fracture toughness, material interfaces, and nonuniform stress distribution in the host rock cannot be investigated by most analytical solutions. In practice, the fracture geometry is unknown and effects of those and other details can be crucial in a design strategy. As a result, sophisticated computer programs have been developed that offer predictions of the shape of the leading edge of a fracture, and are able to estimate how a wide range of design parameters affect the length, thickness, and distribution of proppant within a hydraulic fracture. There are many dozen, or perhaps more, published descriptions of computer programs used to simulate hydraulic fractures. The capabilities of those descriptions are reviewed and compared by Cleary (1988), Palmer and Luiskutty (1986), Advani and others (1985), Mendelsohn (1984), and Veatch (1983 a and b), so a detailed review seems unnecessary in the present work. Contributions to the development of computer codes that predict fracture geometries in three dimensions have been made by Luiskutty and others (1989), Vandamme and others (1988), Settari (1988), Bouteca (1988), Acharya (1988), Morita and others (1988), Settari and Cleary (1986), Settari (1985), Abou-Sayed and others (1984), Settari and Cleary (1984), Cleary and others (1983 a and b), Settari and Cleary (1982 a and b), Cleary (1978a), Daneshy (1973). Carter (in Howard and Fast, 1957) presented the first analysis of leakoff, which was refined by Williams (1970), and generalized to include nonlinear effects by Settari (1983). Analyses of relevant effects, including fluid rheology (Settari and Price, 1984; Cleary, 1980 a and b), back stress due to pressure of pore-fluids (Keck and others, 1984; Cleary, 1980 a and b; Ruina, 1978), heat transfer (Meyer, 1989; Keck and others, 1984; Griffiths and others, 1983; Settari, 1980), proppant transport (Settari and Price, 1984; Daneshy, 1978; Novotny, 1977), and fracture toughness (Theircelin and others, 1989; Morita, and others, 1988; Settari, 1985; van Eekelen,

1980) are commonly included in computer programs analyzing fracture propagation. One of those programs, described by Boone and others (1989), represents fracture shape, pore-fluid pressure, and stress in the vicinity of a vertical fracture as a color image that changes with time on a video monitor.

Interactions between a hydraulic fracture and the ground surface, a topic of particular interest to the proposed applications, have been analyzed by Pollard and Holzhausen (1979), and Narendran and Cleary (1983). In related work, interactions between multiple hydraulic fractures have been analyzed by Narendran and Cleary (1984), and Hanson and others (1979), and consequences of fracture interactions have been utilized in design concepts by Warpinski and Branagan (1989), Ernst (1980), and Huck and others (1980). Theoretical solutions of a fracture encountering interfaces between materials of differing properties are described by Lam and Cleary (1984), Weertman (1980), van Eekelen (1980), and Hanson and others (1978 a and b).

In addition to forecasting the geometry of hydraulic fracture, the results of theoretical analyses are matched against field measurements, such as injection pressure or deformation of the ground surface, to estimate geometry after the fracture has been created. Methods of inverting pressure records were developed in a series of papers by Nolte and Smith (Nolte, 1988 a and b, 1984, 1982, 1979; Nolte and Smith, 1987, 1981), and other investigators (e.g. Crockett and others, 1989) have made contributions as well. The inversion of measurements of surface deformation--commonly obtained using tiltmeters--to estimate the location, orientation, and dimensions of a hydraulic fracture was described by Davis (1983), and applied by Holzhausen and others (1985 a and b).

Another application is the optimization of fracture designs, where the output of a fracture simulator is used as the input of a program that evalutes flow to the fracture (Anderson and Phillips, 1988) and possibly economic considerations, such as costs of fracturing materials and rate of return (Howard and Fast, 1970; Veatch, 1983 a and b). A simple method of optimization, based on the cumulative volume of recovery and described by Elbel and Sookprasong (1987), is relevant to the application of hydraulic fracturing during remediation.

The work cited above includes some notable contributions, but it is by no means an exhaustive survey of papers that address useful applications of hydraulic fracturing; there are many more. With few exceptions, those papers are targeted to applications where hydraulic fractures are created in rock at depths in excess of several hundred meters. Use of the significant body of existing information for the purposes of this research, therefore, will depend on the extent to which hydraulic fracturing of rock at great depth resembles hydraulic fracturing of soil at shallow depths.

The Hydraulic Fracture as a Problem

Hydraulic fracturing of soil at shallow depths has, in the past, generally been regarded as a problem. This is because many soil engineering techniques, which require increasing ambient pore pressures, will be ruined if they induce hydraulic fracturing--with the exception of hydraulic fractures created to measure in situ stresses in soil (Leach, 1977; Massarsch and others, 1975; Tavenas and others, 1975; Bjerrum and Anderson, 1972).

Applications

The collapse of a dam is perhaps the most severe consequence of accidental hydraulic fracturing. One example occurred at the Teton Dam, Idaho, where excessive rates of seepage were noted downstream of the dam shortly after the reservoir behind it was filled in 1976. Seepage rates increased and soon a muddy flow appeared at the downstream toe of the dam. The flow eroded a gully, which cut through the dam from the downstream toe upward to the crest. Fourteen people died and 400 million dollars of property damage resulted from the subsequent failure. An investigation of the tragedy concluded that hydraulic fracturing, due to increases in pore pressure accompanying filling of the reservoir, probably contributed to the dam failure (Jaworski and others, 1979; and references therein). Elsewhere, hydraulic fracturing was attibuted as the cause of leaks that ultimately led to the failure of 14 dams in Oklahoma and Mississippi, and other dams in California, Brazil, and China, according to Sherard (1972), and Jaworski and others (1979).

Ironically, hydraulic fracturing was known to workers in the oil industry as a problem before it was used to stimulate wells. Yuster and Calhoun (1945) recognized that a sudden increase in the rate of inflow during a waterflooding operation (a technique of injecting water in one well to sweep oil toward a recovery well) without an increase in pressure could be caused by hydraulic fracturing, or in their terminology, pressure parting. Hydraulic fracturing caused by excessive injection pressures can reduce the area swept out by the waterflood. New methods of estimating the maximum allowable pressure without causing fracturing during a waterflood continue to be developed (Singh and Agarwal, 1990).

In situ permeability of soil is commonly calculated by holding a constant pressure and measuring the rate at which water flows into a borehole. Bjerrum and others (1972) point out that hydraulic fractures can be created if the borehole pressure used in a permeability test is greater than a critical value, which they relate theoretically to the overburden load and these soil properties: poisson ratio, coefficient of lateral pressure, tensile strength, and compressibility. They claim that if hydraulic fracturing goes undetected during a test, values of permeability calculated from the resulting data can be as much as three orders of magnitude greater than the actual in situ permeability.

In some applications, hydraulic fracturing can be either an asset or a liability, depending on the details of the application. The disposal of liquid waste by injection into wells, outlined in the previous section, is one example. Injection grouting is another. Some designs require grout to uniformly permeate pores in the vicinity of an injection point (borehole), and the specifications of these designs cannot be met if grout flows preferentially into hydraulic fractures (Wong and Farmer, 1974). Moreover, hydraulic fracturing during grouting could result in problems, such as deforming a neighboring foundation, lifting a concrete cut-off from its seat, or markedly increasing the amount of grout required to complete a job (Morgenstern and Vaughn, 1963). Interestingly, however, hydraulic fracturing can also play a useful role in grouting practices. Zhang (1989) indicates that intentionally creating hydraulic fractures during grouting increases the rate of penetration of grout in some formations, and it effectively seals formations by creating an interlocking network of grout sheets. The technique is especially useful in formations, such as karstic limestone cut by clay- and sand-filled caves, where conventional grouting techniques are ineffective. Moreover, the load-bearing capacity of large diameter piles in silty sand is increased by creating grout-filled fractures following pile driving, according to Zhang (1989).

Experiments

The goal of many experimental investigations of the applications described above is to predict the pressure at which hydraulic fracturing occurs under a particular set of laboratory conditions. A noteworthy set of experiments is described by Jaworski and others (1979 and 1981), who examined hydraulic fractures in the vicinities of model wellbores and dam faces. They injected water into cubic blocks of soil, slowly increasing injection pressure and recording flow rate until a marked increase in flow rate indicated the onset of fracturing. This technique is common for other investigations of hydraulic fracturing of soil, although it differs from studies of hydraulic fracturing of rock (e.g. Medlin and Masse, 1979; Zoback and others, 1977; Haimson and Fairhurst, 1967, 1970; Harrison and others, 1954; Scott and others, 1953), which hold flow rate constant and monitor pressure. Jaworski and others (1979) cut slots in the faces of samples and applied pressure to the slots to simulate the role of joints or pre-existing cracks as stress concentrators. Cutting a slot in a sample to nucleate a fracture is common practice in tests designed to measure fracture toughness, as mentioned above.

Significant results of Jaworski and others (1979 and 1981) are as follows:

1. The pressure required to induce hydraulic fracturing from a cylindrical borehole is linearly related to confining stress. A similar relation was observed for the pressure required to induce hydraulic fracturing in rock by Medlin and Masse (1979), and Haimson and Fairhurst (1967, 1970).

2. A large amount of variation was observed in the fracturing pressures, suggesting that fracturing pressure from an open borehole would be difficult to predict. Fracturing pressure was affected by many factors, such as pre-existing flaws in the soil, that could neither be eliminated nor characterized.

3. The fracturing pressure depended on soil properties, increasing with the number of blows used to compact the sample. It increased as the water content decreased.

4. A discontinuity, such as a slot, will nucleate a hydraulic fracture in soil, and the presence of the discontinuity reduces the pressure required to induce fracturing.

In a later study, Mori and Tamura (1987) created hydraulic fractures from cylindrical holes in cylindrical soil samples, using much the same technique as Jaworski and others (1979). Their results confirm the linear relation between fracturing pressure and confining stress. Mori and Tamura conducted tests using various rates of injection, concluding that the fracturing pressure increased as the rate of pressurization increased. Hydraulic fracturing pressures in rock also increase with rate of pressurization, according to Haimson and Fairhurst (1967 and 1970), and Zoback and others (1977).

In one suite of tests, Mori and Tamura applied an axial load that was less than the radial load. Hydraulic fractures were formed either inclined or normal to the axial hole, leading Mori and Tamura to conclude that shear failure controls hydraulic fracturing of cohesive soil. This conclusion contradicts a large body of solid evidence for hydraulic fracturing being a tensile phenomena in other materials. It seems likely that the peculiar orientations of fractures observed by Mori and Tamura resulted from boundary conditions on their test samples. As Medlin and Masse (1979) point out, a cylindrical hole will tend to create a hydraulic fracture containing the axis of the hole. The fracture will change orientations, however, as it grows away from the hole and into a region of different stresses--such as would have been the case under the applied stress conditions used by Mori and Tamura. Large changes in orientations during propagation are accomplished by curving, twisting, or breaking into segments (Pollard and others, 1982), resulting in irregular or intricate fracture forms. The results that are briefly described by Mori and Tamura are consistent with behavior as tensile, or Mode I fractures (Lawn and Wilshaw, 1975), propagating in an abruptly changing stress field; their conclusion that hydraulic fractures in cohesive soil behave as shear failures is unconvincing.

An apparatus used to create hydraulic fractures is described by Sun and Ting (1988), who claim that it offers advantages over apparatuses described previously. Their device is designed to create a hydraulic fracture from a cylindrical hole in a cylindrical sample, which is a standard configuration. The principal novelty appears to be that the pressure acting on the cylindrical hole can be controlled independently from pore pressure in soil adjacent to the hole. This is done by lining the hole with a permeable layer and then inserting a flexible bladder along the length of the lined hole; inflating the bladder controls pressure on the wall of the hole, whereas wetting the liner controls pore pressure in the soil.

Analyses

Studies seeking methods of preventing fracture initiation commonly employ analyses of stresses in the vicinity of pressurized holes. Hydraulic fracturing is assumed to occur when tensile stresses exceeds the tensile strength of the material. Analyses of this type were first based on elastic solutions and used to predict hydraulic fracturing of rock (e.g. Harrison and others, 1954; Schiedegger, 1960; Kehle, 1964; Haimson and Fairhurst, 1967), but have been applied directly to predict hydraulic fracturing of soil (Mori and Tamura, 1987; Jaworski and others, 1979 and 1981). Jaworski and others (1979) point out some discrepancies between theory and data, not the least of which is a large amount of variability in the data. This observation leads them to conclude that the criteria represented by the simple theory were insufficient to reliably predict the pressure required to cause fracturing from an open borehole in soil.

Bjerrum and others (1972), who were concerned with inhibiting hydraulic fracturing during field permeability tests, included in their analysis the effect that driving a piezometer would have on state of stress prior to fracturing. They assume that when a piezometer is inserted, the soil adjacent to it yields, and the radial and circumferential stresses change by an amount that depends on the compressibility of the soil. The radial stress always increases when a piezometer is inserted; by a factor of 1.5 for highly compressible soil to as much as 5.2 for relatively incompressible soil. The circumferential stress at the wall of the piezometer, however, will decrease by a factor of as much as 0.6 for highly compressible soil, or increase by as much as 2.1 for relatively incompressible soil. Deformation resulting from pushing a piezometer into the ground, thus, could either increase or decrease--depending on the compressibility of the soil--the pressure required to initiate fracturing, according to the analysis of Bjerrum and others (1972).

An analysis of the conditions required to create a hydraulic fracture specifically in unconsolidated sediment is presented by Horsrud and others (1982), who use coupled elastic and plastic solutions. Fracture initiation pressures can be reduced by plastic deformation to roughly 10 percent less than that predicted by elastic theory, according to their results. Medlin and Masse (1979) presented both experimental and theoretical evidence confirming that plastic deformation around a borehole reduced the pressure required for fracture initiation.

Predicting the maximum pressure achievable without causing a hydraulic fracture during injection grouting has been an elusive task. The limiting pressure is recognized to increase with depth; values of 22.6 to 102 kPa/m (1.0 to 4.5 psi/ft) of depth are used in regulations defining maximum allowable pressure (Dickinson, 1988). Those gradients apparently are determined empirically. Morgenstern and Vaughn (1963) suggest that a Mohr-Coulomb failure criterion could be adopted to predict hydraulic fracturing during grouting, although the mode of failure--shear--implied by that criteria is unfounded for hydraulic fractures. The analysis of Wong and Farmer (1973) assumes tensile failure and uses an elastic analysis, which includes pore-pressure effects, to examine the initiation of a hydraulic fracture during grouting. This approach is consistent with established methods (e.g. Haimson and Fairhurst, 1967), although it is unclear how well it predicts grouting pressures.

Wong and Farmer (1973) present both a stress analysis and an energy balance approach to analyze the propagation of hydraulic fractures formed during injection grouting. Their analyses assumes that many hydraulic fractures radiate outward and are closely spaced within a certain distance from the borehole. In contrast, the majority of published analyses as well as field and laboratory evidence suggests that only one, or at most a few, fractures grow away from the borehole. Wong and Farmer (1973) indicate that their analyses predict pressures during propagation that greatly exceed those observed in the field.

SECTION TWO

LABORATORY EXPERIMENTS OF HYDRAULIC FRACTURING OF SOIL

The purpose of studying hydraulic fracturing of soil has traditionally been to provide methods of preventing fracture initiation during geotechnical engineering operations. This is because hydraulic fracturing can result in failures during, for example, injection grouting, permeability testing, deep-well injection, or dam construction. As a result of the focus on fracture initiation little is known about the physical appearance, mechanical behavior, or methods of analyzing the growth of a hydraulic fracture in soil.

In contrast, a wide range of useful applications has been developed for hydraulic fracturing of rock. These applications have prompted a broad scope of investigations; consequently a great deal is known about hydraulic fractures in rock.

The goal of the following section is to apply methods of studying hydraulic fractures in rock to aid in understanding hydraulic fractures in soil. Laboratory tests were conducted using a bench scale apparatus designed to create hydraulic fractures in soil. Observations from the laboratory tests, including the appearance of the fractures and injection pressures as a function of time and moisture content, are described in the following section.

During the laboratory tests, hydraulic fractures were created by injecting fluid into samples confined within a triaxial loading cell. The fractures were observed directly by looking through a transparent loading plate in the experimental apparatus, and phenomena related to fracturing were observed indirectly by measuring the pressure of injected fluid as a function of time. The direct observations, combined with descriptions of fracture surfaces from samples split open after testing, yield the important details of the appearance of a hydraulic fracture in clay. Records of injection pressure as a function of time are used to obtain critical pressures at which fracturing takes place. The critical pressure varies over an order of magnitude, depending on the moisture content of the clay and other factors. Moreover, shapes of the records also depend on moisture content, and the nature of this dependency will be described in the following section. Before the observations can be described, it will be necessary to explain the design of the apparatus, the techniques of preparing a sample, and the procedures of conducting a test.

EXPERIMENTAL DESIGN

The experiments were designed to create hydraulic fractures by injecting glycerin into rectangular blocks of soil confined in a triaxial pressure cell. An experimental apparatus and testing procedure were developed to reveal physical characteristics of the fractures and to yield data describing the fracture toughness of soil. Rhodamine dye was added to the glycerin to highlight areas of the fracture surface wetted by the fluid. The pressure of the injection fluid was monitored as a function of time so that fracture toughness could be calculated. Details of the design of the apparatus and the method of sample preparation are described in the following sections.

Apparatus

The experimental apparatus consists principally of a pump system, a fracture cell, and a data acquisition computer (Fig. 2.1). The pump system is used to inject fluid at a constant rate into a sample contained in the fracture cell. Typically, the pressure of the injected fluid increases until fracturing occurs, then decreases during fracture propagation. The computer is used to monitor injection fluid pressures as a function of time and to control the flow rate of the pump.

The fracture cell is a rectangular chamber (inside dimensions are 10 cm by 10 cm by 39 cm) with one moveable side that is used as a loading plate (Fig. 2.2). The loading plate is transparent, so that the interior of the cell can be inspected during a test. The other five sides of the chamber are lined with neoprene bladders. The three principal stresses on the sample are controlled independently by adjusting air pressures in the bladders.

A hole in the loading plate allows access to a soil sample inside the chamber. A spacer plate, placed between the loading plate and the sample, contains a pressure-tight fitting for tubing three mm in diameter. The tubing extends from the pump through the loading and spacer plates and into a thin slot cut in the sample (Fig. 2.2).

The pump used to inject fluid into the sample consists of two hydraulic cylinders driven by a threaded rod attached to a stepper motor. Hydraulic fluid is forced out of the cylinders and into the lower chamber of a pressure interface device, which thereby forces dyed glycerin out of an upper chamber and into the fracturing cell (Fig. 2.1). The flow rate of the pumping system is controlled by regulating the rate of rotation of the stepper motor. Other details of the design and operation of the pumping system are given in Murdoch and others (1987).

A flow rate of 0.225 ml/min was used for all the tests described in the following pages. The Reynolds Number associated with flow of glycerin in the slot at that flow rate is 0.01, and in hydraulic fractures it was less because the aperture of the fractures was less than that of the slot. Laminar flow was assumed to occur in the fractures based on the small Reynolds Number.

Pressure of the injection fluid as a function of time was the primary data recorded during each test. A transducer, accurate to 0.3 kPa, positioned roughly 20 cm upstream of the slot was used to measure pressure once every 200 msec. Pressure losses due to flow from the transducer to the tip of the starter slot are on the order of the accuracy of the transducer, according to calculations using standard methods (Streeter, 1971), so the pressure measured at the transducer will be taken to be the pressure within the slot.

The injection pressure was recorded as a disk file and it was displayed as a function of time on a video monitor. Accordingly, during a test it was possible to

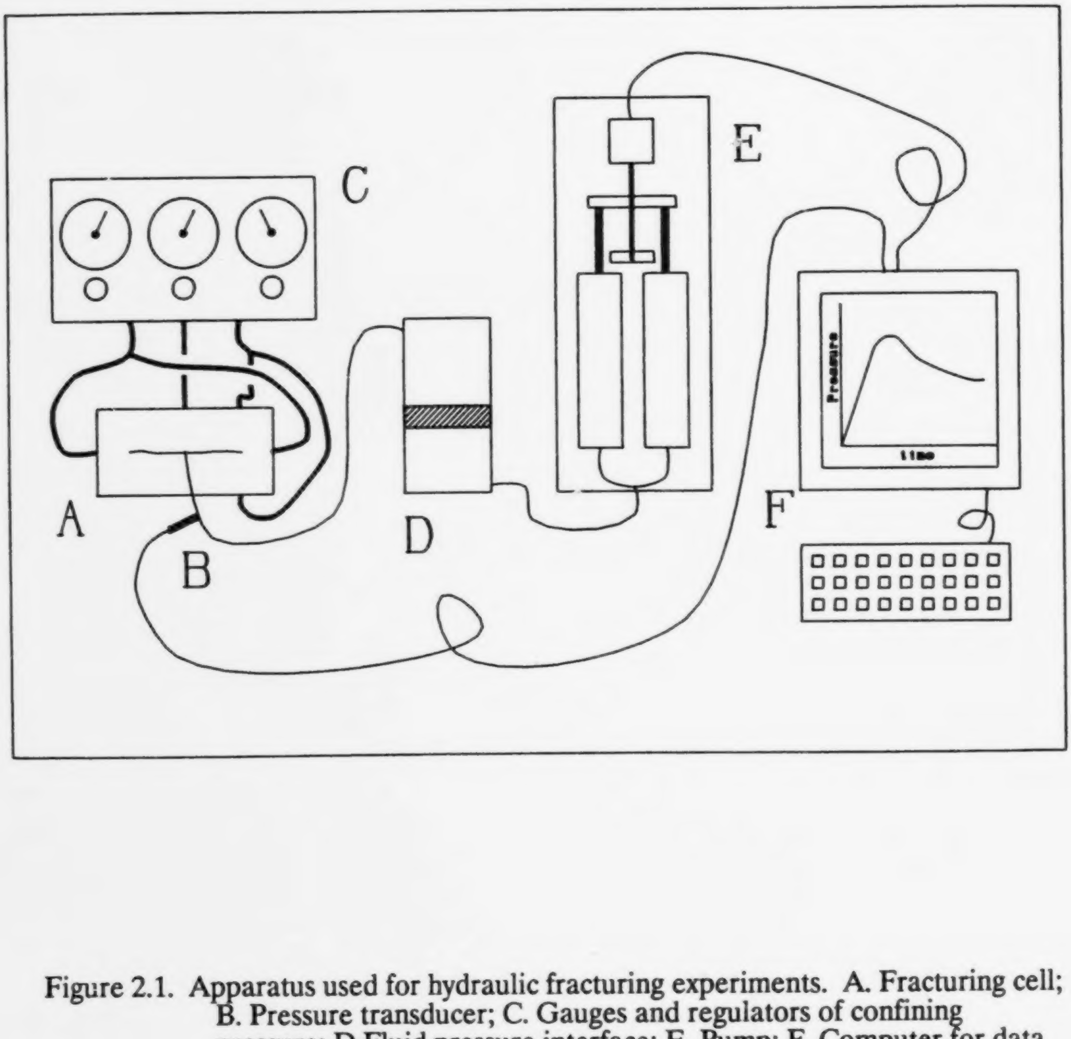

Figure 2.1. Apparatus used for hydraulic fracturing experiments. A. Fracturing cell; B. Pressure transducer; C. Gauges and regulators of confining pressure; D Fluid pressure interface; E. Pump; F. Computer for data acquisition and control.

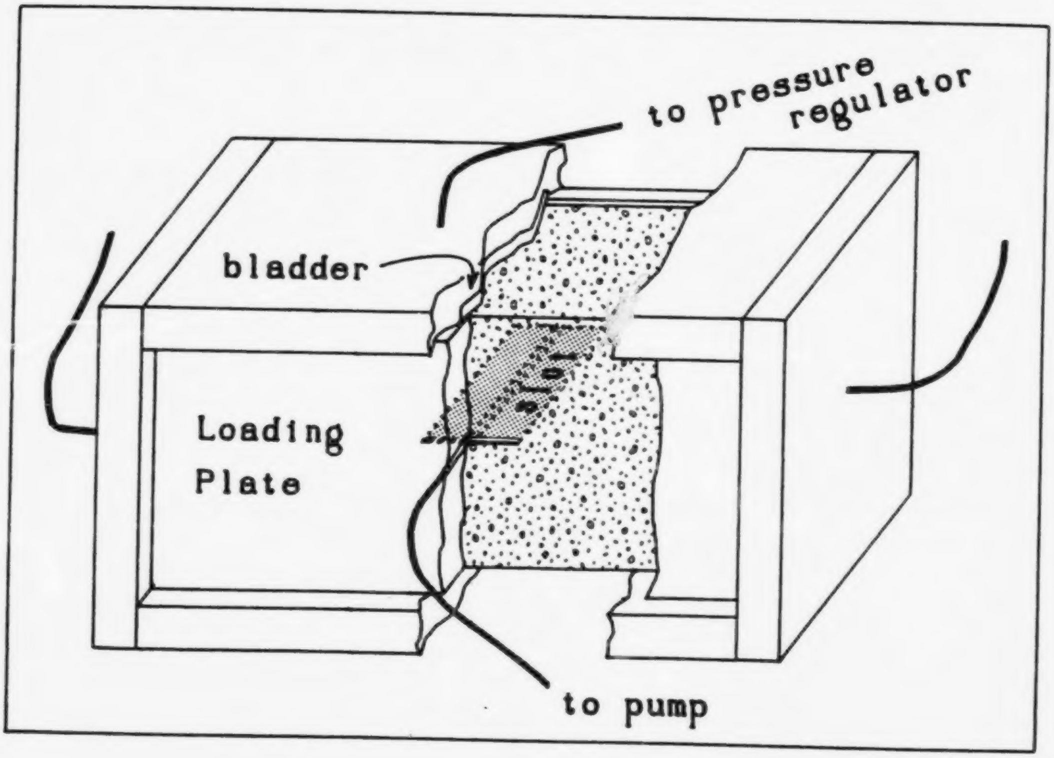
to pressure regulator
bladder
Loading Plate
to pump

Figure 2.2. Cut-away sketch of hydraulic fracturing cell.

observe the pressure record on the monitor, and to see the trace of a hydraulic fracture on the edge of the sample.

Physical Characteristics of the Soils

Two soils were used in the laboratory experiments. Most experiments were conducted using a yellow-brown colluvial clayey silt derived from a pit adjacent to the Center Hill Research Facility, Cincinnati, Ohio. That soil will be termed the Center Hill clay. Approximately one half m^3 of moist Center Hill clay was excavated and stored in air-tight drums, which served as a repository of sample material during testing. Several experiments were conducted using a different soil, a light-brown alluvial silt obtained from an exposure overlooking the Ohio River near the River Downs Racetrack, Cincinnati, Ohio. That material will be termed the River Downs silt.

All samples were molded into shape for the fracturing experiments. A suite of standard analyses was conducted on remolded Center Hill clay and River Downs silt to determine their basic physical characteristics. Two samples of each soil were analyzed, and they are nearly identical in physical characteristics.

The Center Hill clay is a type CL soil, according to the USCS classification based on Atterburg Limits (Table 2.1). It behaves as a plastic material in Atterburg tests over the range of moisture contents used during the fracturing tests (moisture contents were between the liquid and plastic limits). The River Downs silt is type ML, and it shows plastic behavior over a much narrower range of moisture contents (Table 2.1). Moisture contents during fracturing tests of the River Downs silt were less than the plastic limit of that material.

Analysis of grain sizes indicates that the Center Hill clay is dominantly silt and lesser amounts of clay (Table 2.1; Fig. 2.3). Trace amounts of limestone fragments occur in the soil naturally, but they were removed before the soil was used in the fracturing tests. The River Downs silt is mostly silt, with minor amounts of clay. Siderite concretions occur in the silt. These were removed by sieving.

Results from Proctor Tests (ASTM D698) indicate that the maximum density of the Center Hill clay occurs when the moisture content (wt. water/wt.solid) is19.7%. The moisture contents of samples used in the fracturing tests ranged from 19 to 33%; typically greater than optimum moisture content. Bulk densities of samples used in the fracturing tests are either equivalent to or slightly greater than densities from the Proctor Tests (Fig. 2.4).

Sample Preparation

Techniques of preparing soil samples were developed to yield uniform rectangular samples of a desired composition, water content and consolidation history. Samples were prepared in rectangular molds the same size as the inside of the fracturing cell. A mold resembled a rigid box with a top that moved like a piston to consolidate the sample. Geotextile along two sides of the sample facilitated drainage during consolidation.

TABLE 2.1. CHARACTERISTICS OF SOILS USED IN THE STUDY

CENTER HILL CLAY

Atterburg Limits (wt. water/wt. solid)	CH1	CH2	AVE
Liquid Limit	0.429	0.438	0.433
Plastic Limit	0.198	0.200	0.199
Plastic Index	0.231	0.238	0.234
Shinkage Limit	0.188		
Grain size			
Gravel	0	0	
Sand	0.03	0.03	
Silt	0.61	0.62	
Clay	0.36	0.35	

Proctor Test (ASTM D698)
Moisture Content of Greatest Density: 0.197
Maximum Dry Density: 1.68 gm/cm^3 (104.7 lb/ft^3)
Maximum Wet Density: 2.01 gm/cm^3 (126.0 1b/ft^3)

RIVER DOWNS SILT

Atterburg Limits	RD1	RD2	AVE
Liquid Limit	0.221	0.234	0.227
Plastic Limit	0.208	0.200	0.204
Plastic Index	0.013	0.034	0.023
Grain size			
Gravel	0.02	0.0	
Sand	0.05	0.06	
Silt	0.81	0.82	
Clay	0.12	0.12	

Proctor Test (ASTM D698)
Moisture Content of Greatest Density: 0.165
Maximum Dry Density: 1.73 gm/cm^3 (108.2 lb/ft^3)
Maximum Wet Density: 2.06 gm/cm^3 (128.7 1b/ft^3)

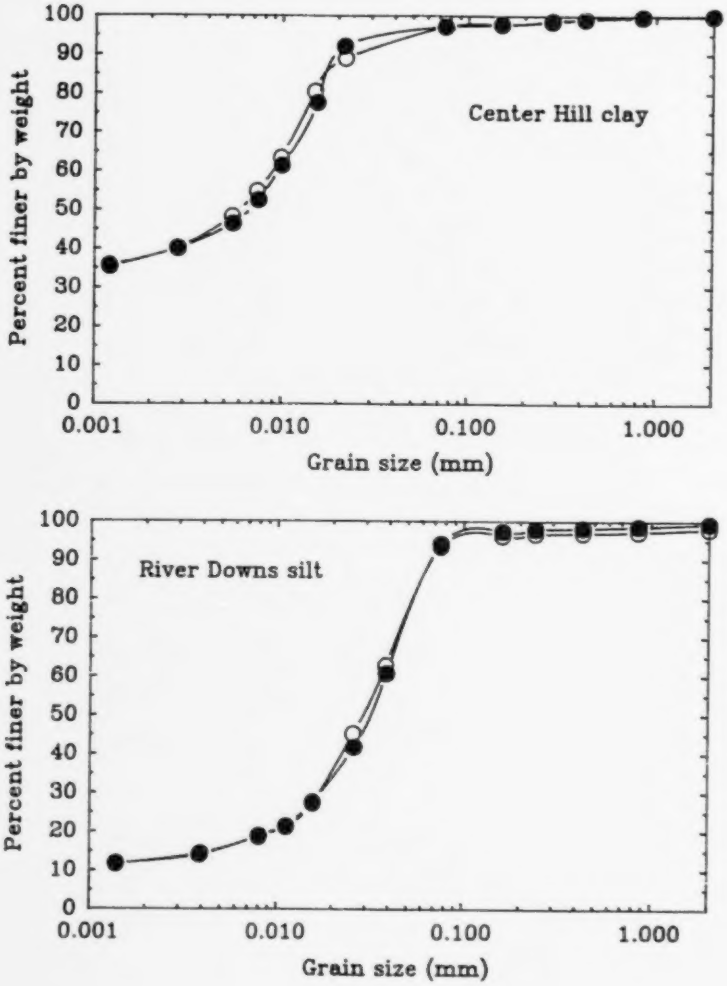

Figure 2.3. Grain-size distribution of soils used in the lab experiments.

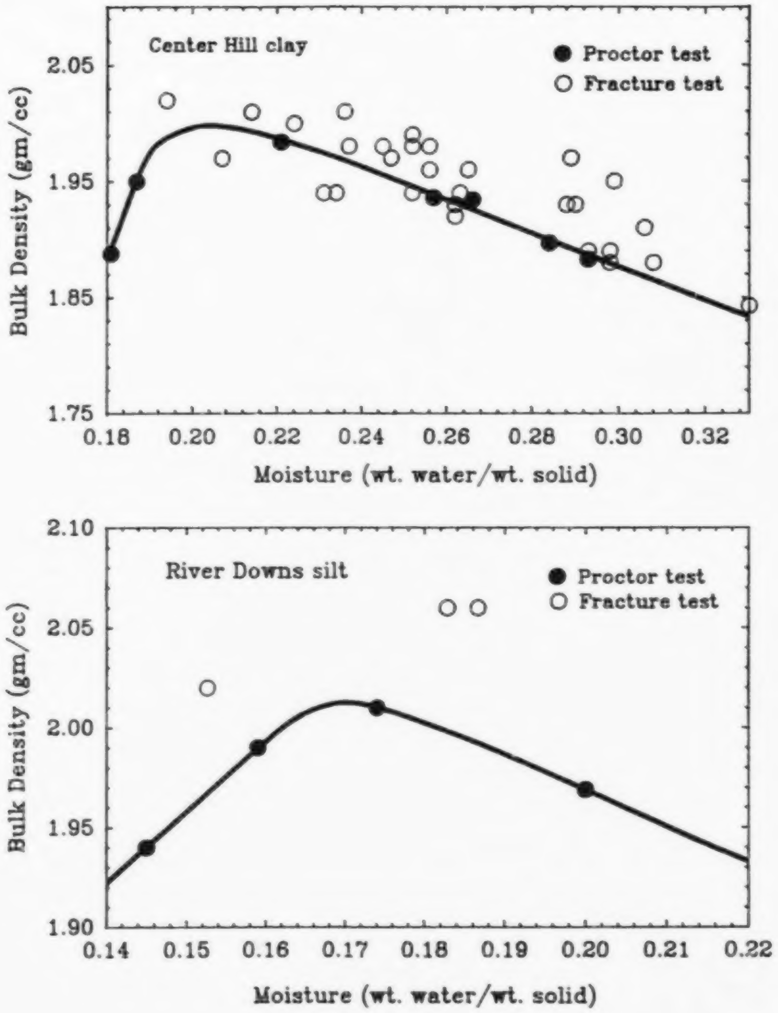

Figure 2.4. Bulk density as a function of moisture content from Proctor tests and fracture tests.

Two methods were used to prepare a sample; one that involved compaction and consolidation, and another that involved compaction alone. When samples were to be consolidated, a layer of soil roughly 2 cm thick was compacted with 30 to 40 blows of a drop-weight hammer. The upper surface of the layer was scarified to a depth of 0.5 to 1.0 cm and another layer of similar thickness was added and compacted. That process was repeated until the soil in the mold was 10.5 cm thick. Four sample molds were filled and then placed beneath the corners of a pallet upon which there were four drums of water. The weight of water in the drums exerted a vertical stress of 69 kPa on the samples. Samples were consolidated under that load for as many as 14 days.

A pneumatic press (SoilTest Model CN-425A) was used to load samples that were prepared only by compaction. The press was modified by attaching a special rectangular load shoe (5.8 cm x 9.8), so that the entire width of the sample mold was loaded by each blow. A layer of soil 2 cm thick was compacted by 80 blows from the press, and a pressure of 139 kPa was applied during each blow. The layer was scarified and another layer added and compacted. That process was repeated until the sample mold was filled to a depth of roughly 12 cm. The sample was removed from the mold and trimmed with a wire saw to a height of 10 cm.

A narrow slot (0.04 mm in aperture) was cut through the middle of each sample (Fig. 2.2) using a special blade-like tool. The slots were rectangular in shape with the long axis of the rectangle spanning the width of the sample. The short axis of the rectangle, or slot length, ranged from 12 to 72 mm depending on the size of the blade used to cut the slot. A hole 3 mm in diameter was cut along the center of the long axis.

The purpose of the slot was to provide a starting fracture that was much larger than existing flaws in the sample. The slot was necessary because measurements of critical stress intensity require knowing the length of a fracture when it begins to propagate (Tada and others, 1985). Natural discontinuities resembling fractures several mm long were common in the samples, so a starter slot of at least 12 mm in length was used to nucleate hydraulic fractures.

A film of silicone grease was applied to the surfaces of the sample to inhibit leaking of the injected fluid where a fracture intersected the sample surface. The grease provided an adequate seal and, because it was nearly transparent, allowed the trace of the fracture on the surface of the sample to be observed through the plexiglass loading plate.

The starter slot was filled with glycerin prior to each test to ensure that air was expelled from the slot. The loading plate was then secured and the cell positioned so that the starter slot was horizontal, eliminating a static pressure gradient normal to the slot (Fig. 2.2).

Confining pressures were applied to the sample by inflating neoprene bladders in the fracturing cell with air. Three sets of pressure gauges and regulators provided independent control of each of the three confining stresses. Most tests were conducted using confining pressures between 35 and 70 kPa (5 to 10 psi). Typically, the confining pressure normal to the starter slot was 20 percent less than the other two confining pressures, which were equal to one another. This loading configuration was used to promote the growth of a hydraulic fracture in the plane of the starter slot. If all three confining loads were equal or if the minimum load was in the plane of the starter slot, the hydraulic fracture would twist or curve yielding complicated forms that were difficult to duplicate.

A Typical Test

Events occurring during the fracturing tests followed a consistent pattern. Typically, pressure increased nearly linearly with time early in the test. At some point the slope of the pressure record began to flatten, reaching zero slope as the pressure peaked and then becoming negative as the pressure decreased with continued injection.

A thin (on the order of 0.05 mm) fracture trace typically could be first seen on the surface of the sample roughly at the time of maximum injection pressure. Most traces were nearly straight, although in many cases they consisted of a family of straight, sub-parallel segments arranged either *en echelon* or staggered. The location of the fracture tip was difficult to establish because the aperture tapered gradually until it became undetectable. Thus the tip could be located within approximately one cm, but the trace was too thin to locate the tip precisely.

The fracture trace grew at cm-long intervals, initially appearing as lines so thin they could barely be seen and then slowly widening to narrow slits with a recognizable aperture. Growth appeared essentially the same when magnified roughly ten times; greater magnification was impossible using available instruments. Although it was impossible to follow the tip of the fracture trace during propagation, the average rate of propagation could be determined from the total fracture length and the total time of injection; it was on the order of 0.5 to 1.0 mm/sec. Medlin and Masse (1984; fig. 9), who used an apparatus similar to the one described above and injected at 0.5 ml/sec (roughly twice the flow rate used here), report that the propagation rate decreases with time from 2 mm/sec early in a test to 0.2 mm/sec late in the test.

A fracturing test was terminated by stopping the pump and opening a pressure relief valve, which allowed the injection fluid to flow back into the injection tube as the fracture closed. The dyed glycerin was promptly removed from the fracture to inhibit staining of the sample by flow unrelated to the process of hydraulic fracturing.

The sample was removed from the fracturing cell and pulled open along the plane of the fracture. A rough, finely-dimpled surface was formed where pristine portions of the samples were pulled apart. In contrast, the surface of the hydraulic fracture was relatively flat, or marked by angular steps. This contrast is important because the leading edge of the hydraulic fracture was undyed, but could be readily distinguished from pristine clay by the difference in textures.

APPEARANCE OF A HYDRAULIC FRACTURE IN CENTER HILL CLAY

More than five dozen experiments were conducted with the Center Hill clay using a variety of loading conditions, sample preparation techniques, moisture contents and durations of consolidation. Hydraulic fractures were created during every experiment, except in a few cases when the injection tube was plugged with clay as it was inserted. Examination and description of the appearance of each fracture revealed features of the fractures that occur in virtually every case. Most of those features exhibited slight variations, depending on the conditions of the test, but they were consistently identified in some form. The features were described in notes and they were traced onto transparent mylar. In the following section, the typical attributes will be used to describe an idealized hydraulic fracture in the Center Hill clay.

In gross form most fractures were nearly symmetric with respect to the axis of the starter slot. The fractures created during the toughness experiments were roughly planar; other experiments resulted in fractures that curved or twisted into complicated forms that will be omitted from the following descriptions. The half-length of a fracture (measured from the hole along the axis of the slot to the leading edge) was roughly uniform along the width (measured parallel to the axis of the starter slot), although half-lengths were slightly shorter near the edges than in the center of most fractures.

Some fractures were asymmetric with respect to their width, that is their lengths were several cm greater along one side than along the other. In some cases, the lengths were greater on the side of the injection tube, whereas in other cases the side opposite the injection tube was longer. In virtually all cases, however, the asymmetry was mirrored across the axis of the starter slot. Slight leakage at one side of the sample, either out of the slot or out of the fracture itself, apparently caused this type of asymmetry. Leakage in most instances occurred during propagation, according to direct observations through the loading plate, so it had little effect on the early stages of nucleation and growth of the fracture.

The typical test revealed a continuous, parent fracture adjacent to the starter slot. The parent fracture broke into discontinuous, lobate planes with increasing distance from the injection hole. Dye staining formed irregular dendritic patterns near the ends of the lobes, but the leading edge of the fracture was beyond the zone reached by the dyed glycerin and is unstained. These features define four distinct zones, arranged in increasing distance from injection hole: 1.) starter slot; 2.) parent fracture; 3.) fracture lobes; 4.) and an unwetted zone at the leading edge.

Starter Slot

The starter slot appears on the surface of a cleaved sample as a smooth strip with a shallow trough, which is one half of the injection hole, along the axis of the strip (Fig. 2.5). The width of the strip depends on the length of the blade used to cut the slot.

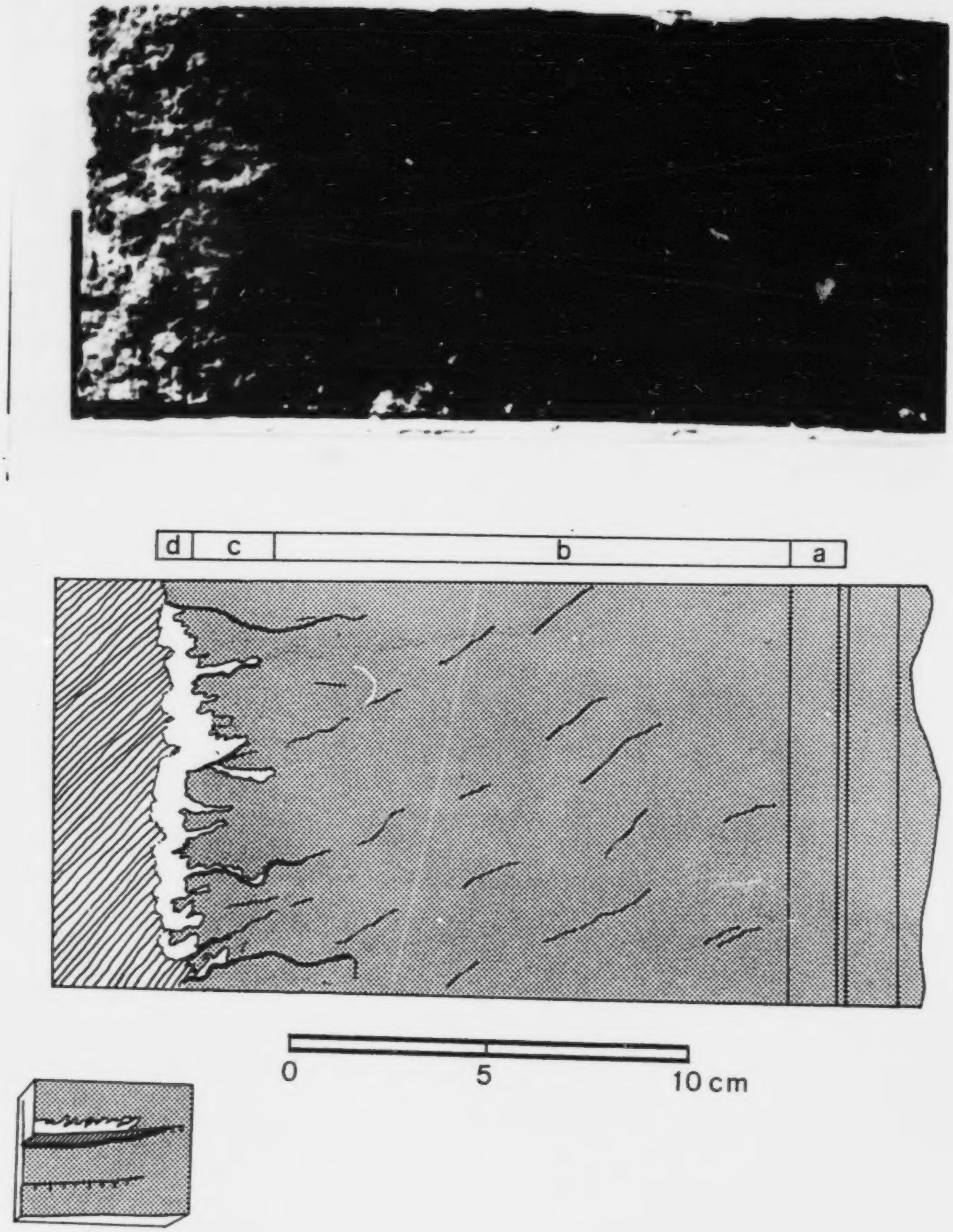

Figure 2.5. Photograph and sketch of the surface of a hydraulic fracture. a.) starter slot; b.) parent fracture; c.) lobes; d.) unwetted tip. Lines on the sketch are prominent linear features on the fracture surface. Heavy lines represent overlap of fracture lobes, as shown in the inset.

Parent Fracture

The main, or parent hydraulic fracture appears as a continuous dyed surface that lies roughly within the plane defined by the starter slot (Fig. 2.5). Locally, parent fractures are twisted or curved, with most of the distorted regions located near the edges of a sample (top of Fig. 2.5). Those distortions are minor, however; the fracture rarely deviates by more than 10° from the orientation of the slot.

The surface of a parent fracture is generally flat, but in detail it is marked by irregularities that have as much as one cm of relief. Some of the irregularities are rounded bulges or dimples. More typically the surface is marked by elongate features; narrow ridges, grooves or angular steps (fig. 2.5). Ridges and grooves typically have one mm or less of relief and the fracture surface on either side of them lies in the same plane. Steps are where the fracture surface abruptly changes height over a narrow interval.

Steps range in size from less than one mm high and several mm long, to 5 mm high and nearly as long as the entire fracture (Fig. 2.6). Lengths of ridges and grooves are on the order of several mm, typically shorter than the steps. The direction of the long axes of the linear features differ, depending on where the feature occurs on the fracture surface. Where they occur near the starter slot, the long axes are perpendicular to the axis of slot. At the other end of the fracture, near the tip, the steps are perpendicular to a tangent across the leading edge. Within the parent fracture, the axes are sub-parallel to one another and within 20° of the line formed by the edge of the sample. As the edge of the sample is approached, however, the linear features curve outward at increasingly higher angles, and at the edge itself the axes are inclined 45° or more (Fig. 2.6).

Steps, grooves and ridges on fracture surfaces are by no means unique to hydraulic fractures in soil; they have been described on the surfaces of tensile fractures in a variety of materials, ranging from glass to metal, plastic or rock (Williams, 1984; Pollard and others, 1982, and references cited therein; Pollard, 1978; Pollard and others, 1975; Daneshy, 1973; Tetelman and McEvily, 1967). A common interpretation is that the steps indicate the direction of propagation when the leading edge of the fracture is at the location of the step (Pollard and others, 1975).

This interpretation is consistent with the patterns of steps on the surfaces of fractures in soil. The typical pattern of steps is shown in Figure (2.7), from which the leading edge at several different times during growth is inferred. The inference suggests that propagation began near the center of the slot and the fracture grew toward the edges as it increased in length (Fig. 2.7). Upon reaching the edge of the sample, the fracture grew roughly parallel to it. Propagation at the edges of the sample apparently lagged behind the center because the direction of growth there has an outward component. Thus, the fracture trace on the surface of a sample, viewed through the plexiglass loading plate, was oblique to the direction of propagation of the fracture contained within the sample. In some cases, as in Figure 2.5, linear features suggest that propagation began near one side of the sample.

Directions of propagation were slightly divergent within the fracture, and strongly divergent near the edges. As a result, all except the center-most of the

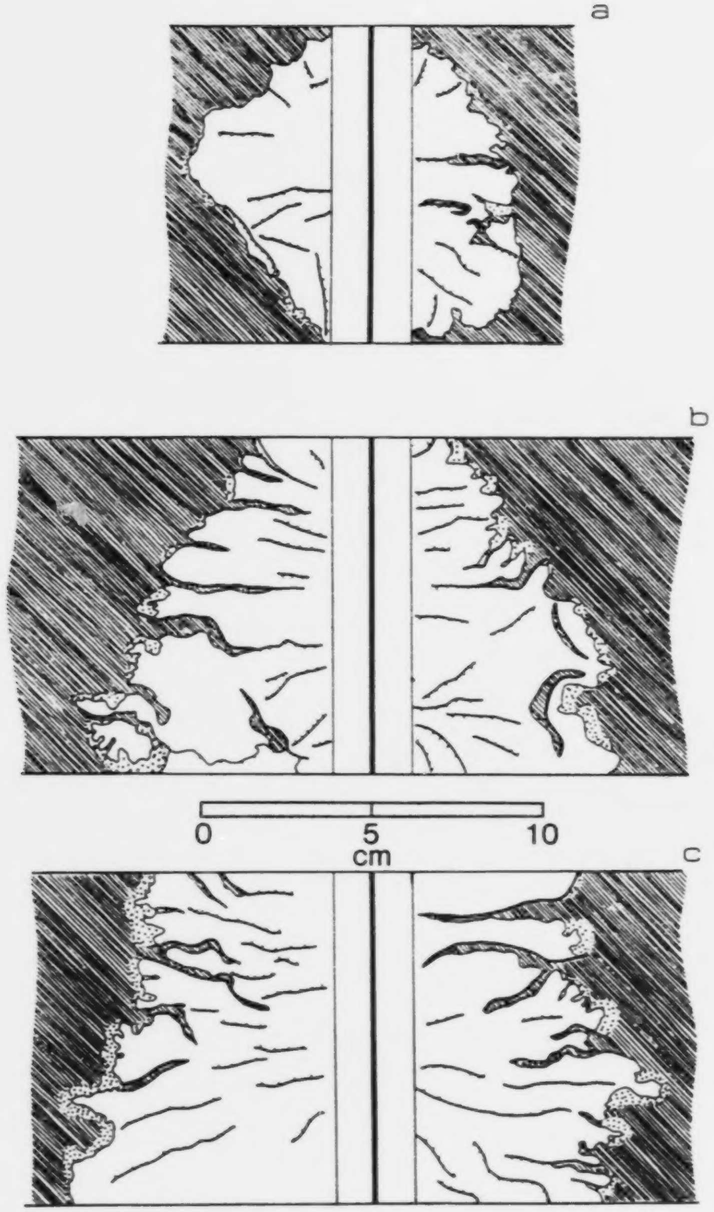

Figure 2.6. Surfaces of three hydraulic fractures of various lengths. Lines on fracture surfaces are linear features and hatch marks on the lines indicate the lower side of a step. Fractured, but undyed areas are stipled. Heavy lines indicate overlap of lobes, as in Fig. 2.5.

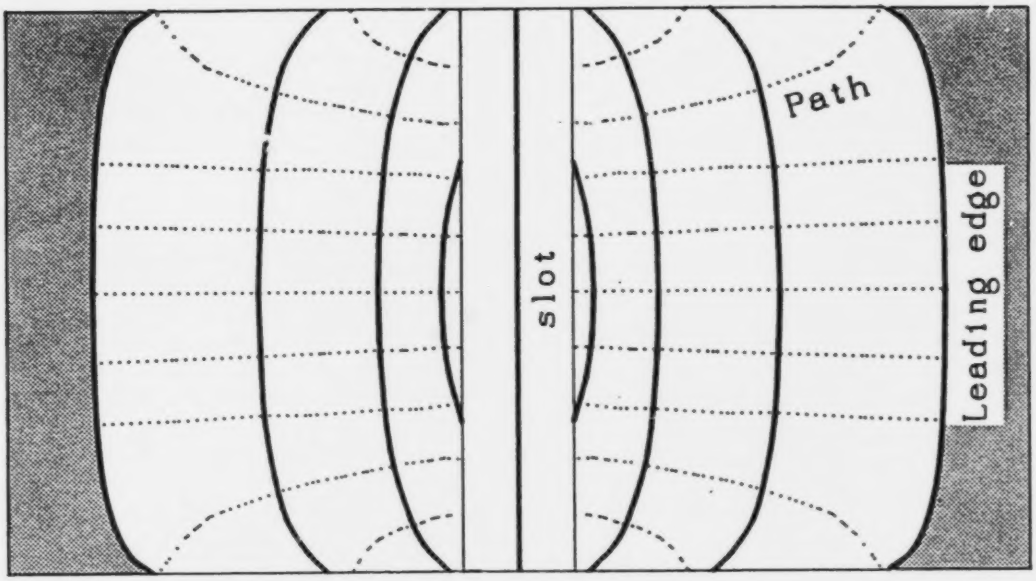
Path
Leading edge
slot

Figure 2.7. Idealized diagram of the position of the leading edge and the path of propagation during growth of a hydraulic fracture in the experiments. Inferred from the results of several dozen tests.

propagation paths eventually fan outward to intersect the edges of the sample (Fig. 2.7).

A few steps on fracture surfaces were nearly parallel to the axis of the starter fracture--at a high angle to the steps that indicate propagation direction (Fig. 2.6a and b). The axes of the high-angle steps are several cm in length and they are nearly straight to gently arcuate. Their location is variable; some of them occur in the vicinity of the starter slot, whereas others are in the vicinity of the leading edge. In many cases, a high-angle step on a fracture surface is related to a smaller fracture that either overlies or underlies the surface. The origin of the high-angle steps is unknown, but they are similar to rib marks, which were observed by Daneshy (1973), who used them to infer the position of the leading edge of the hydraulic fracture prior to the termination of a test.

Lobes

A continuous parent fracture breaks into a family of fracture lobes as the leading edge is approached from the starter slot (Fig. 2.6 and 2.7). The transition from continuous fracture to discontinuous lobes is smooth, marked by slight twisting or curving of lobes with respect to the parent fracture. Lobes occurred in virtually all the tests, although shapes and sizes of the lobes differ markedly between samples.

Lobes range from nearly equant to highly elongate, with aspect ratios from 1:1 to 1:10. In a few cases, fracture lobes originated at the starter slot and the entire fracture consisted of a family of elongate lobes; a continuous parent fracture was absent (upper right side of Fig. 2.6c). The major axes of elongate lobes are within a few degrees of parallel to the edges of the sample.

Fine steps or ridges are present on the surfaces of fracture lobes. Axes of steps are parallel to the major axis near the center of a lobe, but curve outward as the leading edge is approached. At the leading edge of a lobe, the steps are nearly perpendicular to the edge. The elongate lobes, therefore, are inferred to have widened as they increased in length.

As many as several dozen lobes are present in any given sample, and they range in size over more than an order of magnitude. The width of the largest lobe is typically on the order of several cm, roughly one third of the width of the sample. Intermediate-sized lobes, whose widths are on the order of several mm, occur along the leading edges of the larger lobes. Other lobes that are even smaller, roughly one mm in width, fringe the edges of the intermediate-sized lobes.

Several of the larger lobes, the ones bounded by unfractured soil, occur in each sample. Each one of these lobes is in close proximity to one or more neighbors. Three types of spatial arrangement between neighboring lobes were identified during the tests. They are as follows (Fig. 2.8):

1. Neighboring: Lobes are coplanar, and their edges are separated by a narrow band of unfractured material.

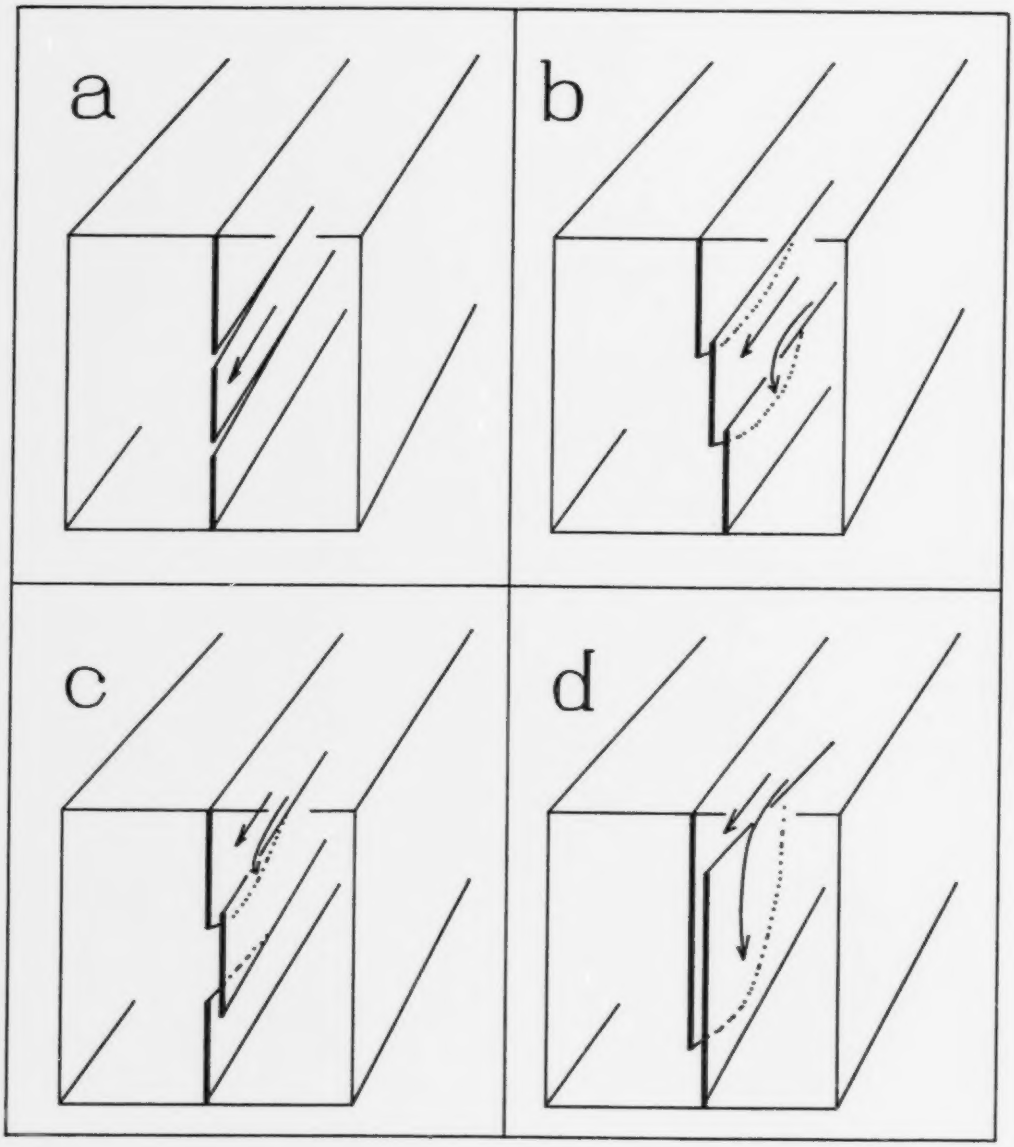

Figure 2.8. Idealized configurations of commonly-occurring fracture lobes. a. Neighboring lobes; b. En echelon overlapping lobes; c. Staggered overlapping lobes; d. Superposed lobes.

2. Overlapping: Lobes lie in slightly different planes, and their edges slightly overlap.

3. Superposed: Lobes are roughly parallel. When viewed normal to the plane of the fracture, one lobe entirely overlaps the adjacent lobe.

Neighboring and overlapping lobes are the most common, occurring in nearly all samples. Typically, the wider lobes tend to be overlapping whereas the smaller ones are neighboring. The sense of overlap between lobes was consistent in some samples, so that traces of the lobes would appear *en echelon* on a surface normal to the long axis of the sample. In other cases, however, the sense of overlapping reversed itself, so that traces of lobes would appear staggered on the normal surface. Typically, the sense of overlap was inconsistent, with some lobes en echelon and others staggered in any given sample (Fig. 2.6).

Superposed lobes, or pair of lobes with a large amount of overlap, occurred most commonly when the magnitudes of the applied stresses differed by a relatively large amount. Superposed lobes were rare in tests where the applied load normal to the starter slot was 80 percent of the loads parallel to the slot (the relative loading typical of all tests described in Section 3). Highly overlapping lobes were more common, occurring in roughly half the samples, when the normal load was between 30 and 50 percent of the parallel load.

Steps on the surfaces of superposed lobes were used to infer the path taken by the lobe as it grew, and some of the results are rather surprising. Typically, superposed lobes appear to be overlapping lobes that widen laterally as they grow in length (Fig. 2.8d). In some cases, however, the steps indicate that the lobe widened laterally and then propagated back toward the starter slot. In a few cases, superposed lobes are roughly circular features that are nearly isolated from both other lobes and the parent fracture. Small fractures, several mm in length, oriented normal to the lobes are the only connection that could be identified between those superposed lobes and their neighbors. Steps indicate that these isolated fractures grew outward in a radial pattern from the small connecting fractures.

The axes of boundaries between adjacent lobes typically can be traced back toward the starter slot to steps on the surface of a fracture (Fig. 2.6). This was observed on several scales; from boundaries between the larger lobes which can be traced to steps on the surface of the parent fracture, to the boundaries between the smallest lobes which can be traced back to fine steps on a fracture surface.

Pollard (1978) has argued that linear features, such as steps, ridges or grooves, on the surface of a tensile fracture result from the coalescence of lobes during growth of the fracture. The close spatial relationship between the boundaries between lobes and the axes of the linear features in the experiments described above support Pollard's argument. Moreover, Pollard cites the development of lobes, steps, ridges and grooves over a wide range of scales (eight orders of magnitude) and in materials ranging from glass to metal and rock. The results of this study indicate that the appearance of hydraulic fractures in clay-rich soil is similar to hydraulic, or other tensile, fractures in general.

Unwetted Tip

A thin band of fractured, but undyed soil ocurred at the leading edge of many of the hydraulic fractures. This undyed zone was identified on the surfaces of split samples based on surface texture and color. The zone lacked dye staining, so it could readily be distinguished from the surface wetted by rhodamine-laced glycerine. The break created when the sample was pulled apart had a rough, dimpled surface and lacked linear features such as steps or ridges (Fig. 2.9). In contrast, the surface in the undyed zone was smooth and nearly planar, marked only by fine steps. In some cases, a fine step in the undyed zone could be traced back into the stained region of the hydraulic fracture (Fig. 2.9).

The similarity in surface textures suggests that the undyed zone represents part of the hydraulic fracture that has not been wetted by the injection fluid, and *unwetted tip*. Accordingly, the hydraulic fractures extended from the hole along the axis of the starter slot to the leading edge of the undyed zone.

The length of the undyed zones varied greatly from one sample to another. In general among samples of similar moisture content and consolidation history, the length of the undyed zone was roughly proportional to the length of the dyed zone (Fig. 2.10). This suggests that those lengths are related by

$$L_{uw} = m\, L_w + L_{wc} \tag{2.1}$$

where m is the slope dL_{uw}/dL_w and L_{wc} is the intercept. First order regression lines are shown in Figure 2.6 for measurements taken from samples of different moisture content.

The length of the unwetted tip relative to the length of the wetted fracture, the parameter m in eq. (2.1), depends on moisture content of the sample (Fig. 2.10). Rhodamine stain was present over the entire fracture surface--an unwetted tip was completely absent--for samples containing less than 21% moisture. The relative length of the unwetted tip m increases as moisture content increases from 21 to 28%. Within that range, the relative length m is roughly linearly related to moisture content, according to Figure 2.10. The relative length is greatest, roughly 25%, at moisture contents between 27 and 28%, and it diminishes as moisture content increases to values greater than 28% (Fig. 2.10). The trend at moistures greater than 28% is based on only a few measurements.

The measurements of undyed zones made on different fracture surfaces and compiled in Figure 2.10 could be used to infer different stages in the growth of the unwetted tip of a single, idealized fracture. We must make this inferrence with caution, however, because it assumes that the glycerin stops moving when propagation ceases. That assumption requires that capillary forces are unable to cause flow after the pump is turned off. To crudely examine the effects of capillary forces, droplets of dyed glycerin were placed on narrow, flat-lying cracks exposed on the surfaces of samples of Center Hill clay. The glycerin flowed 6 to 12 mm into the dry cracks due solely to capillary suction. The dye produced dendritic patterns similar to those at the leading edges of the hydraulic fractures.

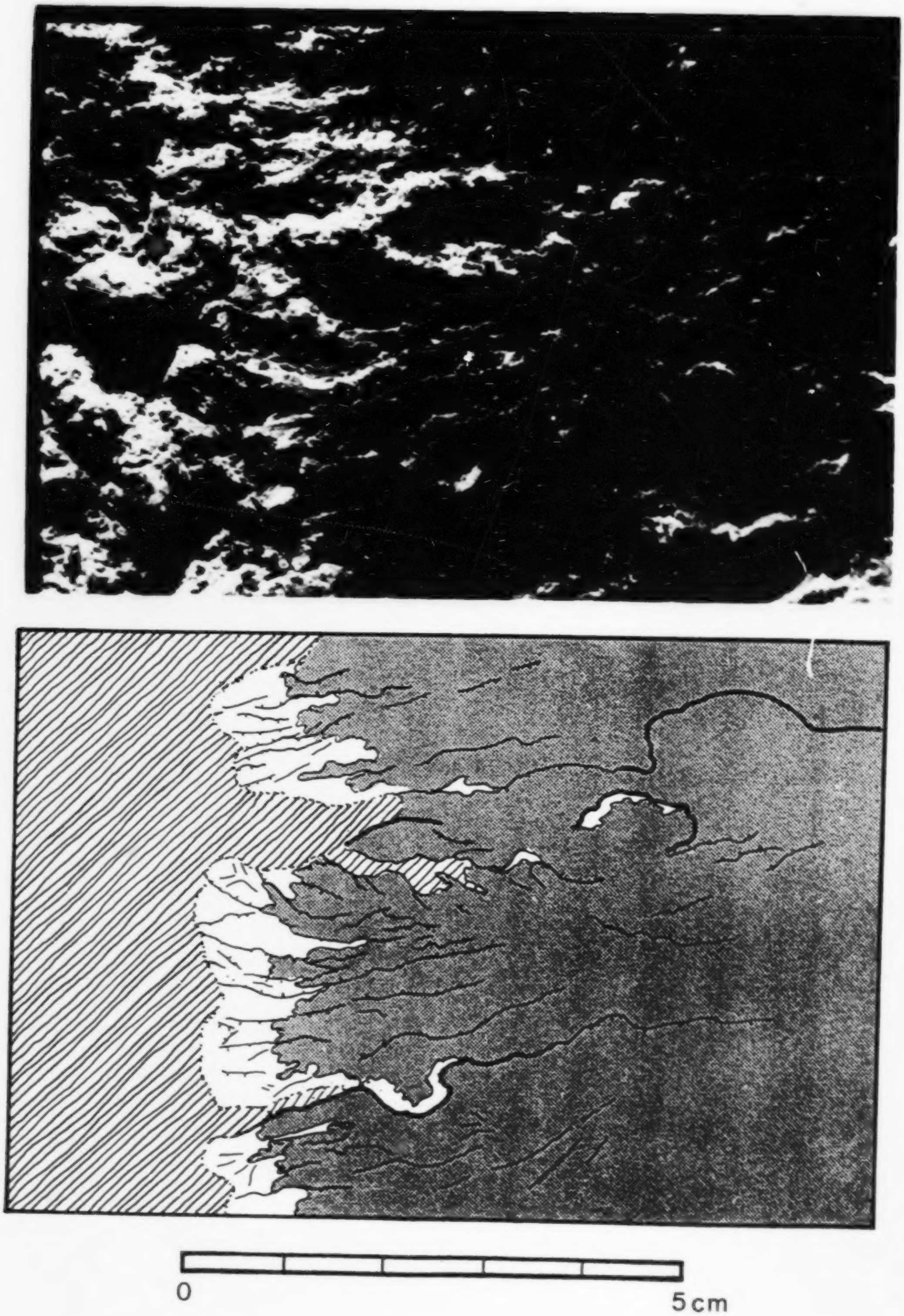

Figure 2.9. Leading edge of a hydraulic fracture. Lines on the sketch indicate linear features as in Figures. 2.5 and 2.6.

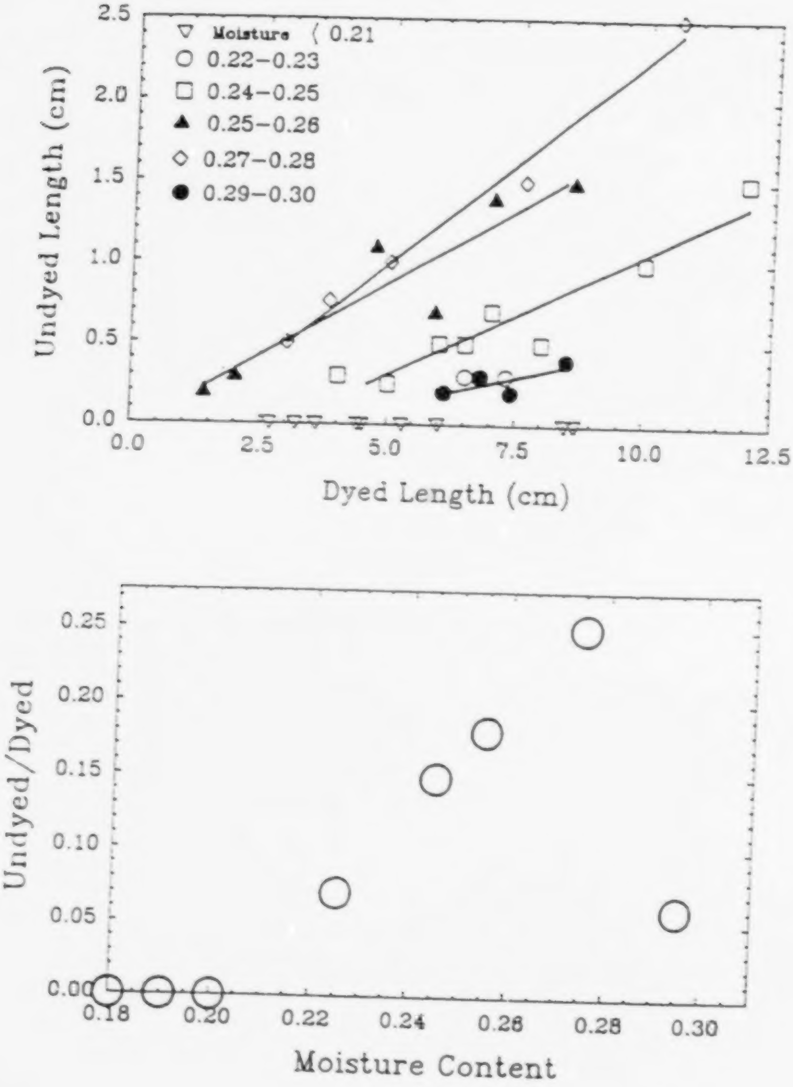

Figure 2.10. Length of undyed zone as functions of dyed length and moisture content (upper figure). Ratio of undyed to dyed length as a function of moisture content (lower figure).

Capillary forces will certainly affect flow in the vicinity of an unwetted tip during propagation, and it seems likely that those forces could cause the glycerin to advance toward the tip even after propagation has ceased. We conclude that the lengths of undyed zones shown in Figure 2.6 are the lower limits of the lengths of the unwetted tips during propagation. Likewise, we must accept the possibility that some of the variation in *m* with moisture content described above could be influenced by changes in post-propagation flow, rather than by changes in the rate of growth of the unwetted tip itself.

RECORDS OF DRIVING PRESSURE

Driving pressure P_d, the difference between the internal fluid pressure and the confining stress normal to a fracture, is a fundamental quantity in analyses of a hydraulic fracture (Kristianovich and Zheltov, 1955; Perkins and Kern, 1961; Geerstma and de Klerk, 1969; Pollard, 1973, Nolte and Smith, 1981; Crockett and others, 1989). As such, P_d is a valuable quantity in the diagnosis of fracture behaviour and it is routinely recorded as a function of time during both laboratory experiments and commercial applications in the field (Nolte, 1988 a and b; Medlin and Masse, 1984; Zoback and Pollard, 1978; Zoback and others, 1977; Hubbert and Willis, 1957). Records of driving pressure were made during all the experiments conducted during this research to compare with similar records from experiments in rock and to examine how various parameters affect the record. During the experiments, driving pressure within the starter slot was obtained by measuring the pressure of the injection fluid as it entered the fracturing cell and subtracting the pressure in the pneumatic bladder acting normal to the slot.

The records of driving pressure as a function of time, hereafter termed *records*, were obtained for a variety of conditions. They will be described in the following section.

Reproducing the Records

Early in the experimental program a suite of four tests was conducted to examine whether the records could be reproduced. Four samples were prepared from a common batch of soil and consolidated together beneath the loading pallet described above. The properties of the samples were similar: densities were within 0.01 gm/cm^3 and moisture contents differed by less than one percent. Slot lengths, applied loads and other factors were identical.

Forms of the records for the four samples (Fig. 2.11) are similar, characterized by the following periods:

Period I: Nearly constant positive slope

Period II: Slope diminishes, but remains positive

Period III: Slope is negative

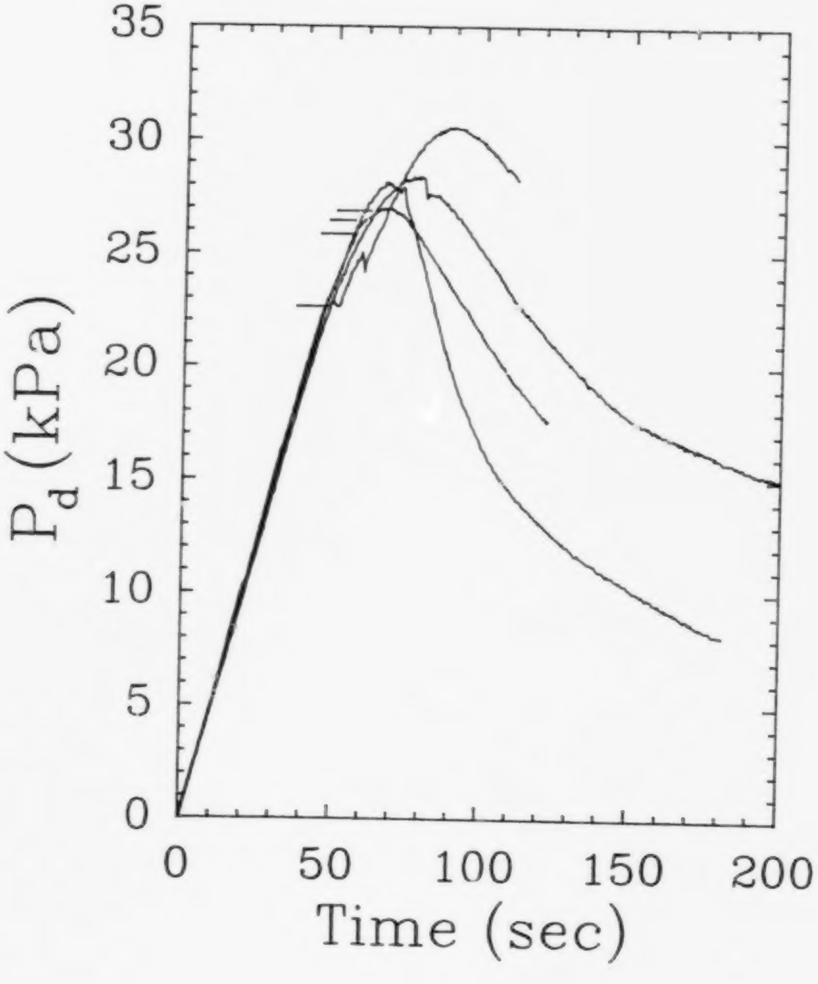

Figure 2.11. Records of driving pressure as a function of time from tests conducted on similar samples.

The records are nearly identical during Period I. The boundary between Period I to Period II was identified by marking the location of the break in slope typical of Period I. Three of the records in Figure 2.11. show smooth changes in slope, whereas one of the records shows an abrupt step in the record. Pressures marking the boundaries between periods are indicated by short markers on the records.

The driving pressures marking the change in slope are within 1.0 kPa for three of the samples, and they range over 4.1 kPa, from 22.8 to 26.8 kPa, for all four samples. The driving pressures average 25.4 kPa and show a standard deviation of 1.86 kPa, which is within seven percent of the average.

The forms during Period II are similar for three of the records, showing a gradual decrease in slope. The other record is marked by two short intervals during which the slope changes drastically as the pressure decreases and then increases abruptly. That record is similar to the others, however, if the two short intervals are ignored. Slight, abrupt changes in pressure were observed in other records, but their occurrence was unpredictable.

The maximum driving pressure marks the boundary between Periods II and III, and it ranges over 3.7 kPa (from 27.0 to 30.7 kPa), roughly the same range as the boundaries between Period I and II. The record showing the least pressure between Periods I and II yields the greatest pressure between Periods II and III. The average maximum pressure is 28.8 kPa, and the standard deviation is 2.03 kPa.

During Period III, driving pressure decreases and approaches a constant slope that is similar for three of the records. A constant slope is approached by the record of the fourth sample, but it is steeper than the other three. Slopes of two of the records diminish with continued propagation during Period III.

The records appear to be reproducible in both form and magnitude up to the time of maximum pressure. Variations in the pressures marking the boundaries of the Periods are within 10 percent of the total driving pressure. The records during Period III are similar in form, but their magnitude at any given time ranges over 10 kPa or more.

The forms of the records described above resemble the records presented by Medlin and Masse (1984) and Daneshy (1976a), both of whom used apparatus similar to the one used here but conducted their experiments using limestone or sandstone. The principal difference between the records from tests where rock is fractured and those in Fig. 2.11 is the slope early in Period III; it is generally steeper when rock is fractured. However, considerable differences are seen in the forms of records of hydraulic fracturing tests using rock, and some of them are nearly identical to those in Figure 2.11 (e.g. Daneshy, 1976a; fig. 6).

Previous studies of hydraulic fracturing of soil (Mori and Tamura, 1987; Jaworski and others, 1981; Jaworski and others, 1979; Bjerrum and others, 1972) have measured the rate of flow into a sample while keeping pressure constant, and then slightly increasing injection pressure until fracturing occurs. The records of those studies are typically presented as injection pressure plotted with respect to flow rate, and they are difficult to compare to the records from tests presented here where injection rate was held constant.

Fracture Development with Respect to the Record

Most tests were terminated sometime during Period III, but several tests were terminated during Periods I and II in an effort to correlate the development of a fracture to the form of the record. Samples similar to the ones described in the previous paragraph were prepared so that the pressures marking the boundaries between Periods could be anticipated. The surfaces of fractures terminated at different times are shown in Figure 2.6a through c. The times when each of those tests was terminated are shown on an idealized record (Fig. 2.12).

Most tests terminated during Period I showed a starter slot enveloped by unfractured soil; a hydraulic fracture was absent. In two cases, small hydraulic fractures were observed even though the tests were terminated prior to a break in slope in the pressure record. These incipient fractures were less than 1.0 cm longer than the starter slot, and short unwetted zones occurred at their leading edge.

Tests terminated during Period II, however, show well-developed hydraulic fractures several cm in maximum length. The edges of the fracture during Period II typically are contained within the sample, that is the fracture has not yet reached the edge of the sample (Fig. 2.6a).

Another test was terminated early in Period III, roughly five seconds after the maximum pressure. The sample from this test contains a fracture that is longer than the one terminated during Period II, and it has intersected the edges of the sample (Fig. 2.6b).

The third sample shown in Figure 2.6c was terminated several tens of seconds into Period III and it shows a fully-developed fracture cutting from one edge of the sample to another.

Those observations indicate that the break in slope of the record (Fig. 2.11) indicates that hydraulic fracturing is taking place. In some cases, incipient fracturing apparently occurs prior to the break in slope. Incipient fracturing cannot be detected on the pressure records, at least by the methods of recording pressure used for this work, so we will assume that fully-developed fracturing starts at the break in slope. The driving pressure at the break in slope P_{df} is taken as the critical driving pressure required to initiate fracturing.

Following the onset of fracturing, driving pressure continues to increase during Period II and then decrease during Period III. Increasing driving pressure during propagation indicates a period of *stable* growth of a hydraulic fracture, whereas decreasing pressures indicate *unstable* growth (Tetelman and McEvily, 1967; Zoback and others, 1977; and Zoback and Pollard, 1978). These terms are used because if the driving pressure were held constant a stable fracture would be held open but would not propagate, whereas an unstable fracture would continue to propagate at constant pressure. Thus, the three Periods of the injection record relate to three different processes during a test:

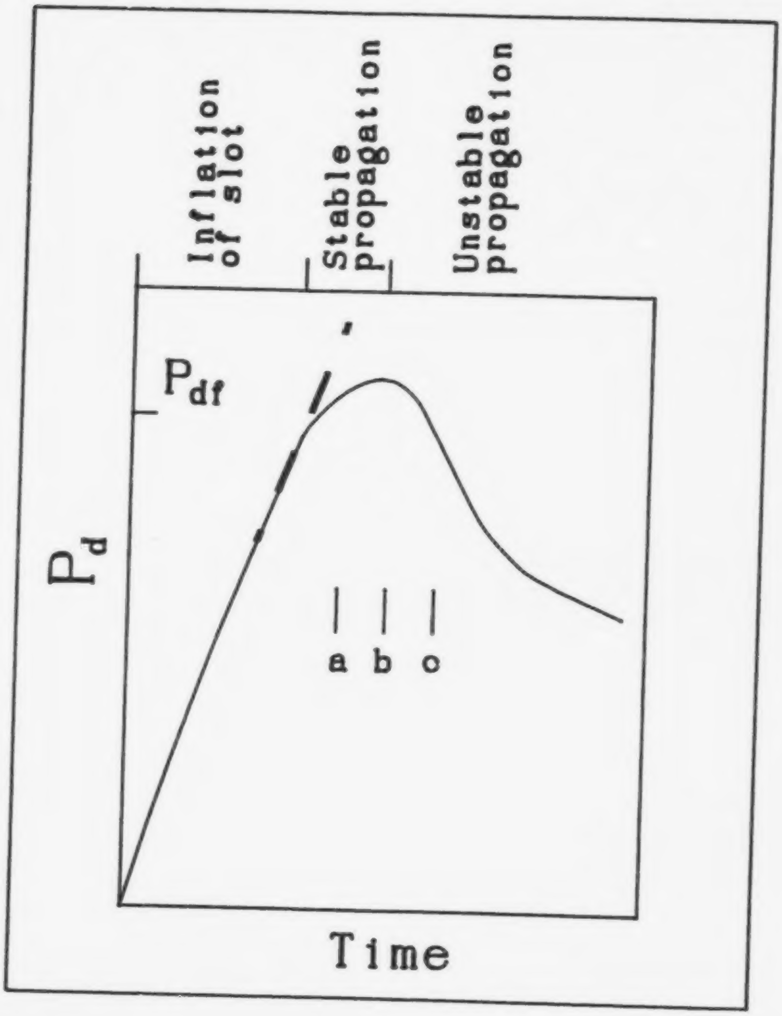

Figure 2.12. Idealized record of driving pressure as a function of time. Letters correspond to times of termination of tests resulting in fractures shown in Figure 2.6a, b, and c.

Period I: Inflation of the starter slot

Period II: Stable propagation of a hydraulic fracture

Period III: Unstable propagation

In an earlier section linear features were used to infer that the fracture initiated within the sample and then grew outward to the edges as it increased in length. This interpretation is supported by the images shown in Figure 2.6, and suggests that stable growth occurs from the time when the fracture initiates to when it intersects the edges of the sample.

Williams (1984) presents one explanation relating this behavior to the geometry of the specimen. He shows that a notched rectangular specimen will be under conditions of plane strain at its center, whereas it will be under plane stress near its edges. The resistance of a material to fracturing in plane strain is less than in plane stress, because conditions of plane strain reduce plastic deformation at the crack tip (Williams, 1984). According to this explanation, the increase in driving pressure during Period II occurs as the fracture grows from the center of the sample into material offering greater resistance to propagation. Williams' arguments are based on a sample whose outer surface is unconfined, whereas the samples used in this study were confined in a triaxial pressure cell. Friction between the outer surfaces of a sample and the walls of the fracturing cell would further inhibit propagation as a fracture grew toward the edge of the sample.

Zoback and Pollard (1978) show that propagation of a hydraulic fracture can be initially stable, regardless of the geometry of the sample. They attribute this stability to viscous losses in driving pressure in the incipient fracture. It is possible that a similar mechanism contributes to the stable propagation during Period II.

Effects of Moisture Content

Suites of samples were prepared by placing soil of differing moisture content into the sample molds. Soil in the molds was consolidated for 10 to 14 days, until displacement during loading was negligible. The resulting samples differed in moisture content and bulk density, but were otherwise similar. It is possible that moisture content varied slightly within the samples, due to incomplete equilibration. Drainage during consolidation was only possible through geotextiles on the two sides of the sample that were parallel to the starter slot, however, so that moisture contents would be uniform along the planes of the fractures. Fractures were created in the samples and the results of one suite of tests, which is representative, is shown in Figure 2.13.

The form of the record of injection pressure is markedly affected by increasing the moisture content of a sample. During Period I, it causes a slight decrease in the slope, but the most striking effects are seen during Periods II and III. The pressure marking the transition between Periods I and II diminishes as moisture content increases. Furthermore, the slopes of both Periods II and III become more gentle, resulting in a flattening of the curved part of the record.

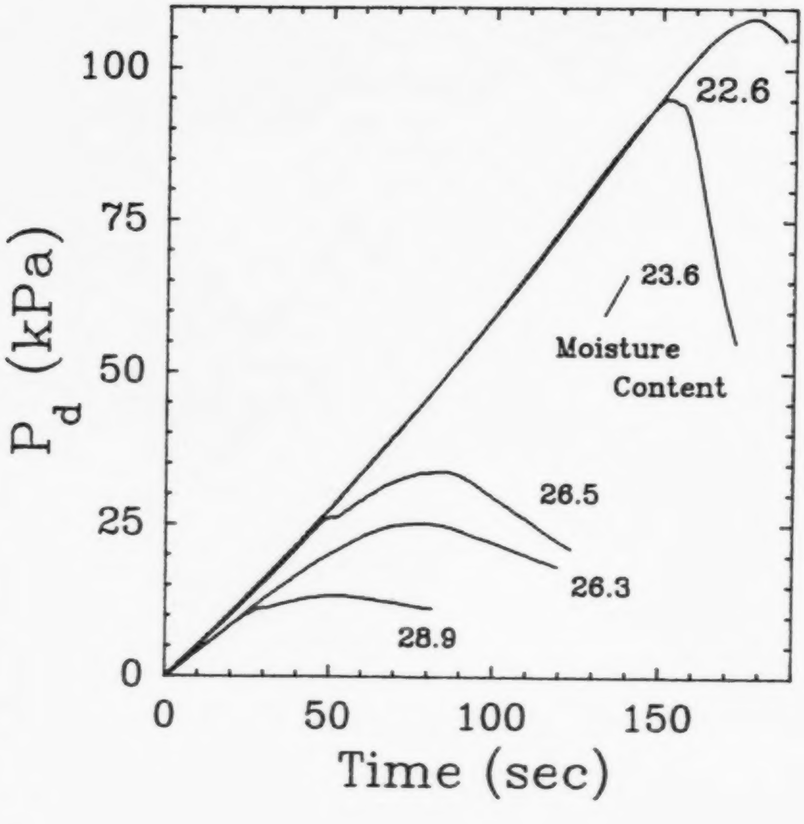

Figure 2.13. Records of injection pressure as a function of time for samples of various moisture contents.

Driving pressures required to initiate hydraulic fracturing decrease by an order of magnitude, from more than 100 kPa to 10 kPa, by increasing the moisture content of the samples by only six percent. Once propagation begins, the period of stable growth, Period II, becomes longer as moisture contents increase. The transition from stable to unstable fracture growth, indicated by a change from positive to negative slope on the record, is well-defined for relatively dry samples but it becomes subtle for relatively wet samples. Despite this subtlety, however, periods of both stable and unstable growth could be identified in all tests.

Explanation of the effects of moisture content on the fracture process will require development of several theoretical models in Section 3, but an explanation of how the slope dP_d/dt differs with moisture content during Period I can be readily explained. The starter slot is inflating during Period I and the different slopes appear to be related to an increase in modulus as moisture content decreases. According to Tada (1985) the volume of a pressurized slot in plane strain is

$$V = 2\pi P_d w a^2 (1 - \nu^2)/E \qquad (2.2)$$

where w is fracture width, a is the fracture half length, ν is Poissons ratio, and E is the elastic modulus. Differentiating with respect to time and assuming[1] that

$$dV = Q\,dt \qquad (2.3)$$

where Q is the rate of injection yields

$$dP_d/dt = QE/[2\pi a^2 w(1 - \nu^2)] \qquad (2.4)$$

neglecting the effect of the small hole along the axis of the slot. The slope during Period I is linearly related to elastic modulus of the sample, according to eq. (2.4). Uniaxial compression tests conducted on the clay show that the elastic modulus decreases by at least an order of magnitude over the range of water contents of the samples. We conclude that a decrease of elastic modulus could cause the observed change in slopes of the records. The changes in slope, however, are small compared with the change in modulus. This probably results from volume changes in tubing and the pressure interface of the pumping system, which contribute to the slope during Period I but are overlooked in eqs. (2.3 and 2.4).

Effect of Slot Length

The effect of varying the length of the starter slot is summarized in Figure 2.14, which shows the records from four experiments conducted on similar samples

---

[1] This assumption requires that none of the glycerin leaked out of the fracture into the clay.

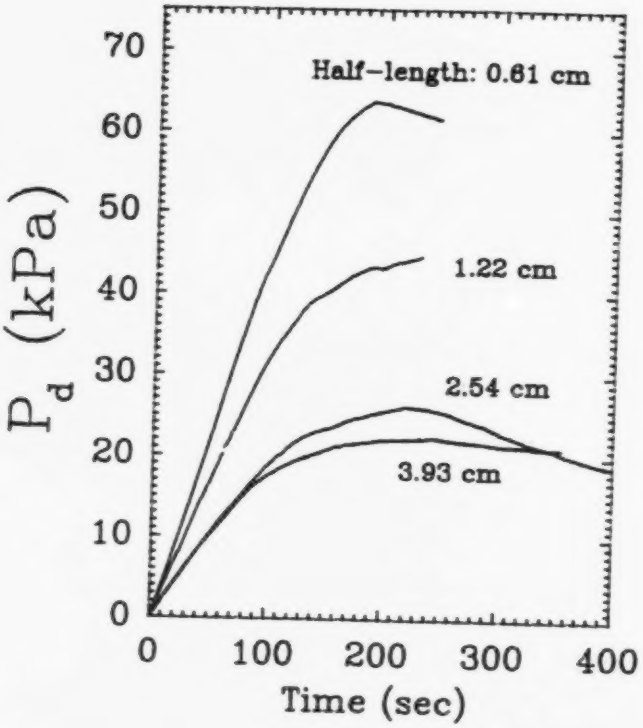

Figure 2.14. Records of injection pressure as a function of time using various lengths of starter slots.

differing only by the lengths of their slots. Other experiments conducted on pairs of similar samples (one large sample split into two) confirm the features shown in Figure 2.14.

A decrease in the pressure at which fracturing occurs P_{df} is the most striking effect of increasing slot length. The relationship between P_{df} and half-length of the slot *a* is characterized by the empirical function

$$P_{df} = C\,a^{n} \tag{2.5}$$

in which $C = 39.3$ and $n = -0.61$. Many other materials, including rock, steel, ceramics and glass, show a relationship similar to eq. 2.5, with values of *C* related to fracture toughness of the material, and values of *n* varying slightly from -0.5 (Williams, 1984; Lawn and Wilshaw, 1975; Daneshy, 1976b; Clifton and others, 1976).

The pressure at which failure occurs is by no means the only effect of increasing the length of the starter slot; the shape of the record is also affected. Records from tests using shorter slots show a period of stable growth, during which pressure increased by 10 kPa or more, followed by a period of unstable growth during which driving pressure decreased markedly. As slot length increases, however, the period of stable growth becomes longer and driving pressure increases by a smaller amount--several kPa--during stable growth. During unstable growth, the amounts of decrease of driving pressure are less for fracture started from the longer slots than from the shorter ones (Fig. 2.14).

SUMMARY AND DISCUSSION

Observations in the preceding section suggest a scenario for the development of a hydraulic fracture in soil that is straightforward, yet more detailed than previous works (Mori and Tamura, 1987; Brunsing and Henderson, 1984; Jaworski and others, 1981; Bjerrum and others, 1972). The early stage of injection at a constant rate was characterized by inflation of the starter slot, which resulted in a roughly linear increase in driving pressure. A hydraulic fracture formed when the driving pressure reached some critical value, the magnitude of which diminished with either an increase in the length of the slot, or a decrease in the moisture content of the soil. Driving pressure continued to increase during the early stages of propagation. At some point, either at the onset of propagation or after the fracture had reached some critical length, the injection fluid lagged behind the leading edge of the fracture leaving an unwetted zone at the tip. Once it began to form, the length of the unwetted tip increased roughly in proportion to the length of the wetted zone of the fracture.

The slope of the pressure record decreases from roughly the onset of propagation, resulting in a concave downward form. The forms of the records differed in detail, however, depending on the length of the starter slot and the moisture content. A short slot resulted in a record that was tightly concave, with the pressure diminishing sharply following the onset of propagation. A longer slot caused the concavity of the record to broaden, so that the pressure increased slowly and then decreased slowly during propagation. Keeping the slot length constant, but decreasing the moisture content resulted in a similar change in the shape of a record: it was sharply concave when the samples were relatively dry, but it became broader and flatter as the moisture content increased.

Moisture content affected the development of the unwetted tip as well. An unwetted tip was absent, that is stain covered the entire fracture surface in samples less than 21% in moisture (roughly the plastic limit). As moisture content increased, the length of the unwetted tip relative to the length of the dyed fracture increased, until it reached a maximum length of 0.25cm in samples of 28% moisture. Preliminary evidence indicates that the unwetted tip decreases in relative length as moisture content increases to values greater than 28%.

The growth of the unwetted tip appears to be a fundamental feature of hydraulic fractures in Center Hill clay at moisture greater than the plastic limit. That feature is by no means unique to clay; unwetted zones at the leading edge of hydraulic fractures in rock have been observed in experiments by Medlin and Masse (1984). Their apparatus differed from the one used in this research in that theirs was fitted with ultrasonic transducers which yielded data on aperture and fluid content as a fracture was growing. They observed marked attenuation of the ultrasonic signals near the tip of a growing fracture and inferred that the tip of the fracture was filled with air. Results from one of their experiments (Medlin and Masse, 1984; fig. 6) indicates that the unwetted zone first forms at the starter slot, it grows to length L_{uw} and then is roughly constant as the length of the wetted zone L_u increases during propagation. This differs slightly from our results, which indicate that L_{uw} increases with L_w.

Similarity between surface textures of the unwetted tip and the wetted fracture, as well as the continuity of linear features from the wetted fracture to the unwetted tip indicate that the unwetted tip is open and a part of the fracture itself. This is in contrast to so-called decohesion zones, or process zones, identified or postulated from studies of fracturing of metal, polymer or rock. The process zone is an interval over which the material becomes separated. In tensile fractures, of which hydraulic fractures are a special case, processes of decohesion involve the nucleation and growth of voids or microfractures (Williams, 1984; Tetelman and McEvily, 1967). The process zone is characterized by vestiges of material cohesion resulting from the strength of intact material remaining between voids, and as such it differs from the fracture itself where the material is completely separated and cohesion is absent. Process zones composed of clusters of voids have been described at the tips of fractures in metals (Shockey and others, 1979; Tetelman and McEvily, 1967; Irwin, 1957) and polymers (Williams, 1984; Weidmann and Doell, 1979). Ouchterlony (1982) postulates a process zone in rock that consists of dilating microfractures, which produce acoustic signals that are commonly used to monitor the fracturing process in rock (Ouchterlony, 1982; Zoback and others, 1977). Time-lapsed sequences of photographs by Knauss (1976) capture the coalescence of voids resulting in the formation of fracture surfaces in polymers.

Phenomena occurring in the process zone of a fracture in clay have received little attention. In normally-consolidated kaolin, micron-sized voids occurring between aggregates of grains were observed to grow by coalescing during the early stages of shear loading (Smart and Dickson, 1979). To our knowledge, processes at the tip of a fracture in clay under tensile loading have yet to be studied, but it seems reasonable to assume that those processes involve microfracturing or void growth ahead of the fracture itself. Whatever processes are involved, the zone in which they occur appears to be ahead of, and distinct from, the unwetted tip.

In cross-section, an idealized hydraulic fracture in clay is inferred to be composed of a zone wetted by pressurized injection fluid, an unwetted zone near the tip where fluid pressure is zero, and a process zone in front of the tip where decohesion of the clay takes place. The idealized cross-section is shown in Figure 2.15, where lobes are assumed to be absent for simplicity.

Hydraulic fracturing of clay was inevitable in the laboratory experiments; it occurred in all samples that could be properly prepared. We tried to inhibit fracturing by increasing the water content and softening the clay. The wettest sample that could be prepared as described above, however, could be hydraulically fractured and the appearance of the fracture in that sample resembled that of drier samples. Samples of extremely high water contents were too soft to be handled and we were unable to prepare them using the procedures described.

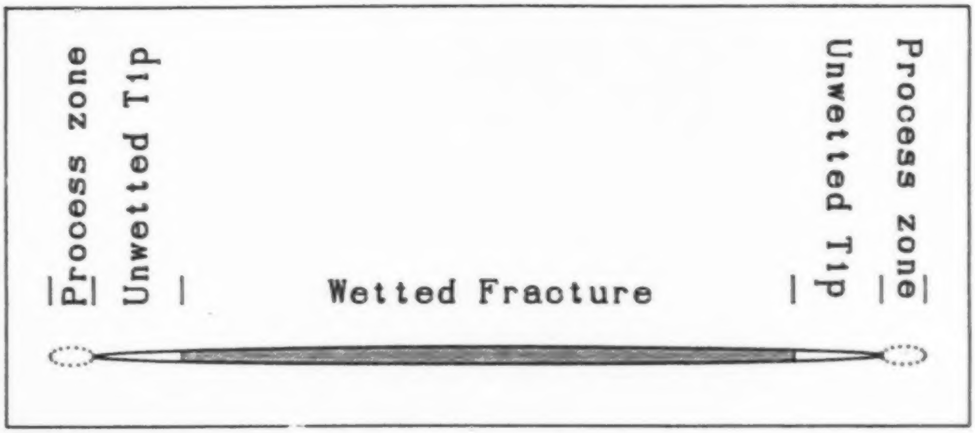
Process zone
Unwetted Tip
Wetted Fracture
Unwetted Tip
Process zone

Figure 2.15. Idealized cross-section of a hydraulic fracture in clay.

SECTION THREE

ANALYSIS OF HYDRAULIC FRACTURING OF SOIL

Since the work of Kristianovich and Zheltov in the mid-1950s, the principles of elasticity theory have been used to analyze the onset and propagation of hydraulic fractures in rock. Those principals have resulted in a significant body of published papers describing both methods of formulating and solving for various fracture geometries and boundary conditions, and techniques of applying those methods to design field applications. Details of the methods vary considerably, but the use of elasticity theory to determine deformation of material enveloping the fracture is virtually universal.

The broad knowledge-base of published analyses based on elasticity theory would be an extremely valuable tool in designing hydraulic fractures under near-surface conditions. The application of such methods to analyze the hydraulic fracturing of soil, however, is currently untested. The appearance of fractures created in clay resembles the appearance of hydraulic fractures created in rock, as well as that of tensile fractures in a range of other materials. This semblance is encouraging, but appearance alone is insufficient to provide grounds for adopting a mechanical theory. Previous investigators of hydraulic fracturing of soil (Mori and Tamura, 1987; Horsrud and others, 1982; Jaworski and others, 1981 and 1979; Massarsch, 1978; Leach, 1977; Wong and Farmer, 1973; Bjerrum and others, 1972; Morgenstern and Vaughan, 1963) have developed analyses based on theories of elasticity or plasticity to provide predictions of pressures required to induce hydraulic fracturing from a cylindrical hole in soil. Those analyses are also encouraging, but they are limited to predicting initiation from a borehole and reveal little about the behaviour of the fracture itself.

Is elasticity theory applicable to hydraulic fracturing of clay? The purpose of the following chapter is to answer that question by analyzing critical aspects of the lab experiments. The method of analysis will be acceptable if it can predict or explain:

1. The onset of fracturing
2. Essential features of a hydraulic fracture
3. Forms of pressure records observed during propagation

Those criteria will be addressed using analyses based on linear elastic fracture mechanics, a branch of elasticity theory. Results of the analyses will be compared with the results of lab experiments, and the degree to which they are similar will determine applicability of the approach.

The analyses that will be developed are intended to predict effects, principally the growth of an unwetted zone at the fracture tip, that are commonly ignored by investigators who study hydraulic fractures in rock. Unwetted zones do develop in hydraulic fractures cutting rock, however, so the results of the analyses may be relevant to hydraulic fractures in both

The growth of unwetted zones at the tips of hydraulic fractures in rock is particularly well documented by Medlin and Masse (1984). Those investigators used an apparatus that was similar to the one used in this work. One important difference, however, is that their apparatus was fitted with ultrasonic transducers yielding information on fracture length, aperture, and fluid content *during propagation*. The experimental method used in this work was only able to yield pressures during propagation.

The primary goal of the following chapter is to explain results of lab experiments of hydraulic fracturing of soil. Certain experimental results of Medlin and Masse will also be used in the following chapter because they offer data describing propagation.

PREDICTING THE ONSET OF HYDRAULIC FRACTURING

The stresses in the vicinity of a straight fracture in an infinite elastic medium are concentrated at the fracture tip. In the vicinity of the tip, stresses are proportional to $r^{-1/2}$ where r is the radial distance from the tip. That relation results in a singularity in the stresses at the fracture tip itself, at $r = 0$. The strength of the singularity is characterized by the stress intensity factor K which is given by (Inglis, 1957; Tada and others, 1985)

$$K = \sigma\sqrt{\pi a}\; f(b) \tag{3.1}$$

where σ is the applied stress, a the half-length of the fracture, and $f(b)$ is a function of the geometry of the fracture and the enveloping material.

The driving pressure P_d (Secor and Pollard, 1975) of a hydraulic fracture is the difference between the internal fluid pressure p, which tends to open the fracture, and the confining stress σ, which tends to close it, so

$$P_d = p - \sigma \tag{3.2}$$

Three *modes* of deformation are generally recognized in fracture mechanics (Lawn and Wilshaw, 1975), where mode I involves only dilation and modes II and III involve shear parallel to the fracture walls. Each mode results in its own stress intensity factor, but shear stresses cannot be supported on the walls of a fluid-filled hydraulic fracture, so the following work will be limited to K_I the mode I stress intensity factor.

A basic assumption in linear elastic fracture mechanics is that the onset of fracturing occurs when the stress intensity equals a critical value K_{Ic}. The magnitude of K_{Ic} is commonly regarded as a material property characterizing the resistance of a material to fracturing. If the critical stress intensity is valid material property of clay, it can provide a means of predicting the driving pressure required to initiate fracturing.

Critical stress intensities of soil were determined through eq. (3.1) by obtaining a critical driving pressure P_{dc} at the first change in slope of the pressure record from the lab experiments described in Chapter Two. Other accepted methods, such as those decribed by Ouchterlony (1982) for fracture toughness testing of rock, pick the critical load at fracturing based on a certain (5 percent) deviation from linearity of the record of load with respect to crack opening displacement (COD). Measurements of COD were impossible to make using our apparatus, however, and our observations suggested that fracturing occurs at, or perhaps even slightly before, the first change in slope of the pressure record.

In general, the function $f(b)$ in eq. (3.1) is equal to unity under the ideal conditions of a straight slot of zero initial aperture in an elastic medium of infinite extent. It is less than unity and can be taken as a correction factor for practical constraints such as finite sample size. Tada and others (1985) give expressions for $f(b)$ for a straight slot containing an axial hole, and for a straight slot embedded in a rectangular sample of finite size. Those conditions represent relevant corrections for the experimental apparatus used in this work. However, correction factors determined for the geometries of the lab apparatus are minor (within five percent of 1.0), so $f(b)$ was set equal to 1.0 in the determinations of K_{Ic}. The critical stress intensity was calculated using

$$K_{Ic} = P_{dc}\sqrt{\pi a} \tag{3.3}$$

Tests were conducted to determine the relation between K_{Ic} and the length of the starter slot (Octerlony, 1982). These tests consisted of preparing sets of similar samples and cutting slots of a different length in each sample. Sixteen sets of samples of Center Hill clay were prepared, where one set consisted of four full-length samples, two sets consisted of three full-length samples, and the other sets consisted of one full-length sample cut in half to give two half-length samples. One set of three full-length samples composed of River Downs silt was also tested. The samples were fractured using procedures described in Chapter Two and K_{Ic} was determined using eq. (3.3).

According to the results of those tests (Fig. 3.1), doubling the length of the starter slot resulted in an average variation of 0.104 (variation was determined as the absolute value of the difference between two measurements divided by their average). That average value includes the results of several sets of unusually large variation (one value of 1.0, and two others greater than 0.4). Nevertheless, the average variation caused by doubling the length of the initial fracture is similar to the variation of 0.081 observed among results from four identical samples described in the previous chapter.

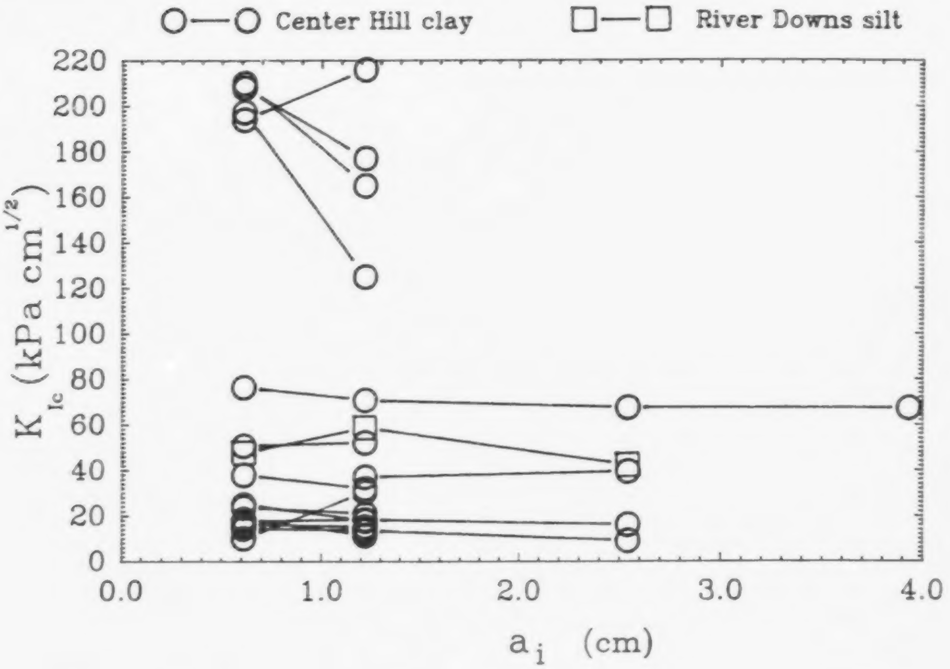

Figure 3.1. Critical stress intensity as a function of half-length of starter slot for similar samples of Center Hill clay and River Downs silt.

The critical stress intensity of rock and metal is observed to increase slightly as a function of slot length, if the slot length is less than a critical value that depends on K_{Ic} and a tensile yield strength (e.g. Ochterlony (1982); Schmidt (1977); Kaufmann and Nelson (1974), and references therein). As the length of the starter slot increased in the experiments using soil, the critical stress intensity decreased for ten of the sample sets, it increased for four of the sets, and it both increased and decreased for two sets of samples (Fig. 3.1). Although K_{Ic} decreased for more sample sets than it increased, there appears to be no systematic relation between K_{Ic} and a. It is unclear whether K_{Ic} is independent of a for the Center Hill clay, or whether the critical length for that dependence is less than the slot lengths used in this study.

The results of the previous two paragraphs indicate that K_{Ic} can be used to predict (within roughly 10 percent) the driving pressure required to propagate a hydraulic fracture in Center Hill clay. Likewise, the few tests conducted using River Downs silt suggest that K_{Ic} can be used to predict hydraulic fracturing in that material as well. It is apparent from Figure (3.1), however, that the value of K_{Ic} varies over more than an order of magnitude for samples of the Center Hill Clay. Thus, some method of anticipating K_{Ic} will be required to make a useful prediction of the onset of propagation.

Moisture content and duration of consolidation varied from one sample set to another, and they both have a marked affect on the critical stress intensity. Among samples that were prepared by compaction alone, K_{Ic} is greatest, roughly 200 kPa $cm^{1/2}$, at moisture contents between 0.17 and 0.21. The critical stress intensity decreases abruptly to roughly 35 kPa $cm^{1/2}$, however, as moisture content increases from 0.21 to 0.22. The moisture content of this sharp change in K_{Ic} is slightly wetter than the plastic limit of the soil. Further increases in moisture slightly decrease the average K_{Ic}, although the decrease is small and K_{Ic} is practically independent of moisture content over the range 0.22 to 0.30.

Critical stress intensity is neglible for samples of moisture content greater than 0.32. This means that the break in slope of the pressure record, from which the onset of fracturing was inferred, occurs when the pressure of the injection fluid is equal to the confining stress. Hydraulic fractures produced during these tests are physically indistinguishable from other fractures produced when K_{Ic} is greater than zero.

Consolidation appears to toughen the Center Hill clay (Fig 3.2b). Critical stress intensity of samples that were consolidated for four days using procedures described in the previous chapter are greater than they are for the compacted samples of similar moisture. Moreover, increasing the duration of consolidation to 14 days further increases K_{Ic}, according to Figure 3.2b. The forms of the three curves in Figure 3.2b are similar, however; they all show K_{Ic} decreasing markedly (from roughly 200 kPa $cm^{1/2}$ to between 30 to 50 kPa $cm^{1/2}$) over a few percent of moisture.

Limited tests conducted on the River Downs silt show that K_{Ic} is four or five times less than K_{Ic} of the Center Hill clay at similar moisture content (Fig. 3.2). This result suggests that fractures will develop in the silt at lower driving pressures than in the clay, if the two materials contain the same weight percent water. Lab experiments to confirm this suggestion were not conducted, but it is consistent with the common behavior of the two materials; the silt readily fractures and crumbles, whereas the clay tends to resist crumbling when pieces of the material are worked manually.

Discussion

The critical stress intensity is a material property of clay that depends on moisture content and duration of consolidation, according to the results of this investigation. Driving pressure marking the onset of propagation of a hydraulic fracture in the Center Hill clay could be roughly predicted by estimating K_{Ic} from water content and consolidation history and measuring the length of a pre-existing fracture. The effects of other parameters, such as compaction effort, will also affect K_{Ic} (e.g. Jaworski and others, 1979) although the present study was limited to effects of moisture content and duration of consolidation. the requirements of an acceptable theory of hydraulic fracturing of soil, the ability to predict propagation of a pre-existing fracture, appears to be satisfied by the critical stress intensity factor.

The use of K_{Ic} as a fracture criterion generally requires that the fracture process zone, where inelastic behavior such as microcracking or void coalescence occurs, is small compared with the dimensions of the fracture and the specimen (Tada and others, 1985; Williams, 1984; Ouchterlony, 1982; Rice, 1968). Schmidt (cited in Ouchterlony, 1982) describes a method of estimating the size of the process zone based on a maximum normal stress criterion. That method tacitly assumes that the dilation of microcracks is the dominant phenomena occurring in the process zone, an assumption that is accepted for rocks (Ouchterlony, 1982) and seems reasonable for clayey soil as well. The maximum length of the process zone L_p is given by

$$L_p = 0.269\ [K_{Ic}/(\sigma_y + \sigma_c)]^2 \tag{3.3a}$$

where σ_c is the mean confining stress, and σ_y is the tensile yield stress required to open microcracks in the process zone. Several investigators have

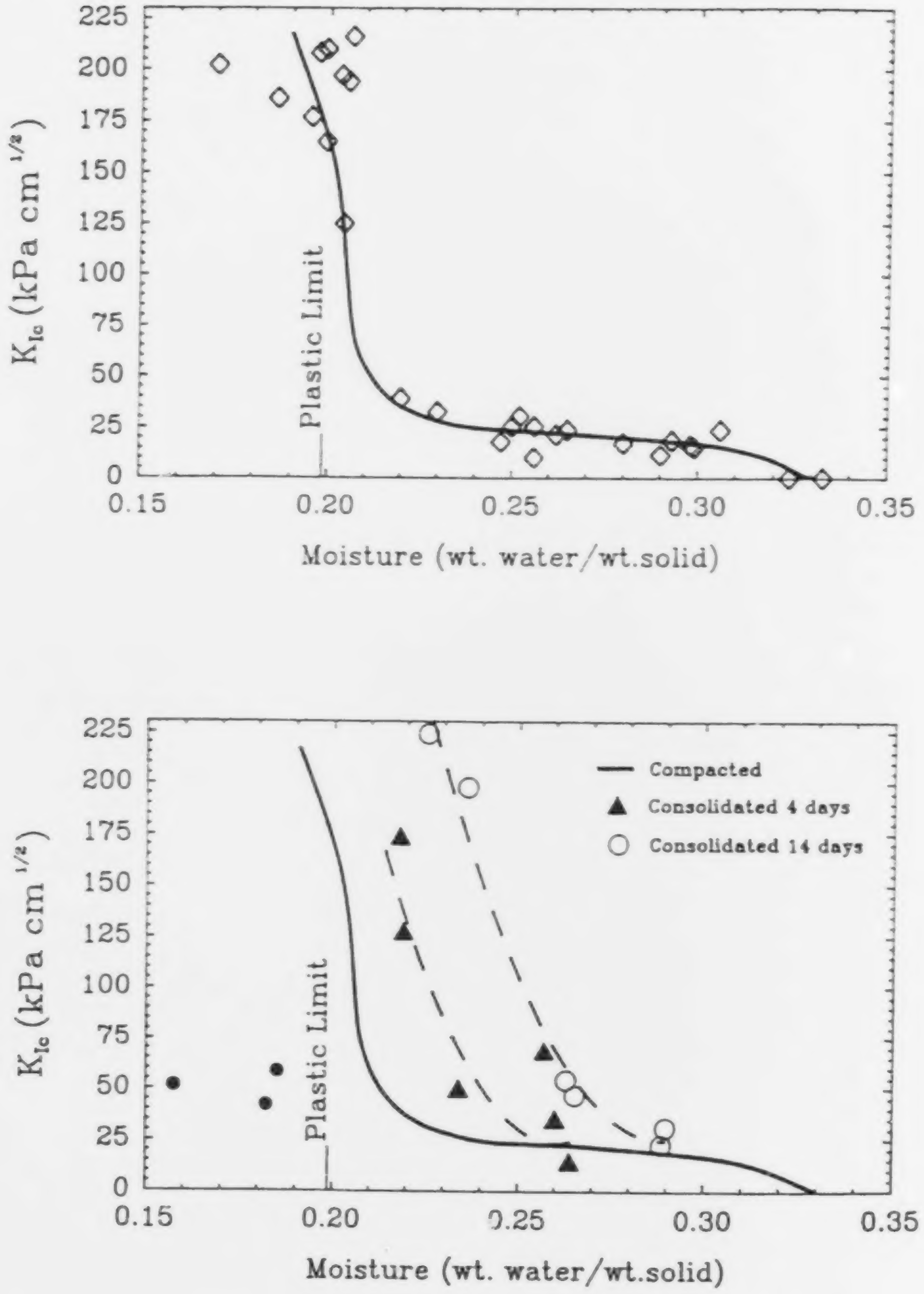

Figure 3.2 Critical stress intensity of Center Hill clay as functions of moisture content and duration of consolidation. Filled circles on lower plot are for River Downs silt.

described methods of measuring tensile yield strength of soil (Snyder and Miller, 1985; Snyder, 1980; Vomocil and Chancellor, 1967; Farrell and others, 1967), but all of those methods make use of special equipment that was unavailable during this study. The tension of pore-water, however, could be taken as a tensile yield strength because dilation of microcracks in the process presumably must overcome the pore-water tension. In a sample of 0.20 moisture under load in the fracturing cell, the pore-water tension was 60 kPa, according to measurements made using a tensiometer (SoilMoisture Model 2100). Measurement of a sample containing 0.27 moisture yielded inconclusive results, perhaps because the sample was saturated and the gauge attached to the tensiometer was only able to measure suction; the tensile strength of the 0.27 material will be assumed to be zero. The critical stress intensity for 0.20 moisture is roughly 180 kPa cm$^{1/2}$, whereas for 0.27 moisture it is 50 kPa cm$^{1/2}$ (Fig. 3.2).

The maximum length of the process zone ranges from 0.47 cm for 0.20 moisture down to 0.13 cm for 0.27 moisture, according to eq. (3.3a) and data in the preceeding paragraph. The length of the initial slots ranged from 1.22 to 5.05 cm, and the length from the end of the slot to the end of the sample was greater than 5 cm. The process zone in the Center Hill clay was always at least several times smaller than both the initial starter slot and the sample. This suggests that K_{Ic} should be a reasonable predictor of fracturing, according to Tada and others (1985) and Williams (1984), who state that the accuracy of K_{Ic} improves as L_p diminishes to lengths significantly less than the length of the starter slot or the sample. It is apparent from eq. 3.3a that L_p decreases as either tensile strength or confining stress increase, so that the accuracy of K_{Ic} should improve as confining pressures increase to values greater than the 69 kPa used in the lab. Confining pressures of most anticipated field applications, for example, would exceed 69 kPa. The relation between the size of the process zone and the accuracy of K_{Ic} also may explain why the drier samples, which have the larger process zones, exhibit the greatest variability of K_{Ic} (e.g. Fig. 3.1).

We recognize that in some cases incipient fracturing may occur at driving pressures less than those marked by a break in slope in the record. A change in slope of the pressure record was the only method available to detect the onset of fracturing during the present work. Values of critical stress intensity presented here should be taken as *apparent* intensities for the onset of fully-developed hydraulic fracturing and they may overestimate the critical stress intensity obtained from other types of tests, such as a compact tension test or three-point bend test (Tada and others, 1985).

The method described above is by no means the only one that uses principals of linear elastic fracture mechanics to predict the onset of tensile fracturing of soil. Briones and Uehara (1977b) cracked rectangular beam-shaped samples of soil in a bending apparatus and proposed a material characteristic (their eq. 9) that is equivalent to

$$K_{Ic} \cong \sigma_t \sqrt{\pi a} \tag{3.4}$$

where σ_t is assumed to be the tension of pore fluid, and a is an effective length of pores, or microcracks in the soil. Their expression is based on the classic works of Griffith (1920) and Irwin (1957), and it is identical in form to eq. (3.1). The tension of pore fluid can readily be determined using a tensiometer, but Briones and Uehara (1977b) were unable to determine appropriate effective sizes of pores in their soil samples, and thus were unable to determine K_{Ic} through eq. (3.4).

Snyder (1980) and Snyder and Miller (1985) use methods of linear elastic fracture mechanics to develop another analysis predicting the tensile fracture of soil. They recognized the importance of pore size and shape in nucleating tensile fractures, and they were fully aware of the practical difficulty of measuring critical shapes and sizes of pores. To address this problem, Snyder (1980) introduces a parameter based on the degree of saturation that is intended to characterize the role of pore size and shape in the fracturing process. According to Snyder (1980), this approach to characterizing the role of existing flaws yields results that can explain both his own data and published data on tensile cracking of soil. Various other investigators (Rogowski and others, 1968; Farrell and others, 1967; Kirkham and others, 1959) have used methods based on elasticity theory to estimate tensile strength of soil without explicitly considering the effects of pores or microcracks.

The approach used here differs only slightly from that of previous workers. The principal difference--we cut a large slot to nucleate a fracture whereas they omitted the slot--is significant because our method explicitly addresses the role of existing cracks in a sample.

PROPAGATION OF A HYDRAULIC FRACTURE IN SOIL

Predicting or explaining essential features of both the hydraulic fractures themselves and the pressure records during propagation are two more requirements of the analysis. Meeting those requirements will be accomplished by including effects of propagation in the analysis. The propagation of a hydraulic fracture involves two basic processes, the flow of liquid within the fracture and the dilation of the fracture due to deformation of the enveloping medium. The processes are coupled in that the pressure distribution resulting from viscous losses during fluid flow is strongly dependent on fracture aperture, and the aperture depends on the pressure distribution. Flow within the fracture will be treated using methods of fluid mechanics, and dilation of the fracture will be treated using methods of elasticity theory.

Another condition, one that ensures equilibrium propagation, must also be considered. In keeping with the approach of linear elastic fracture mechanics we will require that the criteria for onset of fracturing is maintained throughout propagation. Accordingly, during equilibrium propagation the pressure distribution within the fracture must always result in the critical stress intensity. The fracture is considered to be out of equilibrium if the stress intensity exceeds the critical value, and propagation will cease if the stress intensity is less than the critical value. Other methods of maintaining equilibrium propagation are described by Geertsma and Haafkens (1979).

Conceptual Model

A conceptual model of fracture growth is the sequence of events describing the progression from an inflated slot to a typical fracture in the lab samples. This model of growth will be inferred from lab observations and from simple reasoning, and it will used as a framework for formulating theoretical analyses of propagation.

The model begins with a narrow slot cut in the material (Fig. 3.3). The slot is inflated at a constant volumetric rate, resulting in an increase in fluid pressure and an increase in the intensity of stresses at the edge of the slot. All the inflow during inflation results in dilation of the slot, so the flow rate diminishes along the fracture and must be zero at the tip. The fracture begins to propagate when the stress intensity equals the critical stress intensity for the material, according to the principles described earlier. Separation of material at the fracture tip during the onset of propagation occurs in response to the intensity of stress within the enveloping material. The stress intensity depends only on the magnitude and distribution of pressure, and it is independent of properties governing the flow of the fluid in the fracture. Indeed, separation of material at the fracture tip will occur when the critical stress intensity is achieved even if the fluid in the fracture is totally immobile and unable to fill the newly formed region (e.g. Clifton and others, 1976).

This concept is important because it suggests that the newly-formed region at the tip can be unfilled by injected fluid immediately following the onset of propagation. In other words, the tip of the fracture could be unwetted from the start of fracture growth. The lab experiments conducted for this work were unable to yield conclusive information about the fracture tip at the onset of propagation; however, Medlin and Masse (1984, fig. 6) clearly show that the unwetted region forms at the onset of hydraulic fracturing of rock.

The lengths of unwetted zones appeared to be proportional to the lengths of the wetted parts of fractures in the lab experiments conducted on clay samples of similar moisture content. In relatively moist samples, the length of the unwetted zone appeared to be linearly related to the length of the wetted zone from the start of the fracturing, whereas in drier samples we inferred that a critical fracture length was required before the linear relation was observed. The latter observation is consistent with our model if we postulate that a short unwetted zone forms at the onset of fracturing in the drier samples and grows slowly until the critical fracture length is

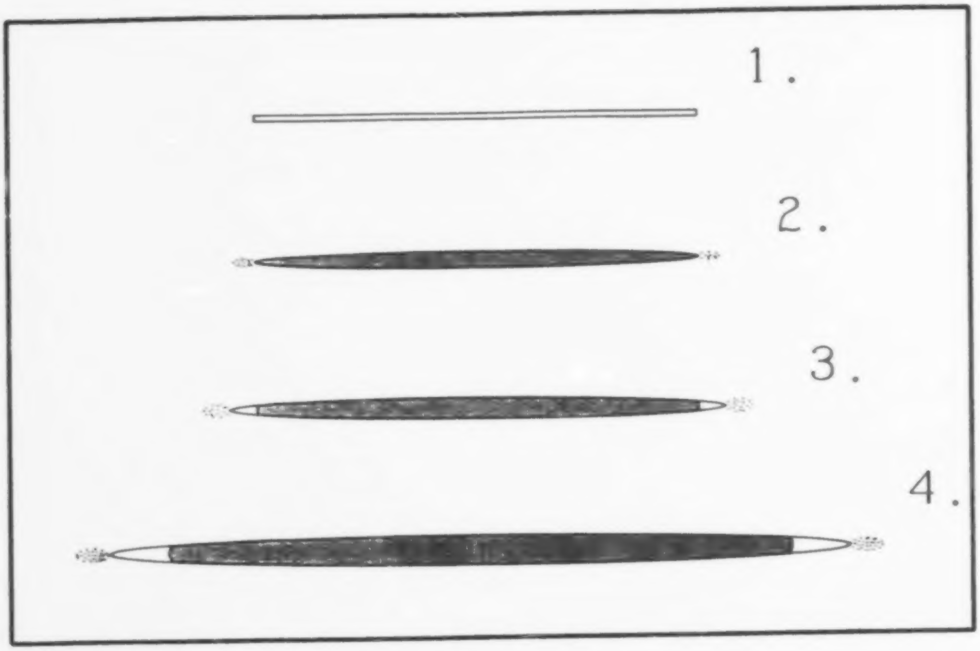

Figure 3.3. Conceptual model of the growth of an idealized hydraulic fracture in lab samples.

reached.

The conceptual model is summarized in four steps shown in Figure 3.3.

1. Pre-existing starter slot cut in a sample
2. Inflation of the slot leading to an increase in stress intensity, depicted by stipling at the tips of fractures in Figure 3.3.
3. The inflated slot begins to grow when the $K_I = K_{Ic}$. Part of the newly-formed fracture is unfilled by injected fluid.
4. The fracture increases in length and partly fills with fluid. A region at the tip of the fracture remains unfilled, and the length of the unfilled region increases during propagtion. Lab measurements suggest that the length of the unfilled region is linearly related to the length of the wetted fracture, although that relation is only approximate.

Analysis of Propagation

Two analyses will be used to examine the conceptual model and to predict the records of driving pressure as a function of time. Both analyses are based on linear elastic fracture mechanics, although they differ markedly in level of complexity. The first analysis that is presented solves the problem of coupled fluid flow and elastic dilation and requires numerical procedures implemented in a lengthy computer program, whereas the other one neglects the effects of fluid flow and results in a simple analytical expression.

Both analyses treat the fractures in two dimensions normal to the axis of the starter slot. The lengths of fractures produced in the lab were roughly uniform with respect to their width, so that the appearance of the fracture in a cross-section normal to the axis of the slot is nearly independent of location along the width. The fractures gapped open at the sample edges, but the aperture at the edges was probably less than within the sample due to friction between the sample and the apparatus. That edge effect, as well as effects related to the development of lobes at the leading edge of the fracture are assumed to be negligible in this formulation. The hole along the axis of the slot will be ignored because including it will markedly increase the complexity of the analyses while adding little insight.

The experimental apparatus was designed to restrict deformation parallel to the axis of the starter slot, placing the entire sample in conditions of plane strain deformation. It will be assumed that plane strain conditions exist at the leading edge of the fracture, and those conditions will be adopted for the analyses. Shear stresses induced at the edges of the sample by the dilation of the fracture will be ignored, and consideration of plane stress conditions at the edge of a notched sheet as described by Williams

(1984; p. 99) seem unwarranted in light of the edge constraint applied by the experimental apparatus.

The numerical analysis is designed to obtain a distribution of pressure within the fracture that simultaneously satisfies equations describing the elastic dilation, viscous fluid flow, and stress intensity. An iterative procedure, which converges in less than ten iterations for most cases, was developed for this purpose. The procedure makes use of the Schwarz-Neumann alternating technique introduced by Pollard and Holzhausen (1979) to analyze static hydraulic fractures, and similar iterative methods are used by Nilson and Griffiths (1986), Cleary and Wong (1985), and Narandren and Cleary (1983) to analyze propagation.

A variety of other methods of analyzing a propagating hydraulic fracture whose geometry resembles the one described here are available (e.g. Nilson, 1986; Spence and Turcotte, 1985; Biot and others, 1982; Geerstma and de Klerk, 1969). The method of solution used in this work was adopted because it is straightforward, yet versatile enough to accomodate a wide range of modifications that may be required in the future.

Overview of the Approach of the Numerical Analysis

The analysis begins by assuming fluid is injected at a constant rate at the midpoint of a pre-existing fracture (Fig. 3.4). Symmetry about the midpoint is assumed and allows us to only treat one half of the fracture. The fracture is embedded in an elastic medium of infinite extent along cartesian axes x and y, and it is of width w along the z axis. The fracture, which is of half-length a_i, lies on the x axis and the y axis is normal to the plane of the slot. Displacements along the z axis are assumed to be zero, reducing the problem to one of plane strain in the x-y plane.

An initial period of injection inflates the pre-existing fracture but does not result in propagation. Pressure within the fracture increases during inflation and propagation begins when $K_I = K_{Ic}$. Propagation is assumed to continue such that the equality $K_I = K_{Ic}$ is always maintained.

The history of growth is analyzed by treating a series of fractures each of which contains a slightly larger volume of fluid than the last. The time since injection began, which yields a growth history, is obtained by dividing the volume of a fracture by the volumetric rate of injection. The volume can only be determined after selecting a fracture length and solving for a pressure distribution, so different methods of changing fracture volume are needed for stationary or moving fractures. During inflation of a pre-existing fracture, volume is increased by incrementing the driving pressure at the fracture tip, whereas during propagation volume is increased by incrementing fracture length.

This method of solution is termed quasi-steady (Nilson, 1986) in that it ignores dynamic effects in the elastic solutions; transient terms only enter

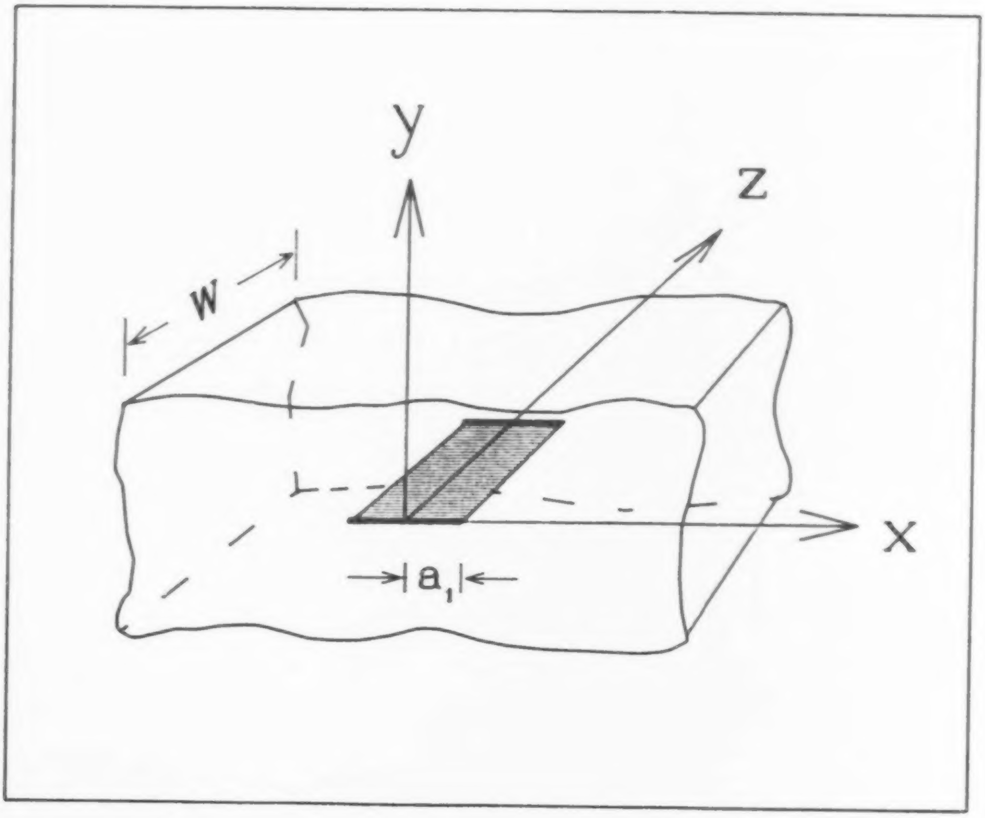

Figure 3.4 Geometry used in analyses.

in the mass balance used to solve the flow equations. Dynamic effects are insignificant, however, when the velocity of a fracture is much slower than the speed of elastic waves in the solid enveloping the fracture. As Nilson (1986) points out, viscous effects in the fluid filling a hydraulic fracture will limit propagation velocity to much less than the wave speeds of elastic solids, so the quasi-steady approach seems to be justified for hydraulic fractures.

Inflation of a Pre-existing Fracture

The steps used to analyze inflation of a pre-existing hydraulic fracture are outlined below.

1. Assume an initial length for the pre-existing fracture and assign the locations of nodal points starting at the midpoint and ending at the tip.

2. Assume a uniform pressure over the fracture that is less than the critical pressure for propagation.

3. Determine apertures at nodal points from elastic solution.

4. Use an expression for flow in the fracture to determine a new pressure distribution at the nodal points. Apertures from step 3 yield effective hydraulic conductivities along the fracture. Mass balance requires that all the flow into the fracture is accomodated by dilation, so that the flow rate decreases along the fracture length and is zero at the tip. At the midpoint, second-type boundary conditions are used to satisfy the constant inflow rate. At the tip, a first-type condition satisfies the stress intensity requirement, that $K_I < K_{Ic}$.

5. Use the new pressure distribution to determine new apertures and iterate from step 2 through 4 until convergence criteria are satisfied. The criteria for convergence used in this work include: *a*.) the maximum difference between pressures on two successive iterations is less than a certain value, typically two percent of the maximum pressure. *b*.) the inflow rate determined by finite differences is within a certain value, typically two percent, of the the specified inflow rate. *c*.) flow rate at the tip is essentially zero. *d*.) mass balance at an arbitrary point along the fracture is satisfied within a certain value, typically five percent.

6. Determine fracture volume by integrating aperture over the length of the fracture, and determine the time since injection began by dividing fracture volume by the volumetric rate of injection. Save the variables of interest.

7. Increase the pressure at the tip and repeat steps 2 through 6.

8. Repeat step 7 until the stress intensity exceeds the critical stress intensity. Estimate the pressure at the tip so that $K_I = K_{Ic}$. This estimate is achieved by interpolation between the previous two solutions and the observation that stress intensity varies nearly linearly with

small changes in pressure at the tip.

9. Repeat steps 2 through 6 for the estimated critical pressure at the tip and check whether $K_I = K_{Ic}$. If this check is satisfied (within two percent) then the current time and pressure distribution mark the onset of propagation of the pre-existing fracture. Additional iteration is required if the check is not satsified, but this was rarely needed.

Propagation of an Inflated Fracture

Two schemes are used to analyze propagation, one that assumes the fluid reacheshe crack tip and another that tracks the leading edge of the fluid and results in an unwetted tip. The former is the simpler of the two and will be described first.

1. Increase the length of the fracture by a small increment and reassign locations of nodal points so that the new fracture is covered by the same number of points as the old one. Assign a uniform pressure distribution. Convergence is improved by assuming the initial pressure satisfies the stress intensity requirement for a uniformly distributed pressure in a fracture of the new half-length.

2. Determine apertures from an elastic solution.

3. Use an expression for flow in the fracture to determine a new pressure distribution. Apertures from step 3 yield effective hydraulic conductivity along the fracture. The difference between the current apertures and those at the previous time step yields the mass balance in the flow equation. At the midpoint, second-type boundary conditions are used to satisfy the constant inflow rate. At the tip, a first-type condition is used to obtain the stress intensity requirement, that $K_I = K_{Ic}$.

5. Use the new pressure distribution to determine new apertures and iterate through step 4 until the convergence criteria are satisfied. Oscillations between successive iterations are common in this iterative sheme, as illustrated by Narandren and Cleary (1983). The rate of convergence is improved by using a weighted average of the previous two iterations until the solution is close to convergence (Nilson and Griffiths, 1986). The final two iterations lacked a weighting factor to ensure that the maximum difference criteria (criteria *a.* above) is satisfied.

6. Determine stress intensity and compare with critical stress intensity. If the stress intensity is within two percent of the critical value, then the solution for the current fracture length is complete. If the critical stress intensity is not satisfied, another solution is obtained using a slightly different pressure at the tip. A third solution is then obtained using a new pressure at the tip. Selection of that new pressure

is based on the observation that stress intensity is nearly linearly related to the specified pressure at the tip. Thus, the previous two solutions are used to estimate a new tip pressure that results in the critical stress intensity. In many cases, the critical stress intensity was satisfied after convergence of the first solution, and it was always satisfied by the linear scheme described above when the increment of crack growth was less than five percent of the crack length and $\mu^* < 1.0$, where $\mu^* = q\mu E^3/K_{Ic}^4$ with q the volumetric inflow rate, μ dynamic viscosity, and E elastic modulus. Larger values of μ^* resulted in numerical instabilities and an alternate method based on adjusting the input pressure was used to obtain convergence. Those larger values of μ^* exceed the range of lab experiments, so the alternate method was unnecessary for the present work.

7. Save variables of interest (e.g. time, driving pressure, length, aperture) and increase fracture length by a small increment. Reassign the locations of nodal points and determine an initial pressure distribution. Repeat steps 2 through 6.
8. Repeat step 7 until the desired fracture length is reached.

Injected fluid completely filling the fracture is a tacit assumption of the analysis described above; however, results of that analysis show that the velocity of fluid near the fracture tip is less than the velocity of the fracture tip itself (Fig. 3.5). This suggests that the fluid is unable to keep pace with the fracture and the the assumption of a completely filled fracture is incorrect (Abe and others, 1976). The analysis was modified to track the position of the wetted front by integrating the fluid velocity at the tip over each time step. The integration was done using a finite difference scheme that is backward in time, which amounts to using the velocity over the previous time step to predict the location of the wetted front at a new time step. As a result, during the first increment of crack growth the fracture front moves forward a small increment but the fluid front remains stationary because its velocity at the previous time step was zero.

The method used to assign locations of nodal points was modified during tracking of the wetted front. The modified method generated one set of points that were spaced evenly between the midpoint of the fracture and the wetted front, and another set of points that were spaced evenly between the wetted front and the fracture tip. Driving pressures were positive and resulted from the pressure of the injection fluid over the first set of points, whereas they were negative and assumed to be equal to the confining load over the second set. The first set of points was used to solve the flow equation and both sets were used to solve for apertures and stress intensity.

Outline of the Analysis

Implementing the method of solution requires the fracture to be discretized into many small segments defined by the nodal points. Apertures and stress intensities are obtained by integral methods cast as summations

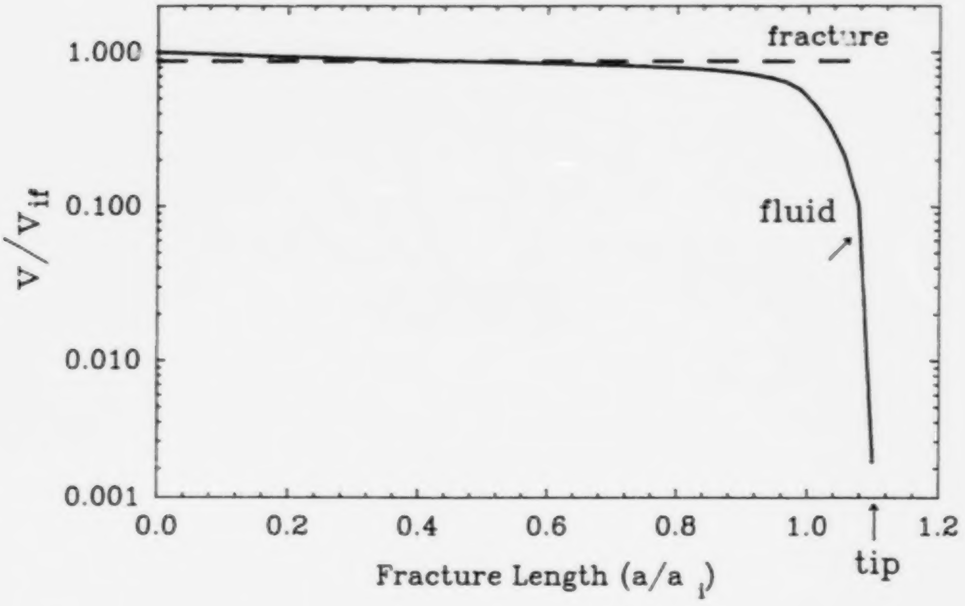

Figure 3.5. Velocities of fluid within a fracture and of the fracture tip, scaled to the velocity of fluid entering the fracture, v_{if}.

over values calculated at each segment, and pressures are obtained using a finite-difference method based on the mid-points of the segments. Details of calculating apertures, stress intensities and pressures are described below.

Consider a fracture loaded by a uniform driving pressure P_{bc} over the segment $b \leq x \leq c$, where b and c are nodal points bounding the segment. The aperture at any point x on the fracture resulting from a load on that segment is (Erdogan, 1962; Tada and others, 1985)

$$\delta(x) = \frac{4P_{bc}(1-\upsilon^2)}{\pi E}\left[(c-x)\cosh^{-1}\frac{a^2-cx}{a|x-c|} - (b-x)\cosh^{-1}\frac{a^2-bx}{a|x-b|} + (\sin^{-1}c/a - \sin^{-1}b/a)(a^2-x^2)^{1/2}\right] \qquad (3.5)$$

assuming plane strain deformation.

A driving pressure of arbitrary distribution $P_d(x)$ over the entire fracture can be approximated by a series of loads, each of which is uniform over a segment and equal to $P_d(x_{mp})$, where x_{mp} is the midpoint of a segment. Summing the contributions of each segment yields the aperture at any point. Assuming there are a total of n segments, where the ith segment is bounded on the left side by b_i and on the right side by c_i leads to

$$\delta(x) = \frac{4(1-\upsilon^2)}{\pi E}\sum_{i=-n}^{n} P_i\left[(c_i-x)\cosh^{-1}\frac{a^2-c_i x}{a|x-c_i|} - (b_i-x)\cosh^{-1}\frac{a^2-b_i x}{a|x-b_i|} + (\sin^{-1}c_i/a - \sin^{-1}b_i/a)(a^2-x^2)^{1/2}\right] \qquad (3.6)$$

An expression for the stress intensity is obtained using a similar approach

$$K_I = (\pi a)^{1/2} \sum_{i=-n}^{n} (P_i/\pi)\Big[\sin^{-1} c_i/a - \sin^{-1} b_i/a$$

$$- [1 - (c_i/a)^2]^{1/2} - [1 - (b_i/a)^2]^{1/2}\Big] \qquad (3.7)$$

which is based on an equation for stress intensity due to loading over a single segment given by Tada and others (1985).

Pressures

Pressures within the fracture are determined by satisfying conditions governing laminar flow that is one-dimensional along the fracture length. Assuming the change in aperture is small over any given segment and the fluid is linearly viscous, then the flow law within that segment is of the form

$$q = -(\delta^3/C_1\mu)(\partial P_d/\partial x) \qquad (3.8)$$

where q is the volumetric flow rate per unit width of the fracture, and μ is the dynamic viscosity of the fluid within the fracture. In general, the constant C_1 depends on Reynolds number R_e and wall roughness. If the walls of the fracture are perfectly smooth, C_1 decreases from 1.5 for R_e of roughly one or greater to 12 for $R_e << 1.0$ (Schlichting, 1960). Wall roughness tends to increase the value of C_1 and the magnitude of the increase depends on R_e. Detournay (1979) reviews experimental studies of the role of wall roughness on flow through a fracture.

The Reynolds Number during flow through a narrow slot is (Detournay, 1979)

$$R_e = 2q/\upsilon \qquad (3.9)$$

which yields $R_e = 5 \times 10^{-4}$ for conditions of the lab experiments. The effects of the roughness of the fracture walls will be ignored, so a value of $C_1 = 12$ will be used (Schlichting, 1960).

Conservation of mass requires

$$\partial\delta/\partial t = -\partial q/\partial x \qquad (3.10)$$

assuming that the fluid is incompressible, that no fluid is stored within the pumping system, and that no fluid leaks off through the walls of the fracture. All those assumptions can be relaxed by modifying the conservation equation. Nilson (1986) shows how to include effects of compressibility of injected fluid and storage within the pumping system. A simple but widely-used analysis of leakoff was first described by Carter (in Howard and Fast, 1957), and more general analyses of the problem are treated by Settari (1983), Dean and Advani (1984) and Pascal (1986), among others.

Substituting eq. (3.8) into (3.10) yields

$$\partial\delta/\partial t = \partial T/\partial x \; \partial P_d/\partial x + T \, \partial^2 P_d/\partial x^2 \qquad (3.11)$$

where the transmissivity T is

$$T = \delta^3/\mu C_1 \qquad (3.12)$$

Boundary conditions at the midpoint of the fracture require that

$$\partial P_d/\partial x = - q_o C_1 \mu/2\delta_o^3, \qquad x = 0 \qquad (3.13)$$

where q_o is the total flow rate per unit width of the fracture and δ_o is the aperture at the midpoint. The pressure at the fracture tip must also be specified to control stress intensity and ensure that $K_I = K_{Ic}$ during propagation, so

$$P_d = P_{dK}, \qquad x = a \qquad (3.14)$$

The flow equation was solved for the boundary conditions described above using an implicit finite difference scheme. Nodal points in the finite difference scheme were midpoints of segments in the elastic solution. Several methods of spacing the points along the fracture were evaluated, but uniformly-spaced points yielded the most satisfactory results. Other methods, which were designed to decrease spacing in the vicinity of the fracture tip, proved to be less stable than the uniform spacing even when the finite difference scheme was written to account for non-uniform spacing. The following description is valid only for uniformly-spaced nodal points, although it is readily modified to accomodate non-uniform spacing.

A second-order finite difference approximation of eq. (3.11) is obtained using Taylor series expansion and the resulting expression is written in implicit form as

$$a_i^j P_{i-1}^j + b_i^j P_i^j + c_i^j P_{i+1}^j = m_i^j \qquad (3.15a)$$

where

$$a_i^j = (T_i^j/\Delta x^2) - [(T_{i+1}^j - T_{i-1}^j)/4\Delta x^2] \tag{3.15b}$$

$$b_i^j = -2T_i^j/\Delta x^2 \tag{3.15c}$$

$$c_i^j = (T_i^j/\Delta x^2) + [(T_{i+1}^j - T_{i-1}^j)/4\Delta x^2] \tag{3.15d}$$

$$m_i^j = (\delta_i^j - \delta_i^{j-1})/[(V^j - V^{j-1})/q_o] \tag{3.15e}$$

in which the subscripts *i* are indices of the the nodal points and the superscripts *j* indicate an increment of time. The total volume per unit width of the fracture is *V*, and the nodal spacing is Δx. The boundary condition at the midpoint of the fracture eq. (3.13) requires

$$a_1 = 0 \tag{3.16a}$$

$$b_1 = -2T_1/\Delta x^2 \tag{3.16b}$$

$$c_1 = 2T_1/\Delta x^2 \tag{3.16c}$$

$$m_1 = (\delta_1^j - \delta_1^{j-1})/[(V^j - V^{j-1})/q_o] - q_o/\Delta x \tag{3.16d}$$

whereas the boundary condition at the tip is written

$$a_n = 0 \tag{3.17a}$$

$$b_n = 1.0 \tag{3.17b}$$

$$c_n = 0 \tag{3.17c}$$

$$m_n = P_{dK} \tag{3.17d}$$

The resulting set of *n* equations was written in tridiagonal form and solved using a commercially-available inversion algorithm.

Tracking the length of the wetted zone a_w was done by integrating the velocity at the tip over time. The fluid velocity v_f at the tip is obtained to first order by the backward difference

$$v_{fm} = -T_m(p_m - p_{m-1})/(\Delta x\delta_m) \tag{3.18}$$

where m is the number of segments wetted by fluid. The change in length of the wetted part of the fracture a_w during a time step is established by

$$\Delta a_w^j = v_{fm}^j \Delta t = a_w^j + - T_m^j (p_m^j - p_{m-1}^j)/(\Delta x \delta_m^j)\ [(V^j - V^{j-1})/q_o] \tag{3.19}$$

and a_w is determined at any given time by summing the increments of growth during the previous time steps.

This approach assumes that pressure within the unwetted zone is constant, which is a reasonable simplification although we recognize that it tacitly ignores the matching of pressures and velocities at the interface between the injected fluid and the fluid filling the tip. It also ignores capillary effects at the boundary between the fluid front and the unwetted tip, as well as contributions that the rate of change of pressure distribution and crack length have on stress intensity (e.g. Cleary and Wong, 1985; eq. 16). The analysis described above could be modified to consider all of those effects, and such modifications could be important in predicting various details of hydraulic fractures. However, we expect that the major conclusions drawn from the analyses will be unaffected, so those modifications will be deferred for future work.

Results

Numerical analyses were conducted using parameters resembling those of the Center Hill clay at moisture contents between 0.26 and 0.27 (Table 3.1). The driving pressure on the unwetted zone P_{duw} was assumed to be zero, implying that the fluid pressure equals the confining stress along that zone. In its present formulation, the analysis is unable to account for effects such as capillary forces, and leakoff, both of which will affect the distribution of pressure at the tip. Accordingly, P_{duw} should be taken as an effective stress that crudely accounts for the factors omitted in the analysis, and its value was estimated based on the form of pressure records generated by the analysis.

TABLE 3.1 PARAMETERS USED IN NUMERICAL ANALYSIS

q_o:	0.00375 cm^2/s	υ:	0.3
μ:	175 cp	E:	10 MPa
C_1:	12	P_{duw}:	0
K_{Ic}:	50 kPa cm$^{1/2}$	n:	34
a_i:	1.0 cm	m:	30

The results show that an unwetted tip begins to develop at the onset of fracturing (Fig. 3.6) and then increases in length during propagation. This result essentially confirms the conceptual model. Moreover, it shows that the difference between the velocity of the fracture and the velocity of the fluid near the tip could be the process responsible for the development of a fracture with an unwetted tip.

The numerical model predicts (Fig. 3.6) that the length of the unwetted zone a_{uw} increases rapidly compared with that of the wetted fracture a_w during an early period of propagation ($a_w < 1.5$). Following this early period, the relative rate of growth of a_{uw} diminishes and is roughly constant with a slope of 0.2 for $a_w > 2.0$.

Measurements made on fracture surfaces created in the lab (Fig. 2.10) show that the average slope a_{uw}/a_w for samples of moisture content 0.26 to 0.27 is between 0.19 and 0.21; similar to that predicted by the analysis (Fig. 3.6). Lengths of undyed zones are a few mm less than that of unwetted zones predicted by the numerical analysis. Those differences are considered small, however, and could be due to advancement of the dyed fluid by capillary forces, a process ignored in the analysis.

Other results of modeling conducted using the numerical analysis indicate consequences of the development of an unwetted tip on driving pressure, fracture length and aperture as functions of time. These consequences are highlighted by comparing results from two analyses; one in which an unwetted tip was allowed to develop as a result of differences between fluid and fracture velocity, and another in which the development of an unwetted tip was prevented by requiring that the fracture remaincompletely filled with fluid. Driving pressure, aperture, and fracture length, have been normalized to the values of those variables at the onset of propagation. The normalized variables include

$$t^* = t/t_{frx} \tag{3.20a}$$

$$P_d^* = P_d/P_{dofrx} \tag{3.20b}$$

$$a^* = a/a_i \tag{3.20c}$$

$$\delta^* = \delta/\delta_{ofrx} \tag{3.20d}$$

where the subscript *frx* indicates the value at the onset of fracturing, and the subscript *o* indicates the value at the origin. All the starred variables have values less than 1.0 during inflation, and values equal to 1.0 at the onset of fracturing according to this definition.

Growth of an unwetted tip has a marked effect on the driving pressure,

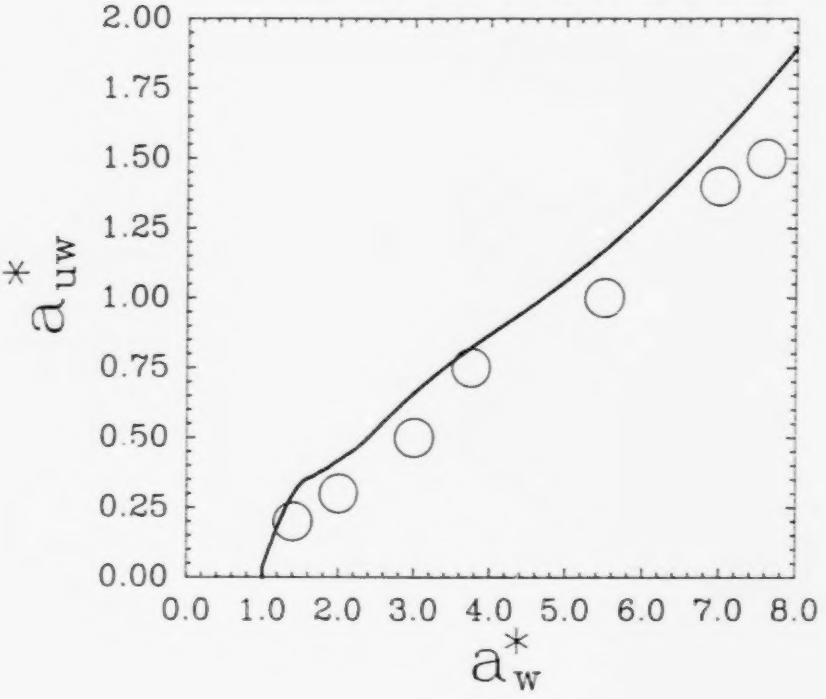

Figure 3.6 Normalized length of unwetted tip with respect to length of wetted fracture, from numerical simulation (solid line) and from lab experiments (data points).

aperture and fracture length as functions of time (Fig. 3.7). The driving pressure increases linearly during inflation and then abruptly decreases at the onset of propagation when growth of the unwetted tip is prevented (Fig. 3.7). Similar results were obtained using a wide range of fluid viscosity, elastic modulus, and critical stress intensity if development of the unwetted tip was prevented. The analysis that tracks the fluid front and results in an unwetted tip shows that driving pressure continues to increase after propagation has begun. Indeed, the slope of the pressure record very early in propagation ($1.0 < t < 1.25$) is only slightly less than during inflation. Driving pressure continues to increase until $t \cong 2$, when it reaches a maximum and then decreases at later times (Fig. 3.7).

Those results have several implications with respect to the lab observations. They indicate that growth of an unwetted tip can cause the early propagation of a fracture to be stable, and that unstable propagation takes place after the fracture has grown to some finite length. Records of driving pressure from the lab experiments consistently show an early period of stable growth followed by a period of unstable growth. We conclude that this behavior results from the early growth of the unwetted zone that was observed on the surfaces of fractures created in the lab.

Clifton and others (1976) performed experiments where they prevented fluid from entering a hydraulic fracture by lining a starter hole with a flexible membrane. Stable propagation was observed when the membrane was in place, and unstable propagation when the membrane was omitted. Their results, which are supported by theoretical analyses, confirm the conclusion that lack of fluid penetration results in stable propagation. The numerical analyses also indicate that fracturing may occur before a noticable change in the slope of the pressure record. This is because the onset of fracturing itself may cause only a minor change in slope, and it is only after the fluid enters the fracture that the slope of the record changes markedly. That could explain the observation of short, incipient fractures in experiments terminated slightly before a change in slope of the pressure record. It also could explain the observations of Zoback and others (1977), who measured acoustic emissions from rock samples to detect the beginning of hydraulic fracturing during lab experiments. They observed increased acoustic emissions while the slope of their pressure records was constant and concluded that the beginning of fracturing was undetectable on the pressure records.

Fracture length and aperture are affected by the growth of the unwetted tip (Fig. 3.7), according to the analysis. The rate of growth of the fracture is reduced, whereas the rate of dilation is increased when the unwetted tip is allowed to grow. Analyses ignoring the formation of the unwetted tip therefore apparently will overestimate length and under estimate aperture. This has important implications in designing field applications of hydraulic fractures where length and aperture are important variables affecting the performance in delivery or recovery.

The actual magnitude of the propagation velocity predicted when the unwetted tip is 0.58 mm/sec, whereas that predicted by the other analysis is 0.81 mm/sec (determined from slopes of Figure 3.7 and $t_{frx} = 4.72$ sec, which is

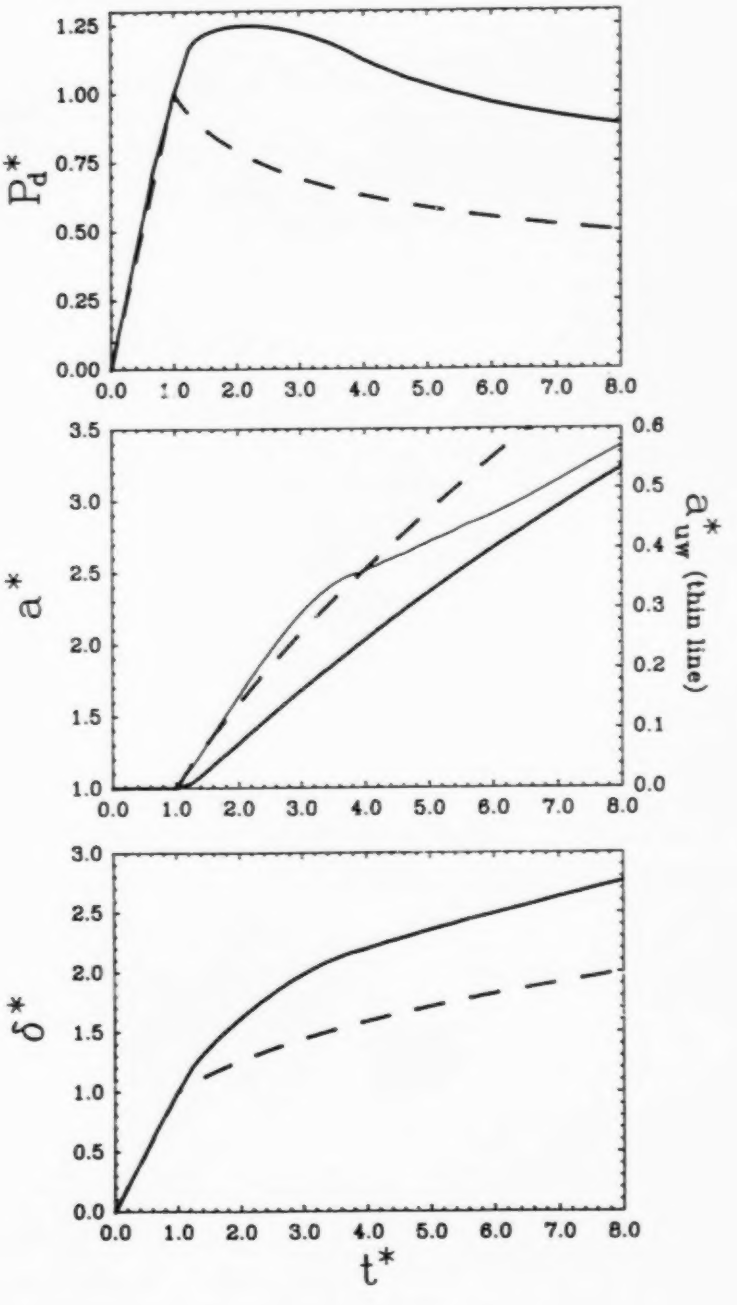

Figure 3.7. Normalized driving pressure, half-length, and aperture as functions of time for a fracture filled fully with fluid (dashed), and for a fracture with an unwetted tip (solid).

determined from Table 3.1 and eq. 3.25c). Propagation velocities in the lab experiments, determined by dividing half-length by duration of propagation, ranged widely from 0.2 to 1.05 mm/sec (Fig. 3.7a). Both theoretical analyses predict velocities that are within the range of observed velocities. A linear regression of the lab data, however, indicates that the average propagation velocity was 0.57 to 0.59 mm/sec for moisture contents between 0.26 and 0.28; the analysis considering an unwetted tip predicts this velocity with remarkable accuracy, whereas the other analysis overestimates it. The rate of growth of the unwetted tip itself varies during propagation (Fig. 3.7). The tip grows rapidly while driving pressure increases during stable propagation. Growth rate diminishes during the transition from stable to unstable propagation, and it is roughly constant later in the period of unstable growth. Our experiments were unable to yield data on growth rate of the tip, however, Medlin and Masse (1984; fig. 6) show that the tip grows rapidly at the onset of propagation, and then the growth rate diminishes and is roughly constant during further propagation.

Driving pressure and aperture were calculated along the length of the fracture during inflation, at the onset of propagation, and during propagation (Fig. 3.8). During inflation driving pressure varies roughly linearly along the fracture, except in the vicinity of the tip where the slope flattens to zero gradient and thus zero flow at $x = a_i$. At the onset of propagation driving pressure is nearly constant, varying a few percent over the length of the fracture. As the fracture lengthens during propagation a zone of low driving pressure, corresponding to the unwetted tip, appears and increases in length.

Stable propagation early in the growth of a hydraulic fracture has been attributed to large viscous losses during flow in a narrow region at the tip (Zoback and others, 1977; Zoback and Pollard, 1978). The results of this work show that, at least for conditions of the lab experiments, we do not expect a large decrease in pressure due to viscous dissipation in the tip. This is because dilation of the fracture reduces the flow rate along the length of the fracture, according to eq. (3.10). As the tip is approached the decrease in aperture is offset by a decrease in flow rate, so that the pressure gradient determined through eq. (3.8) is gentle. A steeper gradient is obtained if the dilation of the fracture is ignored.

The pre-existing fracture has a nearly elliptical form during inflation (Fig. 3.8). During propagation the form is grossly elliptical, but it is marked by a slight upward concavity centered on the leading edge of the pressurized fluid. Similar fracture profiles were obtained by Nilson and others (1985; fig. 3).

Analytical Solution

The numerical solution described above is cumbersome to use because it requires as much as an hour of execution time on a desk-top computer (IBM 386, 16 Mhz) to complete an analysis. Making two simplications in the problem will allow a simple analytical expression to be developed that captures much of the

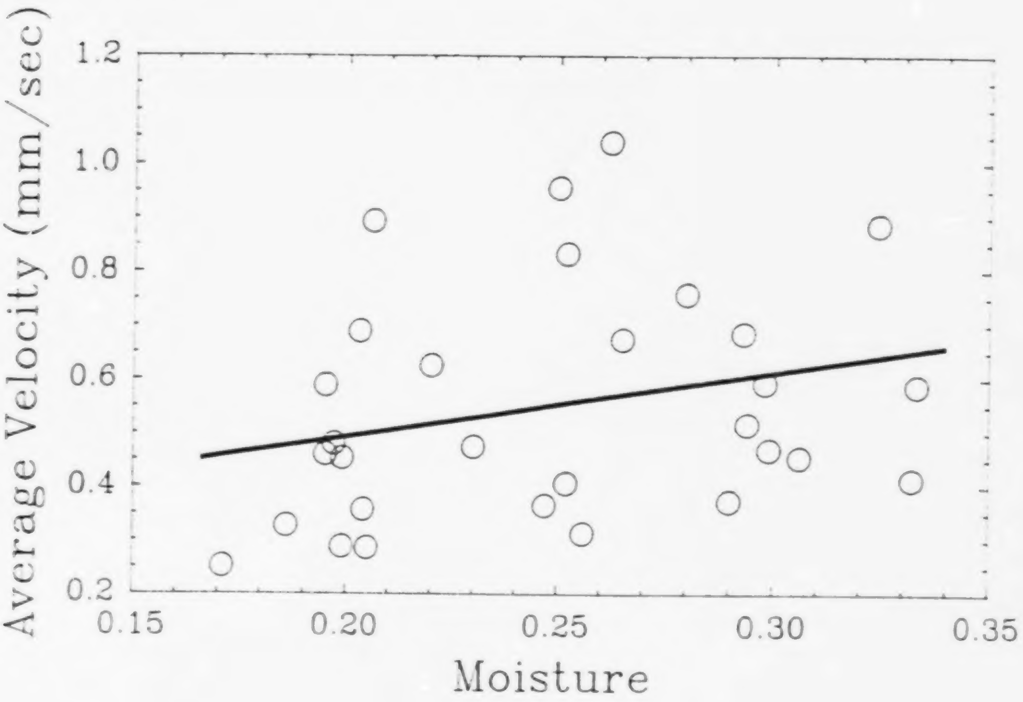

Figure 3.7a. Average propagation velocities from lab experiments. Linear regression line suggests a slight dependence on moisture content.

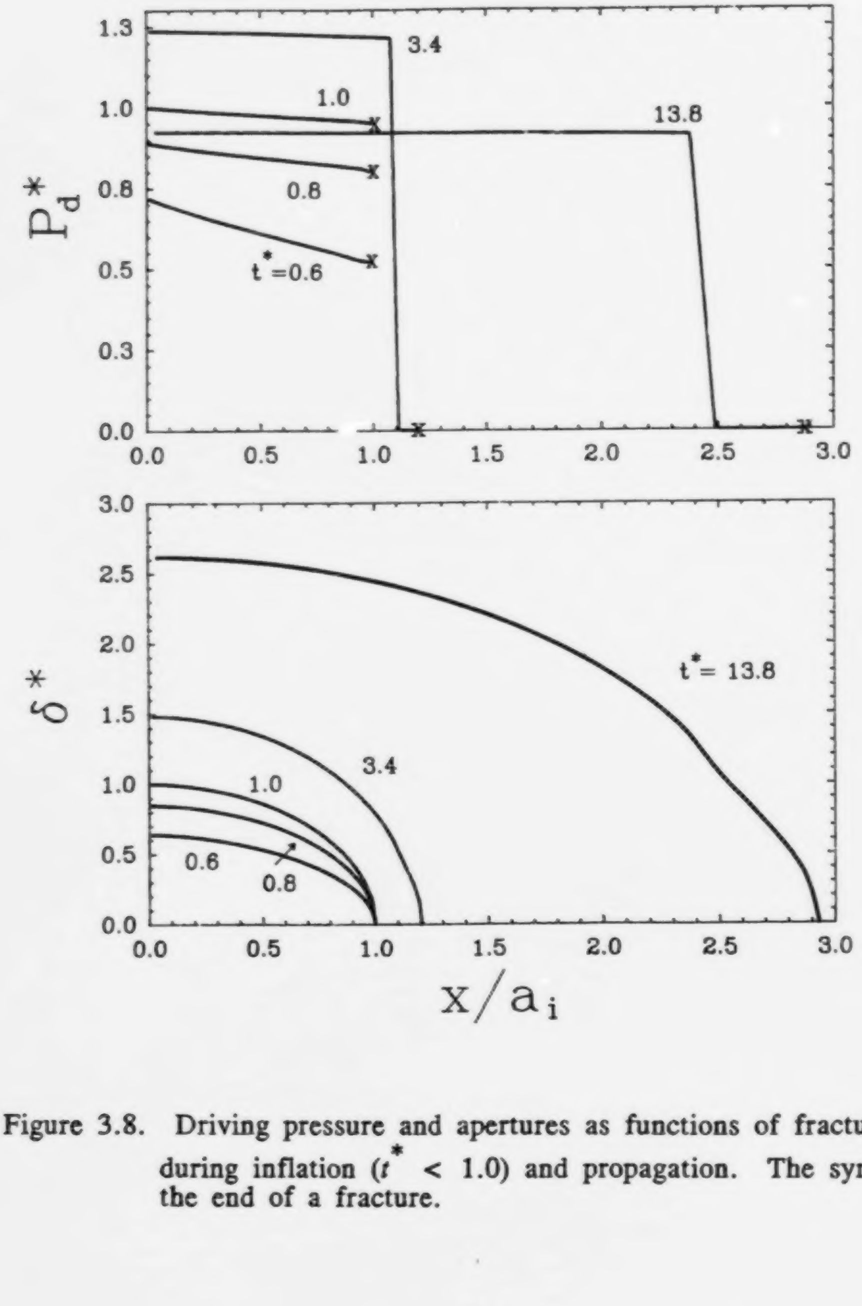

Figure 3.8. Driving pressure and apertures as functions of fracture length during inflation ($t^* < 1.0$) and propagation. The symbol x marks the end of a fracture.

essence of the numerical solution but requires only a few seconds to compile and execute. The results of the numerical solution showed that driving pressure varies only slightly within the fracture, so that one of the simplifications will be to assume that the driving pressure within the wetted fracture is constant. This is the same as ignoring the pressure losses due to viscous dissipation during flow. As a result, the analytical solution will be unable to predict the growth of the unwetted tip. Both the numerical solution and the lab data, however, suggest that the length of the unwetted tip is roughly linearly related to the length of the wetted zone. The other simplification, therefore, is to assume that the length of the unwetted tip is proportional to the length of the wetted part of the fracture.

The geometry of the problem is the same as that used for the numerical solution and described in a previous section (Fig. 3.4). The fracture is filled with fluid to a point b along the x axis, and the pressure p of the fluid is uniform along $0 \leq x \leq b$. Fluid pressure along an unwetted tip, the interval $b \leq x \leq a$, is zero. During inflation the entire fracture is filled with fluid, so $a = b$ before propagation begins. When the unwetted tip develops during propagation b will be less than a, with the length of the unwetted zone equal to $a - b$. The relationship between a and b is assumed to follow that observed in the experiments and expressed in eq. 2.4.

Fluid pressure within the fracture is opposed by a confining stress σ acting normal to the plane of the fracture. Accordingly, the driving pressure is $(p - \sigma)$ on $0 \leq x \leq b$, and $-\sigma$ on $b < x \leq a$.

Static analyses will be used to obtain driving pressure, aperture and half-length. Those analyses will be made functions of time by treating a series of fractures of slightly different volumes, and then determining the time since injection began by dividing fracture volume by volumetric rate of injection. This quasi-static approach is the same as the one used in the numerical analysis.

The fracture will be assumed to be in equilibrium, so that the stress intensity must equal the critical stress intensity K_{Ic} throughout propagation. In the analyses of Kristianovich and Zheltov (1959), and Geertsma and de Klerk (1969) equilibrium propagation is obtained by adjusting either the length of the unwetted tip, or the driving pressure to eliminate stress concentration at the tip; they set K_{Ic} to zero.

A solution to the problem can be obtained by superimposing solutions for two different loading conditions (Fig. 3.9): a.) the load equals p along $0 \leq x \leq b$ and 0 along $b < x \leq a$; and b.) the load equals $-\sigma$ along $0 \leq x \leq a$. A solution to similar boundary conditions was obtained by Barenblatt (1962). The mode I stress intensities K_I, volumes V, and apertures at the origin δ_o of fractures for conditions a and b are (Tada and others, 1985)

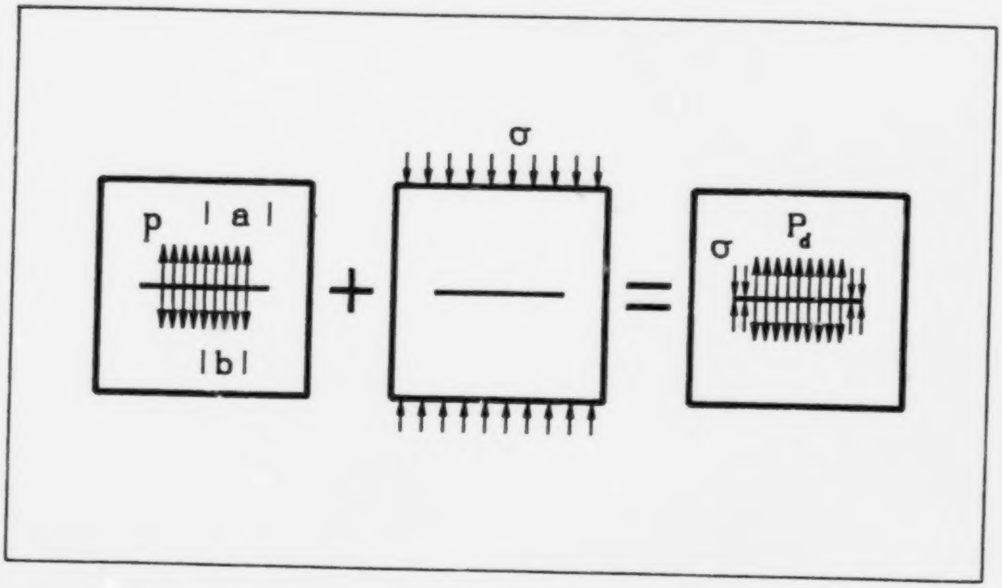

Figure 3.9. Loading conditions used to develop analytical model.

$$K_{Ia} = p\sqrt{\pi a}\ (2/\pi)\ \sin^{-1} b/a \tag{3.21a}$$

$$V_a = (4pa^2 w/E)\ [\sin^{-1} a/b + (b/a)\sqrt{1 - (b/a)^2} \tag{3.21b}$$

$$\delta_{oa} = (8\pi pa/\pi E)\ [\sin^{-1} b/a + b/a\ \cosh^{-1} a/b] \tag{3.21c}$$

$$K_{Ib} = -\sigma\sqrt{\sigma a} \tag{3.21d}$$

$$V_b = -2\sigma\pi a^2 w/E \tag{3.21e}$$

$$\delta_{ob} = -4\sigma a/E \tag{3.21f}$$

where the E, the plane strain modulus, is $E'/(1 - \upsilon^2)$, and E' is the elastic modulus and υ is Poisson's ratio. Adding the two solutions and introducing the driving pressure P_d from eq (3.2) yields

$$K_I = \sqrt{\pi a}\ [P_d\theta - \sigma\ (1 - \theta)] \tag{3.22a}$$

$$V = (2\pi a^2 w/E)\ [P_d\psi - \sigma(1 - \psi)] \tag{3.22b}$$

$$\delta_o = (4a/E)\ [P_d\phi - \sigma(1 - \phi)] \tag{3.22c}$$

where the terms θ, ψ and ϕ depend only on the length of the unwetted zone

$$\theta = (2/\pi)\ \sin^{-1}\ b/a \tag{3.22e}$$

$$\psi = (2/\pi)\ [\sin^{-1} b/a + b/a\sqrt{1 - (b/a)^2}\ ] \tag{3.22f}$$

$$\phi = \sin^{-1} b/a + b/a\ \cosh^{-1} a/b \tag{3.22g}$$

The rate of injection Q is constant, and assuming that both the fluid and the pumping system are incompressible, and that none of the fluid flows out of the fracture, then

$$V = Qt \tag{3.23}$$

where t is the time since pumping began. Substituting eq. (3.23) into eq.

(3.22b) yields

$$t = (2\pi a^2 w/QE)\ [P_d \psi - \sigma(1 - \psi)] \tag{3.24}$$

For convenience driving pressure, time, half-length and aperture at the origin will be normalized in terms of those variables at the onset of fracturing, so

$$P_{dchar} = K_{Ic} \big/ \sqrt{\pi a} \tag{3.25a}$$

$$a_{char} = a_i \tag{3.25b}$$

$$t_{char} = 2\pi a_c^2\ wP_{dc}/QE \tag{3.25c}$$

$$\delta_{char} = 4P_{dc} a_c/E \tag{3.25d}$$

Dividing eq. (3.22a) by eq. (3.25a) and solving for normalized driving pressure P_d in terms of normalized half-length a

$$P_d^* = P_d/P_{char} = [a^{*-1/2} + \sigma^*(1 - \theta)]/\theta \tag{3.26}$$

Similarly

$$\delta_o^* = \delta_o/\delta_{char} = a^*[P_d^*\phi - \sigma^*(1 - \phi)] \tag{3.27}$$

$$t^* = t/t_{char} = a^{*2}\ [P_d^*\psi - \sigma^*(1 - \psi)] \tag{3.28}$$

$$\sigma^* = \sigma/P_{dc} = \sigma\ (\pi a_i)^{1/2}/K_{Ic} \tag{3.29}$$

$$a^* = a/a_i \tag{3.30}$$

In the plots that follow normalized driving pressure, half-length and aperture were obtained as functions of dimensionless time by incrementing a^* and using eqs. (3.26) through (3.30).

Effects of Growth of an Unwetted Tip

According to the solution derived above driving pressure, half-length, and aperture as functions of time depend on the growth of the unwetted tip, manifested as the ratio b/a, and on the magnitude of dimensionless confining stress. Observations described in Chapter Two suggest that the length of the unwetted tip is linearly related to the wetted length after the fracture has reached some critical length a_{cr}. Rearranging eq. (2.4)

$$b/a = (ma + a_{cr})/(a + ma) \tag{3.31}$$

where m is the ratio of wetted to unwetted length.

Results from the lab tests showed that m and a_{cr} are roughly constant for a soil of a particular moisture content, but they both increase as moisture decreases. For the purpose of this section, I will assume that m and a_{cr} are material constants that govern the growth of the unwetted tip according to eq. (3.10). The effects of m, a^*_{cr}, and σ^* on dimensionless driving pressure, half-length, and aperture are shown in Figures 3.10 through 3.12. In those Figures, the quantities used to form the dimensionless groups require that inflation of the slot occurs during ($t^*_d < 1.0$), and propagation occurs during ($t^*_d > 1.0$).

When $m = \infty$ the unwetted zone is absent and eqs. 3.26 through 3.28 reduce to

$$P^*_d = t^{*-1/3} \tag{3.32a}$$

$$a^* = t^{*2/3} \tag{3.32b}$$

$$\delta^* = t^{*1/3} \tag{3.32c}$$

for values of $t^* > 1.0$. Driving pressure shows a sharp decrease following the onset of propagation for $m = \infty$ (Figure 3.10). The rate of growth of the fracture (slope of Figure 3.10b) is greatest at the onset of propagation, and diminishes slightly with time. The rate of dilation (slope of Figure 3.10c) is greatest before propagation begins, when the slot is dilating. Aperture continues to increase during propagation, but the rate at which it does so diminishes with time.

Finite values of m change the form of the pressure record significantly; driving pressure increases slightly early in propagation, and then decreases at later times (Fig. 3.10). Thus, the presence of the unwetted tip results in an early period of stable propagation followed by an unstable period. The period of stable propagation is brief for large values of m, but increases in duration as m decreases in value. The rate of growth of the unwetted tip, embodied in m, therefore tends to stablize fracture growth.

Fracture length and aperture are also affected by m (Figure 3.10). The rate of growth of the fracture diminishes as m decreases. The decrease in growth rate is offset by an increase in the dilation rate, so that conservation of volume is maintained. Accordingly, the fracture becomes shorter and fatter as the relative length of the unwetted tip increases.

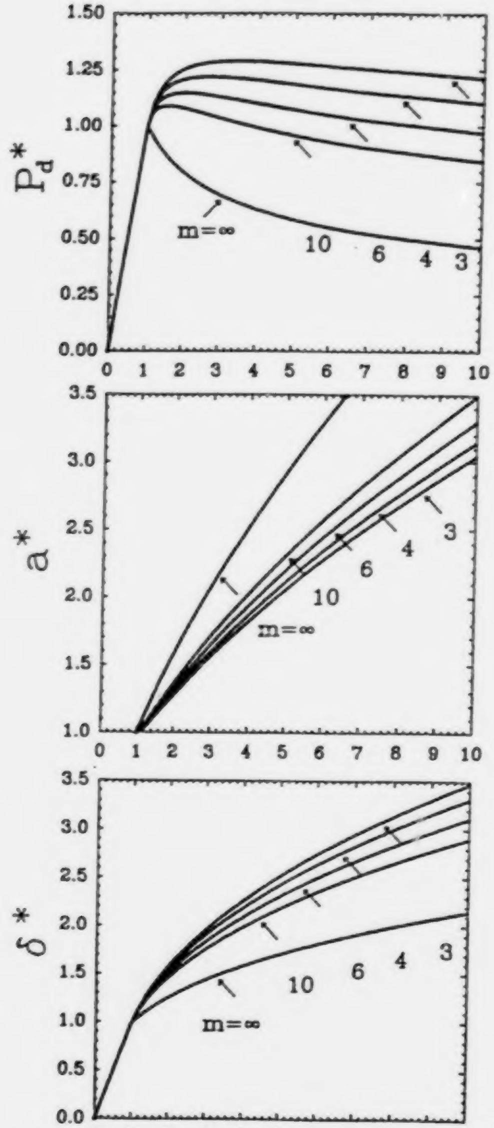

Figure 3.10 The effect of parameter *m* on dimensionless driving pressure, half-length and aperture. Other parameters are constant: a^*_{cr} = 1.0, σ^* = 0.5.

Experimental data suggest that in some samples the unwetted tip develops after the fracture reaches a critical length a_{cr}. Observations early in the growth of fractures in those samples are unavailable, so we will simply assume that the unwetted tip grows slowly from the onset of propagation and more rapidly when the critical length is reached. This suggests that eq. 3.31 should be modified for the period beginning at the onset of propagtion and ending when $a = a_{cr}$. We will use

$$b/a = (m_1 a + 1.0)/(a + m_1 a) \qquad (3.33)$$

for $a_i < a < a_{cr}$, which is the same form as eq. 3.31. The parameter m_1 was set equal to three times m to determine curves in Figure 3.11.

A flattening of the slope of the driving pressure record is the principal effect of increasing a_{cr} to values greater than the half-length of the slot. The change in slope occurs when the unwetted tip begins to grow according to eq. (3.31), so that as a_{cr} increases the point when the slope flattens occurs at progressively latter times (Fig. 3.11). Increasing the critical length results in an increase in fracture length, which reflects early growth that is unimpeded by the constraining effects of the unwetted tip. As we saw in the previous figure, an increase in growth rate is accompanied by a decrease in dilation rate (Fig. 3.12).

The normalized confining stress affects the forms of the records, as shown in Figure 3.12, because it is the driving pressure over the unwetted zone. The duration of the stable period early in propagation increases with the magnitude of σ . The rate of growth of the fracture is reduced, and the rate of dilation enhanced by increasing σ (Fig. 3.12).

The same confining stress was used in all the lab experiments, so there are no data on the effects of confining stress from this study. However, dimensionless confining stress is a function of both K_{Ic} and a_i, through eq. (3.29). We saw in a previous section that K_{Ic} of a soil increases as moisture content decreases. The effects of increasing σ^* shown in Figure 3.12, therefore, could occur either by decreasing K_{Ic}, say by increasing water content, or by increasing the slot length.

Results from the preceeding analysis indicate that the unwetted tip makes the soil appear artificially tough. It causes driving pressures to increase, growth rates to diminish and dilation rates to increase. The magnitude of these effects depend on the length of the unwetted zone relative to the fracture length, when the zone begins to grow, and the magnitude of the confining stress acting normal to the zone.

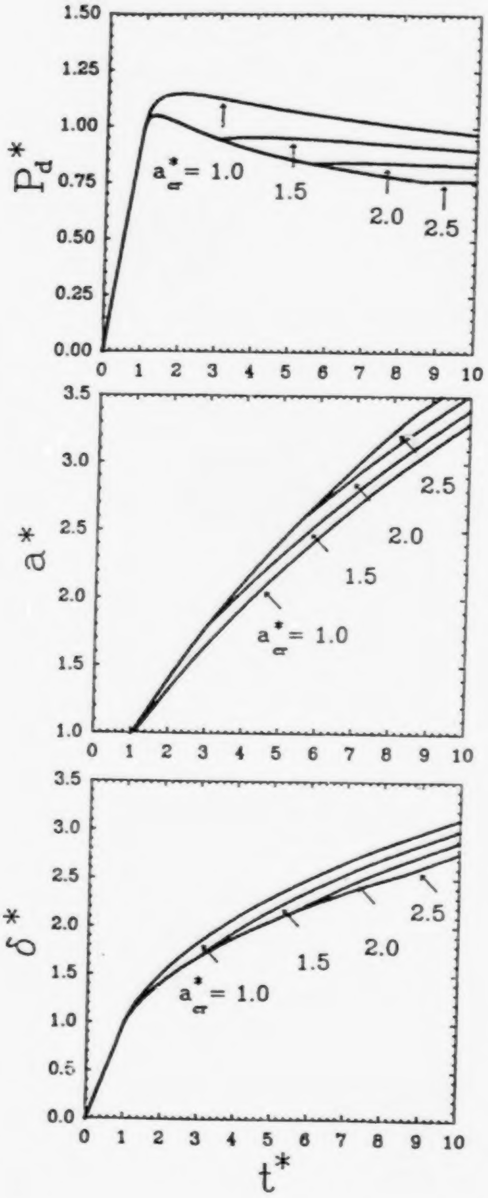

Figure 3.11 The effect of parameter a_{cr}^* on dimensionless driving pressure, half-length and aperture. Other parameters are constant: $m = 6$, $ml = 3m$, $\sigma^* = 0.5$.

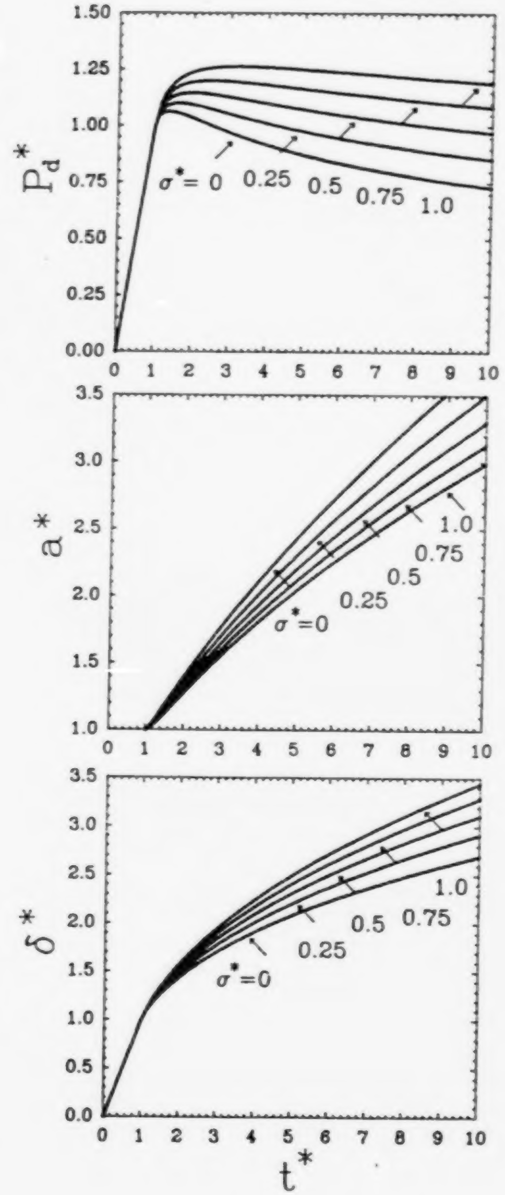

Figure 3.12 The effect of parameter σ^* on dimensionless driving pressure, half-length and aperture. Other parameters are constant: $m = 6$, $a^*_{cr} = 1.0$.

Comparison With Results From The Lab

Variations in forms of records of driving pressure observed in the lab experiments can be explained using the analysis described above. To do so, we must first include effects of a deformable pumping system on the form of the pressure record. Volumetric distortion of the pumping system causes fluid to either be stored when pressure is increasing or released when pressure is decreasing, so that the flow rate into the fracture will differ from the flow rate of the pump. Distortion can be included in the analysis by modifiying eq. (3.22b) to

$$V = V_f + V_e = (2\pi a^2 w/E)\ [P_d\psi - \sigma(1 - \psi)] + V_e(p) \qquad (3.34)$$

where V_f is the volume stored in the fracture, which is a function of driving pressure, and V_e is the volume stored in the experimental apparatus, which is a function of fluid pressure.

The volume stored in the apparatus was determined as a function of fluid pressure by plugging the injection tube where it enters the fracturing cell (Fig. 3.13) and then running the pump at a constant flow rate. Regression indicates that the function in Figure 3. is represented by

$$V_e = 0.05842 + 0.010615\ p - 0.000021005\ p^2 \qquad (3.35)$$

with $R = 0.995$, where the volume is in ml and the pressure in kPa. For simplicity in the following analysis, deformation of the apparatus is assumed to be linearly elastic and represented by a first order function of the form

$$V_e = Cp \qquad (3.36)$$

where C resembles a volmetric compliance, which is equal to 0.008 ml/kPa for the apparatus used in this work. Substituting eqs.(3.22b), (3.23) and (3.36) into (3.34) and rearranging yields

$$t = (2\pi wa^2/QE)\ [((P_d + \sigma)CE/2\pi wa^2) + [P_d\psi - \sigma(1 - \psi)] \qquad (3.37)$$

Defining the time at the onset of propagation as a characteristic time gives

$$t_{\mathrm{char}} = (2\pi wP_{\mathrm{dchar}}a_i^2/QE)\ [(1 + \sigma^*)CE/2\pi wa_i^2) + 1] \qquad (3.38)$$

and it follows that the normalized time is

$$t^* = \left\{C_e(P_d^* + \sigma^*) + a^{*2}[P_d^*\psi - \sigma^*(1 - \psi)]\right\} / \left\{C_e(1 + \sigma^*) + 1\right\} \qquad (3.39a)$$

where

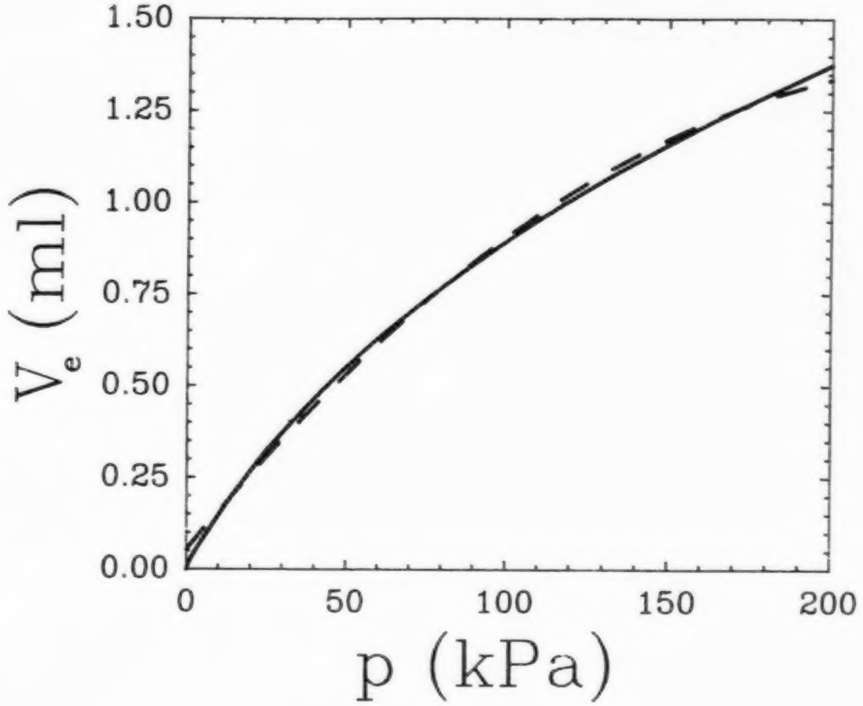

Figure 3.13 Volume stored in pumping system as a function of fluid pressure fluid pressure. Dashed line is second-order regression.

$$C_e = CE/2\pi w a_i^2 \tag{3.39b}$$

which reduces to eq. (3.28) when $C_e = 0$. Values of C_e ranged from 0.02 to 2.0 during the experiments, depending on the modulus of the soil and the slot length.

Dilation of the experimental apparatus affects the forms of pressure records by changing the time scale according to eq. (3.39). The characteristic time increases, reducing the slope of the record during inflation, as the apparatus becomes more compliant. The form of the pressure record during propagation is especially affected early in propagation when a large value of C_e causes the record to steepen (Fig. 3.14). As a result, the slope of the record during early stable propagation may be nearly indistinguishable from the slope during inflation of the starter slot. The term C_e also results in a steepening of the record early in the unstable period of propagation. Steep slopes during this period are commonly observed in both field and lab investigations of hydraulic fracturing of rock, where large moduli could result in large values of C_e.

The rates of growth and dilation of the fracture both increase dramatically, indicating an increase in the volumetric growth rate, as C_e increases (Fig. 3.14). The volumetric rate of growth of the fracture increases, even though the pump is running at a constant rate, because fluid is released from storage in the pumping apparatus when driving pressures diminish during unstable propagtion. Accordingly, the flow rate into the fracture will be greater than the flow rate of the pump during unstable propagation. This conclusion is confirmed by observations of minute bubbles in glycerin flowing through a translucent tube leading to the fracturing cell; their velocity was less during inflation and stable propagation than it was during unstable propagation.

The revised expression for t^* in eq. (3.39) was used to compare results from the analytical solutions to the forms of records from the experiments. Results from the lab experiments showed that the form of the record of driving pressure depended on both the moisture content and the slot length. As moisture content decreases, the driving pressure required to initiate fracturing increases, the period of stable growth early in propagation shortens, and the downwardly concave shape of the record becomes tighter. Similar changes in the records occur when the slot length decreases.

Records of driving pressure are similar to results from the analytical solution (Figs. 3.15 and 3.16) using parameters listed in Table 3.2. The parameters were estimated from lab data, except m which was adjusted to yield the best fit to the data--using m estimated from lab data yields driving pressures that greatly exceed the ones that were observed. The general forms of the records for samples of different moisture content are predicted by the analysis. The driving pressure at the break in slope and the duration of the early period of stable growth are within a few percent of those observed. The

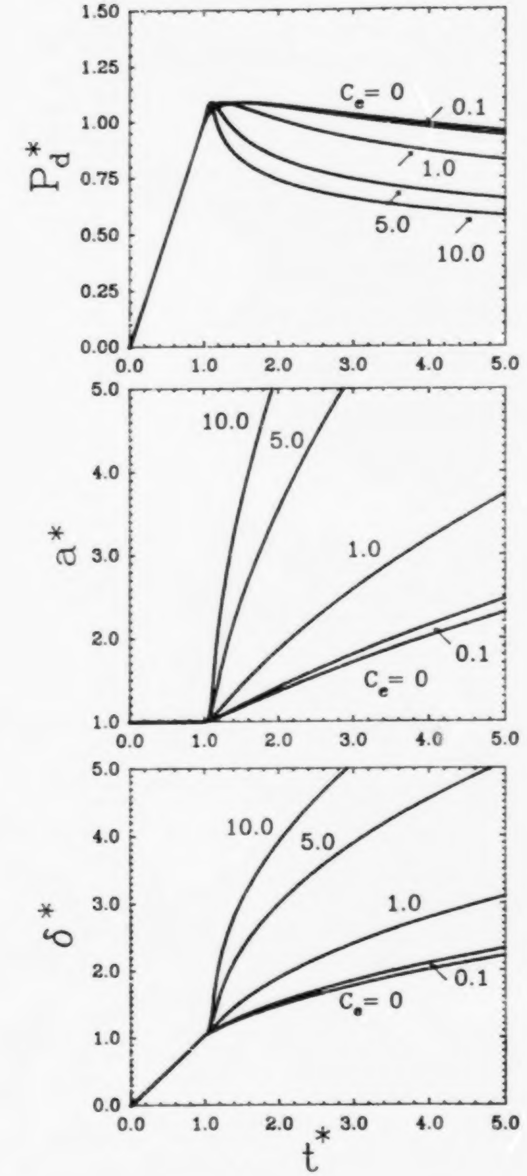

Figure 3.14. Driving pressure, half-length and aperture as functions of time and compliance of pumping system. *m*: 10; a_{cr}: 1.0; σ^*: 0.5.

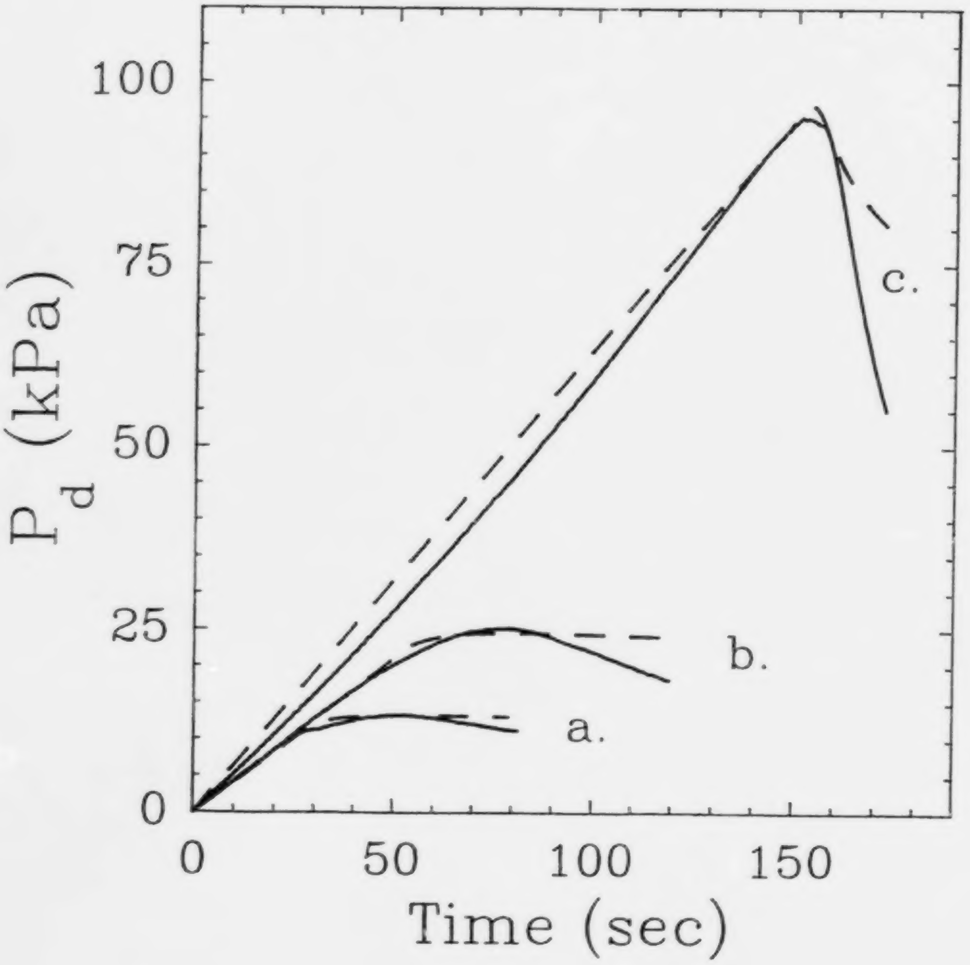

Figure 3.15. Records of driving pressure as a function of time from experiments and from analytical solution (dashed) for samples of various moisture contents.

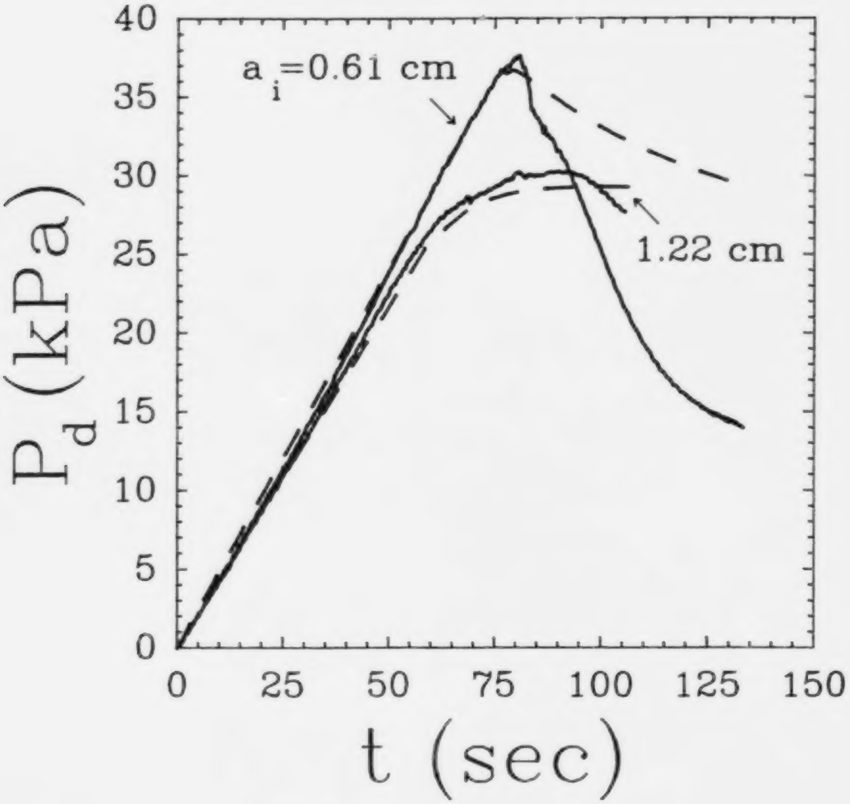

Figure 3.16 Records of driving pressure from experiments and from analytical solution (dashed) for two tests that differed only in the length of the starter slot.

slope of the records during unstable propagation steepens with increasing moisture content in both the analysis and the lab data

The effect of changing the slot length is predicted by the analysis (Fig. 3.16). Driving pressure at the break in slope increases, the duration of stable propagation decreases, and the slope during unstable propagation increases as the length of the initial slot decreases.

The analysis overestimates the driving pressure during unstable propagation in all the examples (Fig. 3.15 and 3.16). Small amounts of the injection fluid leaking out of the edges of the sample, due to imperfect seals between the samples and the apparatus, probably caused the driving pressure during propagation to be less than that predicted by the analysis.

TABLE 3.2. PARAMETERS USED IN ANALYSES

Curve	Moisture	m	K_I kPa cm$^{1/2}$	t_c (sec)	C_e	a_i (cm)
Fig.3.15						
a	0.29	75	22	28	0.05	1.22
b	0.26	30	41	50	0.30	1.22
c	0.23	50	186	150	5.0	1.22
Fig.3.16						
a	0.27	30	63	100	0.088	1.22
b	0.27	30	63	95	0.354	0.61

In both Figure 3.15 and 3.16 the parameter m was selected to yield results that matched experimental data. Values of m are an order of magnitude greater than those obtained from experimental observations, so that the length of unwetted tip required for the analytical solution to resemble the observed pressure records is considerably less than the length of the undyed zones on fracture surfaces. This suggests either that the effective length of the unwetted tip may be shorter than the undyed zone observed on fracture surfaces, or that the driving pressure acting over the unwetted tip may be greater than the negative confining stress.

Comparison with Other Solutions

Several other two-dimensional analytical solutions have been published describing the growth of a hydraulic fracture having a geometry resembling the one used here. Khristianovich and Zheltov (1959) solve the case where the fracture has an identical geometry, but the distribution of driving pressure differs slightly from the one used here. They assume that the driving pressure is a maximum at the center of the fracture and diminishes due to viscous losses to 0 at a point b, which is less than the total length of the fracture. The variable driving pressure is approximated by a statically equivalent driving pressure that is uniformly distributed and acts over $0 \leq x \leq b'$ (b' is obtained from Khristianovich and Zheltov, 1959; eqs. 6 and 7). Thus, the driving pressure they use is uniform but its magnitude depends on fluid viscosity, whereas the pressure used here is uniform but independent of viscosity.

The analysis of Kristianovich and Zheltov includes a zone at the tip of the fracture where fluid pressure is equal to the fluid pressure in the confining material. In contrast, the analyses used here assumes that the pressure along the tip zone is zero, and is independent of the pressure of pore-fluid in the soil. Our assumption is certainly valid for partially-saturated soil, where the pressure of the pore fluid is less than zero. The assumption seems reasonable for saturated soils of low permeability as well. This is because the dilation of the crack itself must reduce the pressure within the tip, and the time required for those low pressures to equilibrate with pore-fluid pressures would be longer than the few seconds that the tip remains unfilled by injection fluid. In any case, the assumption used here marks one end and the one of Khristianovich and Zheltov marks the other end of the range of possible pressures within the tip zone.

Geerstma and DeKlerk (1969) solve a problem whose geometry is similar to the one used here, except they provide for a distribution of pressure within the fracture that varies from a maximum at $x = 0$ to zero at $x = b$. They obtain the pressure distribution by integrating over the interval $0 \leq x \quad b$ an equation for flow through a narrow rectangular channel, and assuming that the pressure within the fracture is zero over $b < x \leq a$. Both Geerstma and DeKlerk, and Kristianovich and Zheltov introduce an unwetted zone remove the stress singularity at the fracture tip. This concept, which is applied to brittle fracture by Barenblatt (1962) and to ductile fracture by Dugdale (1963), is mechanically different from the one used in this work. We show that the unwetted tip can develop due to a difference between the velocities of the fluid and the fracture, and the length of the unwetted zone is therefore related to differences between the two velocities. In the other model, the length of the unwetted zone is related to the magnitude of K_{Ic} and is independent of the relative velocities. These differences are subtle, but, inasmuch as the size of the unwetted zone strongly affects the length and aperture of a fracture, the mechanism for growth of that zone plays an important role in predicting fracture dimensions.

Spence and Turcotte (1985) built on the work of Geerstma and DeKlerk by deriving an analytical solution that includes effects of both viscous dissipation of pressure in the fracture and finite fracture toughness. The general solution of Spence and Turcotte requires numerical integration; however, for specific cases where the system is dominanted by either fracture toughness or viscous dissipation the solution reduces to algebraic expressions. Predicting the migration of igneous sheet intrusions was the primary goal of Spence and Turcotte, and they have omitted an investigation of the pressure distribution at the tip of a hydraulic fracture.

Perkins and Kern (1961) present a solution for a long, rectangular fracture that is elliptical in shape in sections taken normal to the long axis. They obtain a pressure distribution by using an equation for flow through a narrow elliptical channel, and assuming the driving pressure is zero at the end of the channel. Nordgren (1972) modified the solution of Perkins and Kern (1961) to include effects of dilation and leakoff on the pressure distribution in the fracture. Both Perkins and Kern (1961) and Nordgren (1972) ignore the problem of stress concentration at the tip of the fracture, so conditions of equilibrium propagation are not explicitly satisfied.

Medlin and Masse (1984) and Geerstma and Haafkens (1979) point out that the analytical solutions described above can be written as power law functions relating driving pressure, half-length, and aperture to time

$$P_d = c\, t^{\beta} \tag{3.40a}$$

$$a = d\, t^{\chi} \tag{3.40b}$$

$$\delta = e\, t^{\varepsilon} \tag{3.40c}$$

The solution derived for this work reduces to a set of power law functions by setting $b/a = 1.0$, which is the same as setting the length of the unwetted tip to zero (eq. 3.32). Values of the exponents given by the present solution (using $b/a = 1.0$) are identical to those derived by Geerstma and DeKlerk, and by Spence and Turcotte (Table 3.3), and they are similar to values from Kristianovich and Zheltov.

—TABLE 3.3. EXPONENTS FROM VARIOUS ANALYTICAL SOLUTIONS

β χ ε	β	χ	ε
Kristianovich and Zheltov*	-0.3	0.6	0.4
Kristianovich and Zheltov**	-1/4	1/2	1/2
Geerstma and DeKlerk	-1/3	2/3	1/3
Spence and Turcotte	-1/3	2/3	1/3
Perkins and Kern	+1/5	4/5	1/5
This work (b/a = 1.0)	-1/3	2/3	1/3

---

* Values cited by Medlin and Masse (1984)

** Based on eqs. (33), (36) and (45) of Kristianovich and Zheltov (1959)

The values are markedly different from those given by Perkins and Kern (1961), however. In particular, the solution of Perkins and Kern (1961) yields a positive value for β, whereas the others yield negative values. Positive value of β indicates that driving pressure increases throughout propagation, whereas pressure was observed to decrease in the experiments suggesting that a negative value of β is appropriate.

Forms of the constants c, d, e from the present solution are similar to those given by Spence and Turcotte for a fracture whose resistance to propagation due to fracture toughness is much greater than resistance to flow (Table 3.4). Fracture toughness enters as the same power for both solutions, whereas the powers on flow rate and elastic modulus are similar but slightly different. The solution of Spence and Turcotte contains μ, the viscosity of the injection fluid, whereas the one presented here assumes μ is zero.

—TABLE 3.4. COMPARISON OF CONSTANTS

Constant	Spence and Turcotte	This paper
c	$0.7842\left[\frac{[2(1-\upsilon)(1+\upsilon)]^{3/4}K^4}{E'^{3/4}\mu^{1/4}Q^{5/4}}\right]^{1/3}$	$\left[\frac{2K^4w(1-\upsilon^2)}{QE'}\right]^{1/3}$
d	$0.5599\left[\frac{E'^{3/4}\mu^{1/4}Q^{5/4}}{K[2(1-\upsilon)(1+\upsilon)]^{3/4}}\right]^{2/3}$	$\left[\frac{QE'}{2(1-\upsilon^2)wK\pi^3}\right]^{2/3}$
e	$0.5685\left[\frac{[2(1-\upsilon)(1+\upsilon)]^{3/2}Q^{1/2}K^2}{E'^{3/2}\mu^{1/2}}\right]^{1/3}$	$\left[\frac{32(1-\upsilon^2)^2QK^2}{wE'^2\pi^6}\right]^{1/3}$

Values of the exponents in the power law form depend on the geometry of the fracture, whereas the constants indicate how the system will respond if either the material or the pumping process are changed. An increase in fracture toughness will cause the driving pressure to increase, and the fracture to shorten and thicken. An increase in elastic modulus, however, decreases the driving pressure and causes the fracture to lengthen and become more narrow. Increasing the rate of injection reduces the driving pressure, but it causes the fracture to both lengthen and thicken.

Medlin and Masse (1984) estimated apparent values of the exponents β, χ, and ε from lab data by determining the average slope of driving pressure, half-length, or aperture plotted with respect to time on a log-log scale. They found that apparent values of χ and ε decrease, whereas β increases as confining stress increases (Figure 3.17).

The experimental apparatus of Medlin and Masse resulted in conditions resembling two-dimensional plane strain, so the analysis described above was used to examine the effect of confining stress on apparent values of the exponents. The ratio b/a is independent of a, but increases with confining stress according to Medlin and Masse (1984; fig. 7). Figure 3.17. is based on figure 7 in Medlin and Masse, but values of b/a have been extrapolated for the purpose of this analysis. A driving pressure at failure of approximately 500 psi is apparent from figure 3 (Medlin and Masse, 1984), and this value will be used to determine σ for all the calculations--K_{Ic} and slot length are assumed to be constant. The apparent value of β was determined by linear regression of the logarithms of P_d and t, and the other exponents were determined in a similar manner.

The analysis is able to predict the experimental values of β throughout the range of confining pressures. At relatively low confining pressure, β increases with confining pressure, but it remains roughly constant at intermediate to high confining pressure. Figure 3.18 shows that increasing σ tends to increase β, whereas decreasing the length of the unwetted tip, with σ according to Figure 3.17, tends to decrease β. At confining pressures greater than 14 MPa these effects apparently balance one another according to the data of Medlin and Masse and the results of the analysis. We conclude that those changes in the form of the pressure record, expressed as changes in β, can be explained by the effect of confining stress acting on the unwetted tip.

The analysis yields values of χ and ε that exceed those observed in the experiments of Medlin and Masse. Flow out of the fracture and into the enveloping material, or *leakoff*, is a possible explanation of the discrepency. The present analysis is unable to account for leakoff, but the analysis of Nordgren (1972) shows that leakoff will decrease the values of χ and ε. Moreover as Medlin and Masse (1974) point out, conservation of mass requires that $\chi + \varepsilon = 1.0$ if no leakoff occurs, and that sum will be less than 1.0 if leakoff does occur. At equal confining stress, sums of χ and ε determined experimentally by Medlin and Masse (Fig. 3.18) are all less than 1.0 and those sums decrease with increasing confining pressure. This information substantiates the conclusion that leakoff is a possible explanation for why the data of Medlin and Masse on χ and ε are less than the results of the analysis.

DATA QUALITY

The objective stated in the Quality Assurance Project Plan (memo

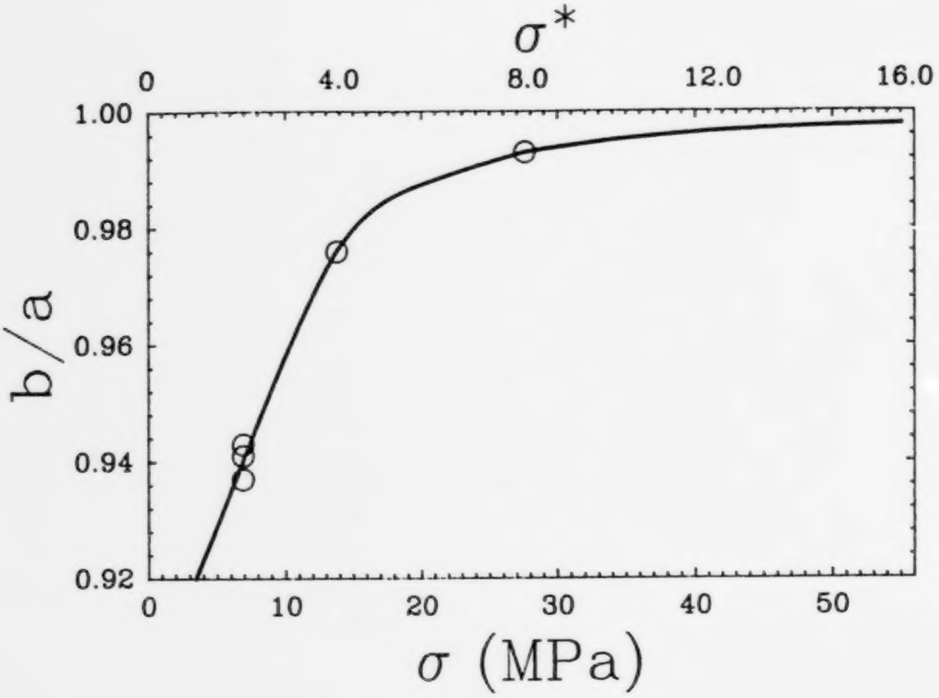

Figure 3.17 The ratio of wetted to total length of a fracture as a function of confining stress. Data from Medlin and Masse (1984).

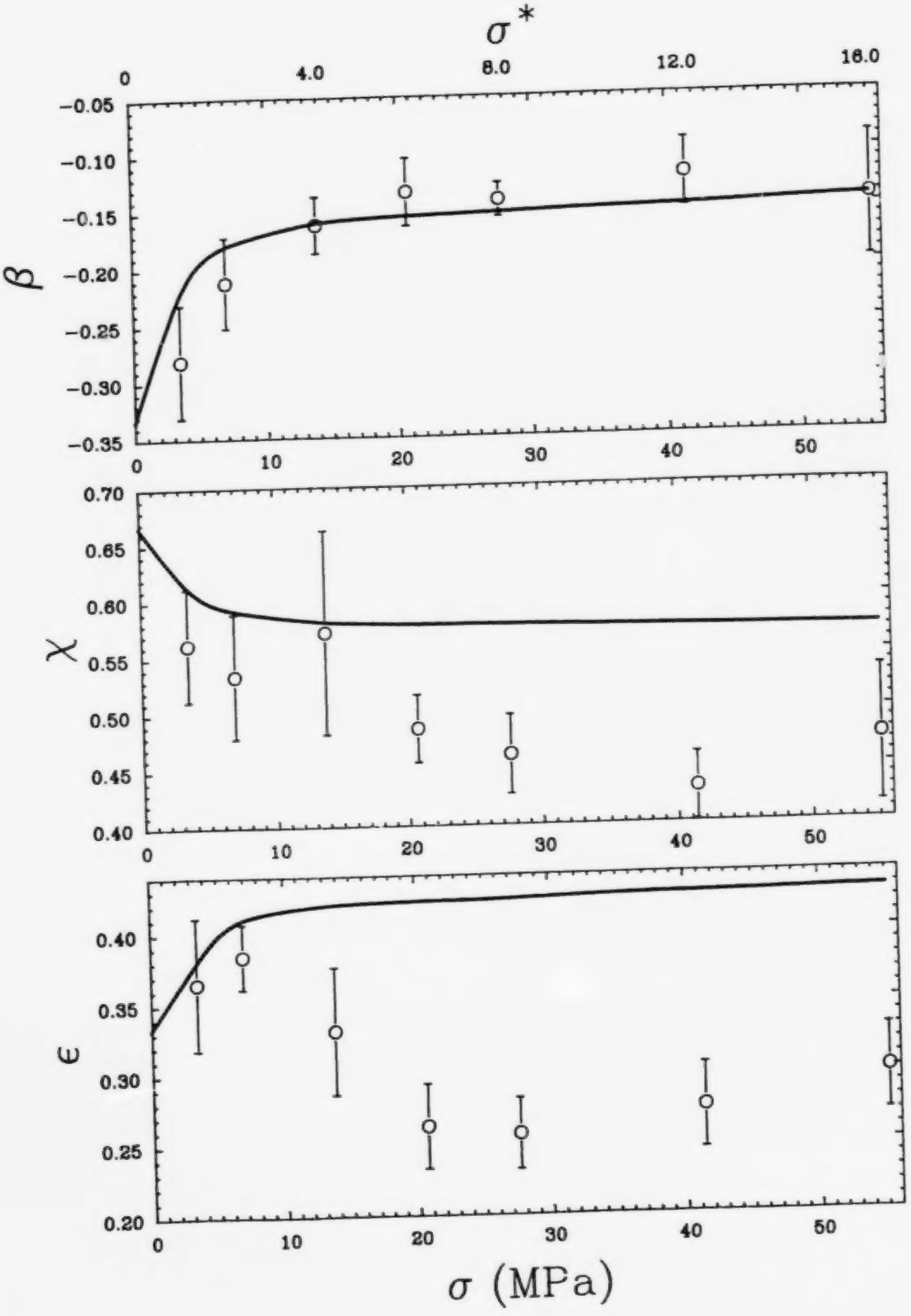

Figure 3.18. Variation of exponents in eq. (3.40) as functions of confining stress. Data from Medlin and Masse (1984), solid line from analytical solution.

submitted to David L. Smith, 3 October 1988), was to make measurements of K_{Ic} that can be duplicated to within 15 percent. In Chapter Two, we showed the results of four tests conducted on similar samples. The three of the four values of initiation pressure were tightly clustered, they were within 2.5 percent of their average value. The fourth measurement was less than the other three. The average of all four measurements is 25.4 kPa and that fourth value is 22.8 kPa, which is 10 percent less than the average. Critical stress intensity is determined directly from initiation pressure, and so it will have the same range of values as described above.

Earlier in this chapter, results showed that doubling the slot length caused variations of K_{Ic} that averaged 10.4 percent. The critical stress intensity both increases and decreases as the slot length increases, indicating that the variations that were observed reflect experimental error, rather than a systematic dependence on slot length as reported by Ouchterlony (1982).

Critical stress intensity measurements can be duplicated to within 15 percent of an average value using the methods described in the text.

The principal measurements, the methods of obtaining them, and the accuracies of those methods are presented in Table (3.5).

TABLE 3.5. EXPERIMENTAL MEASUREMENTS

Measurement	Method	Accuracy
Sample size	scale	±0.1 cm
Length of slot	micrometer	±0.001 cm
Density	Weight/Volume	±0.01 gm/cc
Confining pressure	Gauge	±0.005 kPa
Injection pressure	Transducer	±0.002 kPa
Injection rate	pump calibration	0.00003 cc/sec
K_{Ic}	calculation	0.007 kPa cm$^{1/2}$

Pressure gauges and transducers were purchased at the beginning of the project, and were maintained in good working order. Gauges used to measure confining pressure were calibrated using a pressure transducer. The transducers were calibrated at the factory.

The precision of the critical stress intensity measurements is impossible to assess because published values of that parameter are unavailable for soil.

All the tests that we set out to conduct were accomplished during the study. Completeness was 100 percent.

The results are expected to represent K_{Ic} determined using similar techniques of sample preparation, experimental apparatus, and method of loading. Experimental methods that facilitate detecting the onset of fracturing, perhaps by acoustic or optical methods, probably will show that fracturing occurs slightly prior to the break in slope of the injection record, which was used in this study to infer fracturing. As a result, critical stress intensity measurements obtained by those methods will be less than those cited here.

DISCUSSION

A satisfactory analysis of hydraulic fracturing of soil should yield a method of predicting the driving pressure at the onset of fracturing as well as the forms of pressure records during propagation, and it should explain the development of essential features of a fracture, according to requirements put forth in the introduction of this chapter. Elements of linear elastic fracture mechanics were used to develop various analyses to test against those requirements.

The critical stress intensity at the onset of fracturing is independent of the length of the initial slot, and appears to be a material property of the soil used in this study that will serve as an acceptable predictor of fracturing. Moreover, theoretical estimates suggest that the size of the process zone at the tip of a fracture in the Center Hill clay ranges from one to a few mm, which is small compared to lengths of initial slots and further supports the applicability of K_{Ic} as a predictor of fracturing.

The critical stress intensity of the Center Hill clay ranged over an order of magnitude for various moisture contents and durations of consolidation, so that that lab data will only yield rough estimates of conditions in the field. An in-situ method of determining K_{Ic} would yield values more suitable for field applications. Nevertheless, the lab results are significant in that they show that K_{Ic} is a meaningful property describing fractures in clay.

The development of a hydraulic fracture in the Center Hill clay at moisture contents less than 0.21 includes the growth of an unwetted zone at the tip of the fracture. A theoretical analysis of coupled fluid flow and elastic deformation shows that the velocity of fluid near the tip of a fracture is less than the velocity of the fracture itself, thus providing a mechanism for the development of the unwetted tip. Tracking the position of the fluid front by the theoretical model yields lengths of the unwetted and wetted parts of the fracture that are similar to lengths observed on the surfaces of fractures created in the lab. Detailed analyses of the rate of growth of the unwetted tip as a function of moisture content (e.g. Figure 2.10) are the subject of future investigations.

An early period of stable propagation, characterized by increasing driving pressures, was observed in nearly every lab test. Stable propagation early in the growth of a hydraulic fracture can be explained by an increase in resistance to propagation resulting from growth of an unwetted tip. This explanation is confirmed by results of both numerical and analytical solutions to fracture growth. An alternate explanation of stable propagation resulting from large viscous losses due to flow in a narrow region near the tip of a growing fracture (Zoback and others, 1977; Zoback and Pollard, 1978) could also explain the lab data but it is inconsistent with the results of the numerical analysis.

Results of the numerical solution using parameters typical of the lab experiments show that the fluid pressure within a fracture is nearly uniform. This suggests that a simple analytical analysis, which assumes uniform pressure, could provide insight into the general behavior of the fractures. Pressure records from the lab can be reproduced using the analytical model by selecting an appropriate function describing the growth of the unwetted zone. The analytical model also provides an explanation of the dependence of the form of pressure records on confining stress, which was observed in hydraulic fracturing experiments conducted using rock specimens (Medlin and Masse, 1984).

The methods of linear elastic fracture mechanics meet the requirements of an acceptable model of hydraulic fracturing of soil. Modifications of the analysis to account for large-scale plastic yielding at the fracture tip appear to be unnecessary. The present methods could readily be adapted to account for appreciable plastic yielding during hydraulic fracturing (e.g. Biot and others, 1982), although measurements that are more detailed than those used here would be required before such methods seem warranted.

Much of the published analyses on hydraulic fracturing of rock appear to be generally applicable to hydraulic fracturing of soil. Analyses that track the position of the wetted front, such as those by Abe and others (1976), Roegiers and others (1982), Griffiths and Nilson (1986), or Nilson (1986), appear to be particularly well-suited to predicting hydraulic fracturing of soil.

Analyses that assume that the fracture is completely filled with fluid will overestimate lengths and underestimate apertures as compared with analyses that allow for the development of an unwetted tip. Inasmuch as fracture length and aperture control the performance of a fracture in delivery and recovery, it is clear that understanding processes at the fracture tip will improve the ability to design field applications of hydraulic fractures in either soil or rock.

SECTION FOUR

SETTING AND DESIGN OF THE FIELD TEST--1988

The 1988 field test was conducted at a site 10 km north of downtown Cincinnati on the western side of the valley of Mill Creek, a southerly-flowing tributary of the Ohio River. The site is on the southeastern side of an area owned by the ELDA Company, who currently uses it as a municipal landfill.

Investigation and preparation of the test site took place during several months in Spring 1988. The actual test, however, only required 12 hours and was completed in one day, 15 June 1988. Ten hydraulic fractures were created during the test. Field evaluation of the results of the test took place during the six weeks following the test.

SITE CHARACTERISTICS

The vicinity of the test site is an area of gently sloping ground bounded on the northwest by a vertical face and on the southwest by moderate slopes into an excavated trough (Fig. 4.1). The southern side of the trough is bounded by a north-facing vertical cut, the eastern end of which is shown on the southwestern corner of Figure 4.1. The ground surface at the time of the test had been excavated during operations at the landfill to several meters below the natural ground surface.

The site itself is an elongate strip trending N20E and roughly 80 m long. The northern end of the site is on a gentle, south-facing slope, whereas the southern end of the site is on level ground (Fig. 4.1). The slope of the ground surface is important because it apparently affected forms of the fractures.

Geology

Glacial till, probably of Illinoian age, underlies the test site. The thickness of the till is unknown, but it is more than several tens of meters. Three stratigraphic units were identified in the till based on exposures in vertical faces near the site, on boring logs, and on exposures in trenches cut in the test site (Fig. 4.2 and 4.3). The upper till unit, Unit 1, is 0.5 to 2 m thick and consists of massive light brown-grey clay and silt containing 5 to 15 percent rock fragments. Coarse gravel, cobbles, fragments of limestone and organic matter are disseminated through Unit 1.

The middle unit, Unit 2, is dominantly flat-lying beds that fine upward from coarse gravel to clay. A typical bed consists of orange-brown cobbles and gravel at the base that grades upward to orange-brown coarse and fine sand, to light brown silt, and to light brown clay at the top. The graded beds range in thickness from 0.1 to 0.4 m, and in most exposures are several m to several tens of m in lateral extent. Locally, the forms of the beds are irregular and highly contorted with large changes in thickness occurring over several m. An example of the irregular bed forms is shown in Figure. 5.9. Massive beds of grey clay and silt are locally interfingered with graded beds. The total thickness of Unit 2 ranges from 3 to 7 m.

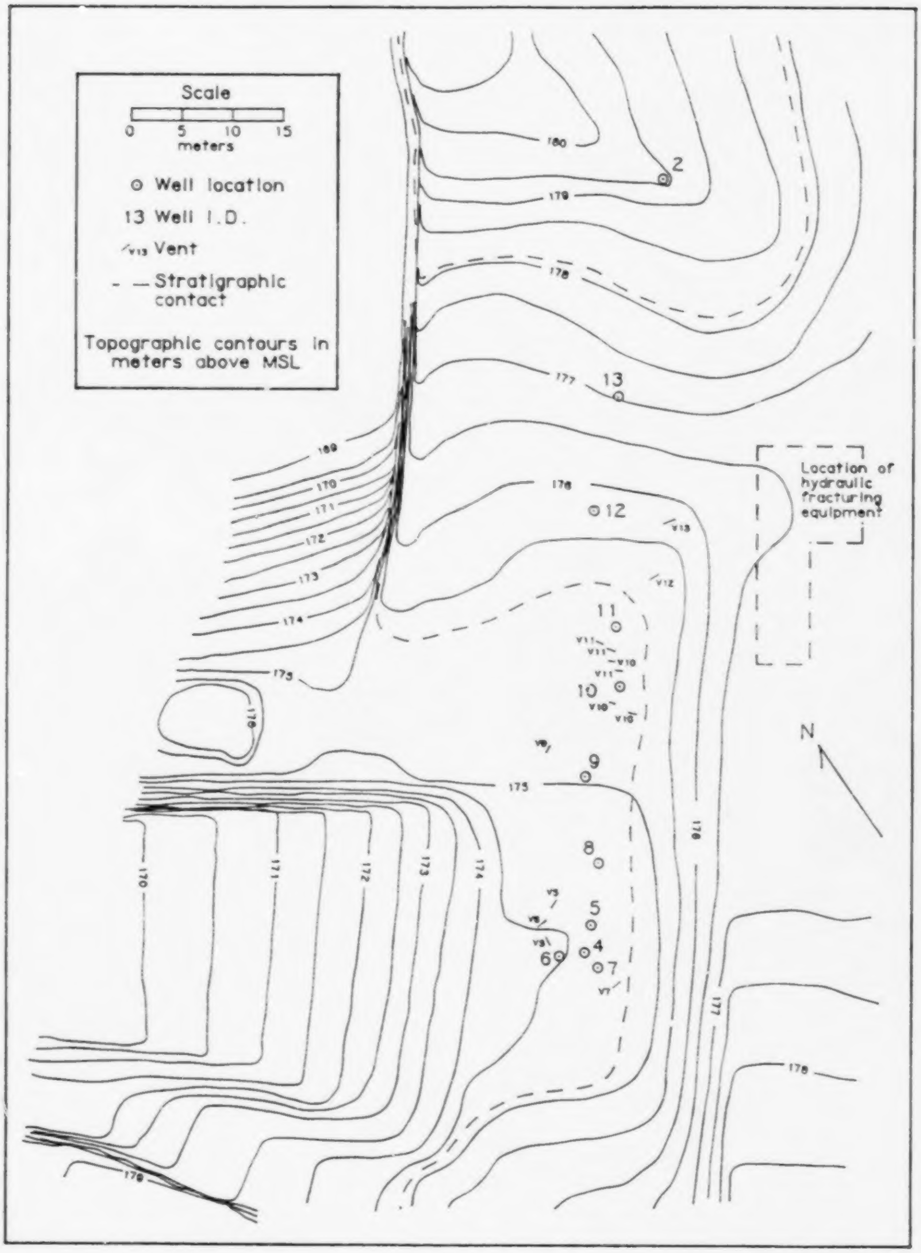
Scale
0 5 10 15
meters
Well location
13 Well I.D.
V13 Vent
Stratigraphic contact
Topographic contours in meters above MSL
Location of hydraulic fracturing equipment
N
180
179
178
177
176
175
174
173
172
171
170
169
2
13
12
11
10
9
8
5
4
6
7
V13
V12
V11
V10
V9
V5
V3
V7

Figure 4.1. Topography and locations of boreholes, vents, and hydraulic fracturing equipment at the ELDA test site.

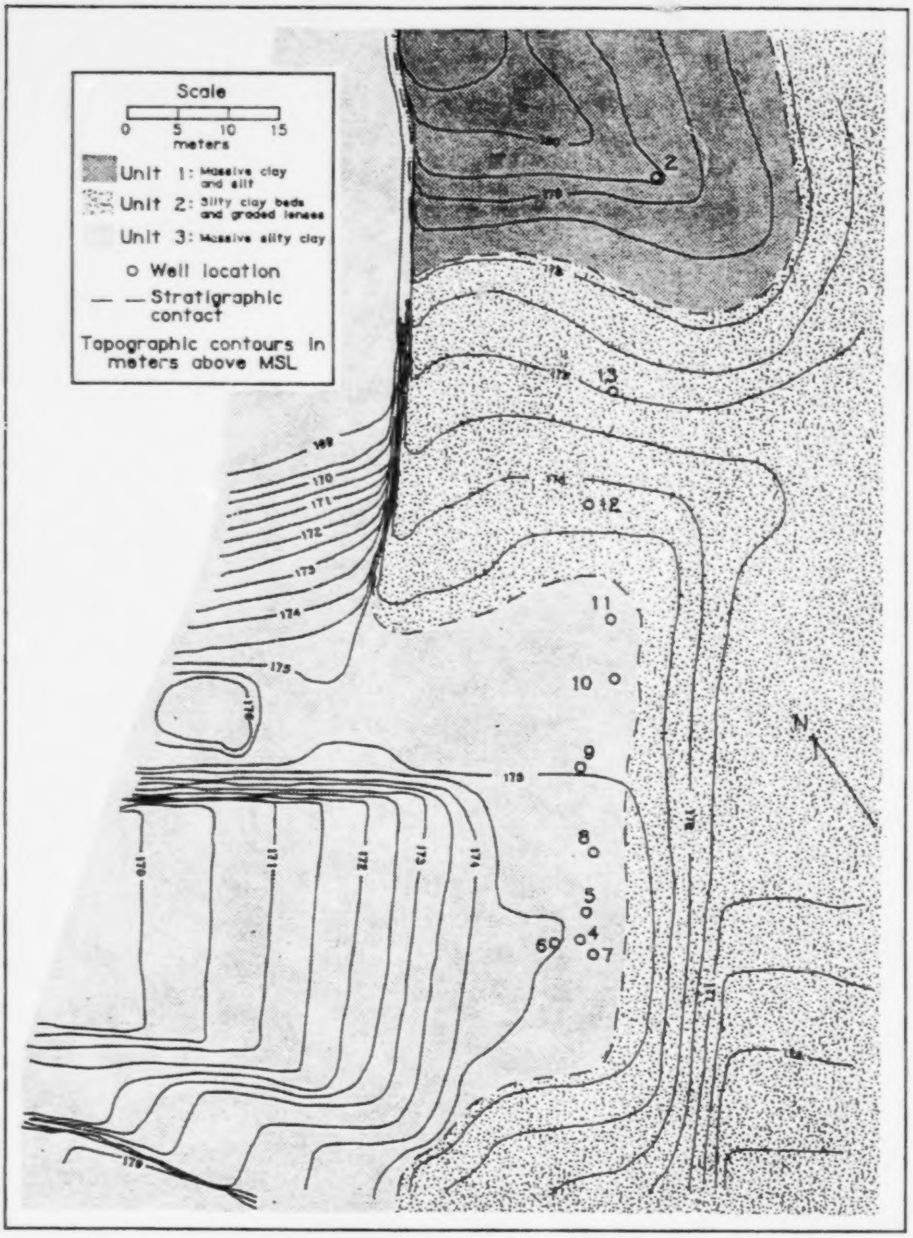
Scale
0
5
10
15
meters
Unit 1: Massive clay and silt
Unit 2: Silty clay beds and graded lenses
Unit 3: Massive silty clay
o Well location
— — Stratigraphic contact
Topographic contours in meters above MSL
N
2
13
12
11
10
9
8
5
4
6
7
169
170
171
172
173
174
175
176
178

Figure 4.2. Geology of the ELDA test site.

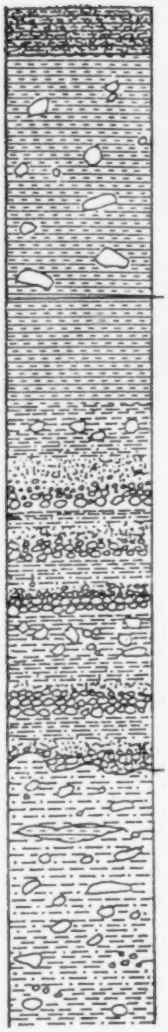

Weathered till topsoil, 0 to 0.3 m thick.

UNIT 1

Light brown to grey, massive clay and silt containing 5 to 15 percent disseminated gravel, cobbles and rock fragments. Roots common. One half to 2 m thick.

Sharp, planar contact.

UNIT 2

Light brownish-grey, massive silt. One m thick, thins south of site.

Upwardly-grading beds and lenses of gravel, sand silt and clay that range from 0.1 to 0.4 m thick; and massive to laminated beds of grey silty-clay 0.2 to 1.0 m thick. Irregular, contorted bedforms common. Total thickness 4 to 7 m.

Irregular contact.

UNIT 3

Light grey, massive, silty-clay containing 5 to 20 percent disseminated gravel, cobbles and rock fragments. Irregular lenses of silt, or yellow-brown sand present locally. Lower contact not exposed, at least 8 m thick.

Figure 4.3. Stratigraphic section from the vicinity of the ELDA test site.

The upper surface of a light brown, massive silt bed several dm in thickness marks the contact between Units 1 and 2. The contact is planar and nearly flat-lying, differing in elevation by roughly 0.1 m over the study area.

The lower till unit, Unit 3, consists of massive, grey silty-clay containing 5 to 20 percent disseminated rock fragments. Pods and beds of light grey silt, or brown sandy-gravel occur locally. The lower contact is not exposed, so the thickness of Unit 3 is unknown. The upper surface of the massive grey clay of Unit 3 marks the contact between Units 2 and 3. The contact varies in elevation by several meters in the vicinity of the site.

Hydraulic fractures were created in Units 2 and 3. Fractures at boreholes 2 and 13 were in Unit 2, the one at borehole 12 propagated upward from Unit 3 into Unit 2, and the others were contained within Unit 3.

Hydrology

Eleven of the 14 boreholes drilled during exploration of the site were dry when we created the hydraulic fractures. In those boreholes that did contain water, the water depths were less than 20 cm at the time of fracturing. Some other boreholes contained water several days prior to fracturing, but the day before fracturing we found soft mud, but no standing water, at the bottom of those holes (Table 4.1).

A regional water table is present several tens of meters or more below the level of the boreholes, but it was insignificant to the test.

During testing the silty clay that comprises most of the till was unsaturated (ratio of water volume to pore volume of 29%). Water that was observed in boreholes apparently drained from perched zones within sand and gravel lenses in the till.

Effects of the hydrologic conditions in a borehole on the results of hydraulic fracturing were undetectable.

In situ State of Stress

The state of stress in the till was measured in situ using a method of analyzing injection pressure after creating a small-volume (10-20 ml) hydraulic fracture. The method of analysis of the pressure record is used routinely for research in rock mechanics (Zoback and Pollard, 1978; Gronseth, 1979), but the apparatus used to create the small hydraulic fractures in soil was designed for this project.

The apparatus consists of a heavy-walled steel pipe (1/2" Nominal Schedule 80 pipe, O.D.: 2.13 cm; I.D: 1.42 cm) fitted with a conical point. The point consists of an outer beveled ring attached to the pipe, and an inner, bullet-shaped point attached to a steel rod extending the length of the pipe. A cap fits on the end of the pipe and prevents the rod and inner point from moving when the pipe is driven into the ground.

TABLE 4.1. CONDITIONS OF BOREHOLES PRIOR TO TESTING.

BOREHOLE	DEPTH OF CASING (m)		CONDITIONS	
		(6/9/88)	(6/13/88)	(6/14/88)
2	2.76	DRY	DRY	N/A
3	1.39	N/A*	N/A	N/A
4	3.65	DRY	DRY	DRY
5	1.64	DRY	DRY	DRY
6	1.86	DRY	MUDDY	DRY
7	1.83	DRY	MUDDY	DRY
8	1.89	N/A	1.45**	1.77
9	1.86	0.88	MUDDY	MUDDY
10	2.10	1.98	1.58	2.07
11	1.98	DRY	DRY	DRY
12	1.99	1.47	1.80	1.80
13	2.01	1.18	MUDDY	MUDDY
14	1.85	DRY	DRY	DRY
15	2.23	1.24	1.71	1.77

*: N/A, data not available.
**: Water level in m below ground surface.

To measure lateral stress the pipe is pushed into the ground using a post-hole driver (Fig. 4.4); we were able to drive the pipe to depths of 2 m in both till and colluvium. The rod and inner point is retracted exposing soil at the bottom of the pipe. A coring point, shaped like a thin-walled tube 0.63 cm in diameter, is driven into the soil at the bottom of the pipe and cuts a cylindrical hole roughly 10 cm in length (Fig. 4.4). Water is injected into the pipe using a positive displacement pump and the pressure is monitored using a pressure transducer and a data acquisition computer. Lateral pressure of the soil against the pipe seals the system and a hydraulic fracture is created from the cylindrical hole at the bottom of the pipe (Fig. 4.4).

The least compressive in situ lateral stress is obtained by assuming that it is equal to the pressure of the injection fluid when a hydraulic fracture closes after pumping has ceased. This pressure is commonly termed the instantaneous shut-in pressure, P_{isi}. When the pump is turned off after a hydraulic fracture has been created, the pressure of the injection fluid commonly shows two well-defined periods of behavior (Medlin and Masse, 1984). During the first period, the pressure decreases rapidly as fluid flows out of both the borehole and the fracture and into the enveloping material. The rate of decrease of pressure diminishes, however, as the fracture closes. During the second period, the pressure decreases slowly, at a nearly constant rate, as the fluid leaks only out of the walls of the borehole.

There are a variety of methods used to infer P_{isi} from the record of injection pressure as a function of time (e.g. McLennan and Roegiers, 1982; Aamodt and Kuriyagawa, 1982; Gronseth, 1979; Zoback and Pollard, 1978; Nolte, 1979; Muskat, 1937).

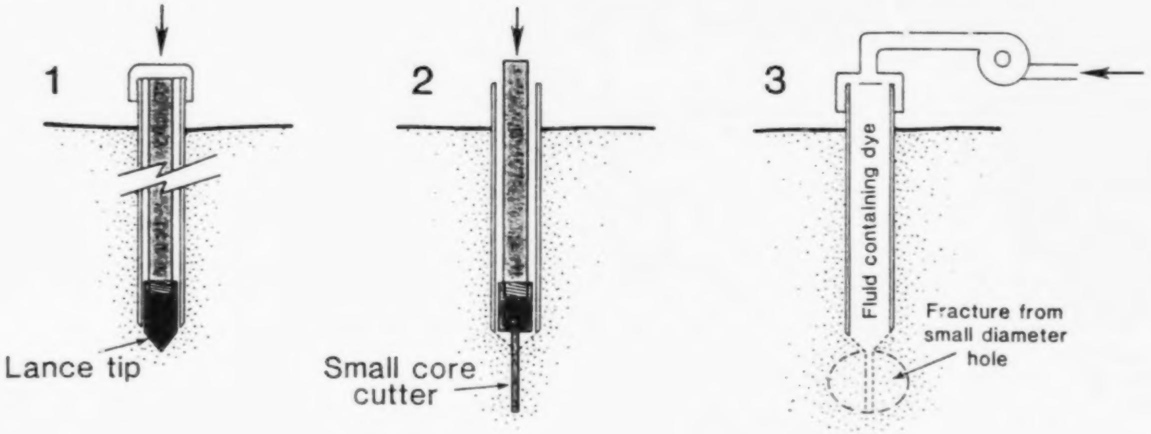
1
Lance tip
2
Small core cutter
3
Fluid containing dye
Fracture from small diameter hole

Figure 4.4. Method of creating small hydraulic fracture to measure the least horizontal confining stress.

A relatively simple method, suggested by Medlin and Masse (1984), is to use the maximum pressure during the second period of pressure decline. This pressure is obtained by fitting a straight line to the record and recording the earliest point of intersection between the line and the record (Fig. 4.5).

According to the experiments of Medlin and Masse (1984), P_{isi} obtained in this manner can over-estimate the actual applied stress, and the amount of over-estimation depends on the rate of flow out of the fracture and other factors. Roughly one dozen experiments were conducted using the laboratory apparatus described earlier to test whether this method of obtaining P_{isi} would yield the confining stress in soil. Hydraulic fractures were created from a cylindrical hole 0.63 cm in diameter and 10 cm long (the same size as in the field apparatus) cut in Center Hill clay. The results are encouraging; P_{isi} obtained from the method described above was typically within five percent of the confining stress applied to the sample (Fig. 4.5a).

In the field at the ELDA site, tests were conducted at a depth of 1.2 m in silty-clay till (Unit 3). The injection pressure rapidly increased to 1200 kPa and then abruptly decreased indicating the onset of fracturing (Fig. 4.5b). We turned off the pump after 60 seconds, at which time the pressure decreased rapidly for roughly 10 seconds and then the rate of decrease started to diminish. The rate of decrease became roughly linear at 65 seconds. A second test was conducted by turning on the pump until the pressure reached a peak and started to diminish (indicating further propagation), and then turning off the pump. The pressure record of the second test is similar to that of the first (Fig. 4.5b). Fluctuations in pressure during the linear part of the second test probably resulted from vibrations caused by heavy earth-moving equipment operating nearby.

An instantaneous shut-in pressure of 320 kPa was obtained during the test at the ELDA site (Fig. 4.5b). The transducer was 2.15 m above the fracture, so a correction for the static pressure gradient was added to obtain an estimate of the lateral confining pressure. The vertical confining stress is assumed to be the unit weight of the till times the depth of the test.

Using those methods, the lateral confining stress is inferred to be 340 kPa (roughly 50 psi), and the vertical confining stress roughly 26 kPa (3.9 psi). The ratio of vertical to lateral confining stress is 1:13 at a depth of 1.2 m.

Hydraulic Conductivity

Saturated hydraulic conductivity, K_s, of till was measured in situ at several locations using a Guelph borehole permeameter, a device manufactured by Soilmoisture Equipment Company, Santa Barbara, CA. The device is designed to measure K_s in boreholes penetrating unsaturated porous media. In general, the device uses a Mariotte bottle device to hold a constant level of water in a borehole, and allows flow rate out of the well to be measured as a function of time. A test is conducted until the flow rate becomes constant. Details of the operation of the Guelph Permeameter are available from the manufacturer.

The saturated hydraulic conductivity is obtained from the steady-state solution of flow from a cylindrical hole in an unsaturated porous media (Reynolds and Elrick, 1985). Two methods of solving for K_s are available. The most accurate method requires measurements of flow rate at two different heads (water levels in the borehole). This

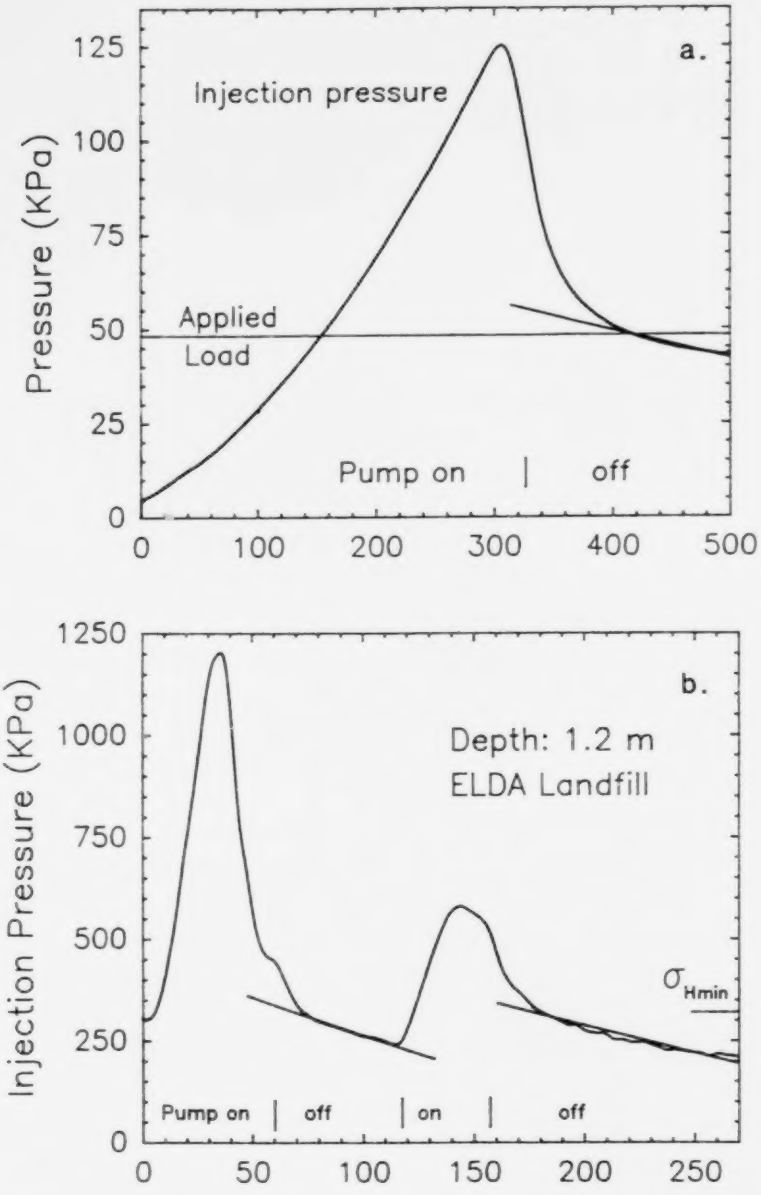

Figure 4.5a. Injection pressure as a function of time during a lab experiment. 4.6b. Injection pressure as a function of time at the ELDA test site using field apparatus designed to estimate lateral confining stress.

method requires a homogeneous porous media, and will yield erroneous values if layers or discontinuities are present.

Another method of determining K_s requires measurements of flow rate at only one value of head, and it can be applied in layer media. The accuracy of this method is less than of the method described above because this one requires an estimation of the ratio of K_s and the matric flux potential. Fortunately, however, the ratio can be estimated from descriptions of the till to yield values K_s that are within 20 percent of K_s determined by other methods, according to Elrick and others (1988). This accuracy is considered sufficient for our purposes.

Both methods of calculating K_s were used, but we found that the method requiring two measurements typically yielded unsatisfactory values of K_s (values were less than 0). As a result, the method requiring one measurement and an estimation of the ratio of K_s and matric flux potential was used for all estimates of K_s.

In general, the saturated hydraulic conductivity of silty clay is between 1.5×10^{-6} cm/sec and 1.9×10^{-7} cm/sec, whereas those measured in silty sands and gravels are an order of magnitude or more greater; between 1.0×10^{-5} cm/sec and 3.5×10^{-5} cm/sec. Measurements of K_s were made at five locations, and the values are tabulated below (Table 4.2).

Physical Characteristics of the Till

A suite of tests was performed in the laboratory on samples of the ELDA Till to determine standard geotechnical characteristics. The tests were conducted by Patricia Strube, a geotechnical soils analyst at the Center Hill Research Facility. The methods used to make the measurements are described in the ASTM Handbook on Soil Testing. Samples from four shelby tubes pushed into the till at the ground surface were used for the analyses.

TABLE 4.2. SATURATED HYDRAULIC CONDUCTIVITIES OF TILL

Location	Depth (cm)	Material	K_s (cm/sec)
1	40	silty clay	7.5×10^{-7} to 1.5×10^{-6}
2	45	silty clay	1.0×10^{-6} to 1.4×10^{-6}
3	150	silty clay	1.9×10^{-7} to 8.9×10^{-7}
4	30	silty sand and gravel	1.0×10^{-5} to 2.4×10^{-5}
5	42	silty sand and gravel	3.0×10^{-5} to 3.5×10^{-5}

TABLE: 4.3 PHYSICAL CHARACTERISTICS OF SILTY-CLAY TILL

	ET1	ET2	ET3	ET4	AVE
Atterburg Limits					
Liquid	22.6	22.9	24.8	25.0	23.8
Plastic	12.5	10.5	11.4	15.7	12.5
Shrinkage	19.8	15.5	15.3		16.8
P. I.	10.1	12.4	13.4	9.3	11.3
Grain sizes (by wt.)					
Gravel	0.13	0.18	0.10	0.11	
Sand	0.29	0.28	0.34	0.33	
Silt	0.36	0.31	0.34	0.37	
Clay	0.22	0.23	0.22	0.19	
Void Ratio:	0.34				
Porosity:	0.25				
Moisture:	11.6	13.5			
Degree of Saturation:	0.29				
Bulk Unit Weight:	2268kg/m³ (141.6 lb/ft³)				
Bulk S.G.:		2.2			
Dry Unit Weight:	2031kg/m³ (126.8 lb/ft³)				
Specific gravity, solids:		2.68			

The characteristics of the ELDA Till are similar to those of other tills analyzed by Strube in the vicinity of Cincinnati. It is a *hard* soil, requiring more than 30 blows during a standard penetration test (Navfac, 1982), and it is relatively dense (bulk unit weight of 2268kg/m³ or 141.6 lb/ft³) compared with colluvial soil or alluvium.

The till is well-graded from particles of clay size to sand size or larger. Cobble- to boulder-sized rock fragments are common in field exposures, although they were absent from the sample used for the grain size analysis (Table 4.3; Fig. 4.6).

Results from tests of the Atterburg Limits plot above the A line and indicate that the till is a CL type soil, in the nomenclature of the Unified Soil Classification System (ASTM D2487).

BOREHOLES

Eleven boreholes were hydraulically fractured during the field test. Most borings are approximately 10 m from their neighbors (Fig. 4.1), except at the southern end of the site where a cluster of four borings are each 2.5 m from their nearest neighbor (Fig. 4.1).

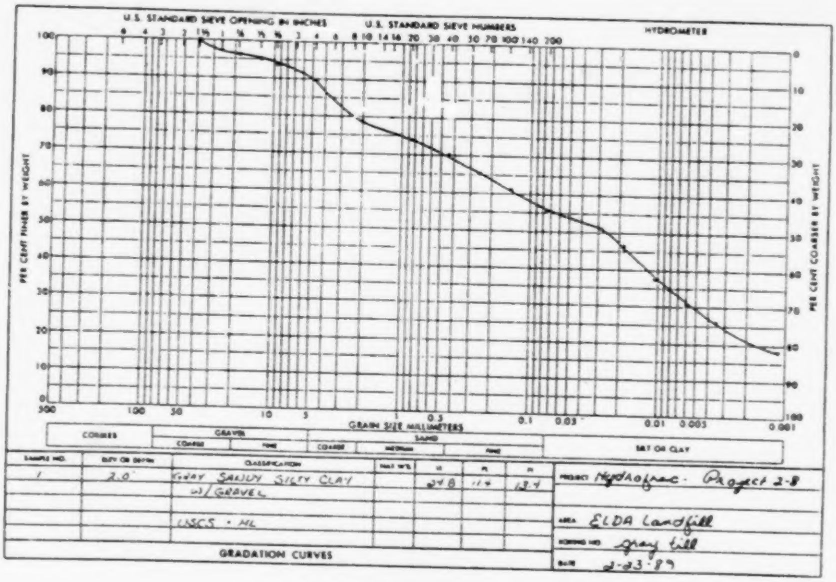

SAMPLE NO.	ELEV OR DEPTH	CLASSIFICATION	NAT W%	LL	PL	PI
1	2.0'	GRAY SANDY SILTY CLAY w/GRAVEL		24.8	11.4	13.4
		USCS - ML				

PROJECT Hydrofrac - Project 2-8
AREA ELDA Landfill
BORING NO. gray till
DATE 2-23-89

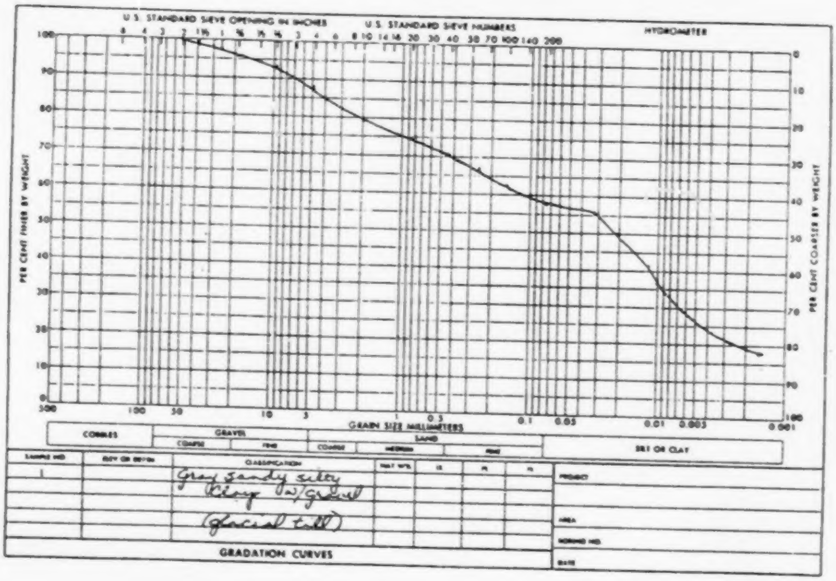

SAMPLE NO.	ELEV OR DEPTH	CLASSIFICATION	NAT W%	LL	PL	PI
1		Gray sandy silty Clay w/Gravel (glacial till)				

PROJECT
AREA
BORING NO.
DATE

Figure 4.6. Grain size distributions in samples of ELDA Till.

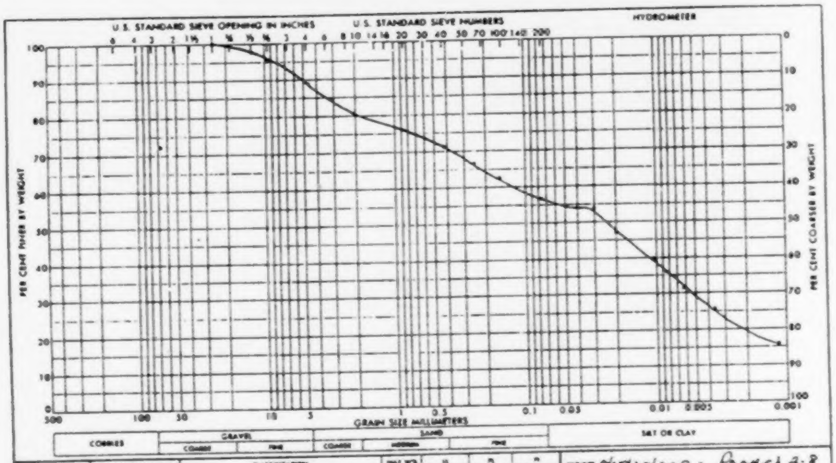

SAMPLE NO	ELEV OR DEPTH	CLASSIFICATION	NAT W%	LL	PL	PI
2	20'	GRAY SANDY SILTY CLAY W/GRAVEL USCS - ML		24.8	11.4	13.4

PROJECT Hydrofrac - Project 2-8

AREA ELDA Landfill

BORING NO gray till

DATE 2-23-89

GRADATION CURVES

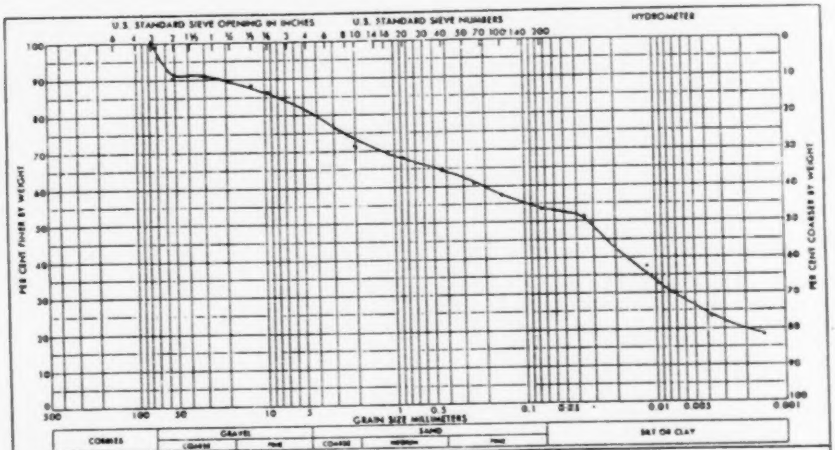

SAMPLE NO	ELEV OR DEPTH	CLASSIFICATION	NAT W%	LL	PL	PI
2	—	GRAY TILL				

PROJECT Hydrofracture

AREA

BORING NO

DATE

GRADATION CURVES

Depths to the bottom of casing ranged between 1.64 m and 1.95 m at nine of 11 boreholes. The other two boreholes were deeper; 2.72 m and 3.81 m (Table 4.1).

Design

Boreholes were designed for the purpose of creating hydraulic fractures. In general, a borehole consists of a steel tube cemented into a boring, and open at both ends (Fig. 4.7). A *basket* is fixed to the lower end of the casing to prevent cement from plugging the bottom of the borehole. The open boring extends several dm below the basket and is partly filled with fragments (cuttings) of till. A narrow *notch*, oriented normal to the axis of the borehole, is cut in the wall of the boring several cm below the bottom of the casing.

Roughly horizontal hydraulic fractures were expected to develop, and the boreholes were designed to nucleate a horizontal fracture at the notch. Although the expectations of horizontal hydraulic fractures were correct, most of the fractures initiated at or above the basket, not at the notch.

Specifications

Borings were made with a Marmon-Herrington drill rig using an auger 7.62 cm (3 in.) in diameter. The auger was pulled out of the hole after each 0.3 m (1foot) of drilling so that samples of the cuttings could be collected. Each boring required between 30 and 90 minutes to complete.

The borings were drilled several dm beyond the depth at which we intended to cut the notch because cuttings filled a zone several dm deep at the bottom of the hole. Tools to retrieve cuttings from the bottom of the hole were unavailable during drilling.

Notches were cut in the walls of the boring using a mechanical device. The device consisted of a talon-shaped blade (made from tool steel 0.3 cm thick) mounted on the bottom of a PVC tube which fit snugly into the boring. The blade was mounted on a rod attached to the inner wall and extending the full length of the tube.

To cut a notch, the blade was brought flush with the tube and the apparatus inserted into the boring until it rested on the top of cuttings at the bottom of the boring. The blade was then slightly extended by twisting the rod at the ground surface. The entire apparatus was rotated, cutting a shallow notch in the wall of the boring. Then the blade was extended further and the notch was deepened by continuing to rotate the apparatus.

When the operation was complete, the wall of the boring contained a notch 3.75 cm deep and 0.3 cm thick (Fig. 4.7). Notches of those dimensions were observed when the boreholes were excavated.

The boreholes were cased with steel tubing 3.75 cm in outer diameter and 3 mm in wall thickness (1 1/4" Nominal Schedule 80 steel pipe). The tubing was obtained at a local plumbing supply store.

Baskets were constructed of annular disks of 3/4" (nominal) plywood, plastic foam and fine steel mesh. Three foam disks were placed on the end of the casing, and a steel

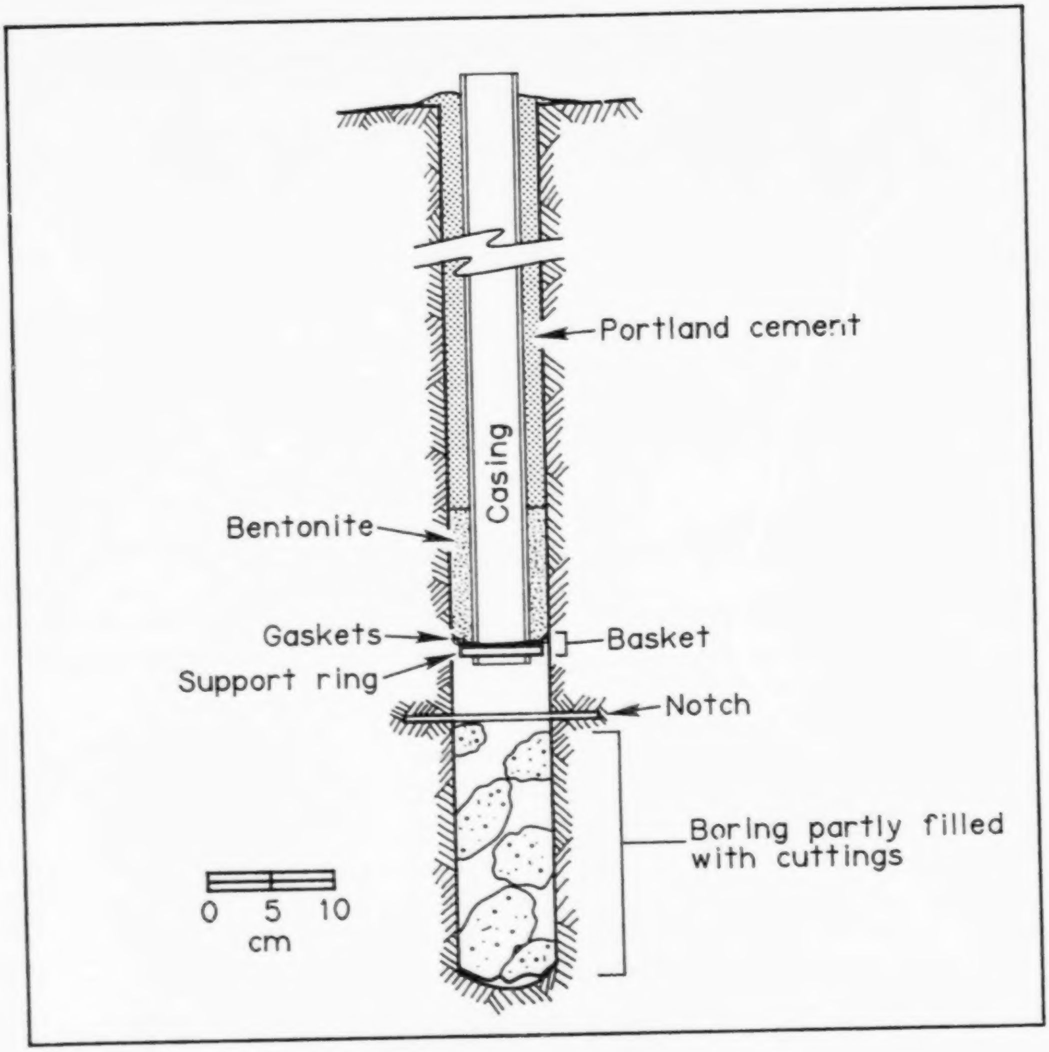
Casing
Portland cement
Bentonite
Gaskets
Basket
Support ring
Notch
Boring partly filled with cuttings
0 5 10
cm

Figure 4.7. A borehole used to create hydraulic fractures.

mesh disk placed beneath them. The outside diameter of those disks was 8 cm, slightly larger than the inside diameter of the boring. The plywood disk served as a support for the other disks. steel band was secured beneath the basket to prevent it from slipping off the end of the casing (Fig. 4.7).

When the casing and basket assembly was inserted into a boring, the plastic and steel disks were flush with the boring walls. Bentonite pellets were placed on top of the basket to seal the annulus between the casing and the wall of the boring. Portland cement, which contained an additive that inhibits shrinking, was poured in the annulus to secure the casing into the borehole. The result was a cemented casing whose lower end was open to the till.

METHOD OF FRACTURING

Hydraulic fractures were created by workers from Halliburton Services, a company specializing in creating hydraulic fractures for the petoleum industry. Most of the methods used during the test are similar to methods used in the hydraulic fracturing of oil wells. We modified the methods slightly, however, because of the shallow depths of the boreholes.

Equipment

The fracturing equipment was mounted on five vehicles: a truck containing a blender and a positive displacement pump, two trucks containing sand, a truck containing water, and a van containing monitoring and control equipment.

Three pumps were used in the operation: a Triplex positive displacement pump, and two centrifugal pumps, one upstream and one downstream from the blender. The positive displacement pump can generate a maximum of 41,000 kPa (6000 psi), whereas the centrifugal pumps can produce a maximum of between 400 and 550 kPa (60 and 80 psi) and flow rates of 2.4 to 2.8 m^3/min (630 to 750 gals/min).

The Injection Fluid

Sand and several chemicals were added to water in the blender to improve the performance of the fracturing operation. To increase the viscosity of the fluid, we added a guar gum base gel at a concentration of 2.5kg/m^3 (0.025 lbs/gal), and a cross-linking chemical at a concentration of 0.05kg/m^3 (0.0005 lbs/gal). A buffer was used to reduce the pH of the fracturing fluid to between four and five, which is optimal for use of the gel.

The guar gum gel increases the viscosity of the water from 1 to 15 cP. The cross-linking chemical causes the gel to become thixotropic, with an apparent viscosity of 100 to 200 cP and an apparent shear strength of roughly 25 Pa, according to laboratory tests conducted with a rotational viscometer. The high viscosity and shear strength of the gel facilitates the transport of sand into the fracture. Typically, another chemical is blended into the fluid to cause the gel to break down several hours after injection. The breaking chemical improves removal of gel, greatly increasing the permeability of the propped fracture.

Potassium chloride was added to the fluid at a concentration of three percent by weight. The KCl is an additive that is used routinely to inhibit the swelling of clay minerals in hydraulic fractures created by the oil industry. In addition, this material increases the electrical conductivity of the fluid and was used to improve the resolution of fractures by electrical geophysical techniques.

Dye was added to the fluid to stain the fracture surfaces and make them easier to identify during excavation. Three types of dye were tested during the experiment: rhodamine, fluorescein, and fluorescent orange paint pigment. Dye was mixed at a concentration of 1:500 in the first few fractures but it was more dilute (1:1000 to 1:2000) in the last few fractures.

Ottawa sand was mixed with the fracturing fluid to prop open the fractures. Two different sizes of sand, very coarse-grained, 12/20 mesh, and medium-grained, 20/40 mesh, were used. Concentrations of sand ranged from 9% to 18% by volume (2 to 4 lbs. sand/gal. fluid).

The Fracturing Procedure

During routine fracturing operations of oil wells, water is pumped from the water truck and mixed with sand and chemicals in the blender. A centrifugal pump pulls the mixture of water, sand and chemicals from the blender and creates input head for the positive displacement pump. Injection into the borehole is accomplished using the positive displacement pump. Flow rates and injection pressures are monitored in the van.

During our tests, the procedure differed slightly from above in that we used the centrifugal pump at the downstream end of the blender to inject fluid into the borehole. The positive displacement pump was used intermittently, when pressures in excess of 550 kPa (80 psi) were required to initiate fracturing.

The fracturing procedure began by filling the casing with water, so the initial fracture would be created with water rather than gel. Pipes were connected from the borehole to the trucks containing the fracturing equipment, which were parked on the northeastern edge of the site (Fig. 4.1).

Injection using the centrifugal pump caused pressures measured at the borehole to increase to between 400 and 550 kPa (60 and 80 psi) within several minutes. In some cases, a fracture was created soon after the pressure reached 60 to 80 psi, but in other cases 5 to 10 minutes were required before fracturing. Injection pressure was increased using the positive displacement pump if a fracture was not created after approximately 10 minutes. Injection pressures of as great as 820 kPa (120 psi) were required to initiate fracturing at some boreholes (Table 4.4).

The onset of fracturing was determined by an abrupt decrease in the injection pressure. Injection pressures decreased to between 69 and 275 kPa (10 and 40 psi) during the propagation of most of the fractures (Table 4.4). Records of the pressures and volumes as functions of time are presented in the Appendix.

Injection was terminated at the shallow boreholes when fluid vented to the ground surface, and at the deeper boreholes injection was terminated after a predetermined volume of injection. Each fracture was created in less then ten minutes. The pipes extending from the pump truck to the borehole was uncoupled at the borehole immediately after termination of injection. Roughly 100 liters (several tens of gallons) of injection fluid flowed back out of the fracture into the borehole and onto the ground following uncoupling.

Flow rates of between 0.075 and 0.42 m^3/min (20 and 90 gal/min) were used to create the fractures. In general, the flow rate was low during peak pressure and increased as the pressure decreased and the fracture began to grow. Details of the history of flow rates, however, are poorly known because the flow meter used by Halliburton Services was often clogged with sand and non-functional. Clogging apparently occurred because the flow rates that were used were less than those designed to be measured by the meter.

The total volumes of fluid and sand pumped out of the blender were estimated by the operator of the pump truck. Typically the fractures required 0.38 to 0.76 m^3 (100 to 200 gals) of fluid, but the volume ranged from as little as 0.076 m^3 to as much as 1.51 m^3.

The volume of sand pumped to the fractures was typically 0.056 to 0.14 m^3 (2 to 5 ft^3), but it ranged from less than 0.03 to as much as 0.85 m^3 (30 ft^3). These estimates are greater than the volume contained in fractures because they do not account for material that remained in the pipes after fracturing, or that flowed out during venting.

TABLE: 4.4. SUMMARY OF DATA FROM FIELD TESTS

Id	FLUID			SAND		PRESSURE		
	Volume		Dye	Volume	Gr.Size	Max.		Propagation
	m^3	(gal)		m^3		kPa	(psi)	kPa
13	1.51	(400)	rh	0.28-0.42	20/40	620	(90)	140-340
11	0.11	(30)	rh	0.057	20/40	340	(50)	140
12	0.45	(120)	rh	0.08-0.14	20/40	410	(60)	140
2	0.46	(110)	rh	0.85	12/20	410	(60)	140-280
10	0.57	(150)	rh	0.22-0.24	12/20	410	(60)	340
4	0.57	(150)	fo+fl	0.17-0.22	12/20	760	(110)	480
9	0.76	(200)	fo+fl	0.08-0.14	20/40	820	(120)	200-275
5	0.76	(20)	fo	0.03-0.08	20/40	410	(60)	410
8	0	(0)	fo	0	20/40	3700	(540)	--
7	0.38	(10)	fo	0.03-0.08	20/40	550	(80)	550
6	0.57	(150)	fo+fl	0.14	20/40	550	(80)	200

rh: rhodamine red
fo: fluorescent orange pigment
fl: fluorescein

Shown in the order in which the fractures were created.

The amount of sand observed in some of the fractures was much less than the amount pumped from the blender. For example, 0.122 m^3 (4.2 ft^3) of sand filled the fracture at borehole 13 (details of this calculation are described in Section 6), but 0.28 to 0.42 m^3 (10 to 15 ft^3) were pumped from the blender. Approximately 0.1 m^3 of the missing sand is inferred to have been deposited in pipes extending from the pump truck to the boring, and roughly 0.05 m^3 flowed out of the fracture during venting.

Hydraulic fracturing was attempted at eleven boreholes, and fractures were successfully created at ten of those boreholes. Hydraulic fracturing did not occur at borehole 8. Two attempts were made to fracture borehole 8; during the first injection pressures reached 1720 kPa (250 psi), and during the second injection pressures reached a maximum of 3700 kPa (540 psi). Following both attempts, we discovered plugs of sand several dm from the bottom of the casing that presumably blocked the injection fluid. The cause of the sand blockage is unclear. One explanation is that the gel in the injection fluid broke down and was unable to adequately transport sand. The flow of the gel is sensitive to heat and could have been affected by the ambient temperature (which was 38 °C on the day of the test), according to Mark Roberts, field engineer with Halliburton Services.

Shortcomings of the Equipment

Shortcomings of the hydraulic fracturing equipment used during the test are all related to scale: the equipment was designed to create fractures one to several orders of magnitude larger than the ones we created. As a result sensing devices such as flow meters and pressure transducers used by Halliburton were unable to accurately measure the low flow rates and pressures of the test.

The blending system was unable to consistently deliver a quality mixture of injection fluid at the relatively low volumes required. This resulted in variations in fluid properties between fractures, according to observations of the fluid flowing back out of fractures. In some cases, especially during the last several fractures, the viscosity of the injection fluid was low and this could have been partly responsible for sand settling out before reaching the subsurface.

The fracturing equipment was practically immobile, so pipes as long as 50 m were used to connect the injection pump to the boreholes. The volume of the long pipes was on the same order as the volume of the fractures, which reduced the control of the fracturing process. Moreover, in many cases it appeared that sand settled in the pipes before reaching the fracture.

The team from Halliburton Services made every effort to adapt their equipment to the highly atypical conditions of our tests. The shortcomings cited above in no way reflect the manner in which the equipment was operated. The shortcomings do indicate, however, that conventional equipment used to create hydraulic fractures at oil wells will be too large to create hydraulic fractures of the size used during this test. Future applications would benefit from equipment designed for the pressures, flow rates, and volumes required to create and prop open hydraulic fractures at shallow depths (tens of meters).

SECTION FIVE

HYDRAULIC FRACTURES CREATED DURING THE FIELD TEST--1988

These two observations, 1) an abrupt decrease in the pressure of the injection fluid, and 2) venting of the fluid several m or more from the point of injection, were critical because they are strong evidence that hydraulic fracturing of soil occurred during the field test. There was little information at the time of the test, however, about fracture geometry, that is the size, shape, orientation, location, and thickness of the fractures. Those parameters largely control how the fracture will affect the recovery of ground water, and so they are of fundamental importance to the goals of this research.

The geometries of the fractures were determined by excavation and mapping. The day after the fractures were created, we mapped the locations of the vents and prepared to excavate the vicinity of each borehole. Two days later a backhoe was rented and brought to the site to begin excavation. The strategy used during excavation was to first cut a trench from the vent to the parent borehole. The fracture was identified at the vent and traced along the trench during excavation. The trench was extended beyond the borehole until the fracture could no longer be identified in the trench walls. Then another trench was cut perpendicular to the first one. Subsequent trenches were placed to intercept the fracture at critical locations based on existing exposures.

The locations of trenches were selected to give the maximum amount of information on the forms of the fractures, while keeping the amount of excavation to a minimum. In general, the technique was successful, but in a few cases (boreholes 2, 4, and 9) the fractures could not be identified during excavation, so a full array of trenches was not completed. Careful investigation following excavation did reveal the locations of fractures at borehole 9, but the backhoe was no longer available to complete excavation.

Two boreholes that were incompletely excavated (2 and 4) were several meters deeper than the others and they lacked a vent from which to start excavation. We discovered a fracture adjacent to borehole 2, but the fracture was poorly developed so excavation was discontinued. At borehole 4, the maximum depth that could be reached by the backhoe was 0.3 m above the bottom of the casing. Monitoring techniques indicated that a fracture developed at borehole 4, but after considerable effort we were unable to locate the fracture.

Traces of fractures on the walls of the trenches were identified and marked with brightly-colored flagging. Many of the fractures lacked sand and could be identified only after detailed excavation revealed traces of dye staining.

The appearance of the fractures on the walls of the trenches depended on the material filling them. Where fractures were filled with sand, they appeared as thin white layers in the grey till. Gel mixed with the fracturing fluid allowed some hydraulic fractures to be identified because the gel appeared as a mucous-like or rubbery film on the fracture surfaces. Many of the fractures lacked sand or gel and could be identified only by trace amounts of dye on the fracture surfaces. Rhodamine was the most effective dye, staining fracture surfaces deep purple (a color that was readily distinguished from natural iron oxide stain, which is dark red).

Fluorescent paint pigment yielded satisfactory results, although the distribution of the pigment was less uniform than the distribution of the rhodamine stain. The paint pigment fluoresced and could be detected in the field using a UV lamp. However, the UV lamp was not used routinely to detect the dye because the florescence could only be detected when the trenches were covered with a tarp to reduce ambient lighting. Both of those dyes effectively stained fracture surfaces when mixed with injection fluid at concentrations of roughly 1:500, and they could be detected on fracture surfaces at concentrations of 1:1000 to 1:2000. Fluorescein dye was ineffective at staining the surfaces of fractures, even though it resulted in a strongly-colored injection fluid.

FORMS OF THE HYDRAULIC FRACTURES

Hydraulic fractures were created at shallow depths so that they could be excavated and mapped in detail. The purpose of the excavation and mapping was to determine physical characteristics of the fractures, such as their size, shape, orientation, and thickness. This information is necessary to the design of hydraulic fractures in remedial actions, to infer processes of fracturing, and to highlight features of the fractures that are undesirable. Identifying the undesirable features will allow us to develop techniques that will inhibit their formation.

The geometry of each hydraulic fracture, that is its size, shape and orientation, was determined by mapping exposures of the traces of the fractures on the walls of trenches. Sections obtained from the trench walls were compiled into maps showing the surface of the fracture in plan.

The sections were made by measuring the location of the fracture traces relative to a horizontal datum, which was constructed by positioning fine string with a hand level and securing it to the trench wall. The location of a fracture trace could be mapped to within a few cm using this technique. Sections were mapped at a scale of 1:12 and reduced to the sizes shown in the following pages. The locations of most of the fracture traces are accurate to within one line width on the following sections.

The fractures shown in the following maps and sections represent exposures that could be confirmed because they contained sand, dye, or gel. The concentration of those materials decreased as the leading edge of a fracture was approached, and we determined the leading edge as the last exposure of injected material. Commonly, however, an unfilled fracture extended several dm or more ahead of the point that was mapped as the leading edge. The unfilled fractures probably were caused by hydraulic fracturing, but they were omitted from the sections because their origin was uncertain.

The forms of each of the hydraulic fractures will be described in the following pages. An idealized form has been inferred from the descriptions and will be presented at the end of this section.

Borehole Four

A hydraulic fracture could not be identified in two trenches cut adjacent to borehole Four. Monitoring of injection pressure and surface tilts indicates that a hydraulic fracture was formed, but we were unable to excavate deep enough to reach it.

Borehole Five

A hydraulic fracture occurs on the northern side of borehole five (the fracture will be referred to as HF5). In general, the fracture is continuous in the vicinity of the borehole, and it splits into two lobes several m north of the borehole (Fig. 5.1). One lobe vented on the northwestern side, and the other remained in the subsurface on the northeastern side of the borehole (Fig. 5.1).

The northwestern lobe is shaped like a trough that plunges 20° to 30° toward the borehole (Figs. 5.1 and 5.2). Each side of the trough is roughly planar and the sides differ in strike by 135°. The sides of the trough split near the ground surface, and they vent as separate fractures striking roughly tangential to the major axis of the fracture. As the hydraulic fracture approaches the ground surface it flattens for several dm, and then curves abruptly upward one dm below the ground surface. The fracture is nearly vertical where it intersects the ground surface at the point of venting (Fig. 5.2).

The northeastern lobe of HF5 splits from the northwestern lobe roughly 1.5 m north of the borehole. The dip of the northwestern lobe is slightly greater than that of the northeastern lobe, so that the northwestern lobe climbs above its neighbor with increasing distance from the borehole. In plan view, the two lobes are separated by unfractured ground; no overlap was observed (Fig. 5.1).

A vertical fracture striking N62E cuts the host till adjacent to the open interval and the bentonite-filled zone of the borehole. At 15 cm above the bottom of the casing (adjacent to the bentonite), the dip of the fracture flattens abruptly over several cm. Within 20 cm of the bottom of the casing, the fracture dips 25° to the south, and this dip is typical of most of the fracture. The vertical fracture is apparently unrelated to the notch at borehole five.

Borehole Six

Hydraulic fracture six resembles HF5 in that it consists of a steeply dipping fracture adjacent to the borehole, a zone that is flat-lying in the vicinity of the borehole, and several shallowly dipping lobes (Fig. 5.1). The vertical fracture is relatively large compared with HF5; it is at least one m in length and it extends upward from the notch to a height of 1.25 m (Figs. 5.1, 5.2 and 5.3). The strike of the vertical fracture is N23W, nearly perpendicular to that of the vertical fracture at HF5.

The hydraulic fracture is nearly flat-lying within approximately two m of the borehole, a distance that is similar to the depth of initiation of the fracture. At a

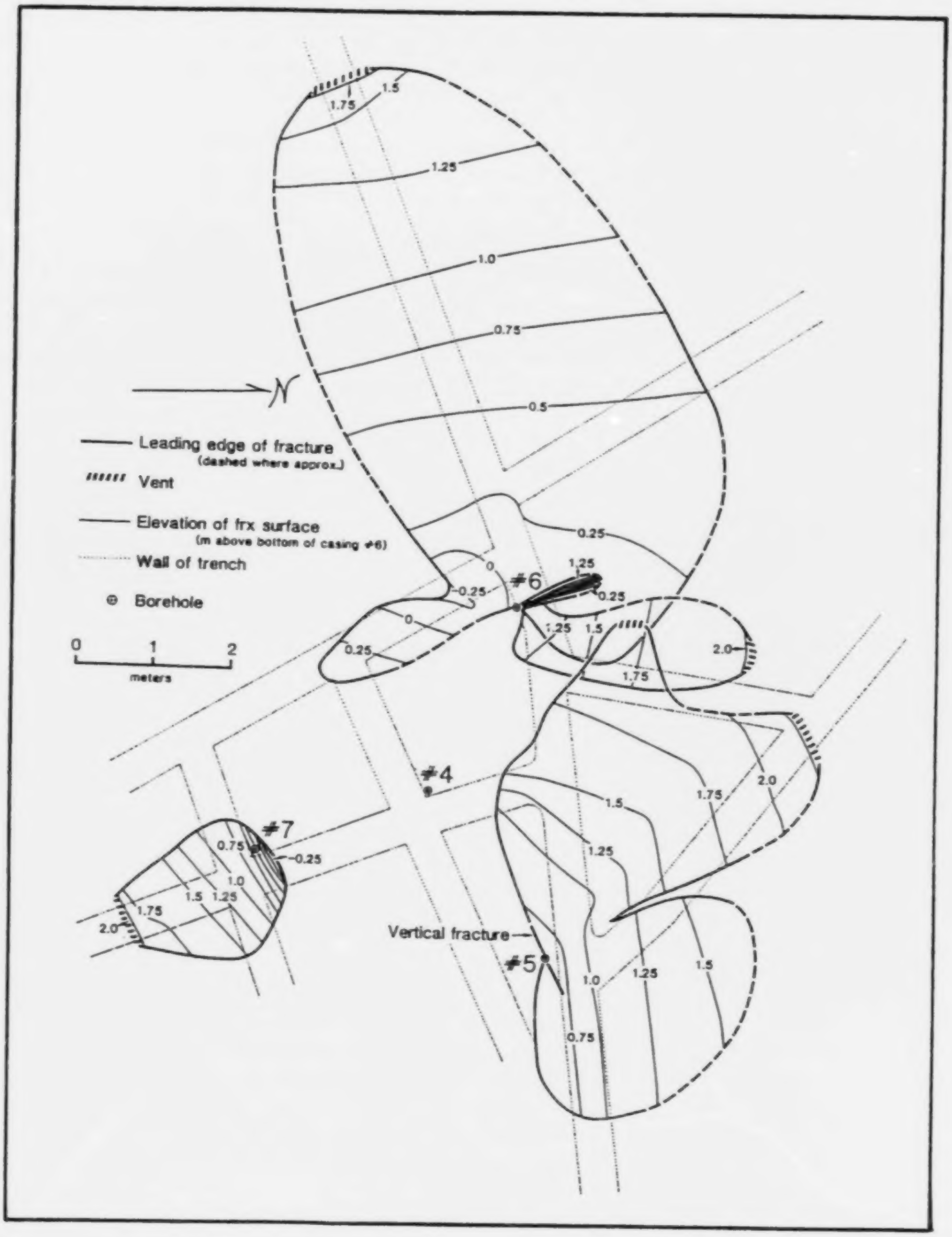
N
Leading edge of fracture (dashed where approx.)
Vent
Elevation of frx surface (m above bottom of casing #6)
Wall of trench
Borehole
0 1 2
meters
#6
#4
#7
#5
Vertical fracture
1.75
1.5
1.25
1.0
0.75
0.5
0.25
0
-0.25
2.0

Figure 5.1. Hydraulic fractures HF5, HF6, and HF7. Structural contours are on the fracture surfaces.

distance of one to two meters from the borehole, the fracture changes orientation abruptly, curving upward to dip shallowly toward the borehole (Fig. 5.2).

A large fracture lobe extends south of the borehole to a vent roughly 8 m to the WSW. This lobe is roughly planar in form and dips toward the borehole at 14° (Figs 5.2 and 5.3). In plan, the large lobe is elongate with an aspect ratio of roughly 2:1. The borehole is near the end of the long axis of the lobe (Fig. 5.1).

The fracture trace along the major axis of the large lobe is, in general, straight from where the fracture begins to turn upward to the vent. In detail, however, the fracture is gently-stepped, consisting of riser intervals that are 20 to 40° steeper than the average dip of the fracture. The riser intervals are a dm or less in length and they are spaced roughly one m apart along the fracture. Till cut by the fracture was studied carefully for variations in texture or composition that could be related to the location of risers, but no such variations were found. The step-like form of the trace appears to be unrelated to variations in till detectable in hand sample.

Two smaller lobes were identified; one of them is at the same elevation as the large lobe and extends to the SSE, whereas the other is 1.5 m above the large lobe and extends to the north where it vents roughly three m from the borehole (Fig. 5.1).

The upper, northern lobe apparently is connected to the vertical fracture in the vicinity of borehole. There are several isolated fracture segments a few dm in length exposed between the lobe and the vertical (Fig. 5.2), but apparently a direct connection of the upper lobe and the vertical fracture was removed during excavation.

The vent at the large lobe resembles the vents at HF5 in that the fracture trace flattens (Fig. 5.3) and then turns abruptly upward when it is within one dm of the ground surface (Figs. 5.2 and 5.3). The strike of the fracture at the vent is sub-parallel to the strike of the vertical fracture at the borehole.

The vent at the smaller, northern lobe of HF6 resembles the other vents, but the fracture flattens at an unusually shallow depth of 3 to 8 cm. The fracture cuts beneath the ground surface at this shallow depth for 0.5 m before turning upward and venting.

Borehole Seven

Hydraulic fracture seven is the smallest observed during excavation. The fracture is steeply dipping adjacent to the borehole and it flattens gradually with increasing distance from the borehole (Fig. 5.4). The dip of the fracture decreases to 25° toward the borehole roughly at 0.5 m from the vent. The average dip of HF7 was greater than the other fractures because the transition from vertical to gently-dipping fracture was relatively gradual. This behavior is important because it shows that HF7 intersected the ground surface after growing a small distance from the parent borehole, compared with the lengths other fractures (Figs. 5.1 and 5.4).

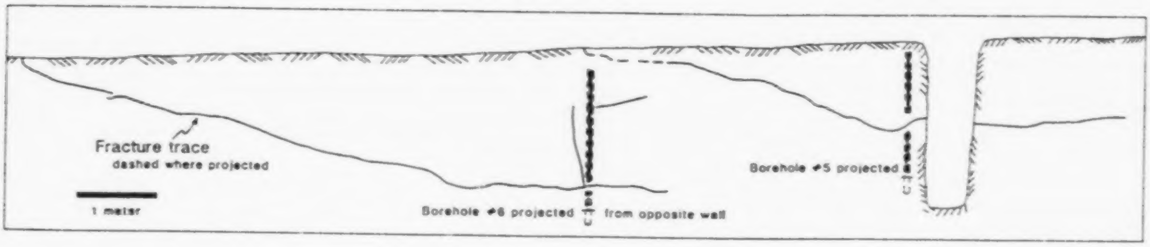
Fracture trace
dashed where projected
1 meter
Borehole #6 projected from opposite wall
Borehole #5 projected

Figure 5.2. Trace of hydraulic fractures HF5 and HF6 on the northern wall of the longest east-west-trending trench shown in Figure 5.1. Boreholes are projected onto the section.

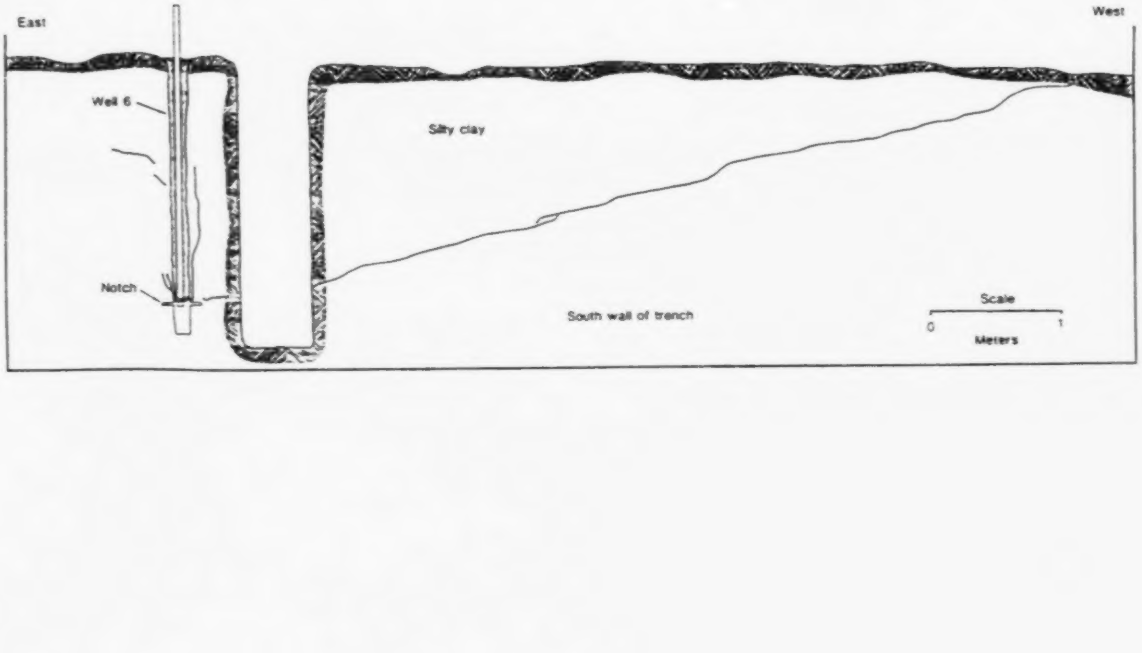
East
West
Well 6
Silty clay
Notch
South wall of trench
Scale
0
1
Meters

Figure 5.3. Trace of hydraulic fracture HF6 on the southern wall of the same trench as in Figure 5.2.

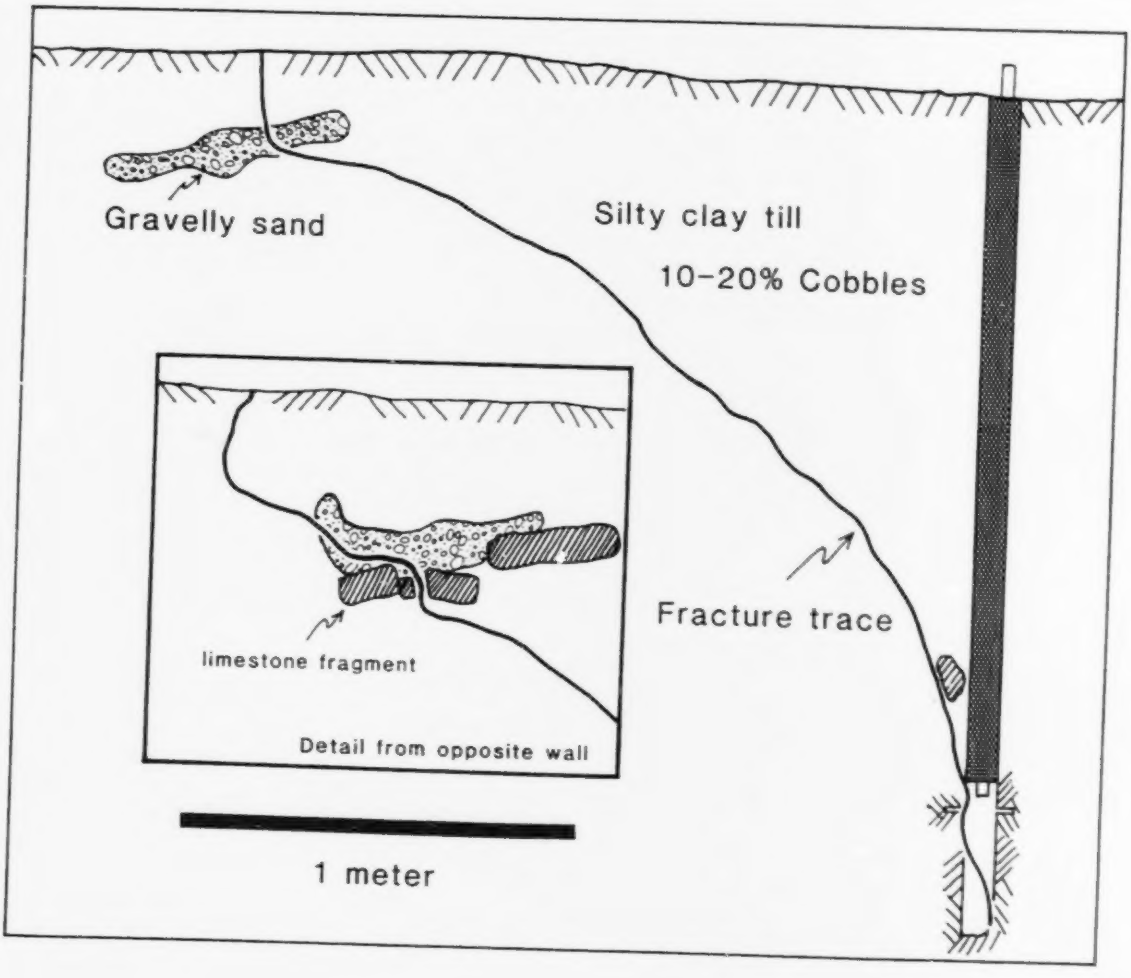
Gravelly sand
Silty clay till
10-20% Cobbles
Fracture trace
limestone fragment
Detail from opposite wall
1 meter

Figure 5.4. Trace of hydraulic fracture HF7 on the western wall of the trench cut along the major axis of the fracture. The section was made prior to excavating the tranverse trench shown in Figure 5.1.

In other respects, HF7 resembles the other fractures. The steeply dipping part of HF7 cuts the open zone below the basket and contains the axis of the boring. It is apparently unrelated to the notch. In plan view, the fracture is slightly elongate, with an aspect ratio of 1.5:1. The borehole is at the end of the long axis (Fig. 5.1). The vent at HF7 is typical: the fracture flattens as it approaches the ground surface, reaches a depth of 0.2 m and cuts abruptly upward venting as a vertical fracture nearly 1 m in length and striking parallel to the vertical fracture at the borehole.

A lens of gravelly-sand and limestone fragments is cut by HF7. The fracture cuts beneath one limestone fragment, upward through a narrow space between neighboring fragments, and then flattens, assuming roughly the path it was taking before reaching the fragments. Limestone fragments appeared to affect the path of the fracture only locally.

Borehole Nine

The form of HF9 resembles the large lobe at HF6 in that it is roughly elongate, and the parent borehole is near one end of the major axis (the northeastern boundary of the fracture was not excavated and is inferred). The fracture is flat-lying in the vicinity of the borehole, but most of the fracture dips shallowly (17°) to the southeast toward the borehole (Figs. 5.5 and 5.6).

The fracture trace from borehole to vent along the major axis of HF9 is nearly straight, marked only by gentle steps spaced roughly 1 m from each other (Fig. 5.6). The trace resembles those of HF5 and HF6 (Fig. 5.2 and 5.3).

A vertical fracture cuts upward from the notch to the basket of HF9. At the basket, the vertical fracture flattens abruptly, rolling over and becoming flat-lying in the vicinity of the borehole. The exposures of the vertical fracture are marked in Figure 5.6, but the size of the fracture was impossible to determine because the edges were removed during excavation. The vertical fracture strikes N63W, which is at a high angle to the strike of the fracture at the vent.

Borehole 10

The hydraulic fractures at borehole 10 consists of two lobes extending from the borehole in opposite directions, to the northeast and southwest. The two lobes meet at a vertical fracture intersecting the borehole. The vertical fracture is roughly 2 m along strike and 1 m in height, which is similar in size to vertical fractures at HF6 and HF7. The lobes dip between 20 and 25° toward the borehole and are roughly planar (Fig. 5.7).

Vents occur at three locations, two on the southwestern lobe and one on the northeastern lobe. At the vents, the strikes of the fractures are roughly parallel to the vertical fracture intersecting the borehole (Fig. 5.7).

The northeastern lobe cuts across a hydraulic fracture created from borehole 11 (Fig. 5.7), which was created prior to HF10. The line of intersection of the two fracture planes was shallow, so it was excavated by hand and studied carefully. We

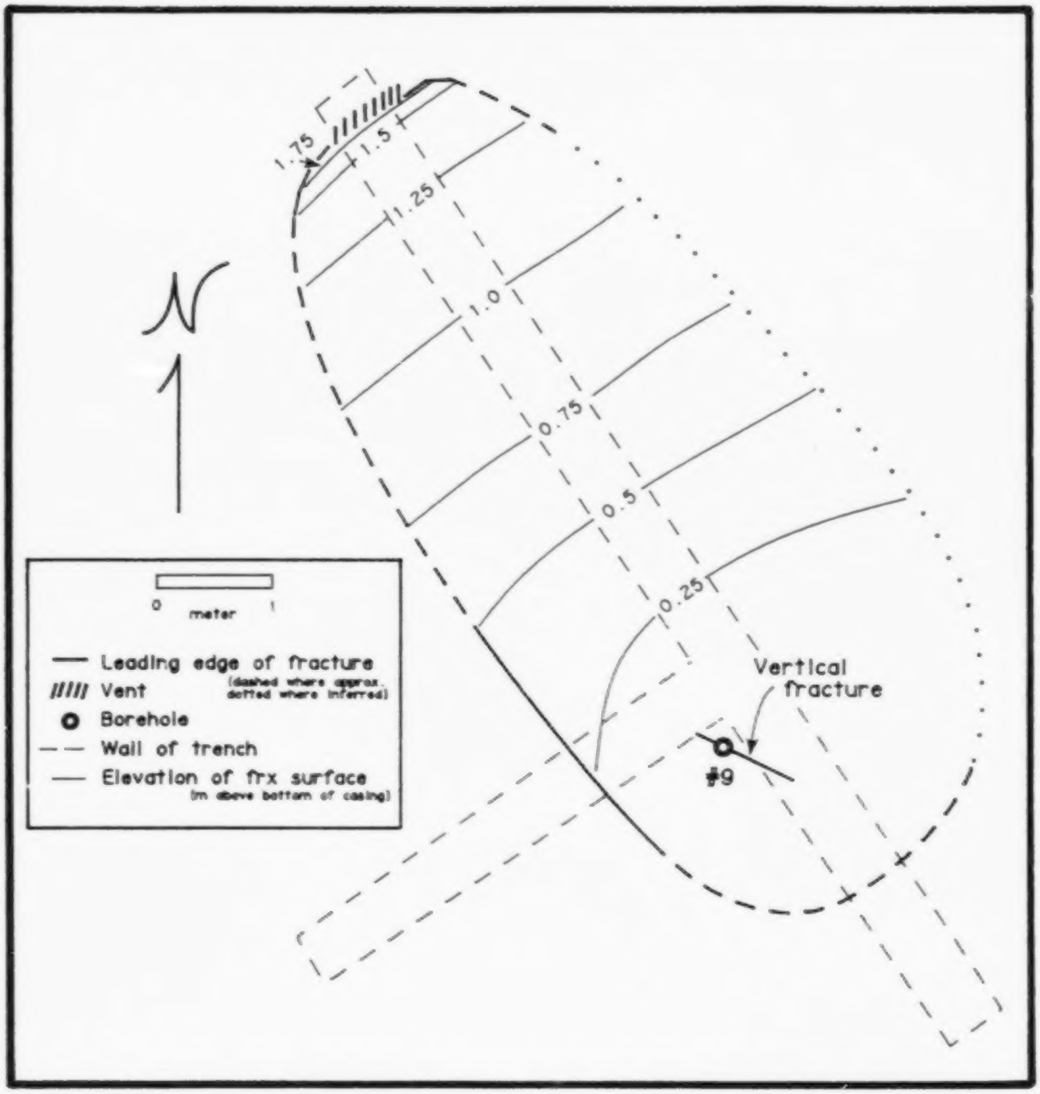
N
1.75
1.5
1.25
1.0
0.75
0.5
0.25
Vertical fracture
#9
0
meter
1
Leading edge of fracture
(dashed where approx. dotted where inferred)
Vent
Borehole
Wall of trench
Elevation of frx surface
(m above bottom of casing)

Figure 5.5. Hydraulic fracture HF9. Structural contours are on fracture surfaces. The northeastern edge of the hydraulic fracture was fracture was covered and has been inferred.

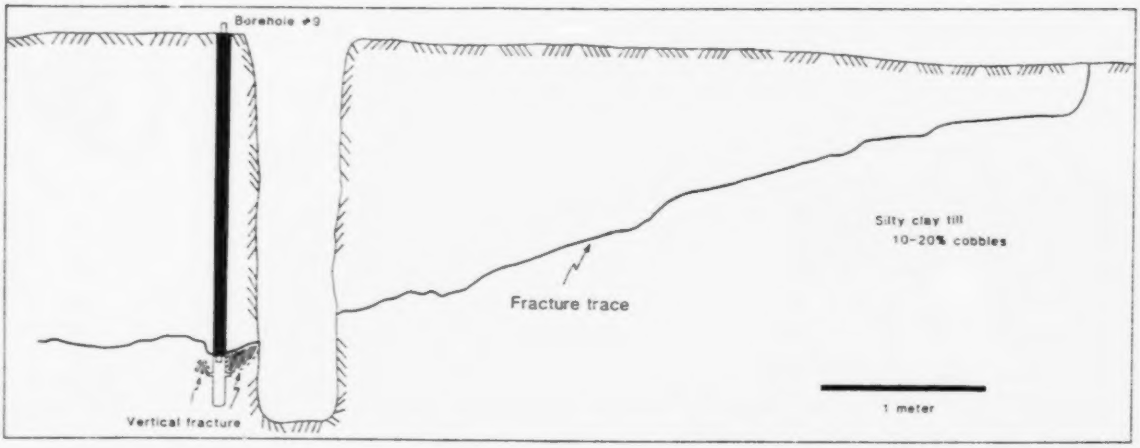
Borehole #9
Silty clay till
10-20% cobbles
Fracture trace
Vertical fracture
1 meter

Figure 5.6. Trace of hydraulic fracture HF9 on the southwestern side of the trench that cuts the major axis of the fracture.

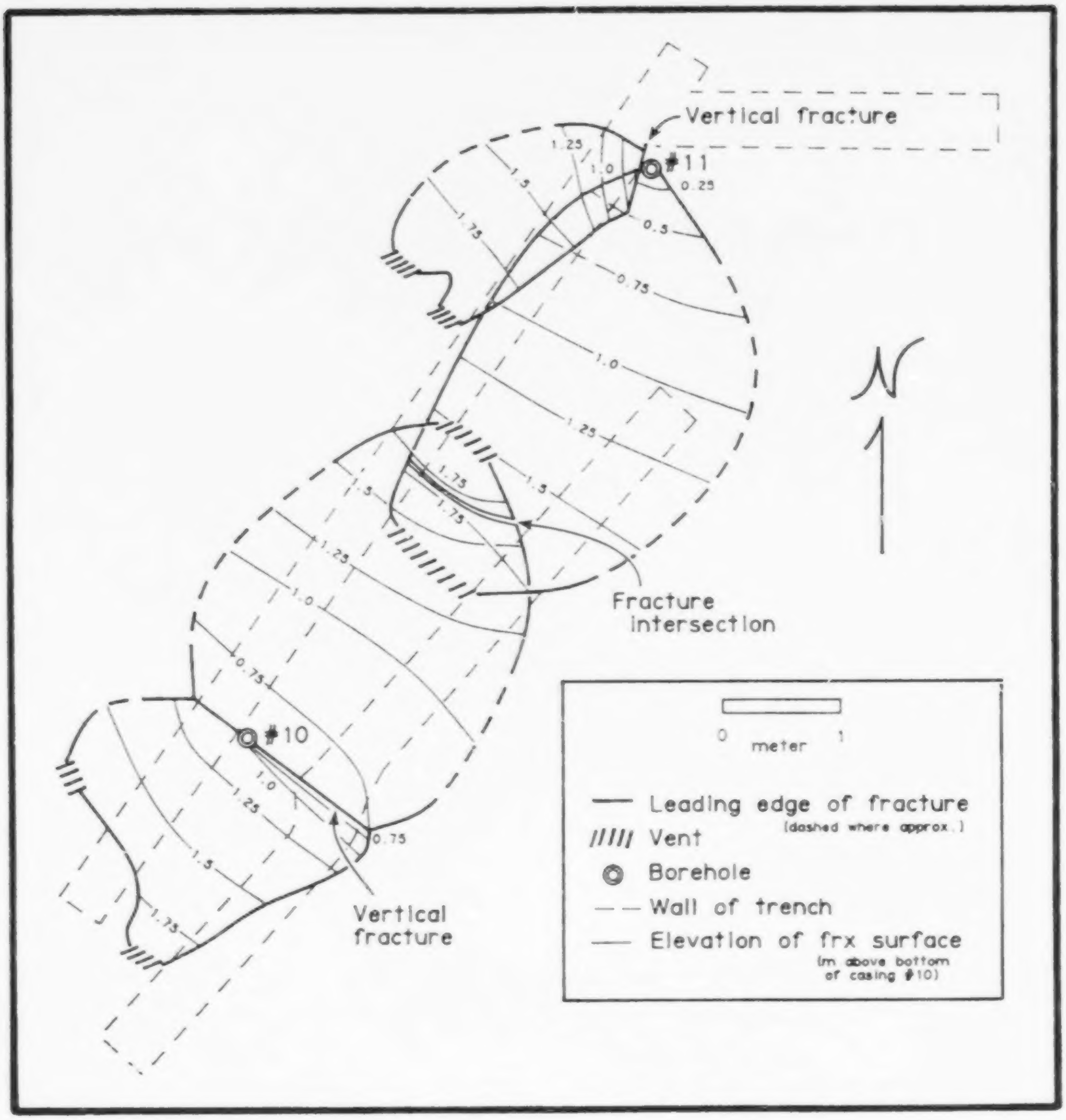
Vertical fracture
#11
1.25
1.0
0.25
1.5
0.5
1.75
0.75
1.0
1.25
1.75
1.5
1.75
1.5
1.25
1.0
0.75
#10
1.0
1.25
0.75
1.5
1.75
Fracture intersection
Vertical fracture
N
0 meter 1
Leading edge of fracture (dashed where approx.)
Vent
Borehole
Wall of trench
Elevation of frx surface (m above bottom of casing #10)

Figure 5.7. Hydraulic fractures HF10 and HF11.

could find no indication that the presence of the earlier fracture (HF11) affected the shape, size, distribution of sand, or any other characteristic of HF10.

Borehole 11

The hydraulic fracture at borehole 11 consists of a main lobe extending to the southwest, and a smaller lobe that lies above and to the west of the main one. The main lobe is slightly elongate in plan with an aspect ratio of 1.5:1. The borehole is at the end of the long axis (Fig. 5.7). The fracture surface is roughly planar, dipping 20° toward the borehole. The main lobe cuts the borehole adjacent to the basket, 0.1 m above the notch.

A vertical fracture occurs at the borehole and extends to the SSW. The bottom of the fracture lies on the notch, and it cuts upward through the main lobe. The vertical fracture breaks into segments above the main lobe, but it appears to be connected to the smaller lobe. The connection was removed during excavation.

The strike of the vertical fracture is at a high angle to that of the vents. Although this relationship between strikes was observed at HF9, it is atypical. It is possible, however, that vertical fractures oriented parallel to vents were present at HF9 and HF11 because the excavations would have removed fractures of that orientation at those boreholes.

Borehole 12

The form of HF12 resembles a plunging trough (Fig. 5.8) formed by two crudely planar sides and a narrow zone that curves sharply. Both sides of the trough dip shallowly toward the borehole, and the strikes of the sides differ by 60°. The northwestern lobe of HF5 also has a trough-like form, but the angle between the sides at HF5 is more shallow than it is at HF12.

The excavation of HF12 was unusual because the easternmost trench cuts roughly parallel to the leading edge of the fracture--other trenches cut the leading edges of fractures at high angles. Exposures in that trench show six lobes fringing the edge of the fracture. The orientation of the lobes could be determined in a few locations at which the lines of their major axes intersected the parent borehole. The lobes range from several dm to 1 m in width and they appear to be longer than they are wide.

The contact between till Units 2 and 3 occurs roughly 0.5 m below the ground surface at HF12. The fracture initiates in massive silty clay of Unit 3 and cuts across the contact into beds of gravelly sand and silt in Unit 2 (Fig. 5.9). The geology exposed on the east wall of the long trench cutting HF12 was mapped in detail to examine the relationship between bedding and the form of the fracture.

The plunge of the trace of the fracture flattens slightly over a meter-long interval where HF12 cuts across the upper surface of a bed of gravelly sand slightly east of the center of the section shown in Figure 5.9. Bedding is irregular, however, and the fracture cuts partly through the gravelly sand and partly through the

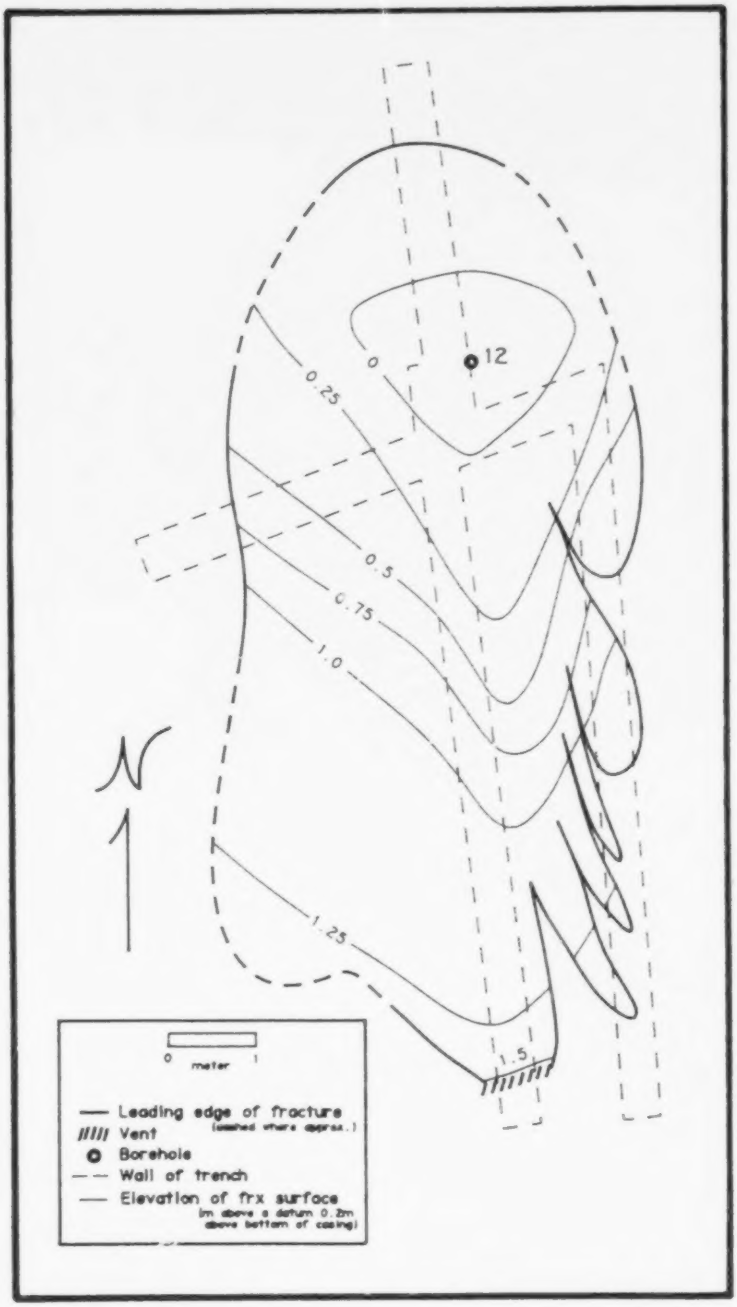
12
0
0.25
0.5
0.75
1.0
1.25
1.5
N
0
meter
1
Leading edge of fracture (dashed where approx.)
Vent
Borehole
Wall of trench
Elevation of frx surface (m above a datum 0.2m above bottom of casing)

Figure 5.8. Hydraulic fracture HF12. Lobes inferred from discontinuous exposures of the fracture on the walls of the trench.

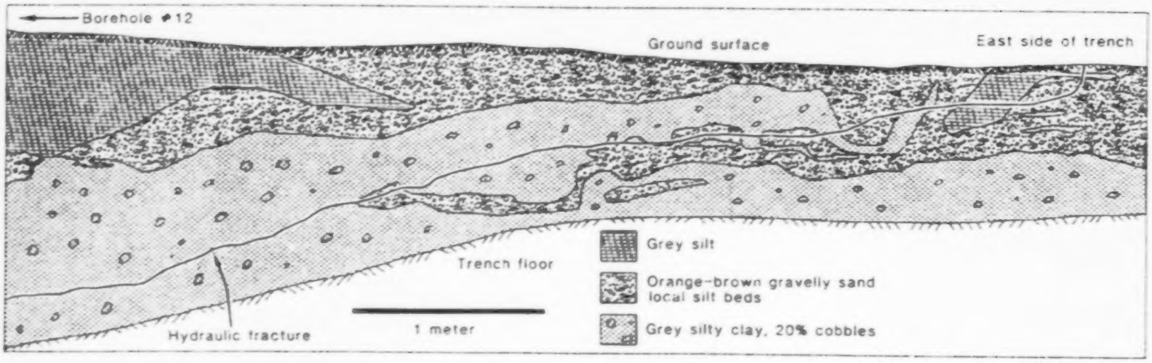
Borehole #12
Ground surface
East side of trench
Trench floor
Hydraulic fracture
1 meter
Grey silt
Orange-brown gravelly sand local silt beds
Grey silty clay, 20% cobbles

Figure 5.9. Geology and trace of hydraulic fracture on the eastern wall of the trench cutting the major axis of the hydraulic fracture HF12.

overlying silty clay. To the east of this zone, the fracture cuts across several beds and there appears to be negligible effect on the form of the trace. As the fracture approaches the ground surface it flattens and then curves sharply upward, a form resembling most other vents.

The trace of HF12 shown in Figure 5.9 is remarkably similar to traces of HF5, HF6, and HF9, where the fractures cut relatively homogeneous silty-clay. Apparently, bedding in the till affected the form of the trace of HF12 only slightly--flattening it near the center of Fig. 5.9. The sharp trough-like form of HF12 is unusual, however, and could be a result of bedding or other heterogeneities in the till. Exposures were insufficient to make that determination.

Borehole 13

The fracture in the vicinity of borehole 13 is the largest one that could be excavated. It is also unusual in several respects other than size. In particular, the fracture is nearly flat-lying and the overlying ground is sloping, whereas at the other fractures the ground is flat-lying and the fracture slopes.

At least four lobes and a main parent fracture compose HF13 (5.10 and 5.11). Typically, a lobe splits and either overlies or underlies the main fracture so that the two overlap in plan (Fig. 5.10). This differs from fractures at the other boreholes where lobes are adjacent and they rarely overlap in plan. The lobes at HF13 are roughly parallel and separated by roughly 0.3 m of unfractured till. As a result, the traces of two fracture planes were commonly found on the walls of trenches cutting HF13 (Fig. 5.12).

Junctions between the main fracture and lobes are well-exposed in two locations, at the eastern and southern sides of HF13. The junctions are several m in length and the lines they form intersect the borehole. The other two junctions are covered, and their locations and orientations are inferred (Fig. 5.12). Double lines are used to indicate junctions in Figures 5.10 and 5.11, and short solid lines at each end of the double lines indicate lobes associated with each junction.

The hydraulic fracture is crudely basin-shaped in the vicinity of the borehole, but it flattens and is nearly flat-lying at distances greater than several meters from the borehole. Most of the southern half of the fracture, for example, differs by less than a few cm from horizontal.

In plan view, HF13 resembles the other hydraulic fractures. It is elongate, with an aspect ratio of 2:1, and the borehole is near one end of the major axis. The longest dimension of the fracture, as measured from the borehole, lies roughly in the direction of the slope of the overlying ground surface (Fig. 5.10 and 5.11).

The vent at F13 is down slope from the borehole, and it occurs where the elevation of the ground surface is slightly greater than that of the bottom of the casing--the vent is 0.75 m above the bottom of the casing. The fracture curves sharply upward at the vent (Fig. 5.12).

Two vertical fractures occur adjacent to the borehole; one is parallel to the long axis of the fracture, whereas the other differs in strike by 125°. Both vertical

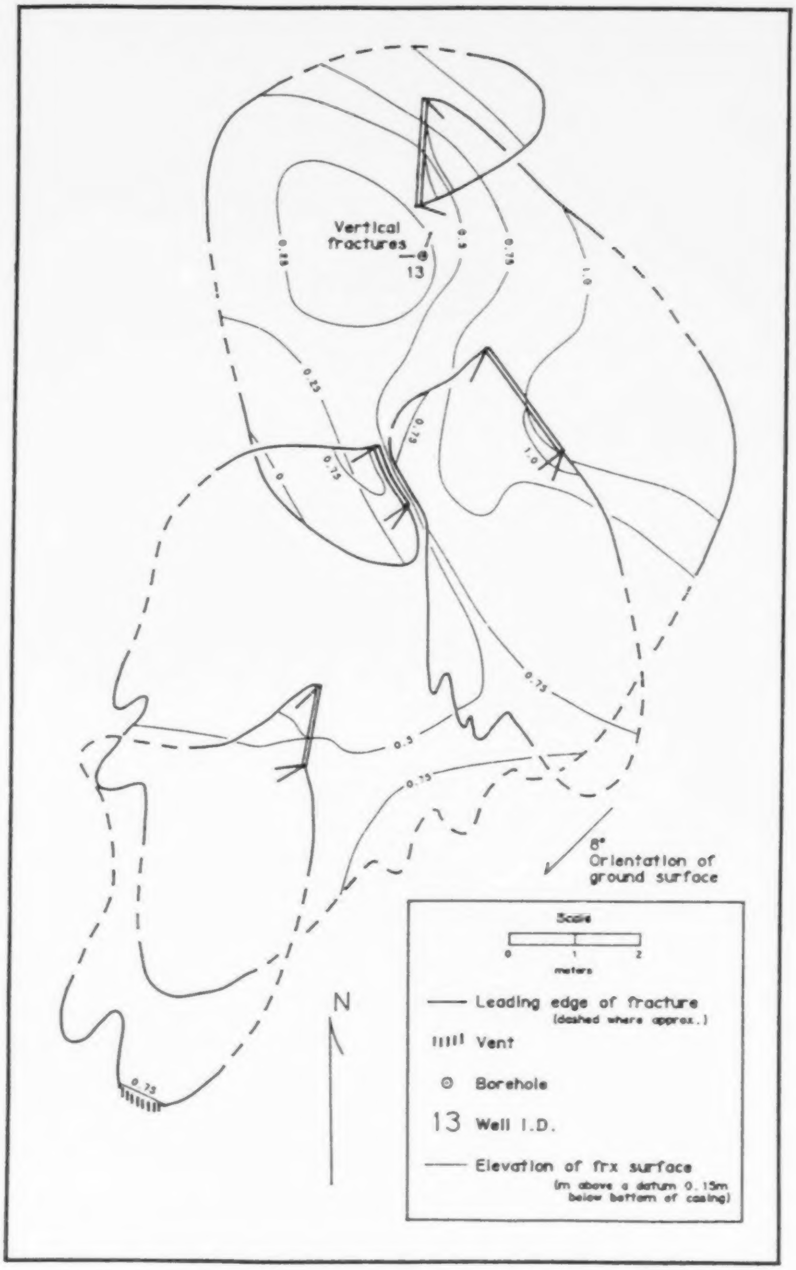
Vertical fractures
13
0.25
0.5
0.75
1.0
0.25
0
0.75
0.75
1.0
0.75
0.5
0.75
0.75
8°
Orientation of ground surface
N
Scale
0
1
2
meters
Leading edge of fracture
(dashed where approx.)
Vent
Borehole
13 Well I.D.
Elevation of frx surface
(m above a datum 0.15m below bottom of casing)

Figure 5.10. Hydraulic fracture HF13 showing structural contours fracture surfaces. Double lines mark the intersections of fracture lobes.

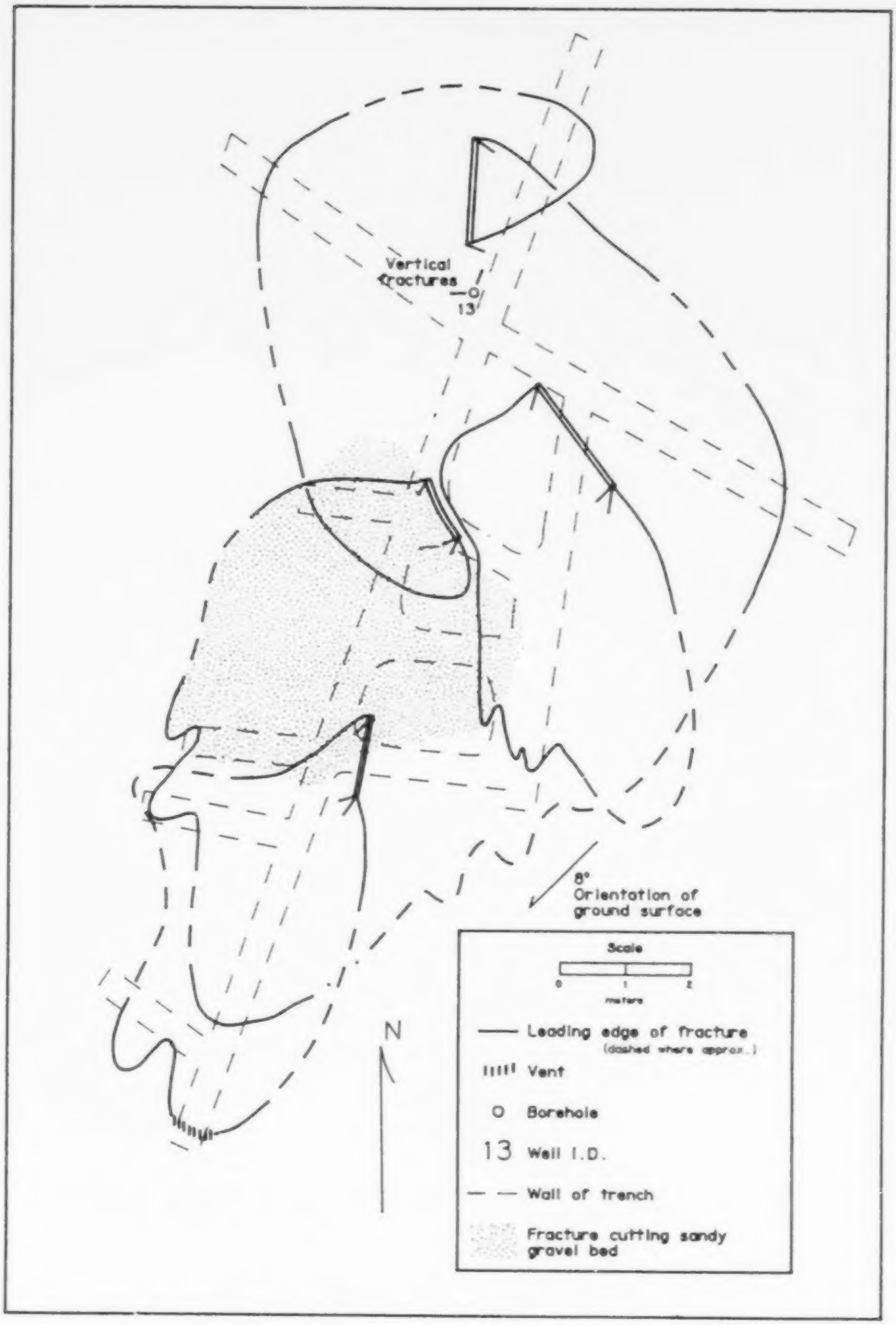
Vertical fractures
13
8°
Orientation of ground surface
N
Scale
0
1
2
meters
Leading edge of fracture (dashed where approx.)
Vent
Borehole
13 Well I.D.
Wall of trench
Fracture cutting sandy gravel bed

Figure 5.11. Outline of HF13 showing area where fracture cuts a bed of upwardly-grading gravel, sand and silt. Fracture cuts massive silty-clay till where unstipled.

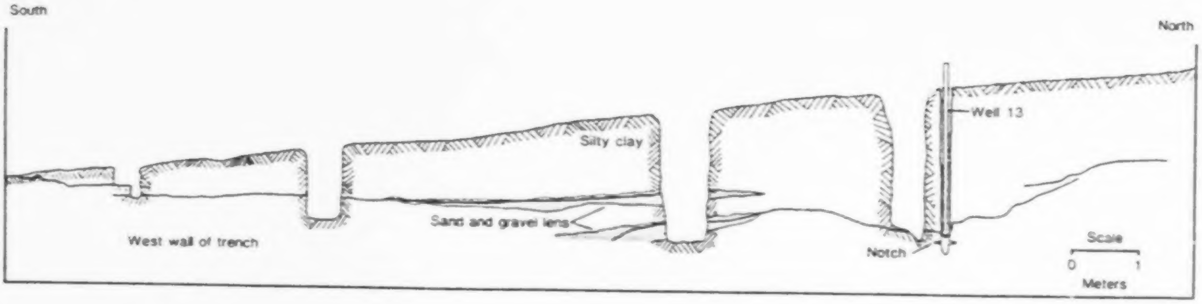
South
North
Well 13
Silty clay
Sand and gravel lens
West wall of trench
Notch
Scale
0
1
Meters

Figure 5.12. Trace of hydraulic fracture HF13 and graded beds on the western wall of the trench cutting the major axis of the fracture. Graded beds exposed above the fracture trace have been omitted.

fractures cut till adjacent to the bentonite seal in the borehole, and are above the level of the notch. The main, sub-horizontal hydraulic fracture is contiguous with the vertical fractures, and is unrelated to the notch (Fig. 5.11, 5.12).

Till in the vicinity of HF13 consists of massive silty-clay and graded beds of silty and sandy-gravel (Unit 2). Most of the fracture is in massive silty clay, but it intersects a graded bed roughly midway between the borehole and the vent (Fig.5.11 and 5.12). The bed is 0.2 m at its thickest and grades from gravel at the base to silt at the top. The fracture cuts relatively soft silt at the top of the bed.

The flat-lying orientation of HF13 is atypical compared with the other fractures, which are dipping. The graded bed could have affected the orientation of HF13 because the silt appeared to be less tough than the enveloping silty clay. However, much of HF13 is horizontal where it cuts through massive silty clay, material that lacks stratification. It is inferred that the general flat-lying orientation of HF13 results from factors other than stratification. In particular, the slope of the overlying ground surface could have affected the dip of the fracture. This inference should be checked with a theoretical analysis, but here it will allow us to ignore the orientation of HF13 in developing an idealized model of a hydraulic fracture.

DIMENSIONS OF THE HYDRAULIC FRACTURES

The plan areas of most of the fractures were between 10 m² and 30 m² (Table 5.1), according to measurements made from the maps described in the previous section. One fracture (HF13) was much larger, covering an area of 90 m², and another fracture was smaller (HF7 was 2.2 m²) than most of the others (Table 5.1).

TABLE: 5.1. DIMENSIONS AND DIPS OF HYDRAULIC FRACTURES

Frx	Depth (m)	Plan Area (m²)	Max. Length (m)	Ave. Dip
HF2	2.77	unknown	unknown	shallow
HF4	3.84	unknown	unknown	shallow
HF5	1.64	13	3.6	25°
HF6	1.85	28	6.4	15°
HF7	1.83	2.2	1.8	variable
HF9	1.75	20	5.5	17°
HF10	1.83	12	3.3	22°,25°
HF11	1.67	9	4.1	24°
HF12	1.98	30	8.2	14°
HF13	1.83	90	13.5	sub-horiz.

The greatest length of all exposed fractures occurred between the parent well and the vent. The maximum length of most of the fractures, where length is measured from the injection well to the leading edge of the fracture, is typically between 3 and 8 m. The longest fracture is 13.5 m, and the shortest one is 1.8 m (Table 5.1).

Ratios of maximum length to depth of initiation typically range between 1.5 and 4, with a maximum of 7.4 and a minimum of 1.0. Fractures HF2 and HF4 did not vent and were too deep to excavate completely, so their lengths are unknown.

Many of the hydraulic fractures are approximately planar between the borehole and the vent. The average dips of the fractures are similar; all of them are within 5° of a 20° dip. The exception is HF13, which is sub-horizontal (Table 5.1).

DIRECTION OF PROPAGATION

Most of the fractures are asymmetric in plan with respect to the borehole. Thus, the fractures acquire a preferred, or dominant direction of propagation as they grow away from their parent boreholes. The dominant direction of propagation, the azimuth of the line between the borehole and a vent, ranges from northeast to west to southeast (Table 5.2). The direction of propagation of HF13 is nearly parallel to the direction of maximum slope of the overlying ground surface, which is 225° (Fig. 5.10 and Table 5.2). At the other fractures, however, the direction of propagation is unrelated to known geologic or topographic features.

The direction of propagation is related to the location of the backhoe used to prevent movement of the casing during fracturing. In most cases, the fractures propagated away from the backhoe. The two exceptions, HF7 and the southwestern lobe of HF10, are small fractures that propagated toward the backhoe, venting near the front wheels of the vehicle (Fig. 5.13). No fractures propagated beneath the backhoe.

Theoretical analyses indicate that hydraulic fractures will propagate in directions of decreasing confining stress. Apparently the weight of the backhoe resulted in vertical stress gradients that were great enough to affect the propagation of the underlying hydraulic fracture.

The dominant direction of propagation is related to the trend of the hydraulic fracture at the vent, and to the vertical hydraulic fractures adjacent to the borehole. Strikes of vertical fractures at the vent are nearly perpendicular to the dominant direction of propagation in every fracture (Fig. 5.13 and Table 5.2). At most fractures, the strike of a vertical fracture at the borehole is also nearly perpendicular to the propagation direction (Fig. 5.13 and Table 5.2). In a few cases, however, the strikes of fractures adjacent to the borehole (e.g. HF9, HF11) are at high angles to the direction of propagation, and in one case (HF13), two vertical fractures differing in strike by 125° were observed. The formation of those fractures is poorly understood, but it could be similar to the results of laboratory experiments where hydraulic fractures were created from cylindrical holes in clay.

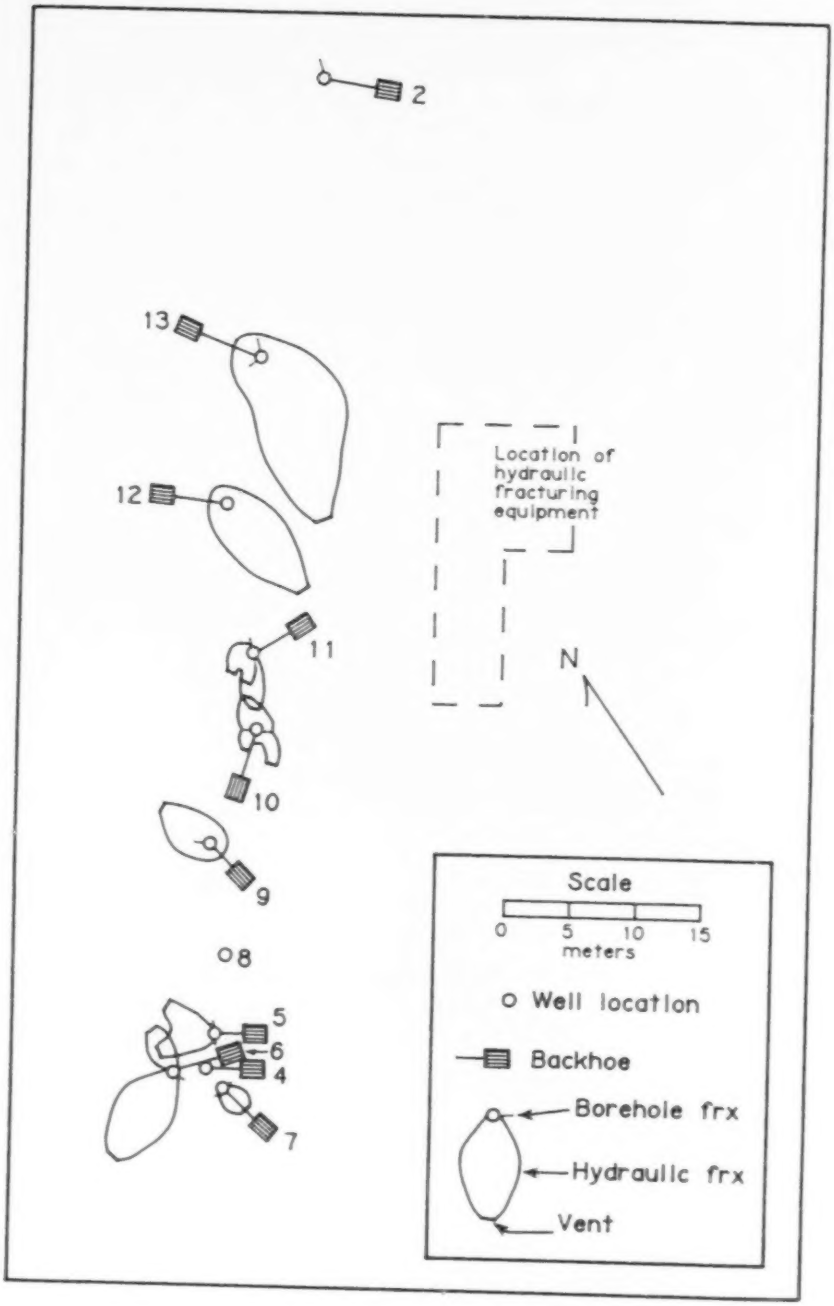
2
13
12
Location of hydraulic fracturing equipment
11
N
10
9
8
5
6
4
7
Scale
0
5
10
15
meters
Well location
Backhoe
Borehole frx
Hydraulic frx
Vent

Figure 5.13. Outlines of hydraulic fractures and locations of a backhoe at the time of fracturing.

TABLE 5.2: AZIMUTHS OF FEATURES OF HYDRAULIC FRACTURES.

	Propagation Direction	Vent Frx	Borehole Frx
HF5	325, 282	60	62
HF6	225, 10	165	157
HF7	150	62	58
HF9	326	35	117
HF10	206, 39	124	128
HF11	205, 240	130	18
HF12	175	75	--
HF13	200	105	265, 20

In some experiments, two co-planar fractures were created, whereas in other experiments, three fractures in a trigonal pattern (striking roughly 120° from another) were created from the cylindrical hole. Haimson and Fairhurst (1970) also describe laboratory experiments where both co-planar and trigonal patterns of hydraulic fractures were created from cylindrical holes in rock. Our experiments and those of Haimson and Fairhurst (1970) show that the two patterns of fractures are possible, although additional work is required to determine the factors that actually cause these patterns to develop.

SUMMARY: AN IDEALIZED HYDRAULIC FRACTURE CREATED DURING THE FIELD TESTS

Forms of hydraulic fractures created during the field test differ in detail, but there are certain characteristics that are common to nearly all the fractures. The common traits were used to infer an idealized hydraulic fracture created in the field tests. The form of the idealized fracture consists of four zones, which are arranged in increasing distance from the parent borehole (Fig. 5.14):

1. Zone One: a sub-vertical orientations adjacent to the borehole.
2. Zone Two: a flat-lying orientation in the vicinity of the borehole (within several m).
3. Zone Three: a planar to trough-like feature dipping gently toward the borehole. This zone composes most of each hydraulic fracture.
4. Zone Four: a steeply-dipping orientation occurring within several dm of the ground surface.

Zone One

Zone One is characterized by one or more vertical fractures containing the axis of the borehole and initiating along the open interval below the casing. Vertical fractures were observed at all boreholes except HF12, where the bottom of the borehole was poorly exposed during initial excavation and the trench was flooded before we could complete excavation.

Two vertical fractures whose strikes differed by roughly 120° occurred at HF13, whereas single fractures were found adjacent to the other borings. More than one fracture may have occurred adjacent to some of the other borings, and they were removed during excavation of the trenches.

Vertical fractures typically flatten upward and become sub-horizontal at the bottom of the basket or adjacent to the bentonite-filled segment of the borehole, one to several dm above the notch. The change in orientation typically is quite abrupt, occurring over a length of several cm and having a radius of curvature of one to two cm.

There are several exceptions to the above generalizations. One is at borehole 7, where a vertical fracture rolls over gradually over a length of 1 to 1.5 m. At two other boreholes (HF10 and HF6) vertical fractures propagate a meter or more above the bottoms of the casing before they roll over and become sub-horizontal. None of the vertical fractures extended from the bottom of a borehole to the ground surface.

A sub-horizontal fracture propagated from the notch at borehole HF6, but none of the other notches contained a hydraulic fracture. The notch at HF6 was two cm below the basket, whereas it was four to eight cm below the basket at the other boreholes.

The features of Zone One are a result of the nucleation of hydraulic fractures in the vicinity of an open borehole. It appears that nucleation occurs as a vertical fracture in the wall of the open boring. The vertical fracture propagates outward and upward and rolls over to a shallowly-dipping fracture either at or above the top of the open interval.

The notches cut in the walls of the borehole were ineffective at nucleating hydraulic fractures. Presumably this occurred because the notches were too shallow to affect the concentration of stress in the vicinity of the borehole. A notch of larger diameter is expected to be more effective at nucleating a horizontal hydraulic fracture at the borehole. We were unable to create a larger notch using the simple mechanical device designed for the project.

Zone Two

Zone Two is characterized by a subhorizontal fracture occurring within several m of the parent borehole. The subhorizontal fracture surrounds the borehole in some cases (e.g. HF6 and HF12). In other cases (HF5 and HF9) the subhorizontal fracture is limited to one side of the borehole, typically the side opposite the main body of the fracture.

The subhorizontal fracture of Zone Two is absent from some of the fractures (e.g. HF7, HF10 and HF11), and it is unclear whether this Zone is typical. A hydraulic fracture lacking Zone Two would resemble 5.14 except the vertical fracture of Zone One would roll over to the shallowly-dipping fracture of Zone Three.

Zone Three

Zone Three composes most of the idealized hydraulic fracture. It is slightly elongate in plan, with aspect ratios between 1.5:1 and 2:1, and the major axis lies along a line between the parent borehole and the vent. The length of the fracture in Zone Three is roughly three times the depth where the fracture rolls over in Zone One.

The fracture in Zone Three is, in general, planar to slightly trough-like and it dips toward the borehole at roughly 20° (dips range between 12° and 25°). In the field, this Zone is commonly composed of several distinct lobes, which taken together result in the idealized form shown in Figure 5.14.

Traces of the fracture in Zone Three are remarkably straight over the length of the zone. In detail, however, the traces are slightly stepped (Fig. 5.14b); they consist of straight segments of approximately one meter connected by risers of roughly 0.1 m (e.g. Figs. 3.7, 3.8, 3.11).

In plan, Zone Three is asymmetric with respect to the borehole. At some of fractures (HF5, HF7 and HF10, HF11), the borehole lies at the edge of the fracture, whereas at others the borehole is contained within the fracture but it lies much closer to one end than to the other. The borehole lies between the load applied by the backhoe and the fracture of Zone Three.

The major axis of the idealized fracture is perpendicular to the strike of the vertical fracture in Zone One.

Zone Four

In Zone Four, the idealized fracture curves upward and is subvertical where it intersects the ground surface. The vertical fracture in Zone Four typically extends to a depth of ten cm, although depths range from a maximum of 30 cm at HF9 to a minimum of 2 cm at the northern lobe of HF6. The vertical fracture of Zone Four is 0.5 m to 1.5 m along strike. It is perpendicular to the major axis of Zone Three, and it is roughly parallel to the vertical fracture in Zone One.

DISCUSSION: DEVELOPMENT OF THE IDEALIZED FRACTURE

A general history of the development and growth of the idealized fracture (Fig. 5.14) will improve our understanding of the processes that occurred during the field test. In the following section, we will use the results of experiments of hydraulic fracturing of rock or soil and the results of theoretical analyses based on linear elastic fracture mechanics to infer a conceptual model of the development of the idealized fracture.

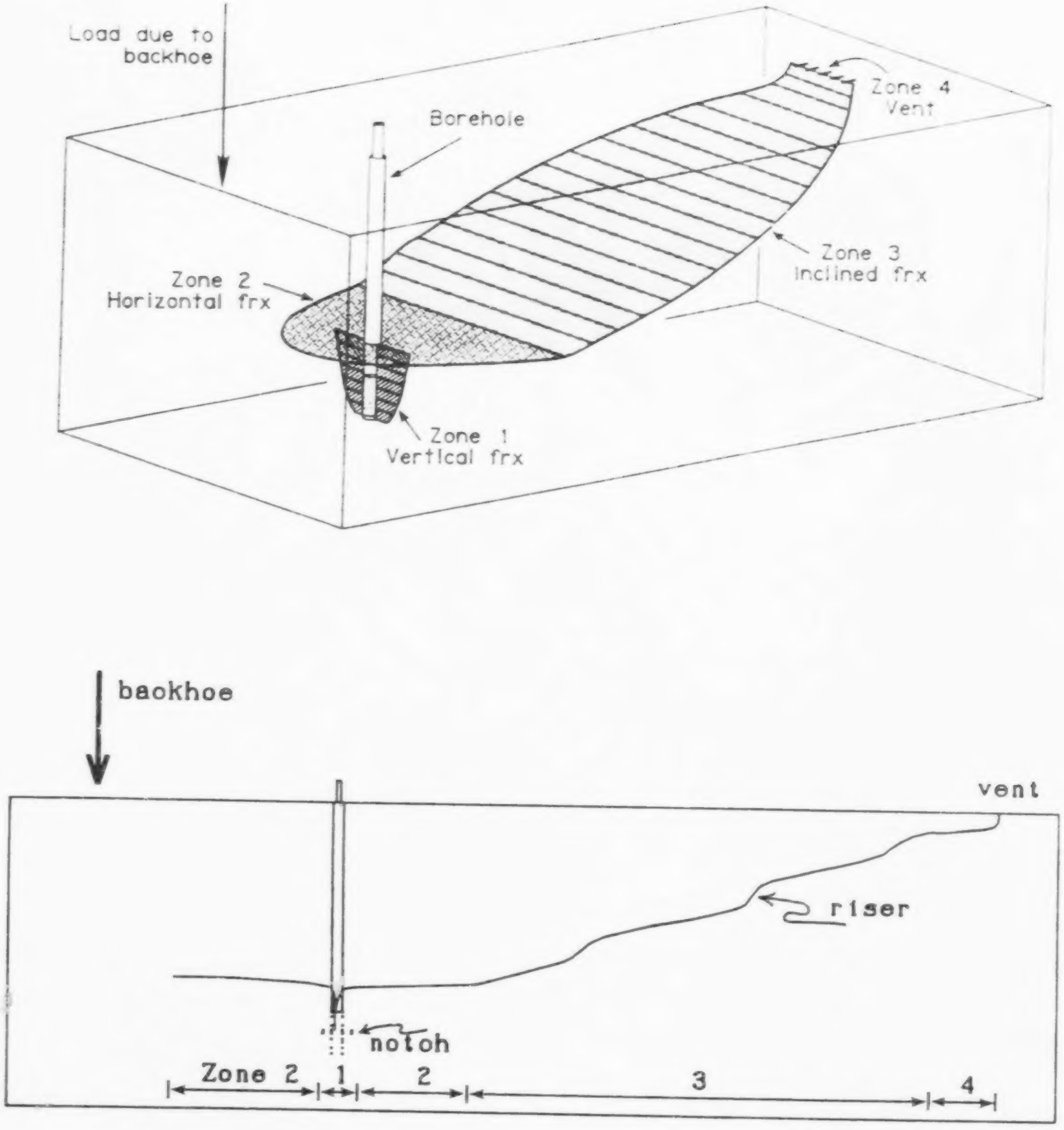
Load due to backhoe
Borehole
Zone 4
Vent
Zone 3
Inclined frx
Zone 2
Horizontal frx
Zone 1
Vertical frx
backhoe
vent
riser
notch
Zone 2
1
2
3
4

Figure 5.14a. Idealized hydraulic fracture created at the ELDA test site. Inferred from exposures of fractures created beneath level ground. a.) Oblique view. b.) Section along major axis of the fracture.

When pumping begins at the start of the fracturing procedure, the pressure within the borehole increases, affecting the state of stress until failure occurs in the till enveloping the open interval of the borehole. The initial fracture is vertical, containing the axis of the borehole and apparently is unrelated to the notch.

Several investigators have reported results from the laboratory indicating that hydraulic fractures nucleated from cylindrical holes in rock will contain the axis of the hole, even though the applied far-field state of stress favored an orientation normal to the axis (Medlin and Masse, 1979; Daneshy, 1973; Haimson and Fairhurst, 1969). Similar results occurred when hydraulic fractures were created from cylindrical holes in soil using the apparatus described in Part I.

This result can be explained by an analysis of stresses in the vicinity of a long pressurized cylindrical hole in an elastic medium where the principal confining stresses act parallel or normal to the axis of the hole (Poulos and Davis, 1974). The analysis shows that pressure within the hole can induce tensile stresses in the enveloping medium that act parallel to the circumference of the hole. Stresses acting parallel to the axis of the hole, however, are unaffected by pressure within the hole. Accordingly, tensile stress adjacent to a vertical borehole develop normal to a vertical plane, regardless of the relative magnitudes of the principal confining stresses. The vertical fractures observed adjacent to the boreholes apparently result from those tensile stresses.

A disk-shaped notch should favor the nucleation of a fracture in the plane of the notch, assuming the minimum applied compression is normal to the notch. Indeed, this was the reason the notches were created. It is clear from the results of the field test that the notches had little effect on the nucleation of hydraulic fractures. Failure to nucleate a horizontal fracture at the borehole is a significant shortcoming of the design of the borehole because it reduces the overall size of the hydraulic fractures. This occurs because the vertical fractures at the borehole grow upward before rolling over, essentially reducing the depth of initiation and limiting the length of the fracture prior to venting.

The development of a vertical fracture could be inhibited by decreasing the length of the open interval in the boring, and by increasing the depth of penetration of the notch. Recently, we have used a high-velocity water jet to cut notches that extend 15 to 25 cm into till, many times larger than the ones cut mechanically during the field test.

Once formed, the vertical fracture grows outward and upward climbing above the open interval of the borehole. At some point, either adjacent to or several dm to one meter above the basket, the vertical fracture changes orientation, or rolls over, flattening abruptly to a shallow dip. Typically, the fractures roll over to a nearly flat-lying orientation, but in some cases they dip 15° to 25° toward the borehole. This change of orientation appears to occur as the fracture grows out of a zone where stresses are influenced by the pressurized borehole and into a zone influenced by the far-field stresses.

The idealized fracture then grows roughly horizontally as much as several m away from the borehole and changes orientation again, curving upward to dip roughly 20° toward the borehole. This change in orientation is inferred to result from a mechanical interaction between the fracture and the overlying ground surface. The interaction has several effects on the propagating fracture, all of which are related to the removal of resistance of the material above the ground surface. Perkins and Kern (1961), for example, analyze one effect of mechanical interaction by comparing the aperture of a shallow circular horizontal fracture, which dilates by lifting the overburden, to the aperture of a deep circular fracture, which dilates by compressing the overburden. They show that fracture apertures depend on the size of the fracture relative to its depth, expressed as the ratio of radial length a to depth of initiation d. Apertures of the two fractures are equal when $a/d = 1.33$, but the aperture of the fracture that lifts the overburden greatly exceeds that of the other fracture when $a/d > 1.33$.

Pollard and Holzhausen (1979) show how mechanical interaction could cause a fracture to turn upward and propagate toward the ground surface. They calculated the stress intensity factors, K_{I} and K_{II}, for a two-dimensional, static, planar fracture of half-length a in an elastic medium bounded by a free surface (the ground surface). The direction of propagation of the fracture can be predicted using the relative magnitudes of K_{I} and K_{II}, according to theories proposed by Cottrell and Rice (1979) or other investigators cited by Pollard and Holzhausen (1979). Those theories state that non-zero values of K_{II} lead to propagation out of the plane of the original fracture. The results of Pollard and Holzhausen indicate that K_{II} of a horizontal fracture increases as a/d increases; K_{II} is negligible when $a/d < 0.3$, it increases gradually when $0.3 < a/d < 1.0$, and it increases rapidly when $a/d > 1.0$ (Pollard and Holzhausen, 1979; fig 5). This is because the upper surface of a horizontal fracture is displaced farther from the axial plane than the lower surface, resulting in shear at the tip and non-zero values of K_{II}.

Those results suggest that the depth of initiation is critical to propagation path. A horizontal fracture considerably shorter than the depth of initiation will propagate horizontally, but as the fracture length approaches that depth the fracture will tend to curve out of plane and propagate upward.

The analyses described in the previous paragraph are for static fractures, and as such they are limited to the favored direction of a miniscule extension of a stationary planar fracture. Dynamic analyses, which track the movement of a fracture as it propagates, show how the interactions described above affect fracture form. Narandren and Cleary (1983) present the results of a dynamic analysis predicting the path of propagation of a horizontal hydraulic fracture beneath a free surface. The results (Narandren and Cleary 1983; fig. 9) show that the fracture is nearly flat-lying when it is short relative to its depth, but the dip increases noticeably when $a/d > 0.7$. The analysis was terminated when $a/d = 1.55$ and the fracture curves upward yielding a shape suggestive of the cross-section of the idealized fracture (Fig. 5.14b and Narandren and Cleary 1983; fig. 9).

Results of theoretical analyses outlined above indicate that we should expect a hydraulic fracture to begin to propagate toward the ground surface after it has grown away from the parent borehole a distance approximately equal to the depth of initiation. Thus, the analyses indicate that the maximum length a fracture reaches before venting is scaled to its depth of initiation. This implies that we could have increased the sizes of the fractures created during the test by using deeper boreholes.

The idealized fracture grows at nearly a constant dip once it begins to propagate toward the ground surface (neglecting vertical growth at the borehole). Processes causing the dip to remain constant are unclear because available analyses (i.e. Pollard and Holzhausen, 1979; Narandren and Cleary, 1983) suggest that the dip will increase as the fracture climbs and the effect of the ground surface increases. One possibility is that during upward growth the vertical stress, resulting from the weight of the overburden at the fracture tip decreases, whereas the lateral stress remains constant. Thus the tendency to steepen, due to effects of the ground surface, is balanced by a tendency to flatten, due to an increase in the ratio of lateral to vertical stress at the tip. This possibility must still be checked

The dip of the idealized fracture is uniform in general, but it varies slightly in detail, resulting in gentle step-like features. The steps suggest that slight deviations from the average dip are rapidly corrected by the fracture curving back to the initial orientation. Cotterell and Rice, who analyze the stability of slightly-curved Mode I cracks, show how a small deviation from the optimal path will result in a step-like form in a fracture (Cotterell and Rice, 1980; fig. 10).

Many analyses of hydraulic fractures assume that they are symmetric with respect to the axis of the borehole, but most of the fractures created in the field test were asymmetric. The hydraulic fracture created beneath sloping ground (HF13) is elongate in the downslope direction. Where the ground is level, however, applied loads seem to influence the direction of propagation because the dominant directions of propagation are typically away from the backhoe parked near each borehole. Apparently gradients in vertical stress, caused by either topography or applied loads, affect the dominant direction of propagation of horizontal or shallowly-dipping hydraulic fractures. This conclusion raises the intriguing possibility of artificially loading the ground surface to cause fractures to propagate in a particular direction.

It is reasonable to expect that hydraulic fractures of similar size and shape as those described here could be created under conditions similar to the ELDA site. It would be misleading, however, to suggest that similar hydraulic fractures can be expected at any site. The large lateral stresses in the till at the ELDA site certainly affected the dips of the fractures, and thus the sizes that they could achieve before venting. Measuring in situ stresses will be a vital first step in predicting the orientation of hydraulic fractures.

The principles of linear elastic fracture mechanics, specifically the applications to hydraulic fracturing of rock, seem to offer general explanations of the development of the idealized fracture created in till at the ELDA site. Predicting the forms of hydraulic fractures at other sites, however, will require a theoretical model specifically tailored to analyze conditions of the near-surface.

SECTION SIX

SETTING AND DESIGN OF THE FIELD TEST -- 1989

Hydraulic fracturing field tests of 1989 were performed at two sites. One was the same as the field test of 1988, located 10 km north of downtown Cincinnati near the southeastern corner of the ELDA Company landfill. The other is located 15 miles north of the ELDA landfill, on the grounds of the Goettle Construction Company.

Hydraulic fracturing at the ELDA landfill site took place in June and July, 1989. Field analysis of the fractures, including trench mapping, took place in July and August, 1989. Preliminary testing of the hydraulic fracturing apparatus was performed at the Goettle Construction Company site in March and April, 1989. Hydraulic fractures for fracture monitoring purposes were created at the Goettle site in July, 1989. Fractures created at the ELDA site were exposed by excavating a network of trenches, whereas fractures at the Goettle site were not exposed. As a result, more is known about the fractures and subsurface at the ELDA site, and the following chapters will focus on that site.

QUALITY ASSURANCE AND CONTROL

The success of the hydraulic fracturing effort is one measure of quality assurance steps taken during the execution of this project. The fact that fractures of similar shape and size were created repeatedly, at different times and locations, is a measure of the success of quality control.

All instruments used during the fracturing process were calibrated according to industry standards. Calibration of custom designed instruments, such as the gauge for measuring the flow rate of the injection pump, was conducted in a series of identical tests, performed by different staff researchers. Dosages of chemical ingredients of fracturing gels were measured with margins of error no greater than 0.1%, hence exceeding petroleum industry standards. Accuracy achieved in measuring borehole depths and notch lengths was comparable to accuracy demanded by field analysis of the fractures (see Section 7).

SITE CHARACTERISTICS

The vicinity of the ELDA test site is an area of gently sloping ground bounded on the southwest by a steep slope, three to four meters tall, and on the northeast by a moderate to steep descent into a deep (> 10 m) trough. The ground surface at the time of the test was the product of soil excavation for fill purposes, and it was three to four meters below the natural ground surface. The ELDA fracturing site is a gently sloping, elongate strip, trending N55W, roughly 50 m long and 10 m wide.

The area used during 1989 is in the vicinity of the area used during 1988. We estimate that the southeastern end of the 1989 site is 40 to 60 m south of the southwestern corner of the area shown in Figure 4.2. Accurate correlation of the two sites was not attempted because all the features shown in Figure 4.2 were removed during excavation activities between autumn 1988 and spring 1989.

Geology

The ELDA site is underlain by glacial till (Illinoian?), composed mostly of clayey silt to silty clay. The stratigraphic level is slightly higher (5 to 10 m) than that of the site of the 1988 test. A two meter section of the stratigraphy, exposed in trenches used to examine the fractures, is described in the following section.

Description of Soil Profiles in Trenches

The soil profile is generally uniform in the SE-NW direction, according to observations in trenches. Gravelly till lies at the top of the soil section, just beneath the ground surface. The thickness of the gravelly till increases to the NW, from 20 cm at the SE end of trench A, to 30 cm at the midpoint of trench A, 20 m away from the SE end, to 50 cm at the NW end of the trench.

Organic-rich silty clay to clayey silt underlies the gravelly till. The thickness of the organic silty clay is 40 cm at both ends of trench A, but it pinches to half that thickness at the midpoint of the trench.

Massive brown silt, 25 to 30 cm thick, underlies the organic silt. At the NW end of the trench, the massive silt is directly underlain by a 90 cm thick unit of laminated silty clay, with interbedded clayey silt. At the SE end and at the midpoint of the trench, the massive silt and the laminated silty clay are separated by other units. At the midpoint of the trench, a 50 cm thick sequence of interbedded, 10 cm thick, laminated clay and 10 to 20 cm thick massive brown silt underlies the upper massive silt. At the SE end, 50 cm of clayey silt with interbedded silty clay lie below the massive silt. At both the SE end and the midpoint of the trench, the 50 cm thick sequence of silt and clay is underlain by 105 to 110 cm of laminated silty clay with interbedded clayey silt.

At the NW end of the trench, the laminated silty clay is underlain by 20 cm of loam, followed by 20 cm of gravelly till, at the bottom of the trench. At the midpoint of the trench, the laminated silty clay is underlain by 10 cm of gravel at the bottom of the trench, and at the SE end of the trench, the laminated silty clay reaches to the bottom of the trench.

Moisture Contents

Moisture contents of three samples extracted from the western intersection of Trenches A and F, were measured in accordance with the ASTM Standard Designation D 2216-80. The three samples represent three different soil types, described above, under Site Characteristics.

Sample 1, extracted 77 cm above the horizontal datum, represents the organic-rich silty clay to clayey silt, which occurred just below the gravelly till throughout the trench network. Its moisture content is 23.7%.

Sample 2, extracted 44 cm above the datum line, represents the massive, brown silt, lenses of which also extend across the entire trench network. Its moisture content is 14.6%.

Sample 3, extracted 15 cm above the datum, consists of laminated silty clay. Although the layer from which Sample 3 was removed lies above the lowest lens of massive silt, the sample represents the same type of soil that constitutes the one-meter-thick, laminated silty clay unit pervasive in the lower half of the entire trench network. Its moisture content is 25.2%.

METHOD OF FRACTURING

Figure 6.1 illustrates the equipment and sequence of operations involved in hydraulic fracturing. Figure 6.2 shows details of the drive head used to prepare a borehole for hydraulic fracturing. Figure 6.3 outlines five steps of hydraulic fracturing.

Equipment

Equipment used to prepare and pump gel and sand mixtures for hydraulic fracturing included two water tanks, two gel mixing tanks (labeled *a* in Figure 6.1), two blenders for crosslinking and adding sand (*d* in Figure 6.1), a water pump, a gel pump (*b* in Figure 6.1), hoses for gel transfer (*c* in Figure 6.1), and a grout pump to inject proppant into the subsurface (*e* in Figure 6.1). Equipment used to create boreholes for fracturing included rod and casing (*f* in Figure 6.1; also see Figure 6.2), a drive head with pointed tip (Figure 6.2), a water jet rod to create starter notches, a high-pressure pump for the water jet, and an electrically powered jackhammer to drive the fracture lance into the ground. Monitoring equipment included an IBM-PC compatible, portable (laptop) computer (*h* in Figure 6.1), a pressure transducer (*g* in Figure 6.1), and a motorized power generator.

The two water tanks were made of plastic, and had capacities of 1.1 m^3 (300 gal.) each. The two elongate gel tanks were made of galvanized steel, and had capacities of 0.95 m^3 (250 gal.) each. The two blenders for crosslinking and adding sand were part of a grouting pump system by Chem-Grout Company of Chicago, Illinois, and they had capacities of 0.2 m^3 (50 gal.) each. Rotary mixing blades within the blenders were powered by a diesel engine, which also powered the moyno-type grouting pump. Crosslinked gel and sand were fed from the blenders directly into the grouting pump, which pumped the blend downhole and into the fractures.

At the Goettle site, a five horsepower centrifugal pump moved water from a nearby lake into the two water tanks, and from the water tanks into the gel tanks. At the ELDA site, the water pump was not needed, because the water tanks were filled directly from a water truck, and water flowed downhill from the water tanks into the gel tanks.

An eight horsepower, 7.6 cm (3 in) centrifugal pump rapidly circulated gel in the gel tank to hydrate the guar gum, and to prevent the formation of lumps, or "fisheyes," in the gel. The same pump also moved gel from the gel tanks into the

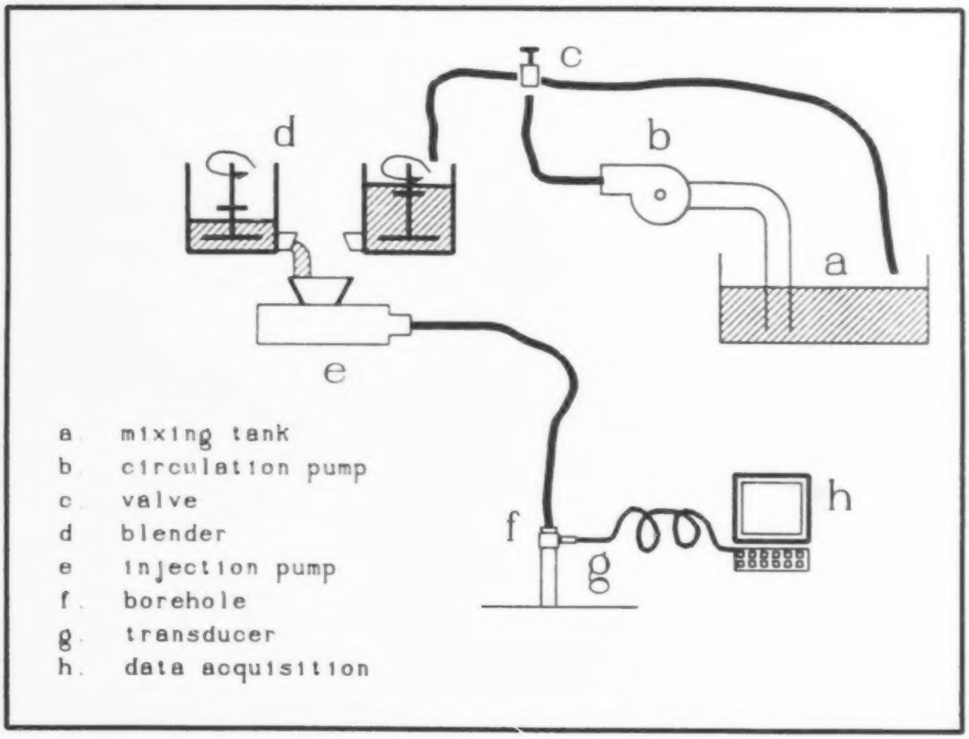
c
d
b
a
e
a. mixing tank
b. circulation pump
c. valve
d. blender
e. injection pump
f. borehole
g. transducer
h. data acquisition
f
g
h

Figure 6.1. Scheme for hydraulic fracturing operation performed during the 1989 field test.

crosslinking blenders. Gel circulated from the gel tank, into the pump, and back into the gel tank through 5 cm (2 in) tubing (Figure 6.1). A "T" valve (labeled *c* in Figure 6.1) in the tubing diverted the hydrated gel into the crosslinking blenders, also through plastic tubing.

A Zenith Supersport 286 laptop personal computer, with 40 megabyte hard-drive was linked to the pressure transducer, which was attached to the borehole casing, in order to monitor pressure changes in the proppant pumping hose (the pipeline) at or above ground surface.

The Injection Fluid

Guar gum-based chemical mixtures were added to the injected water to create a gel capable of carrying sand into the fractures. A complex derivative of guar gum, manufactured by Halliburton Services company -- a major service company to oilfields in the United States -- was used in the first four fractures created at the ELDA site. A simple guar gum, manufactured by Hi-Tek Polymers, Inc., was used in the remaining fractures, including twelve at the ELDA site, and five at the Goettle site.

Comparison of the two gel products led to the conclusion that the simple, nonderivitized guar gum system manufactured by Hi-Tek Polymers is better suited for shallow, environmental applications than the highly derivitized system manufactured by Halliburton Services. The chemical kinetics of the nonderivitized gel corresponds better to the requirements of fracturing at shallow depths.

Guar gum-based gels consist of four main ingredients, which are added to water in a particular, timed order, causing a three-step chemical process. The ingredients include guar gum powder, buffering powder or solution, crosslinking powder or solution, and breaking powder or solution. The three steps are, in order, gelling, crosslinking, and breaking. Gelling and crosslinking increase the viscosity of water by one and two orders of magnitude, respectively. Breaking reduces the viscosity back down to almost that of water (1 cP), after a period of time sufficiently long to allow completion of the fractures.

Gelling increases the viscosity of water from 1 cP to about 15 to 20 cP, caused by the addition of about 3.6 to 4.8 kgs of guar gum powder per cubic meter (0.03 to 0.04 lbs/gal) of buffered, pH-neutral water. Halliburton's WG-18 gum powder, known as a CMHPG (Carboxyl-methyl-hydroxyl-propyl-guar) gum, was required in doses of 4.8 to 5.03 kgs/m^3 (0.04 to 0.042 lbs/gal) to obtain the necessary viscosity. Doses of 3.6 kg/m^3 (0.03 lbs/gal) were insufficient. Hi-Tek Polymer's Jaguar 408-D gum powder, known as a "standard guar," was required in doses of 0.36 to 3.95 kg/m^3 (0.03 to 0.033 lbs/gal).

Halliburton's WG-18 guar gum required 0.3 kg/m3 (0.0025 lbs/gal) of an acidic buffering agent, containing 60% sulfamic acid, supplied by Halliburton Service Company under the name of BA-2. In conjunction with Hi-Tek Polymer's Jaguar 408-D guar gum, a buffer is required only if the water is pH-neutral or slightly caustic, because the guar gum increases the pH of neutral (pH = 7.0) water to about 7.5 or 8.0, whereas a pH value of 7.0 is needed for the successful hydration of the guar gum powder to form a gel. Cincinnati City Water used at the ELDA site was slightly acidic, so that a buffer was not needed. Lake water used at the Goettle site was slightly caustic, with a pH of 7.5 to 8.0, so that a buffering agent was needed. Calcium chloride, added in doses of 4.8 to 5.4 kg/m^3 (0.04 to 0.045 lbs/gal), served both as a buffer, and as an inhibitor of swelling in clays. Calcium chloride crystals were added to Goettle Lake Water before the guar gum powder, to allow sufficient time for the crystals to dissolve.

Once guar gum powder is added to water, sufficient time must pass for the guar to hydrate before the required viscosity is reached and a crosslinker may be added. The hydration time is only about 5 minutes for the Halliburton gel, whereas it is 20 to 30 minutes for the Hi-Tek Polymers gel. This is the first of two critical differences between the chemical kinetics of the two gel systems applied during fracturing at the ELDA site (only Hi-Tek Polymers gel was applied at the Goettle site for the fractures described in this report). Both gel systems require several minutes of agitated mixing of the guar gum, to avoid formation of small lumps of gum, called "fish-eyes" in the oilfield hydraulic fracturing industry.

The viscosity of the hydrated gel is increased to 100 to 200 cP by the addition of a crosslinker. The crosslinker supplied by Halliburton, called CL-19, contains 11 to 30% ethylene glycol, and it was added to the hydrated gel in doses of 1.9 to 2.8 cm^3 per cm^3 (0.0005 to 0.00075 gal per gal). The Hi-Tek Polymers gel required borate as a crosslinker, available under the brand name "Borax," and it was added to the hydrated gel in doses of 0.24 to 0.68 kg/m^3 (0.002 to 0.0057 lbs/gal). The kinetics of the crosslinking reaction are different for the two systems compared in this study. The Halliburton gel typically requires five to six minutes of vigorous agitation for crosslinking to occur. The High-Tek Polymers gel, on the other hand, is crosslinked almost instantly, within seconds after the crosslinker is introduced under vigorous agitation. This is the second of the two critical differences between the chemical kinetics of the Halliburton and Hi-Tek Polymer gel systems.

Concomitantly to the addition of crosslinker, breaker was added to ensure the eventual breakdown of the gel to a liquid solution with viscosity almost equal to that of water. Laboratory tests showed the final viscosity of broken gels to be about 2 cP, for both the Halliburton and Hi-Tek Polymers gels. The breaker supplied by Halliburton, called GBW-3, contains at least 60% of an unspecified carbohydrate material, and it was added in doses of 0.095 to 0.099 kg/m^3 (0.0008 to 0.00083 lbs/gal). The breaker supplied by Hi-Tek Polymers, called Breaker-F, contains a cellulase enzyme, and it was added in doses of 0.12 to 0.30 kg/m^3 (0.001 to 0.0025 lbs/gal). The time required to break down the gel to the final viscosity was 18 to 24 hours for the Halliburton gel, and 24 to 48 hours for the Hi-Tek Polymers gel. Although this contrast between the Halliburton and Hi-Tek Polymers systems may influence scheduling of the application of newly created fractures for remediation purposes, the contrast is nonessential because it does not affect the fracturing process itself.

The two critical differences between the chemical kinetics of the Halliburton and Hi-Tek Polymers gel systems noted above -- the different times required for hydration and crosslinking of the gels -- render the Hi-Tek Polymers gel system more suitable for application to hydraulic fracturing for remediation purposes. The relatively small volumes required for our application makes the long hydration times necessary for Hi-Tek Polymers gel tolerable, since tanks of hydrated but uncrosslinked gel sufficiently large to fill several fractures can be prepared in advance. Moreover, the pumping rate of the system we used is limited by the time required to completely mix a batch of gel, crosslink and sand, so the rapid crosslinking of the High Tek Polymers gel decreased the time required to mix each batch and thus improved the efficiency of our procedure. The gel and crosslink system from Halliburton is designed for procedures used to create hydraulic fractures in the oil industry, which benefit from short hydration times and delayed crosslinking.

The Fracturing Procedure

The borehole used to create fractures during the 1989 tests was designed to inhibit the formation of vertical fractures adjacent to the bore (as in the 1988 tests), and to facilitate the creation of stacks of multiple fractures. A device (Fig. 6.2), which we term a "fracturing lance", is the central element of the design. The lance, illustrated in Figure 6.2, consists of casing (EX casing) and an inner rod (EW drill rod), both of which are tipped at one end with hardened cutting surfaces that are formed into a conical point. A drive head at the other end of the lance secures both the casing and the rod. Individual segments of rod and casing were 1.52 (5 ft) long, and they were threaded together as required by borehole depth, which ranged from 9.6 to 3.9m (2 ft to 12 ft).

To prepare for fracturing, the lance was driven 0.1 to 0.2 m below the bottom of a borehole; either an open hole or through a hollow-stem auger (Fig. 6.3). The rod was removed leaving till exposed at the bottom of the casing. Lateral pressure of the soil on the wall of the casing effectively sealed the casing in the ground, much as cement sealed steel pipe in the borehole during the 1988 tests. Another apparatus, composed of steel tubing with a narrow (diam. 0.025 cm; 0.01 in) orifice at one end, was inserted into the casing. Water injected into that apparatus with a pressure washer pump (rated at 17.2 kPa; 2500 psi,0.02 m^3/min; 5 gpm) formed a jet that cut laterally into the soil. The water jet was rotated, producing a disk-shaped notch extending up to 40 cm away from the borehole (Fig. 6.3). A simple device, built from a steel tape extending the length of a tube and making a right angle bend at the end of the tube, was inserted into the casing and used to verify and measure the radius of the slot. A hydraulic fracture was created, using a procedure that will be described in detail below, and then the rod and point were reinserted and the lance advanced from 7 to 50 cm. The rod and point were retracted and the procedure repeated, creating a second fracture 7 to 50 cm below the first one. Several fractures were created, stacked one on top of another, from a common borehole.

The actual procedure of hydraulic fracturing was commenced by engaging the injection pump--a Robbins and Meyers Moyno 2J6 CDQ pump was on the grouting rig used in the test (*e* in Figure 6.1). At least 0.02 m^3 (5 gal) of water were pumped downhole first, followed by a *pad* of at least 0.02 m^3 (5 gal) of uncrosslinked gel (without sand). The gel was crosslinked and sand added in concentrations ranging from 240 to 1438 kg of sand per cubic meter of gel (2 to 12 lbs/gal). Two sizes of sand were used in the tests; #5 sand ranges from 0.8 to 1.8 mm with a median of 1.5 mm, whereas #7 sand ranges from 0.4 to 0.9 mm with a

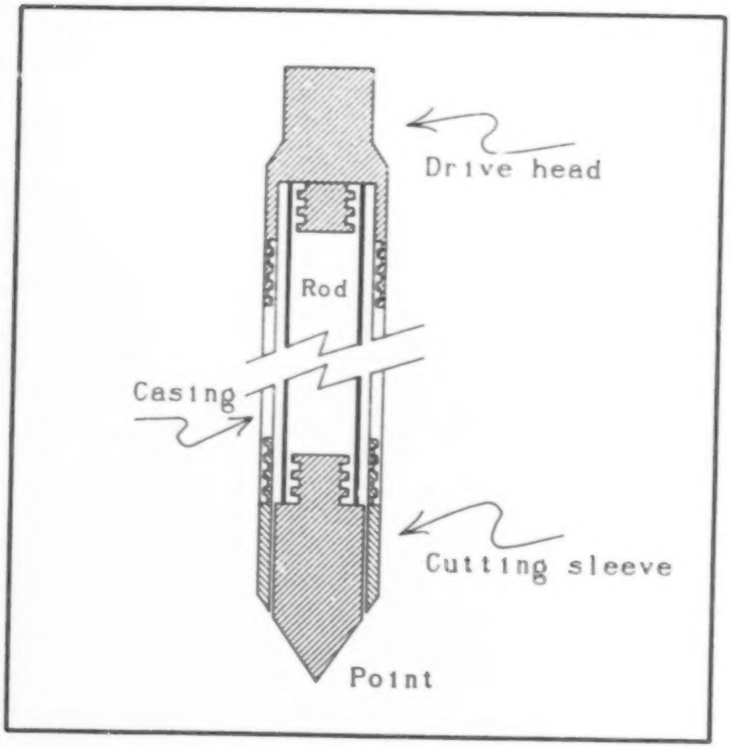
Drive head
Rod
Casing
Cutting sleeve
Point

Figure 6.2. Fracturing lance, used to prepare boreholes for hydraulic fracturing during the 1989 field test.

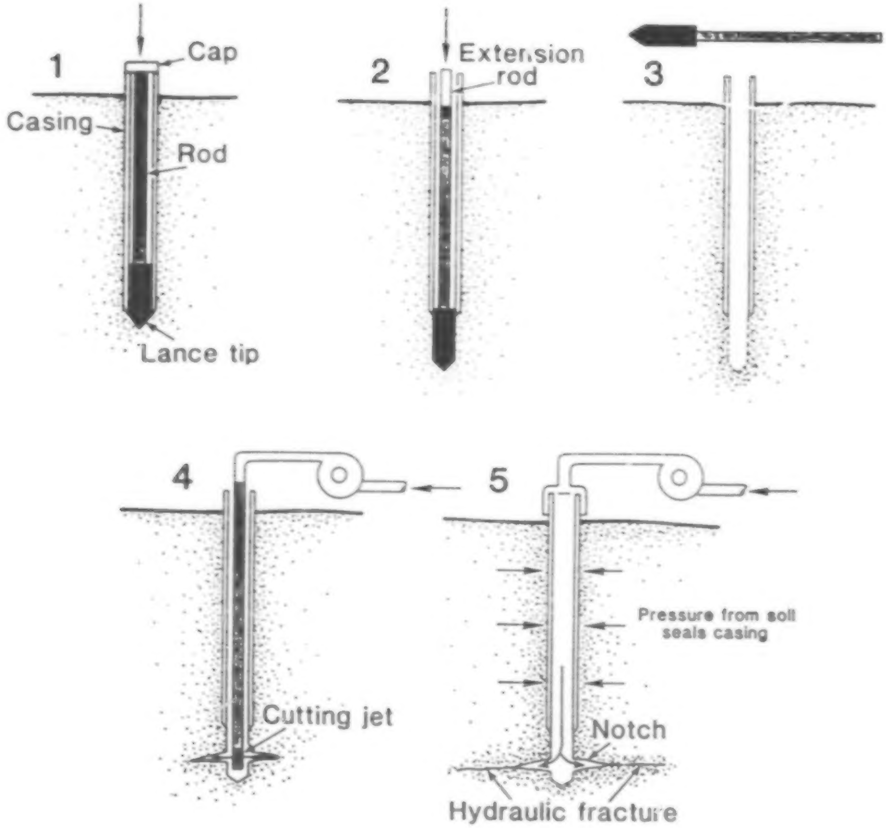
1
Cap
Casing
Rod
Lance tip
2
Extension rod
3
4
Cutting jet
5
Pressure from soil seals casing
Notch
Hydraulic fracture

Figure 6.3. Five steps of hydraulic fracturing: (1) create borehole; (2) extend borehole beyond casing; (3) remove rod and tip of fracturing lance; (4) create starter notch with water jet; (5) create fracture by injecting proppant into notch.

median of 0.75 mm. The sand-laden gel was pumped downhole at a rate of 0.02 to 0.04 m^3/min (5 to 10 gpm).

Injection pressure measured at the top of the borehole increased rapidly to at least 138 kPa (20 psi). As soon as fracturing commences -- typically about 30 seconds after initial engagement of the injection pump -- the pressure dropped abruptly to about 68.9 kPa (10 psi). As pumping progressed, the pressure gradually decreased, although changes in gel viscosity, sand concentration, or pumping rate cause temporary pressure fluctuations.

Assuming unlimited supply of gel and sand, pumping of proppant into the growing fracture would continue until either the fracture vents, or the pump jams. The latter occurs if there is "screen-out", either at the tip of the fracture or at the borehole, causing immobilized sand to back up into the injection hose, or even into the injection pump. At that point, pressure measured by the transducer increases dramatically, and the operation must cease.

Most fracturing episodes performed as part of this study were complete when the planned volume of proppant had been injected.

Discussion of the Fracturing Method

The 1989 tests showed that hydraulic fractures can be created and propped with sand using a simple apparatus intended for injection grouting. An apparatus similar to the one we used should be readily available for rent throughout the United States, and several manufacturers offer similar units for sale.

Use of the lance is more rapid than drilling a borehole and cementing casing, as we did in 1988. Moreover, the technique is versatile; a hole fractured using the lance method can be completed with a gravel pack and screen, or the hole can be left unscreened if a well is not required.

The design of the fracturing lance facilitates the creation of multiple fractures. Of course, methods of creating multiple fractures are well-known in the oil industry, but they commonly require sophisticated packers and explosive charges to perforate casing. The technique used in this research is intended to take advantage of the shallow depths and penetrability of soil, where those sophisticated methods are unnecessary.

There are several drawbacks to the method used during the 1989 tests. The blenders were underpowered, so that mixing sand with crosslinked gel was time consuming. As a result, the rate of blending a batch of sand-laden gel was increased, limiting the injection rate. A more powerful blender, and perhaps another blender design would improve the design.

The progressive cavity pump used to inject slurry suffered excessive wear, and the rotor and stator had to be replaced after pumping almost 11 m^3 (2900 gal) of gel-sand mixtures. The progressive cavity grouting pump, while effective for high concentrations of #7 (0.75 mm grain size) size sand, proved ineffective -- it jammed -- for even moderate to low concentrations of the coarser (1.5 mm grain size), #5 sand. We are currently evaluating several other styles of pump for future applications.

Use of the fracturing lance requires creating hydraulic fractures during drilling of a borehole, rather than after completion of the well. This means that drilling is interupted for fracturing to take place, a practice that would increase the time required to drill each well. Techniques of isolating a zone to be fractured using straddle packers, a common practice in oil wells and water wells, are currently being considered as an alternative to the use of the fracturing lance. In some cases, creating a fracture below the bottom of a borehole and then drilling down through it could result in the deposition of mud, as a skin between the bore and the fracture. Completion and development techniques, which eliminate well-bore skin from the vicinity of hydraulic fractures, will be crucial to obtaining the maximum performance from fractured wells.

SECTION SEVEN

HYDRAULIC FRACTURES CREATED DURING THE FIELD TEST -- 1989

In contrast to fractures created during the field test of 1988, fractures created in 1989 are filled with 5 to 25 mm of sand, making them clearly visible. As in the 1988 field test, fractures were excavated with a backhoe, creating a network of trenches two m deep. Detailed mapping of the trench walls revealed the geometry of the fractures.

A 40 m long, longitudinal trench (trench A, Fig. 7.1) intersects all seven boreholes, and roughly coincides with the minor axes of the elliptical fractures. A 5 to 15 m long, transverse trench also intersects each of the seven boreholes (trenches B - H), roughly coinciding with the major axes of the fractures. A 6 m long trench (trench I), parallel to the longitudinal trench, intersects one of the transverse trenches (trench G).

A horizontal datum line, extending along the entire trench network, was used during mapping. Smooth trench surfaces were cut by knives to allow precise measurement of fracture thicknesses. Dyed proppant sand was barely distinguishable from undyed sand, but the thickness of proppant made dye unnecessary, in contrast to fractures created during the 1988 field test.

Excavation of the trenches was completed one week after creation of the last fracture. Mapping and analysis of the fractures commenced immediately, and continued for three weeks. This section presents the results of mapping and measuring fracture traces in the nine trenches.

QUALITY ASSURANCE AND CONTROL

To assure consistent quality of data, measurements were periodically repeated by different field investigators. Datum lines were checked daily to correct for sagging or other potential sources of inaccuracy.

Accuracy achieved in field analysis of fractures was comparable to accuracy standards for similar analyses of structural field data related to geomechanical studies, or to petroleum exploration and production.

FORMS OF THE HYDRAULIC FRACTURES

At the ELDA site, we created 20 fractures from 7 boreholes, spaced 3.5 to 10 m apart horizontally, and roughly defining a straight line, as shown in Figure 7.1. The boreholes are located on a 10 to 15 m wide bench, bounded to the southwest by a 5 m tall, steep ascent, and to the northeast by a 10 m deep descent. The boreholes are located 2 to 5 m away from the wall. Individual boreholes contain 2 to 5 fractures, spaced 0.1 to 0.3 m apart vertically at the borehole, as indicated in Table 7.1.

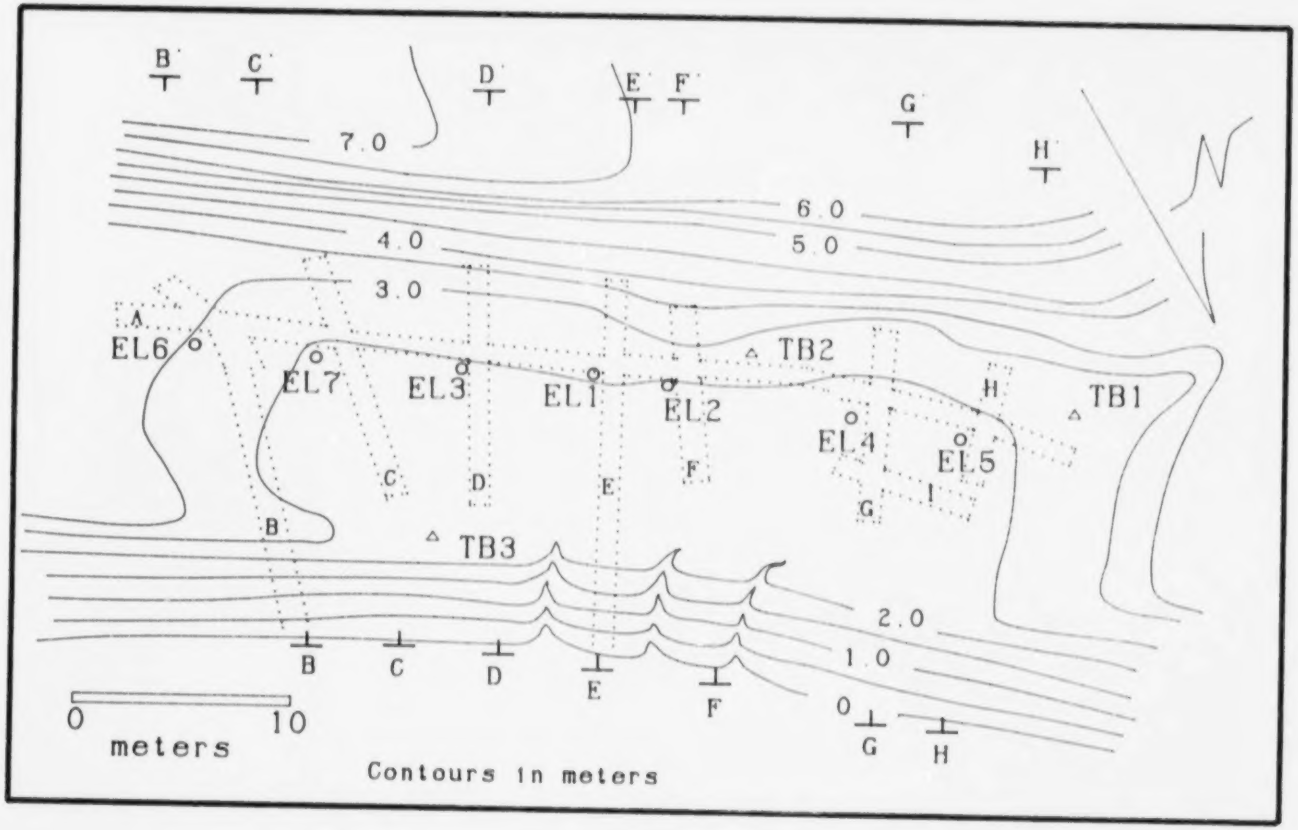
B'
C'
D'
E'
F'
G'
H'
7.0
6.0
5.0
4.0
3.0
A
EL6
EL7
EL3
EL1
EL2
TB2
H
TB1
EL4
EL5
C
D
E
F
I
G
B
TB3
2.0
1.0
0
B
C
D
E
F
G
H
0
10
meters
Contours in meters

Figure 7.1. Map of Elda Landfill site. Solid lines are topographic contours; dotted lines are trench outlines. Locations of boreholes and cross sections are also shown.

TABLE 7.1: FRACTURE SIZE

Fracture	Depth (m)	Major Axis (m)	Minor Axis (m)	Max Dist From BH (m)	Aspect Ratio (m)	Area (m^2)
EL1F1	1.5	8.0	5.0	7.2	1.6	31.4
EL1F2	1.7	4.5	2.0	3.8	2.3	7.1
EL2F1	1.5	5.0	3.5	4.0	1.4	13.7
EL2F2	1.7	3.0	2.0	1.2	1.5	4.7
EL3F1	1.5	8.0	3.5	6.0	2.3	22.0
EL3F2	1.7	5.0	2.5	4.6	2.0	9.8
EL4F1	0.9	5.0	4.0	3.8	1.3	15.7
EL4F2	1.2	7.0	4.0	4.6	1.8	22.0
EL4F3	1.5	5.0	4.5	3.0	1.1	17.7
EL4F4	1.8	4.5	3.5	2.5	1.3	12.4
EL5F1	1.1	8.0	5.0	3.2	1.6	31.4
EL5F2	1.2	7.0	6.0	3.8	1.2	33.0
EL5F3	1.5	3.0	2.5	2.0	1.2	5.9
EL5F4	1.6	1.0	1.0	0.8	1.0	0.8
EL5F5	1.6	----	----	----	----	------
EL6F1	1.4	6.0	5.0	5.0	1.2	23.6
EL6F2	1.6	8.5	5.5	7.0	1.5	36.7
EL6F3	1.9	5.5	4.5	4.0	1.2	19.4
EL7F1	1.3	7.0	5.5	4.4	1.3	30.2
EL7F2	----	7.0	5.0	5.8	1.4	27.5

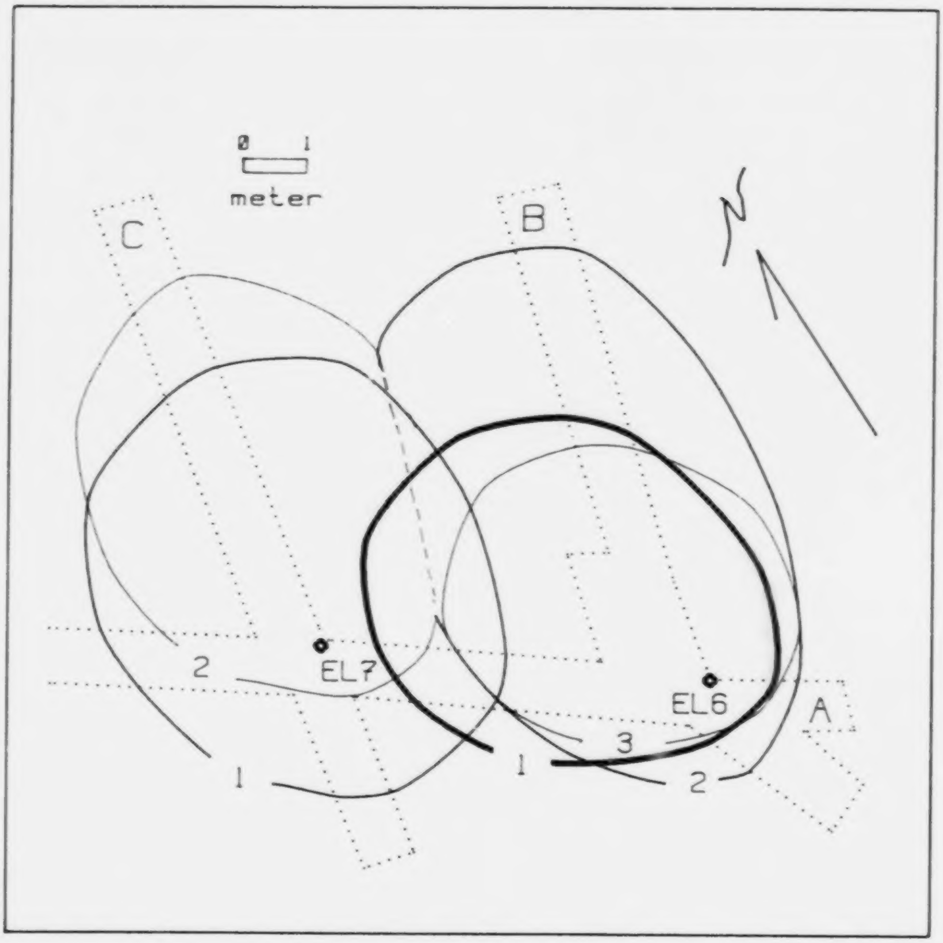
0
1
meter
C
B
N
2
EL7
EL6
A
3
1
1
2

Figure 7.2. Fracture map of trenches B and C. Thickest line shows outline of topmost fracture.

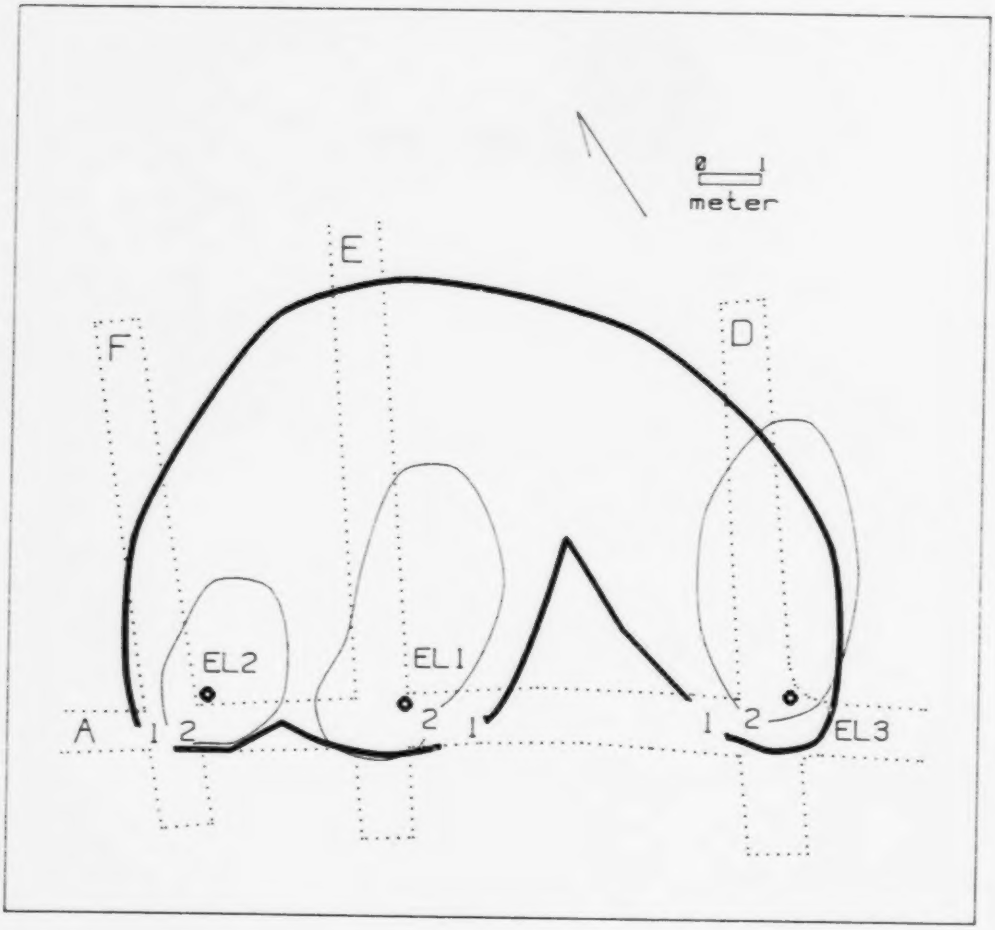
0
1
meter
E
F
D
EL2
EL1
EL3
A
1
2
2
1
1
2

Figure 7.3. Fracture map of trenches D, E and F. Thickest line shows outline of topmost fractures.

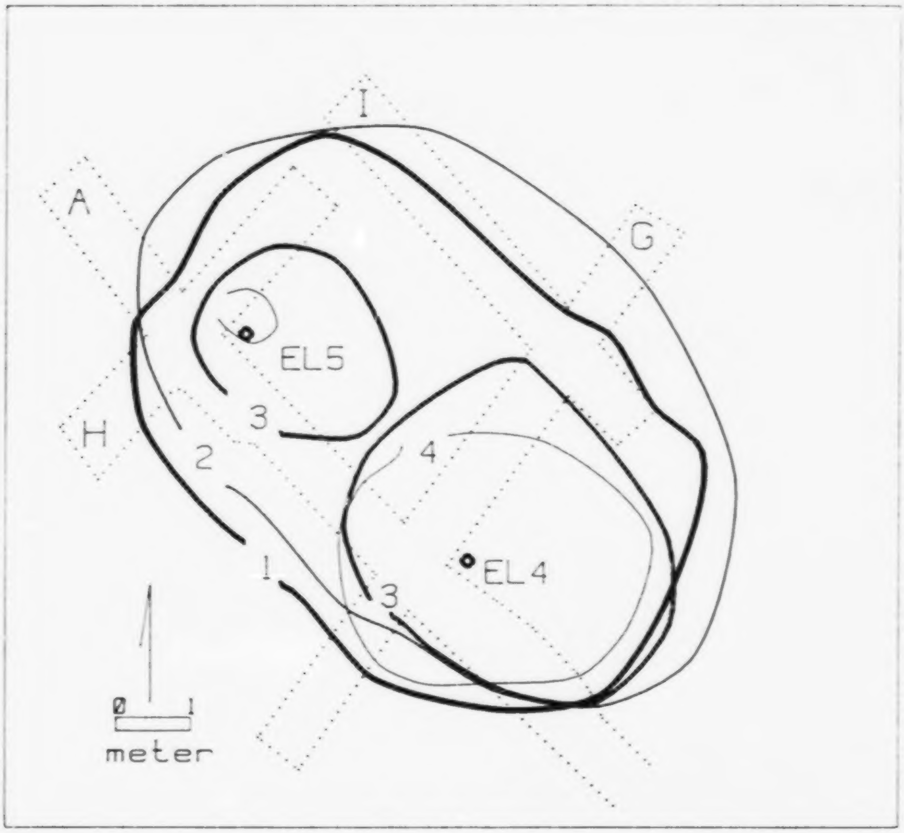
I
A
G
EL5
3
H
2
4
1
EL4
3
0
1
meter

Figure 7.4. Fracture map of trenches G, H and I. Thickest line shows outline of topmost fractures.

Outlines and Dips of Fractures

A network of nine interconnected trenches, shown in Figure 7.1, exposes the fractures and reveals their shapes. Most of the fractures are elliptical in outline, with aspect ratios (length of major axis divided by length of minor axis) ranging from 1.0 (fracture EL5F4 in Figure 7.4) to 2.3 (fracture EL6F2 in Figure 7.2; Table 7.1). The major axes of the fractures are roughly parallel to the dip direction of the ground surface, which is generally parallel to the transverse trenches (trenches B - H) and perpendicular to the wall along the southwest edge of the bench (Figures 7.1-7.4).

Many of the fractures are flat and subhorizontal in cross section, with dips ranging from 0 degrees (fractures El6F2 in Figure 7.12, El3F1 in figure 7.14, El4F1 in Figure 7.17, and EL5F1 and EL5F3 in Figure 7.18); to 5 degrees (fractures EL3F2 in Figure 7.14, and EL1F1 in Figure 7.15). Some fractures are subhorizontal near the borehole, and dip toward the borehole by up to 15 degrees near the fracture margin, thus resembling a shallow bowl or plate (fractures EL6F1 in Figure 7.12, EL7F2 in Figure 7.13, and EL4F3 and EL4F4 in Figure 7.17).

The deepest point of each fracture, which coincides with the borehole in almost all cases, is located near the end of the major axis, close to the wall along the southwest edge of the bench (Figures 7.1-7.4). The only notable exception is fracture EL4F5 (Figure 7.17), in which the deepest point is located approximately 1.3 m north of the borehole, and the borehole is located near the center of the fracture, but closer to the downslope (northeast) edge of the fracture than to the wall along the southwest side of the bench (Figures 7.1 and 7.17).

Venting of Fractures

Five of the fractures created at the ELDA site vented onto the slope northeast of the bench. Fractures EL1F1 and EL2F2 both vented along the same horizon. Fractures EL2F1 and EL3F1 each vented along horizons above the EL1F1 venting horizon. Finally, fracture EL3F2 vented along both the EL3F1 and EL1F1 venting horizons. The vertical distance between the three venting horizons is about 30 cm.

Fluid that vented from all of those fractures was virtually devoid of sand, even though the fluid was laden with sand when injected. Sand proppant filled all the fractures, but it terminated several m before the point of venting, according to exposures on transverse trenches cut along lines between boreholes and vents. Two scenarios seem possible: either the aperture of the fractures in the vicinity of the vents was too small to permit the passage of sand, or sand was deposited because the gel that was carrying it leaked off--this is termed "tip-screenout" by Smith and others (1987). In either case, the gel was separated from the sand by straining through immobilized sand at the fracture tip.

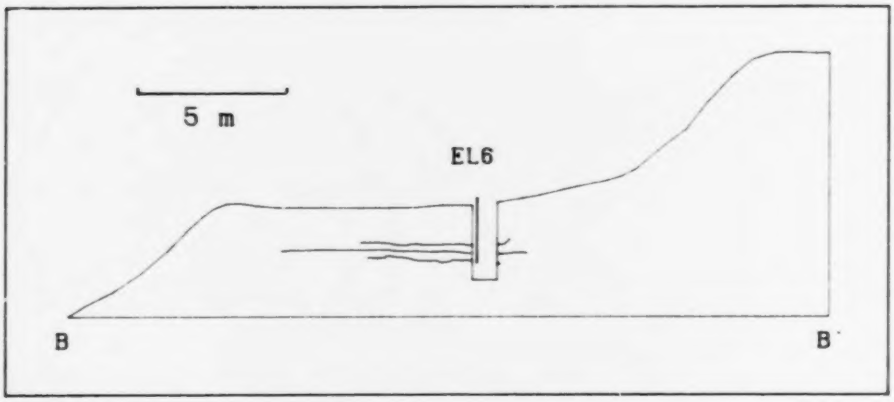

Figure 7.5. Cross section B-B'. See Figure 7.1 for location.

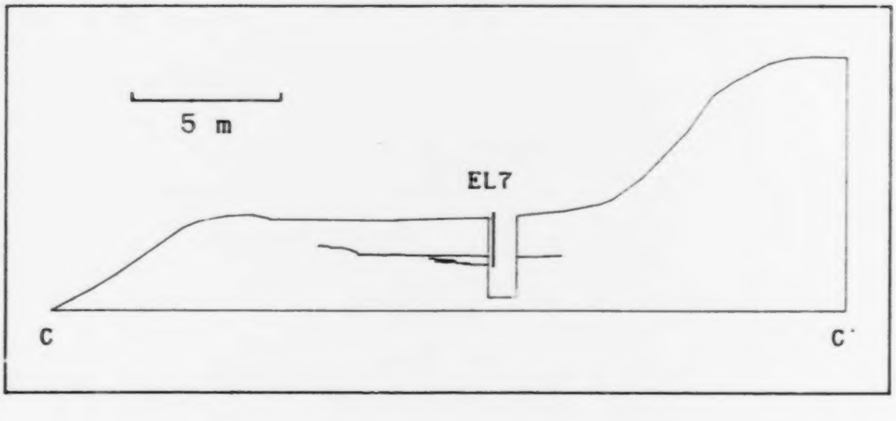

Figure 7.6. Cross section C-C'. See Figure 7.1 for location.

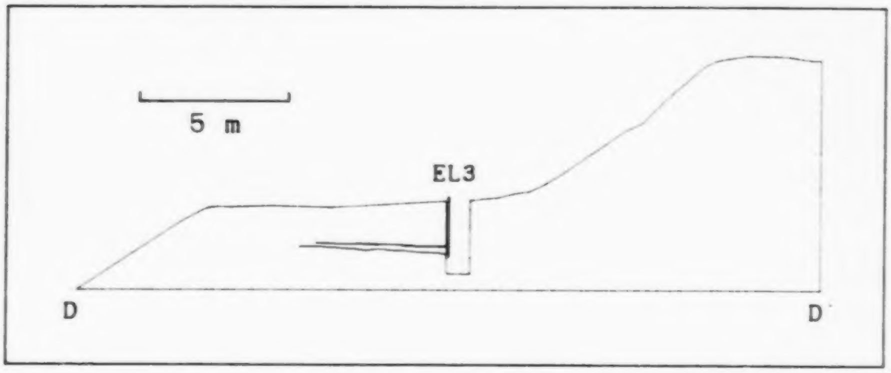

Figure 7.7. Cross section D-D'. See Figure 7.1 for location.

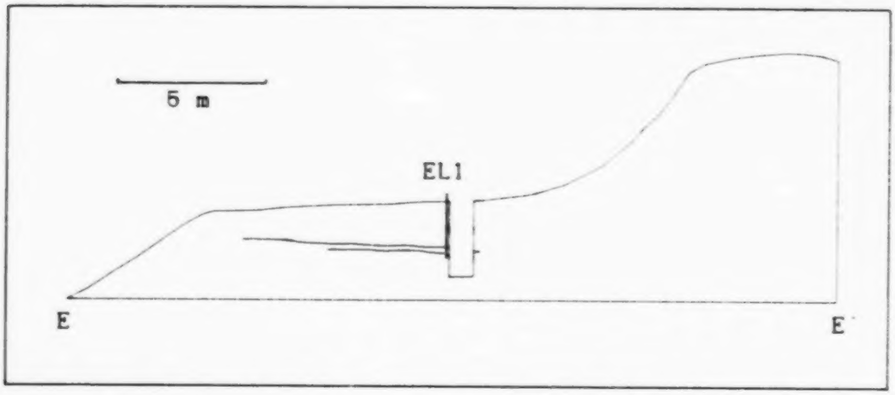

Figure 7.8. Cross section E-E'. See Figure 7.1 for location.

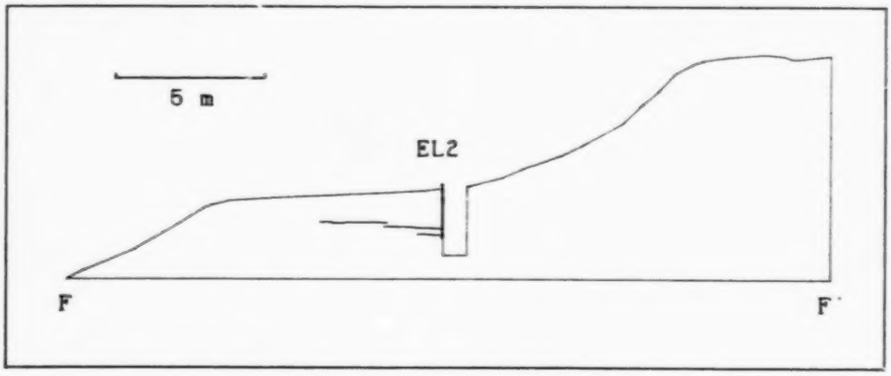

Figure 7.9. Cross section F-F'. See Figure 7.1 for location.

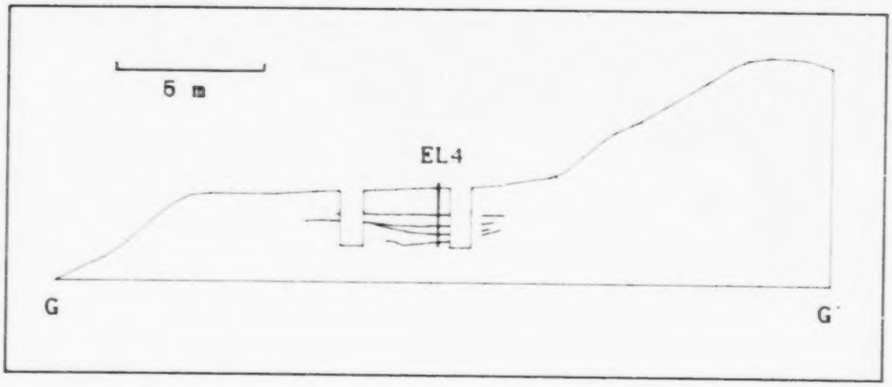

Figure 7.10. Cross section G-G'. See Figure 7.1 for location.

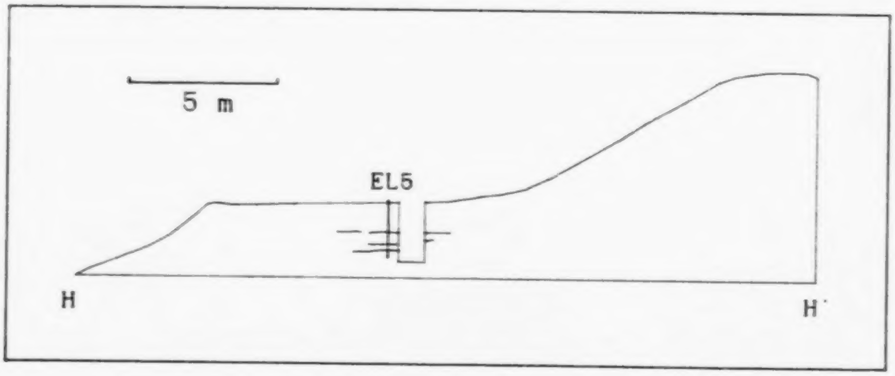

Figure 7.11. Cross section H-H'. See Figure 7.1 for location.

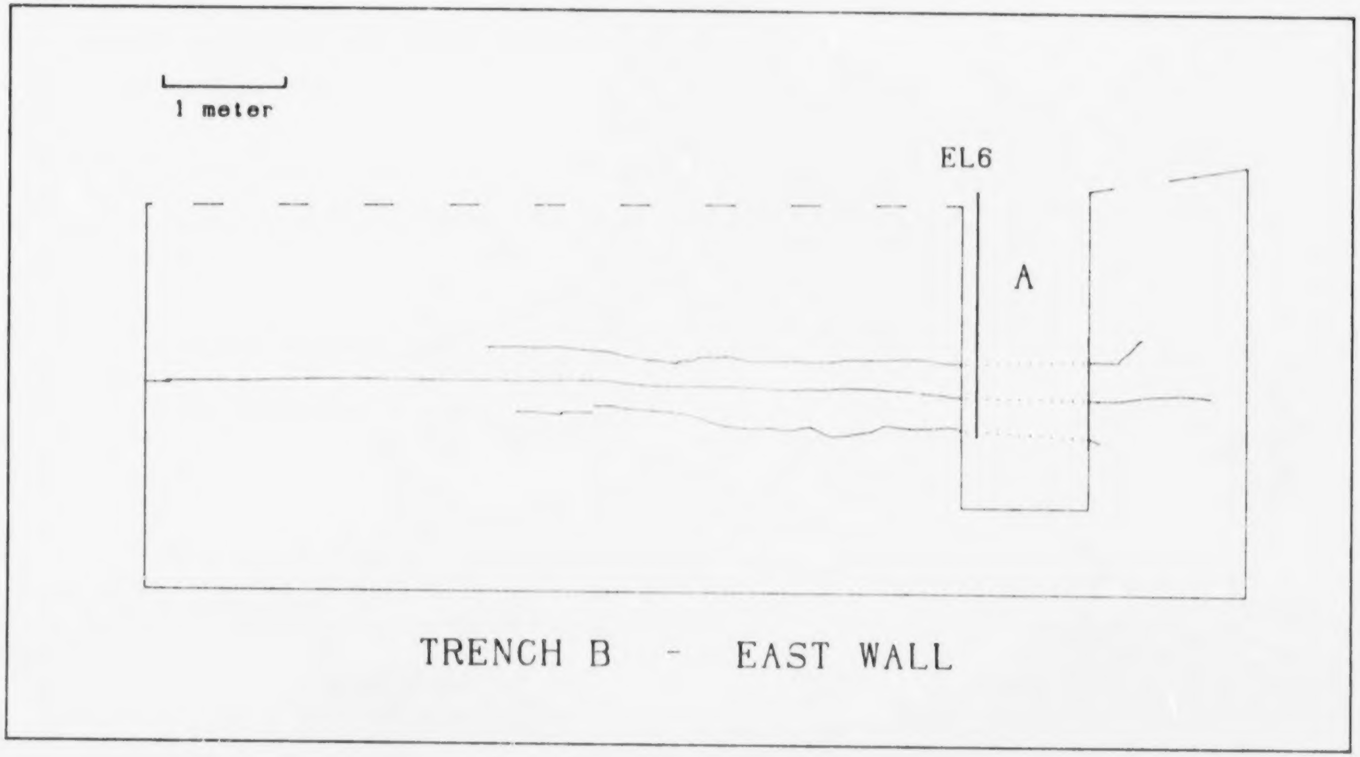
1 meter
EL6
A
TRENCH B - EAST WALL

Figure 7.12. Map of east wall of trench B, showing fracture traces, borehole and ground surface (dashed).

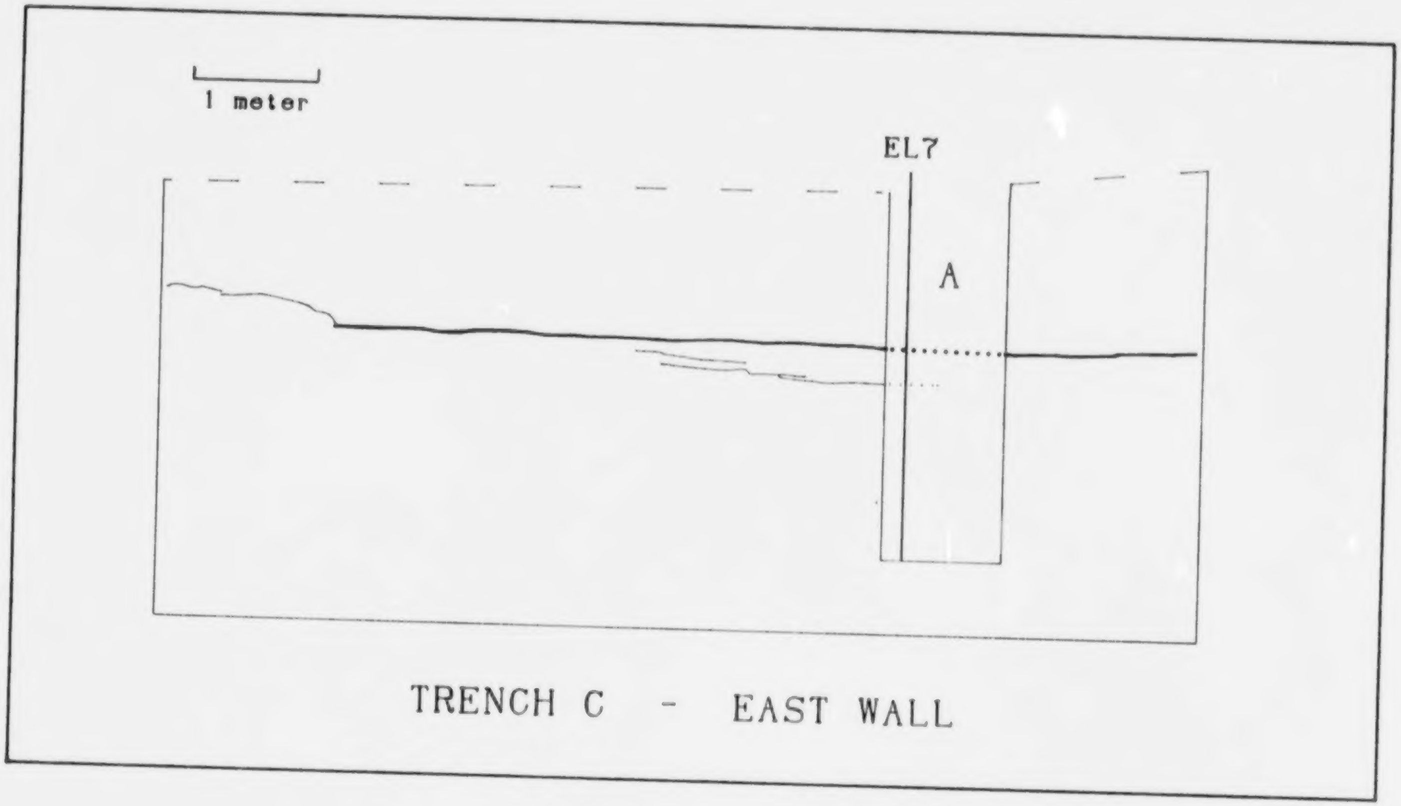
1 meter
EL7
A
TRENCH C - EAST WALL

Figure 7.13. Map of east wall of trench C, showing fracture traces, borehole and ground surface (dashed). Thick fracture is filled with perlite.

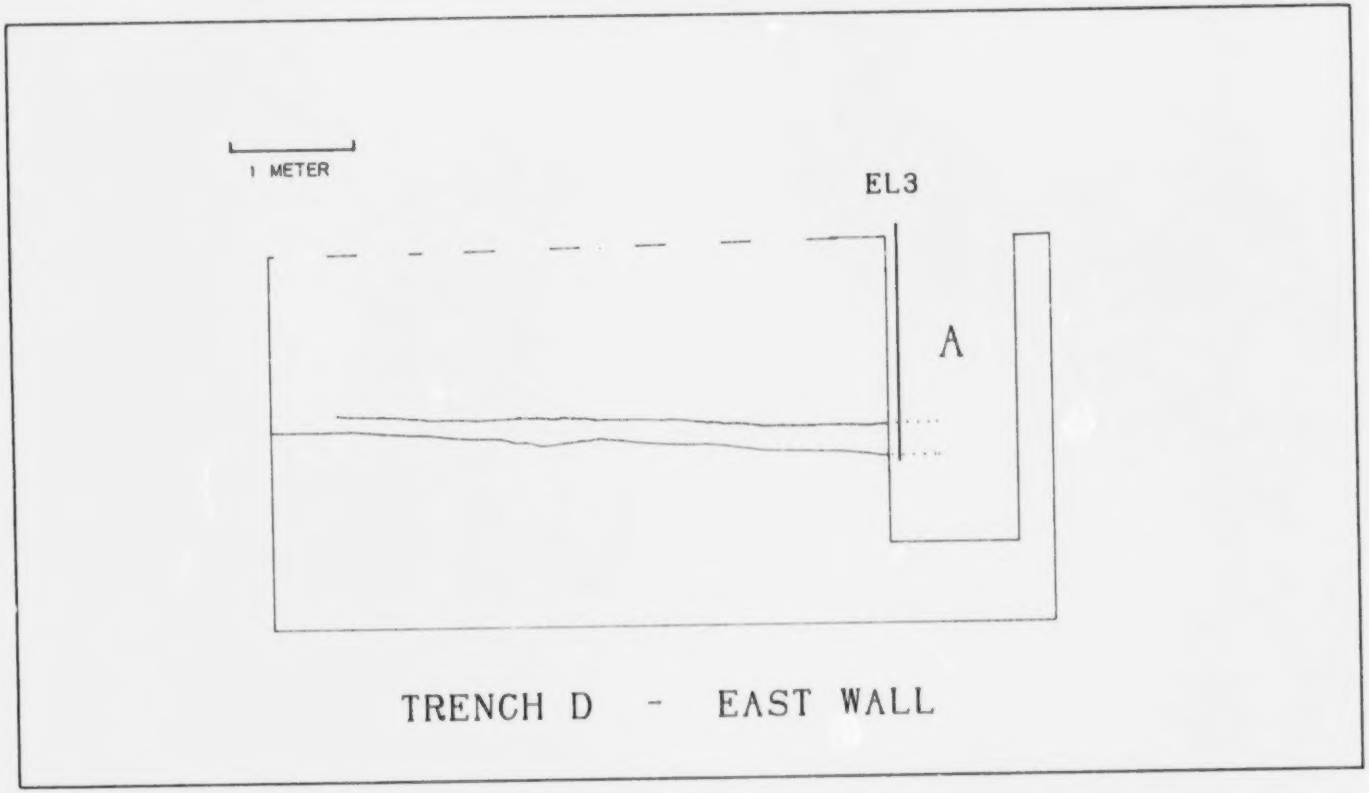
1 METER
EL3
A
TRENCH D - EAST WALL

Figure 7.14. Map of east wall of trench D, showing fracture traces, borehole and ground surface (dashed).

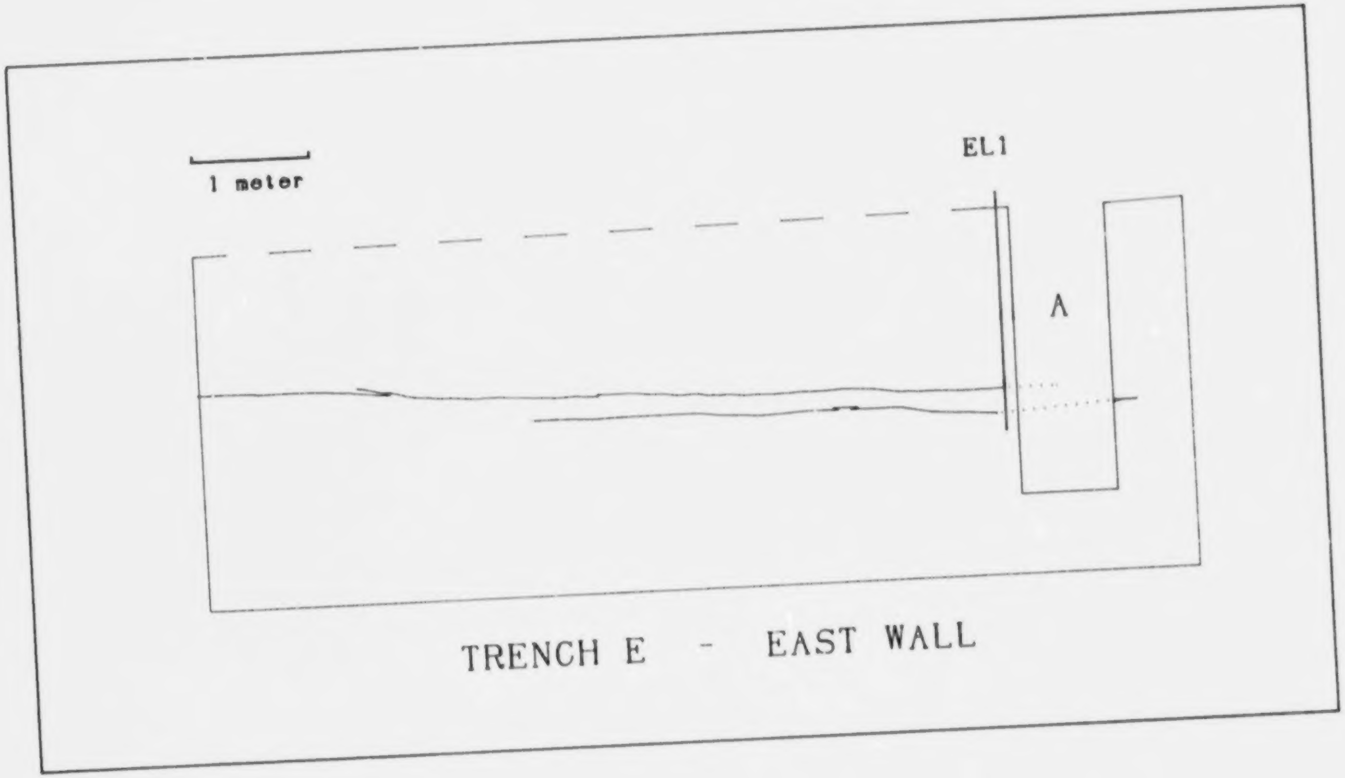
1 meter
EL1
A
TRENCH E - EAST WALL

Figure 7.15. Map of east wall of trench E, showing fracture traces, borehole and ground surface (dashed).

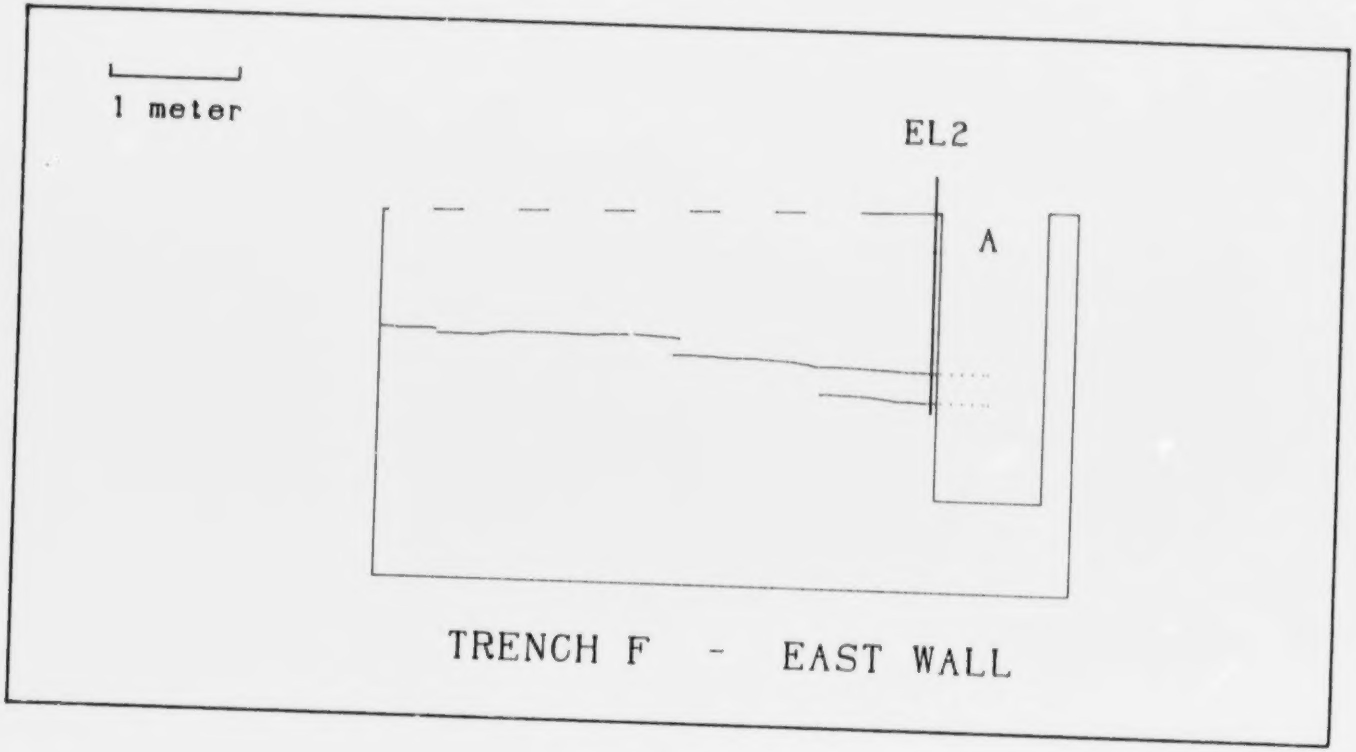
1 meter
EL2
A
TRENCH F - EAST WALL

Figure 7.16. Map of east wall of trench F, showing fracture traces, borehole and ground surface (dashed).

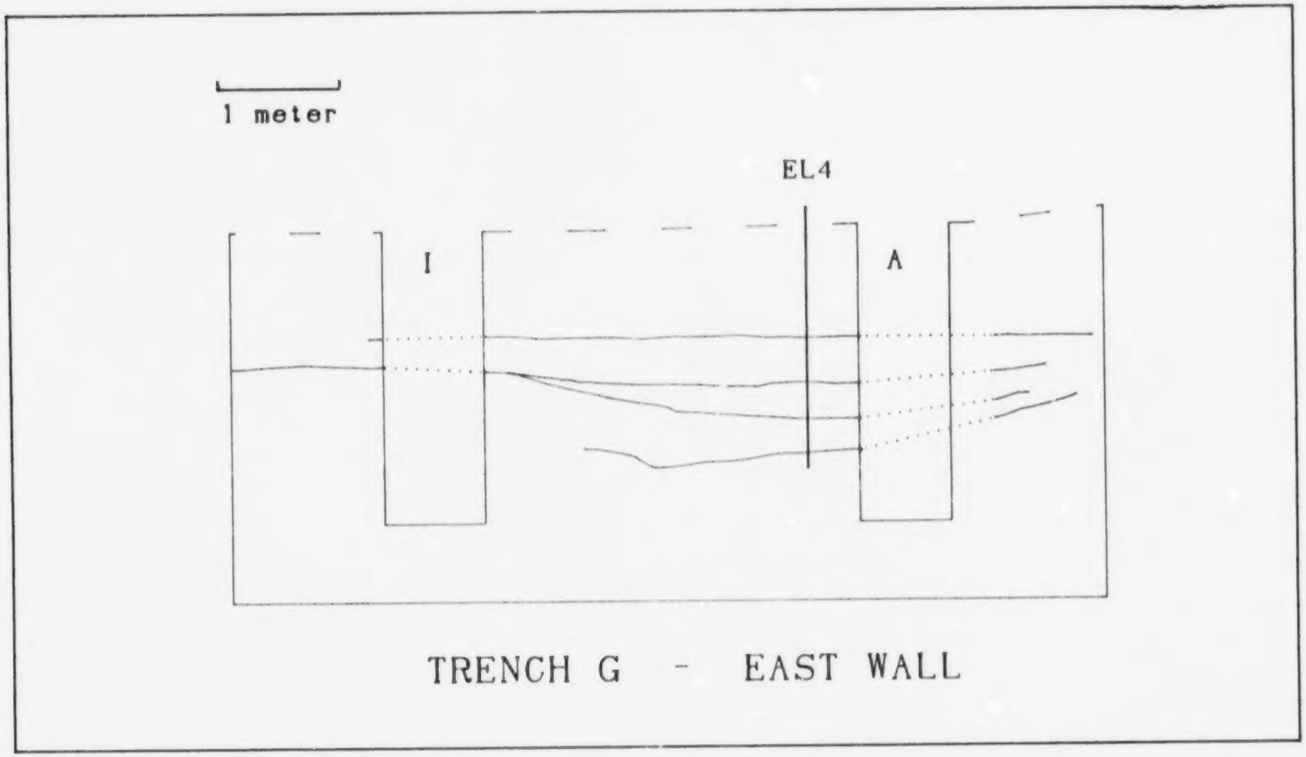
1 meter
EL4
I
A
TRENCH G - EAST WALL

Figure 7.17. Map of east wall of trench G, showing fracture traces, borehole and ground surface (dashed).

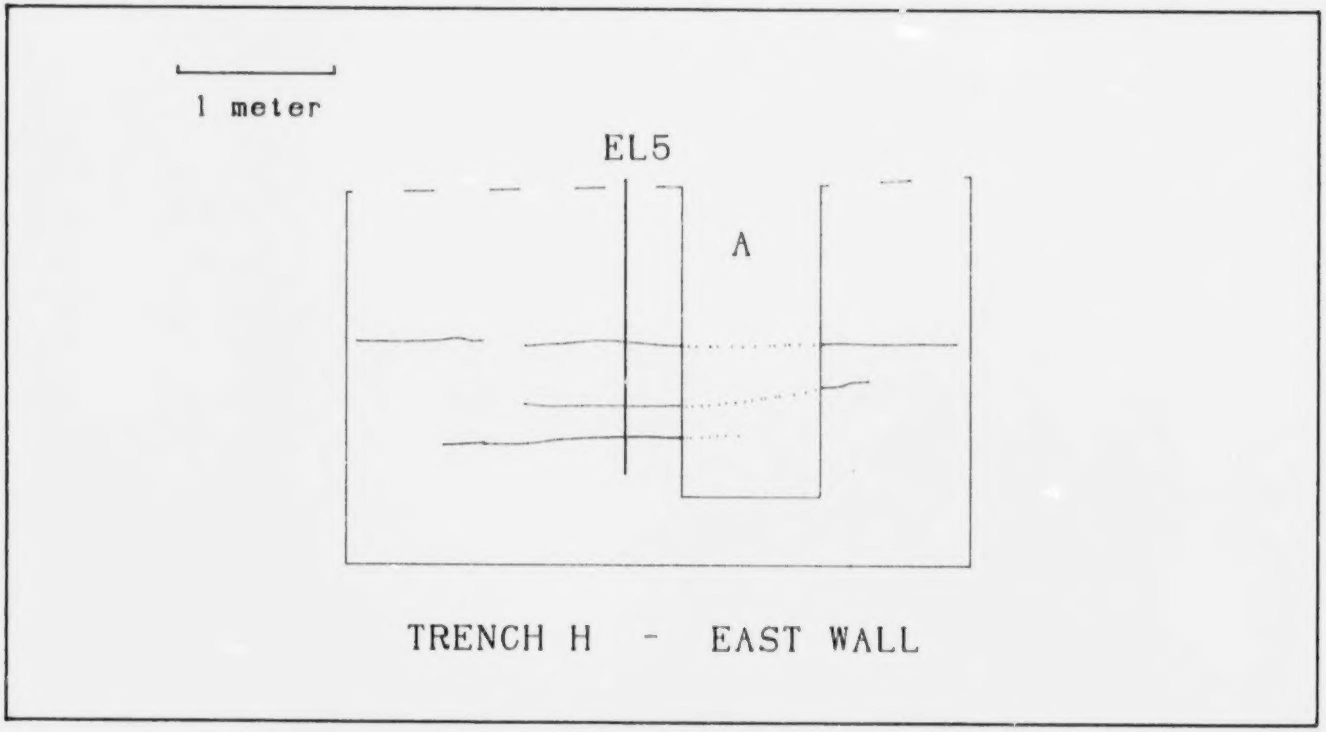
1 meter
EL5
A
TRENCH H - EAST WALL

Figure 7.18. Map of east wall of trench H, showing fracture traces, borehole and ground surface (dashed).

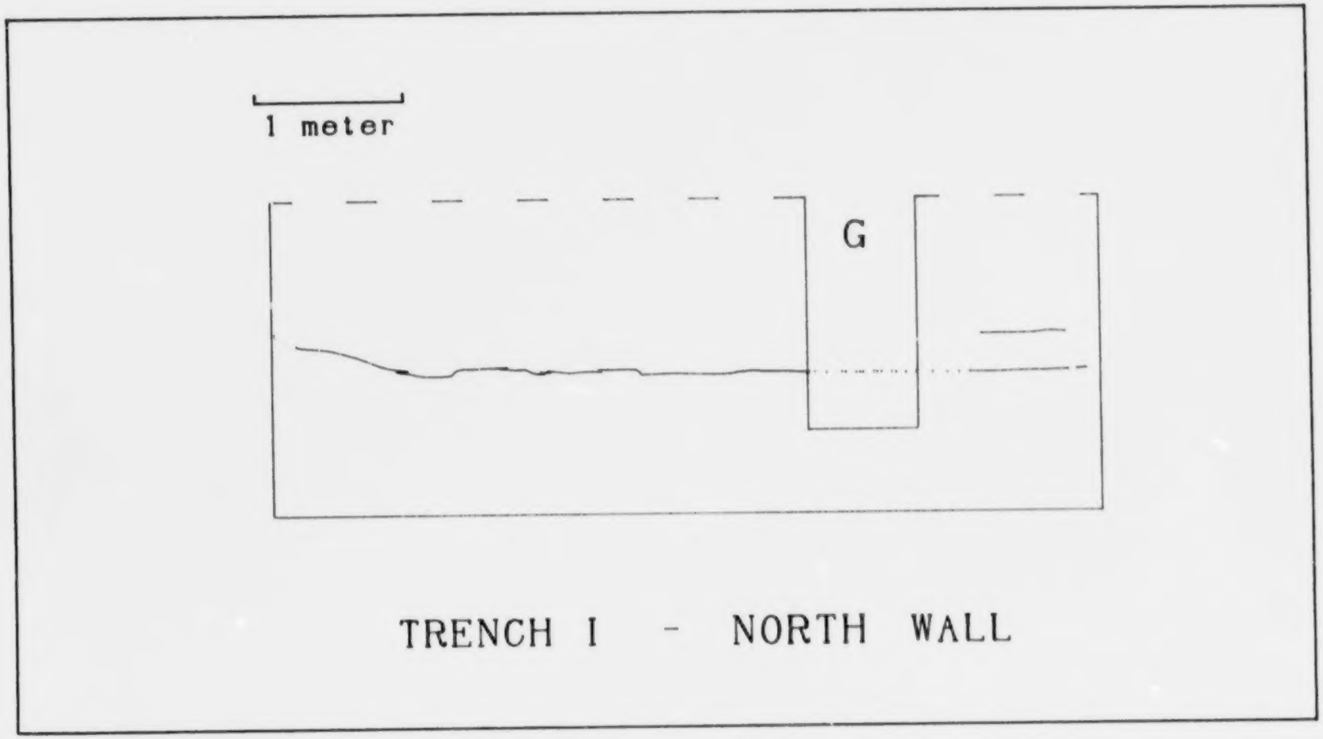
1 meter
G
TRENCH I - NORTH WALL

Figure 7.19. Map of north wall of trench I, showing fracture traces and ground surface (dashed).

Continuity of Fractures

Traces of fractures along trench walls, roughly coincidental with the major axes, are commonly continuous. Continuous fractures represent over half (61%) of the 18 fractures exposed along major-axis cross sections, including fractures EL3F1-F2 (Figure 7.14), EL4F1-F4 (Figure 7.17), EL6F1-F2 (Figure 7.12), and EL7F1 (Figure 7.13). The remaining 39% of fractures exhibit at least one discontinuity along the major-axis cross section.

Discontinuities along fractures either step up or step down, in the direction pointing away from the borehole (toward the fracture tip). Most discontinuous fractures step up by 2 to 12 cm, at lateral intervals of 1 to 2 m. Up-stepping fractures include EL2F1 (Figure 7.16), EL5F1-F2 (Figure 7.18), and EL7F2 (Figure 7.13), representing 22% of all fractures. Some fractures step downward by 4 to 8 cm, about 0.8 of the distance from the borehole to the fracture tip. Down-stepping fractures include EL1F1 (Figure 7.15) and EL6F3 (Figure 7.12), representing 11% of the fractures. Finally, one fracture, EL1F2 (Figure 7.15), steps up by 2 cm at a distance of 1.5 m from the borehole, and steps back down again by 2 cm at a distance of 1.7 m from the borehole. This up-down-stepping fracture represents 6% of the total fracture count.

Fractures that are discontinuous on a trench wall are expected to be joined somewhere out of the plane of the wall. Exposures were insufficient to verify this expectation.

Fracture Margins

The cross sections exposed in the trenches do not afford a clear view of fracture margins, since the terminations of fractures occur only as single points in the cross sections. We did not excavate a fracture surface at its margin, due to time constraints. Our assumption, hence, is that the fracture margins are generally smooth, as shown in Figures 7.2-7.4.

Some evidence suggests that fracture margins may be lobate. Trench I, which reveals the only cross section perpendicular to the direction of proppant flow and at some distance away from the borehole, exposes the trace of merged fractures EL4F2 and EL5F2 (Figure 7.19). Fracture EL4F2 contains weight #5 sand, whereas fracture EL5F2 contains weight #7 sand (Table 7.3). The merged fractures exhibit lenses of weight #5 sand, 10 to 20 cm wide in the horizontal direction, separated by 10 to 40 cm long fracture segments dominated by weight #7 sand. In some cases the lenses of #5 sand are separated by fracture segments occupied exclusively by #7 sand, particularly in the north wall of Trench I (Figure 7.19). These observations suggest that the proppant in fracture EL4F2 propagated along a lobate front.

Coalescence of Fractures

Fractures created at equal depths in neighboring boreholes are prone to merging. The topmost (first) fractures created at boreholes EL6 and EL7 -- EL6F1

TABLE 7.2: FRACTURE THICKNESS

Fracture	Fracture Thickness (mm)	Max Thick. Distance (m)	Borehole Uplift (mm)	Ave Notch Radius (cm)	Max Notch Radius (cm)
EL1F1	11.0	5.0	9.0	15.2	17.8
EL1F2	4.0	1.5	------	14.0	14.0
EL2F1	5.0	3.5	3.0	10.2	12.7
EL2F2	2.0	0.5	3.0	10.2	11.4
EL3F1	8.0	3.5	5.0	11.4	12.7
EL3F2	11.0	2.5	4.0	------	------
EL4F1	8.0	1.0	13.0	17.8	22.9
EL4F2	17.0	2.5	15.5	17.8	20.3
EL4F3	17.0	2.5	11.5	17.8	27.9
EL4F4	16.0	1.5	25.0	11.4	12.7
EL5F1	11.0	2.0	20.5	15.2	19.1
EL5F2	12.0	2.0	17.0	15.2	15.2
EL5F3	10.0	1.5	7.5	19.1	20.3
EL5F4	7.0	0.5	9.0	25.4	38.1
EL5F5	-----	------	------	20.3	26.7
EL6F1	14.0	2.0	------	19.1	22.9
EL6F2	13.0	2.0	------	12.7	15.2
EL6F3	13.0	2.5	------	19.1	38.1
EL7F1	20.0	2.5	23.1	15.2	17.8
EL7F2	10.0	1.5	------	17.8	40.6
GE1F1	------	------	------	------	------
GE1F2	------	------	11.3	------	------
GE2F1	------	------	------	8.9	10.2
GE2F2	------	------	------	------	------
GE3F1	------	------	99.5	------	------

and EL7F1 (Figure 7.2) -- may merge laterally to form a large, single fracture. The two boreholes are spaced 4.5 m apart. Similarly, the topmost fractures at boreholes EL1, EL2 and EL3 -- EL1F1, EL2F1 and EL3F1 -- merge to form a 12 m long, continuous fracture (Figure 7.3). There is a continuous fracture at the topmost (F1) horizon between boreholes EL1 and EL2, which are only 3.25 m apart, but there is a 3 m gap between the tips of fractures EL1F1 and EL3F1 along the cross section connecting the two boreholes, which are 6.25 m apart (Figure 7.3). The two fractures, EL1F1 and EL3F1, merge at an unknown distance north of boreholes EL1 and EL3, indicated by the fact that they vent along the same horizon. The topmost fractures at boreholes EL4 and EL5, spaced 4.25 m apart, also merge, forming a single fracture (Figure 7.4). The fracture is 10 m long, with major axis parallel to the line connecting the boreholes, and with an approximate area of 47 m^2. (Figure 7.4).

The topmost fractures (F1) were created at approximately the same depth (1 m) at all seven boreholes. The greatest distance between two boreholes with a continuous fracture at the F1 horizon, along the cross section connecting the boreholes, is 4.5 m (EL4F1 and EL5F1 in Figure 7.4). The smallest distance between two boreholes (EL1 and EL3) with a unfractured gap between the two F1 fractures, along the cross section connecting the boreholes, is 6.25 m. Those two fractures apparently merged north of the boreholes (EL1F1 and EL3F1 in Figure 7.3) because fluid vented during the formationof EL3F1 at the same location as EL1F1. The smallest distance between two boreholes (EL3 and EL7) with no apparent merging of the F1 fractures is 6.5 m. This suggests that, for injection of the volumes of gel and sand injected into till at the ELDA site, about 6 meters is the maximum distance allowable between boreholes if connectivity of fractures at the same horizon is desirable.

Only two cases of a fracture coalescing with an overlying fracture are documented by the trench sections. The first is in the east wall of Trench C (Figure 7.13), where perlite-filled fracture EL7F2, created 30 cm below sand-filled fracture EL7F1, merges with the overlying fracture at a distance of 2 m north of the borehole. The relatively rapid rise of the perlite-filled fracture probably occurred because the density of the perlite slurry was less than that of the sand slurries. The only example of a rapidly rising, sand-filled fracture merging with an overlying fracture occurs in the east wall of Trench G (Figure 7.17), where fracture EL4F3, created 30 cm below fracture EL4F2, merges with the overlying fracture at a distance of 2.5 m north of the borehole. The concentration of sand in EL4F3 is similar to other, more flat-lying fractures (Table 7.3).

Coalescence of several other pairs of fractures, stacked closely together at the borehole, is inferred from indirect evidence. The fracture EL2F2 was observed to vent from the same horizon as the vent of EL2F1, which was 15 cm above EL2F2 at the borehole. It seems likely that EL2F2 coalesced at some point with EL2F1, even though they appear to be separated in all trench exposures. The same evidence indicates that EL3F2 merged with EL3F1.

In all those cases, the fractures coalesced several m away from the borehole. Two fractures, EL5F3 and EL5F4, merged very close (<20 cm) to the borehole and the two were indistinguishable except in the vicinity of the borehole. The fracture EL5F4 was created 7 cm below EL5F3, the closest spacing we attempted. The

TABLE 7.3: PROPPANT CONCENTRATION

Fracture	Sand Size	Total Sand (#)	Total Gel (gal)	Injected Conc (#/gal)
EL1F1	#7	300	150	2.0
EL1F2	#7 & #5	200	50	4.0
EL2F1	#7	200	130	1.5
EL2F2	#7	500	100	5.0
EL3F1	#7	200	100	2.0
EL3F2	#7	200	40	5.0
EL4F1	#7	200	50	4.0
EL4F2	#5	100	50	2.0
EL4F3	#7	300	50	6.0
EL4F4	#7	250	50	5.0
EL5F1	#7	300	45	6.7
EL5F2	#7	300	45	6.7
EL5F3	#7	400	95	4.2
EL5F4	#5	300	45	6.7
EL5F5	#7	300	45	6.7
EL6F1	#7	600	80	7.5
EL6F2	#7	600	65	9.2
EL6F3	#7	600	50	12.0
EL7F1	#7	1200	130	9.2
EL7F2	PERLITE	50	25	2.0
GE1F1	#7	1200	175	6.9
GE1F2	#7	1200	190	6.3
GE2F1	#7	200	40	5.0
GE2F2	#7	1100	155	7.1
GE3F1	#7	3500	500	7.0

TABLE 7.4: FLOW PARAMETERS

Fracture	Pad Size (gal)	Flow Rate (gal/min)	Peak Pressure (psi)	Stress Intensity kPa(cm$^{.5}$)
EL1F1	5 H20	5	28	698
EL1F2	5 H20	5	21	450
EL2F1	5 H20	10	49	1090
EL2F2	5 H20	10	29	582
EL3F1	5 H20	15	40	920
EL3F2	5 H20	15	13	-----
EL4F1	15 H20	5	36	1082
EL4F2	5 H20	5	31	885
EL4F3	5 H20	5	11	197
EL4F4	5 H20	5	26	526
EL5F1	15 H20	5	32	865
EL5F2	5 H20	5	27	698
EL5F3	5 H20	5	18	441
EL5F4	5 H20	5	7	72
EL5F5	5 H20	5	-----	-----
EL6F1	5 H20 10 GEL	5	24	662
EL6F2	5 H20 10 GEL	5	35	824
EL6F3	5 H20 10 GEL	5	46	1355
EL7F1	5 H20 10 GEL	5	44	1209
EL7F2	5 H20	5	26	852
GE1F1	5 H20 10 GEL	5	38	-----
GE1F2	5 H20 10 GEL	5	85	-----
GE2F1	5 H20 5 GEL	4	29	568
GE2F2	5 H20 10 GEL	4	115	-----
GE3F1	5 H20 10 GEL	5	85	-----

trench cross section (Figure 7.18) does not show this coalescence, because of the scale of the cross section.

We conclude that, for the conditions of the ELDA site, vertical fracture spacings of 30 cm will typically result in distinct fractures. Vertical spacings of 15 cm will result in fractures that merge locally but remain distinct elsewhere, whereas vertical spacings of 7 cm will result in fractures that rapidly merge. Spacings between 15 and 30 cm probably would be a reasonable lower limit.

Surface Texture of Fractures

Cross sections of the fractures (Figures 7.12-7.19) exhibit few undulations or other signs of roughness along the fractures. Borehole EL6 (Figure 7.12) contains good examples of both a typical, smooth fracture -- EL6F2 -- and an exceptionally rough, undulose fracture -- EL6F3. There is no significant difference between the injected sand concentration of the two fractures, so the difference in surface texture, as expressed in the fracture traces, is assumed to be due to inhomogeneities of the soil profile.

DIMENSIONS OF THE HYDRAULIC FRACTURES

Surface areas of the fractures created at the ELDA site, estimated from fracture outlines shown in Figures 7.2-7.4, range from less than one square meter to over sixty square meters (Table 7.1). Data shown in Tables 7.1 and 7.3 reveal no statistically significant correlations between surface areas of fractures on one hand, and injected proppant volumes or injected sand concentrations on the other hand.

Comparison of the relationship between total injected volume of gel and sand (Table 7.3) versus fracture surface area (Table 7.1), for gels with relatively high sand concentrations (600 to 750 kg of sand per cubic meter of gel; 6.0-7.5 lbs/gal), reveals an increase of area by 0.14 square meters per additional 0.004 m^3 (gal) of proppant. For lower sand concentrations 400 to 500 kg/m^3 (4.0-5.0 lbs/gal), the data indicate a decrease of area by 0.07 square meters per additional 0.004 m^3 (gal). These data suggest that factors other than proppant volume influence the surface area of hydraulic fractures. A fracture tip screen-out could inhibit propagation, thereby limiting their surface area.

Comparison of the relationship between the concentration of sand in the injected proppant, measured as pounds of sand per gallon of gel (Table 7.3), versus fracture surface area (Table 7.1), for fractures within narrow ranges of total volume of injected proppant, indicates an increase of area by two to seven square meters per additional pound of sand per gallon of gel. Assuming that sanding-out at fracture tips influences fracture surface area, as suggested above, these data indicate that the likelihood of early "sand-out," and, consequently, of small surface area, is not directly related to the sand concentration, as intuition might suggest. Clearly, more work is needed toward an understanding of hydraulic fracture propagation.

THICKNESS PROFILES OF THE HYDRAULIC FRACTURES

Trenches B through H provide an excellent opportunity to measure the thickness of proppant sand along the major axes of fractures (Figures 7.20-7.26). Although thickness commonly varies by two to five mm over distances of 20 cm or less, third order regression yields asymmetric curves with maximum thickness close to the center of the fracture, and hence, northeast of the borehole. Thirteen fractures (72%) are skewed away from the borehole, so that the midpoint along the fracture trace is located between the point of maximum thickness and the borehole. Four fractures (22%) are skewed toward the borehole, so that the point of maximum thickness is located between the fracture midpoint and the borehole (EL2F2, EL3F2, EL4F4 and EL6F2). Only one fracture (EL4F1) exhibited a symmetrical thickness profile, in which the distance between the fracture midpoint and the point of maximum thickness is less than 10% of the distance between the fracture midpoint and the edge of the fracture.

DIRECTION OF PROPAGATION

Most of the fractures propagated preferentially in the downslope direction, as shown in Figures 7.5-7.11. Maps of fracture outlines (Figures 7.2-7.4), as well as measurements of major axis lengths and maximum distances from boreholes (Table 7.1), indicate that the distance from the borehole to the downslope edge of a fracture may be as much as seven times longer than the distance from the borehole to the upslope end of the fracture. Clearly, the additional overburden pressure on the upslope side prevented fracture propagation under the steep bank bounding the southwest edge of the bench (Figures 7.1, 7.5-7.11).

Contours of the uplift of ground surface during fracturing, discussed in the next section, indicate slightly different orientations of major and minor semi-axes of the elliptical fracture outlines defined by uplift contours than the orientations indicated by trench cross sections. In both cases, though, the direction of propagation is clearly downhill.

DISCUSSION

In some respects, hydraulic fractures created during the 1989 tests are remarkably similar to the ones created during 1988; in plan, both are elongate with aspect ratios of 2:3, and they are highly asymmetric with respect to their parent boreholes. In other respects, fractures created during the two years are much different. Those created during 1989 are nearly flat-lying, and none climbed to the ground surface to vent. Where they did vent, the fractures grew horizontally until they intersected a downwardly sloping ground surface, much like HF13 from the 1988 tests.

The fractures created in 1989 were slightly smaller in area than those of the previous year; however, the sizes of the all the 1988 fractures were limited by venting, whereas most of the 1989 fractures did not vent and they could have been larger if more fluid was pumped into them. Sand filled all the fractures created in 1989, whereas it only filled a few during the 1988 tests. The average thickness of

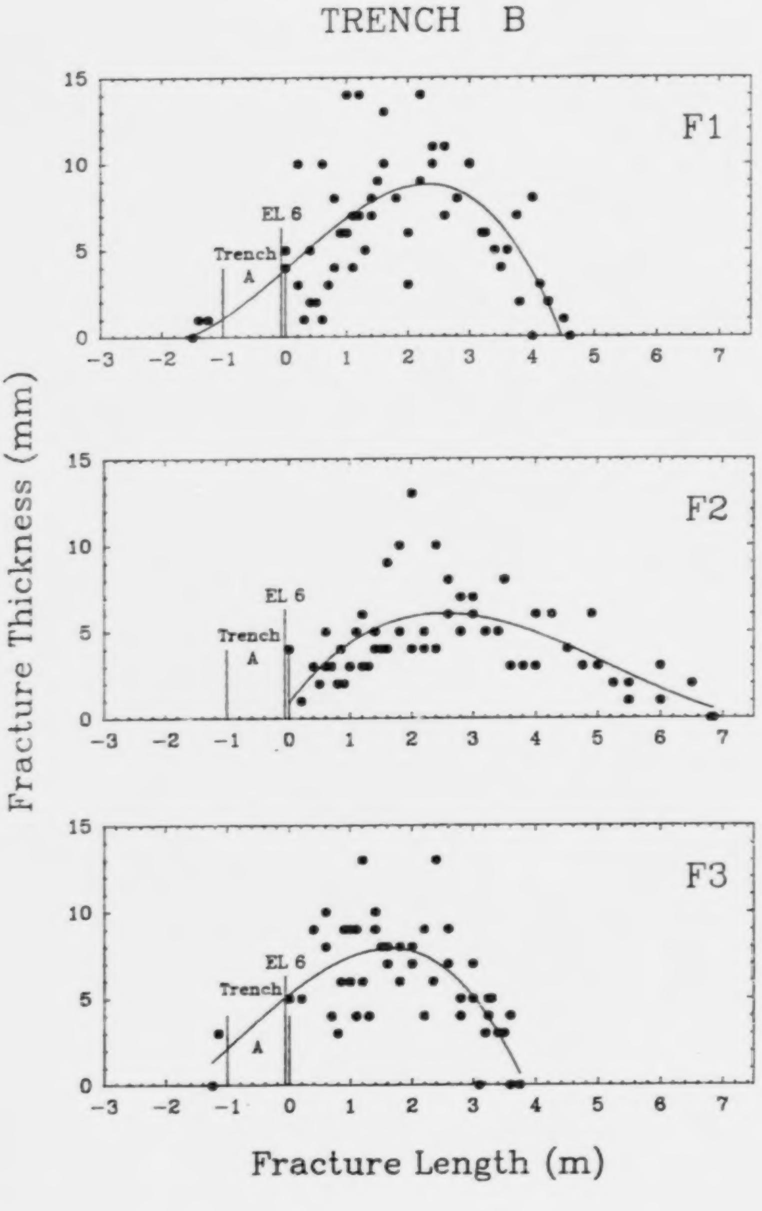

Figure 7.20. Graph of fracture thickness (mm) as a function of the distance away from the borehole (m), for fractures EL6F1 (top), EL6F2 (middle) and EL6F3 (bottom). Thicknesses were measured along east and west walls of trench B.

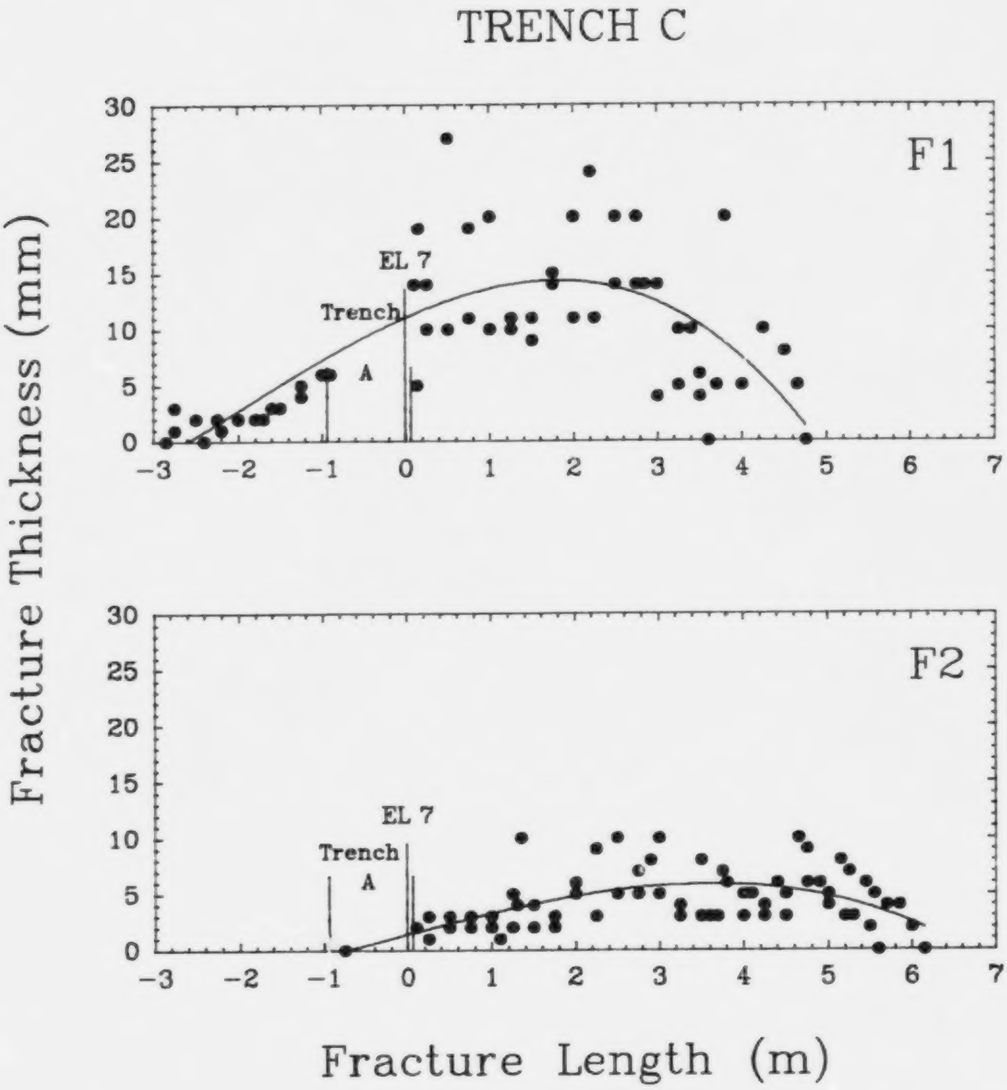

Figure 7.21. Graph of fracture thickness (mm) as a function of the distance away from the borehole (m), for fractures EL7F1 (top), and EL7F2 (bottom). Thicknesses were measured along east and west walls of trench C.

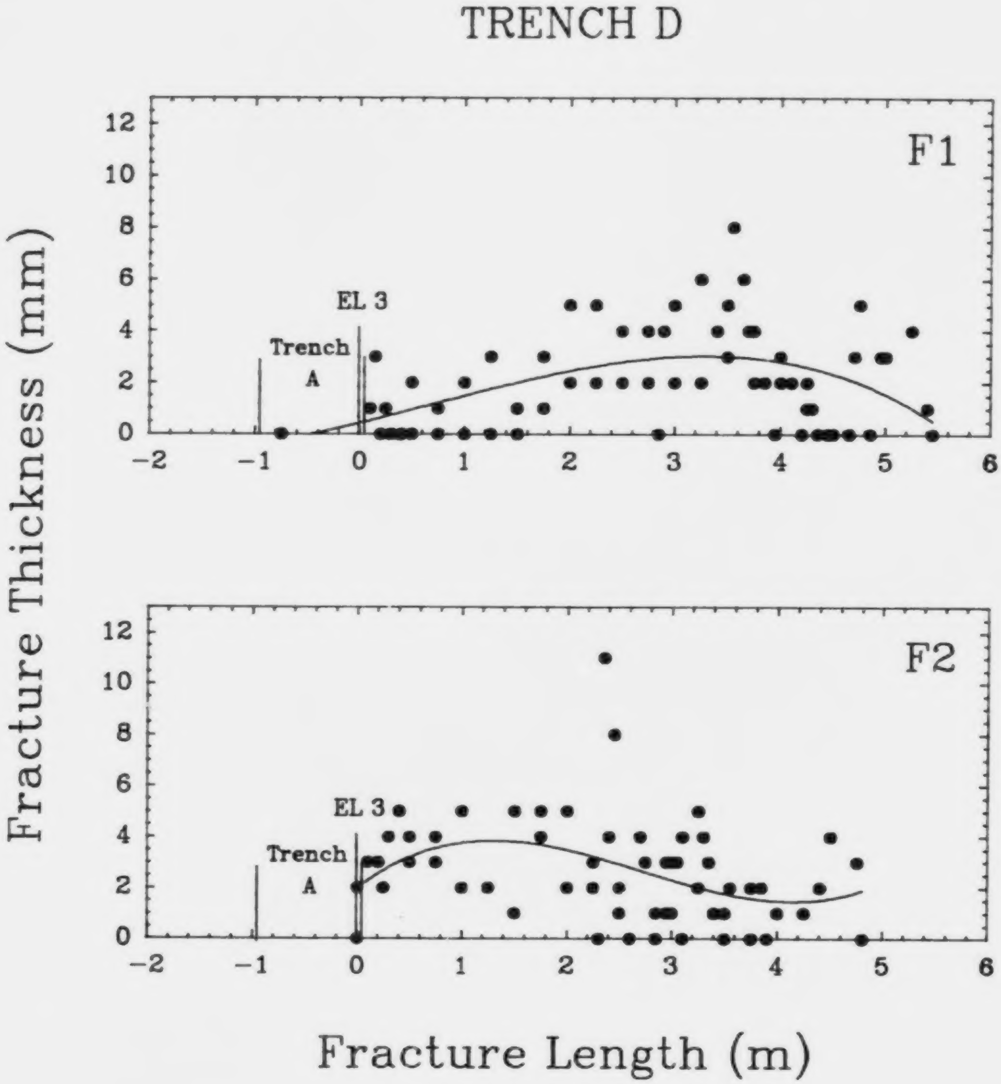

Figure 7.22. Graph of fracture thickness (mm) as a function of the distance away from the borehole (m), for fractures EL3F1 (top), and EL3F2 (bottom). Thicknesses were measured along east and west walls of trench D.

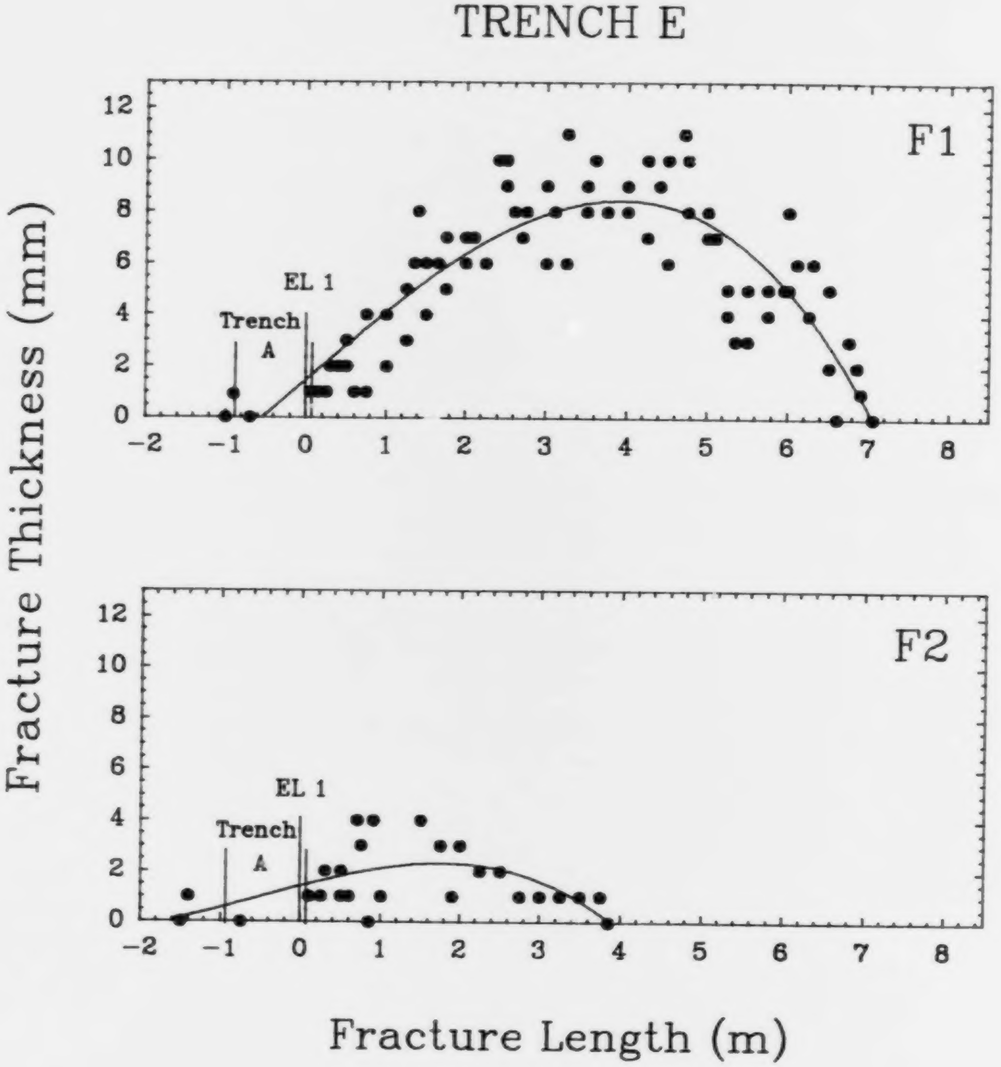

Figure 7.23. Graph of fracture thickness (mm) as a function of the distance away from the borehole (m), for fractures EL1F1 (top), and EL1F2 (bottom). Thicknesses were measured along east and west walls of trench E.

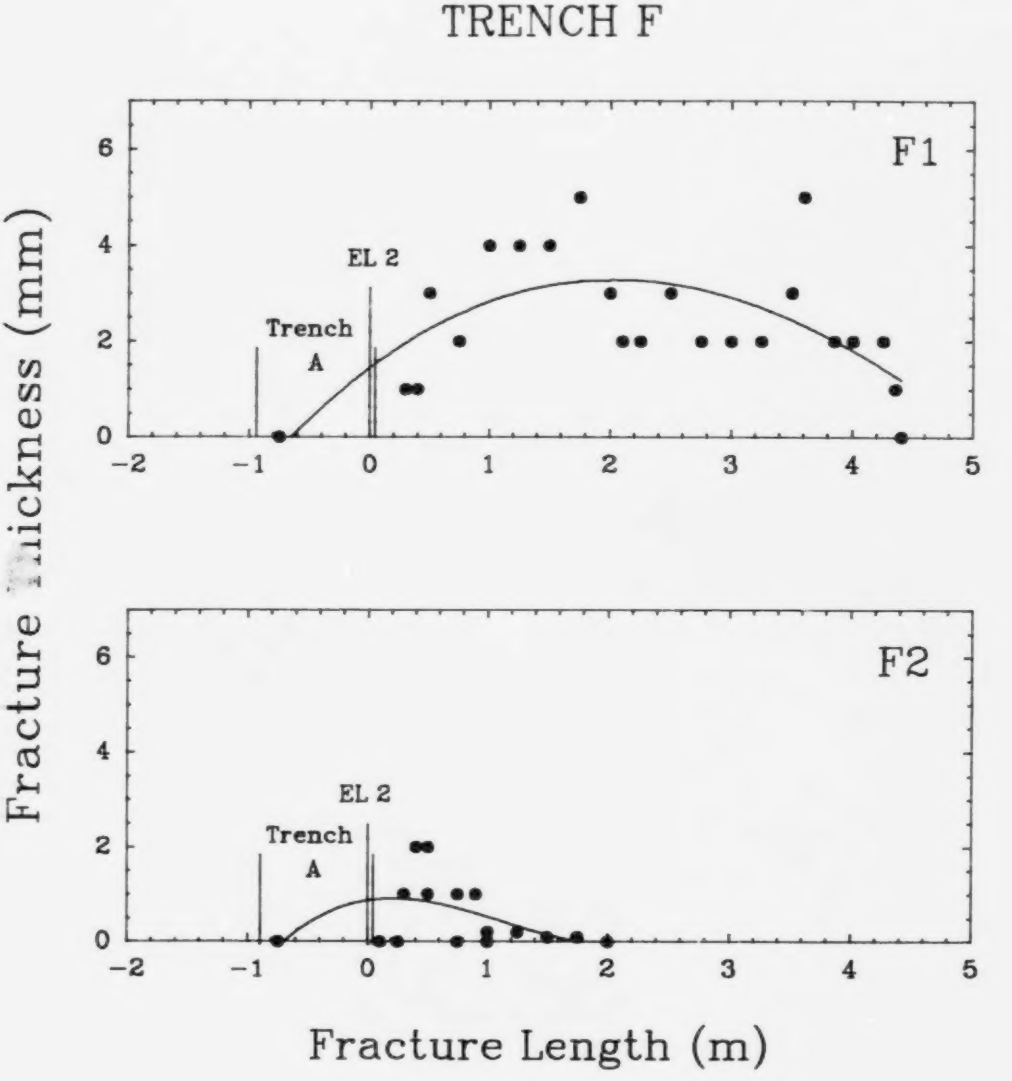

Figure 7.24. Graph of fracture thickness (mm) as a function of the distance away from the borehole (m), for fractures EL2F1 (top), and EL2F2 (bottom). Thicknesses were measured along east and west walls of trench F.

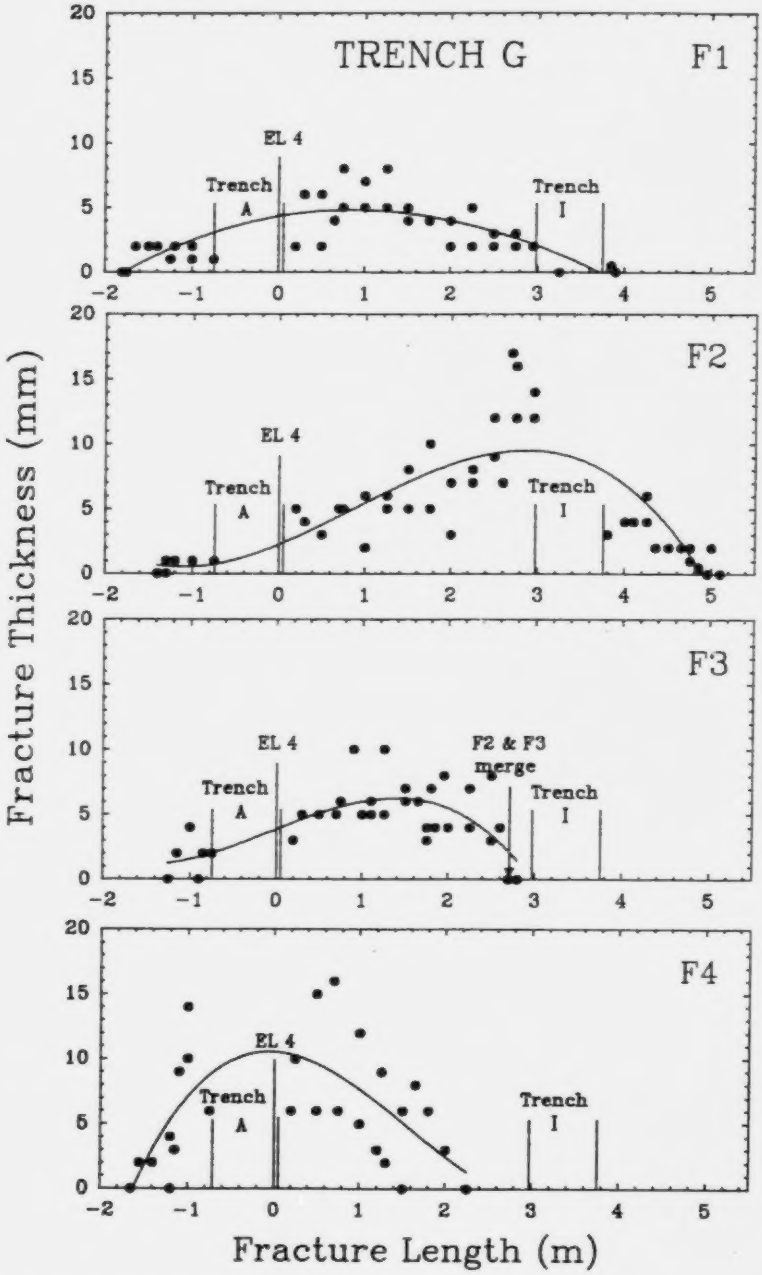

Figure 7.25. Graph of fracture thickness (mm) as a function of the distance away from the borehole (m), for fractures EL4F1, EL4F2, EL4F3 and EL4F4. Thicknesses were measured along east and west walls of trench G.

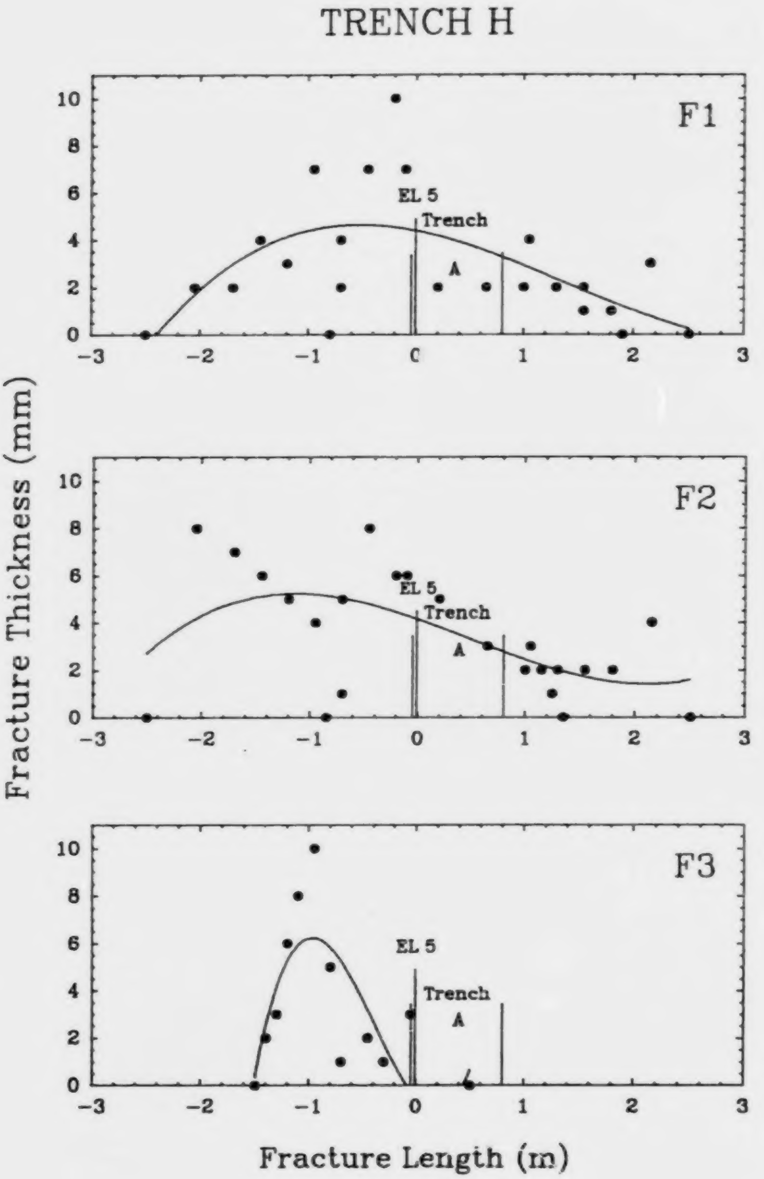

Figure 7.26. Graph of fracture thickness (mm) as a function of the distance away from the borehole (m), for fractures EL5F1 (top), EL5F2 (middle) and EL5F3 (bottom). Thicknesses were measured along east and west walls of trench H.

sand in the 1989 fractures (11 mm) exceeded the maximum thickness (9 mm) from the previous year.

Hydraulic fractures created during the 1989 test increased the steady-state rate of inflow into boreholes in unsaturated ground (data are in Section 1) by factors between 3.1 and 9.0. That amount of increase in flow rate could significantly improve the rate of remediation of a contaminated site. There are certainly aspects of the technology that can be improved -- most of which we are currently pursuing -- but the technology used during the 1989 tests appears to be capable of providing important improvements in remediation. We conclude that the technique of hydraulic fracturing is ready to be tested during remediation.

SECTION EIGHT

MONITORING HYDRAULIC FRACTURES

Monitoring the geometry of hydraulic fractures created to improve remediation should be done for two purposes. On one hand, the performance of a fracture in delivery or recovery is sensitive to its geometry, so monitoring will yield information that will improve the design of delivery or recovery systems. On the other hand, some sites will require that hydraulic fractures do not interfere with features, such as sewers, foundations, or electric cables, so monitoring will yield information that could suppress the growth of errant fractures.

A wide range of methods is available to predict and monitor the geometry of hydraulic fractures. The majority of them were developed within the petroleum industry and they are typically used where hydraulic fractures cut rock at depths of hundreds or thousands of meters; the conditions typical of oil wells. To our knowledge, none of those methods has been evaluated where hydraulic fractures cut soils at depths of a few to several tens of meters; the conditions typical of many remedial applications.

During field tests described in previous chapters we examined four techniques of monitoring processes related to hydraulic fracturing. Those techniques include measuring 1) the pressure of fracturing fluid; 2) tilting of the ground surface over a fracture; 3) uplift of the ground surface; 4) electrical resistivity of ground containing a hydraulic fracture. The objectives of our study were to examine the level of effort required to implement and reduce data from each technique, and to evaluate the potential that it could have in future applications.

INJECTION PRESSURE

The pressure of fracturing fluid varies with time during creation of a hydraulic fracture, and the pressure record is a basic tool of monitoring. The form of the pressure record can be used to infer when propagation starts, as well as various aspects of fracture geometry. Problems such as plugging of the fracture with sand result in large pressure surges that are readily identified on the pressure record.

Method

Injection pressure was recorded during a few of the tests in 1988 and all of the tests in 1989. Pressure was measured at the ground surface using a Druck transducer interfaced with a data acquisition system and lap-top computer. Measurements were taken every second and both written to a disk file and displayed as a plot on the video screen. The pressure records for the tests are shown in Figure 8.1.

Results

Most of the records obtained during the 1989 tests are similar in general form, and consist of the following four basic periods:

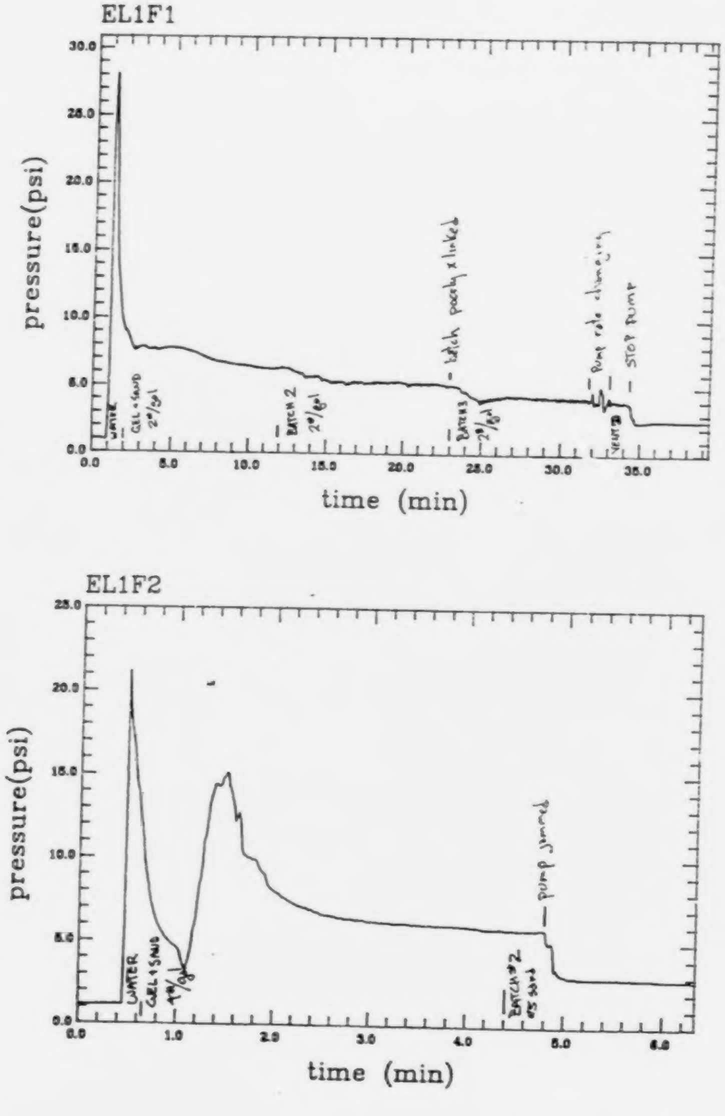

Figure 8.1. Pressure records from fracturing tests during 1989.

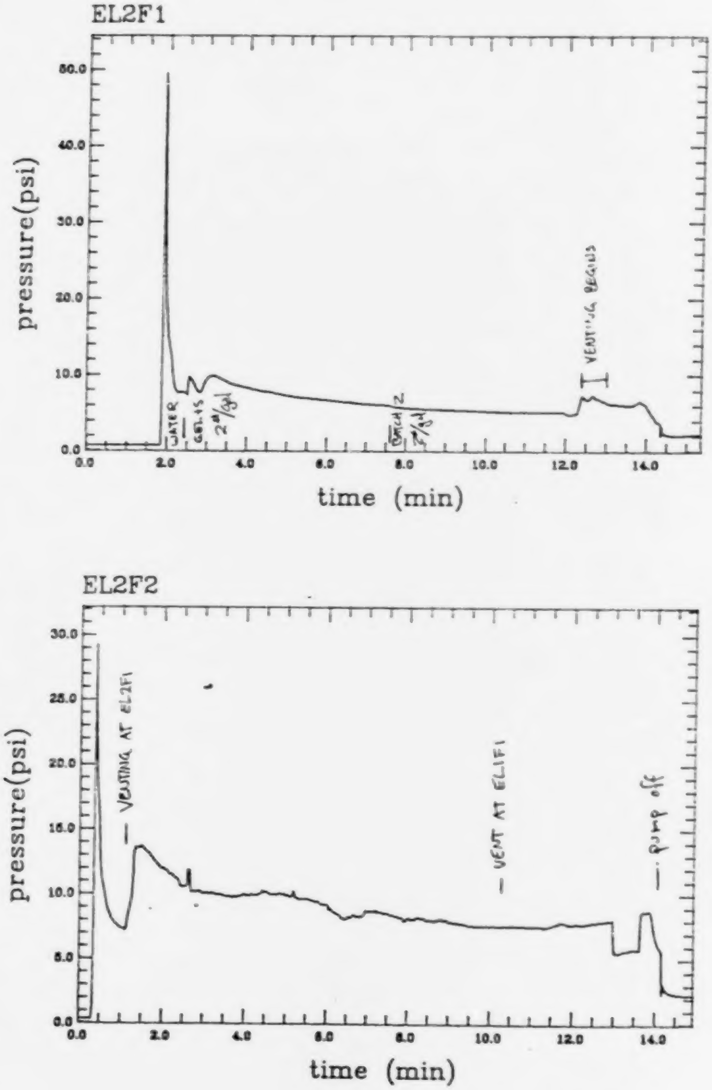

Figure 8.1, continued. Pressure records from fracturing tests during 1989.

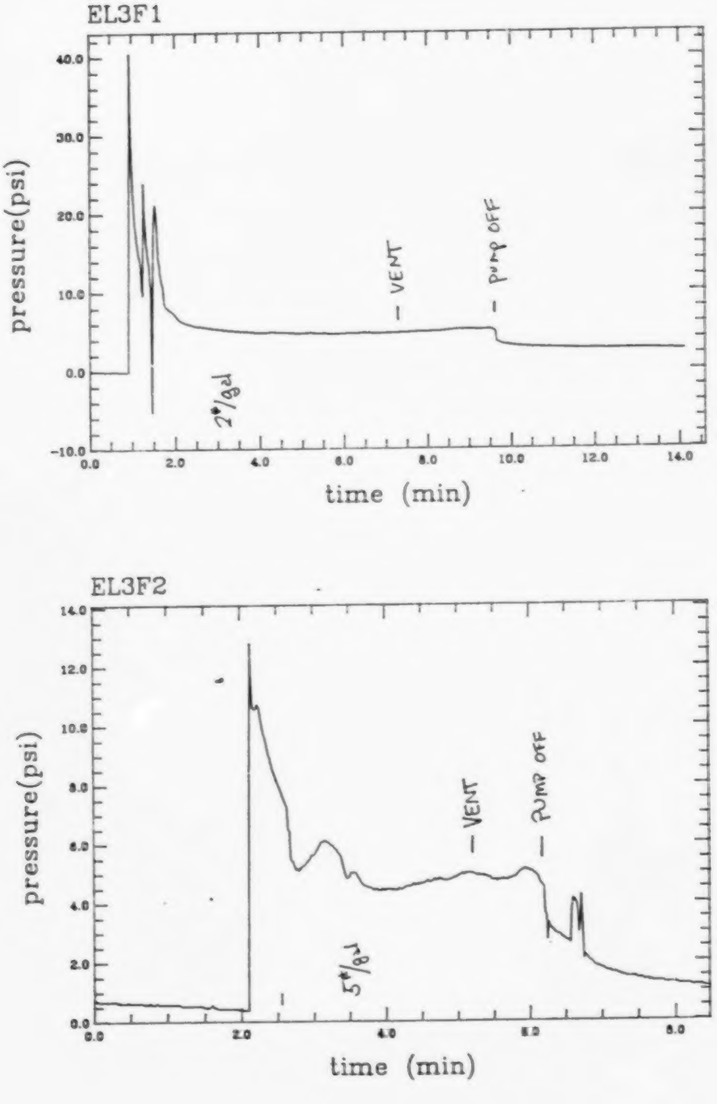

Figure 8.1, continued. Pressure records from fracturing tests during 1989.

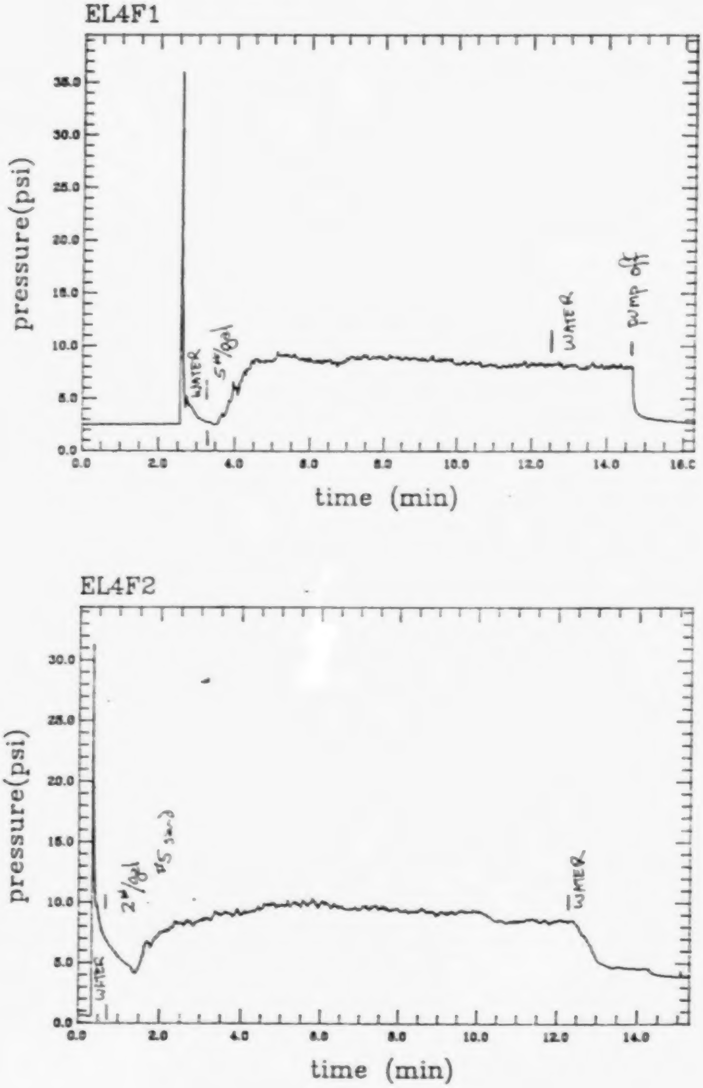

Figure 8.1, continued. Pressure records from fracturing tests during 1989.

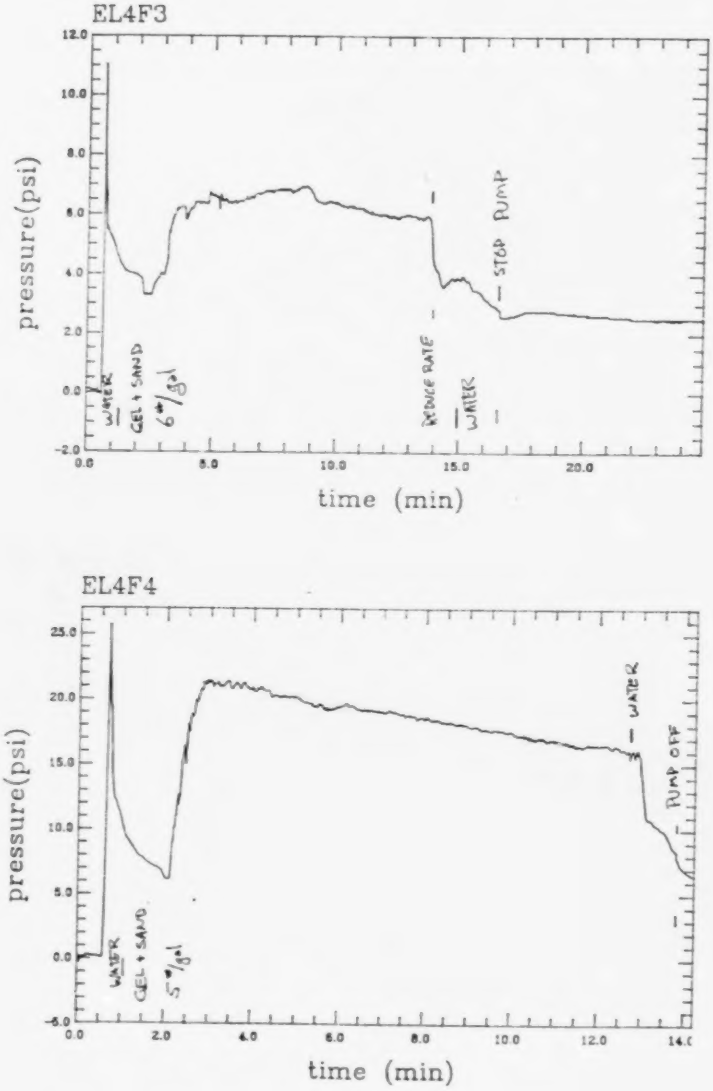

Figure 8.1, continued. Pressure records from fracturing tests during 1989.

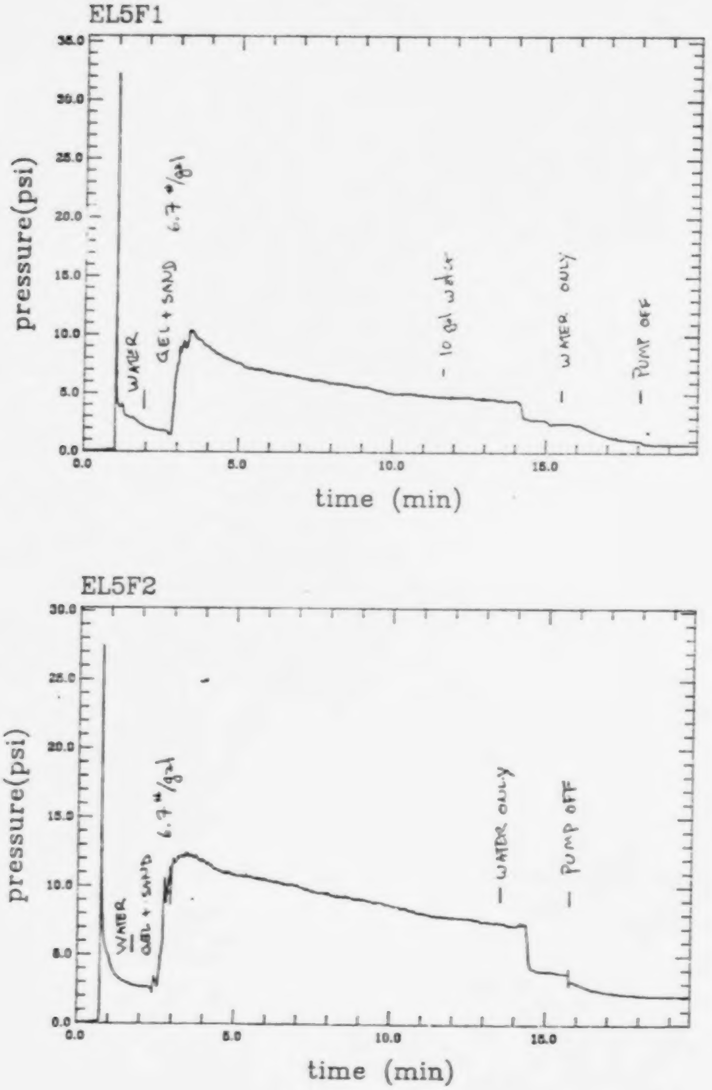

Figure 8.1, continued. Pressure records from fracturing tests during 1989.

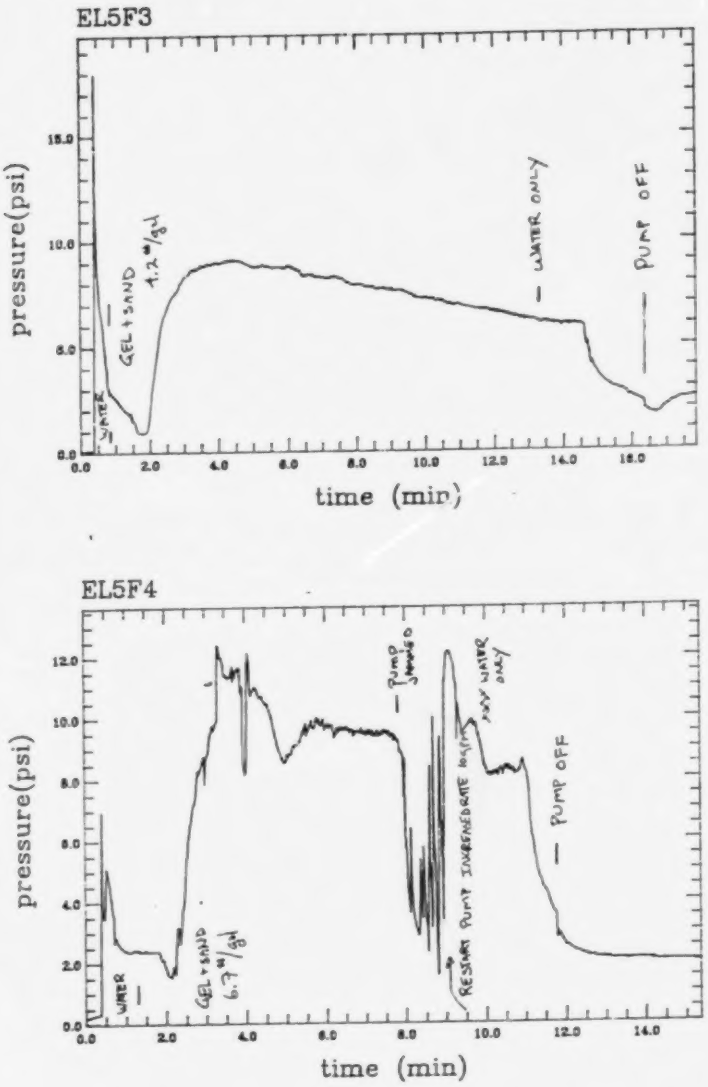

Figure 8.1, continued. Pressure records from fracturing tests during 1989.

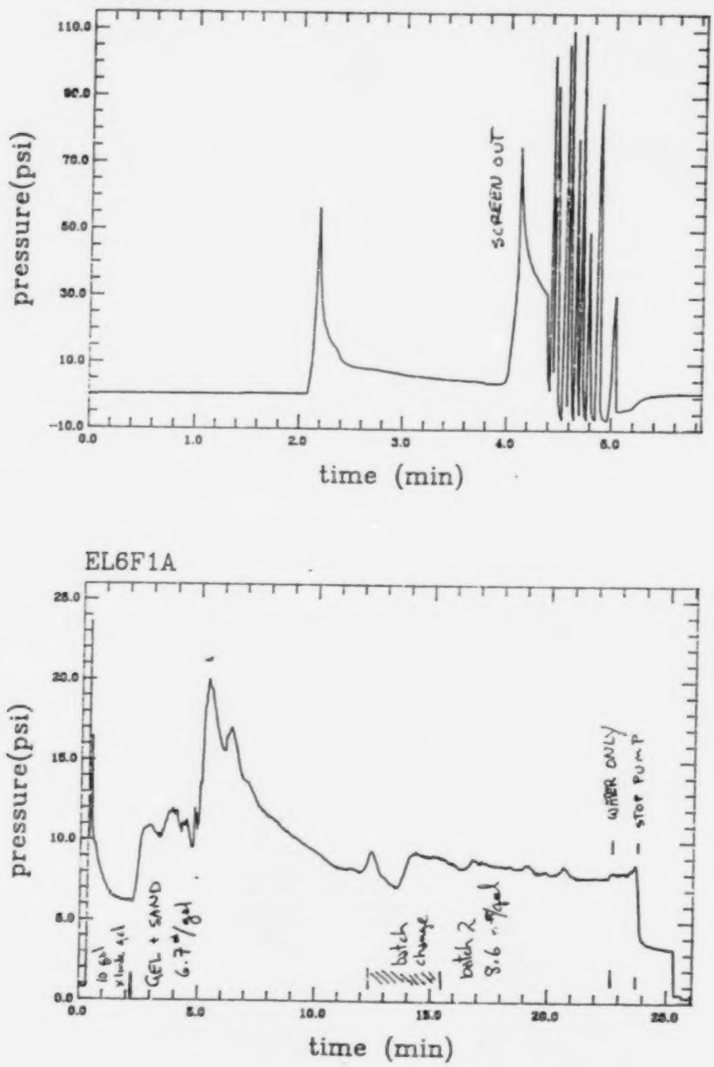

Figure 8.1, continued. Pressure records from fracturing tests during 1989.

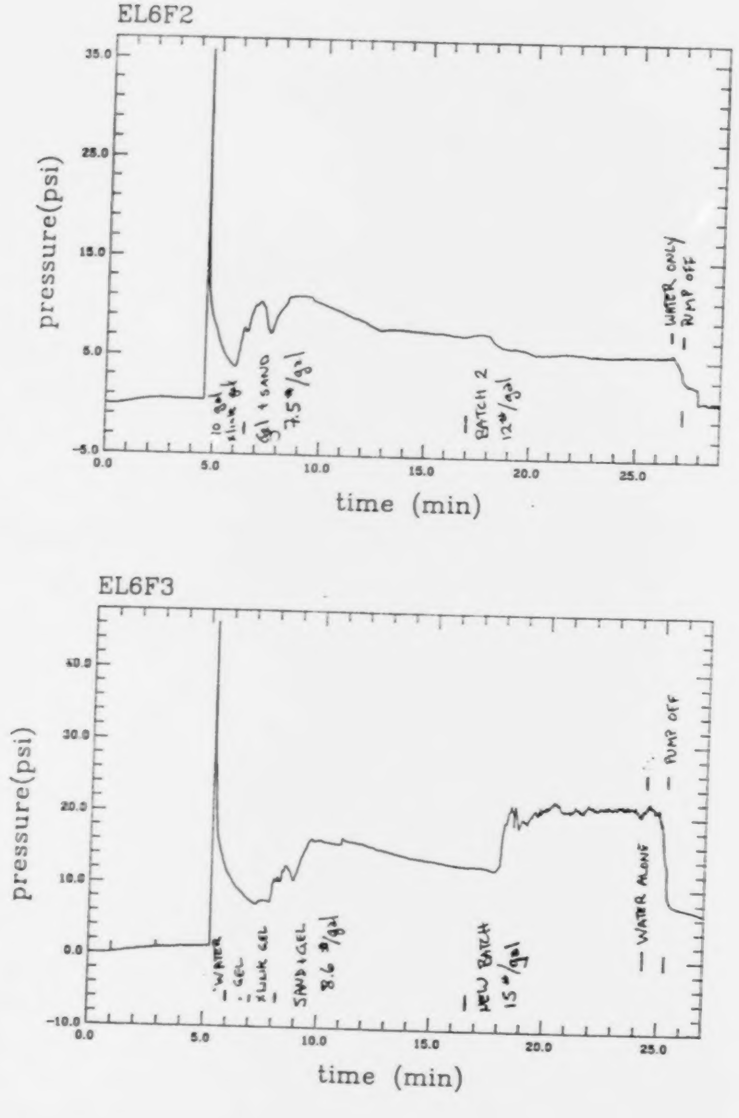

Figure 8.1, continued. Pressure records from fracturing tests during 1989.

EL7F1

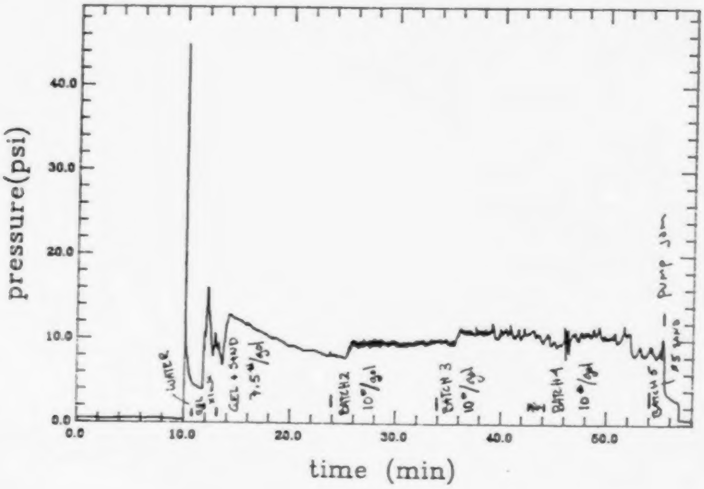

EL7F2

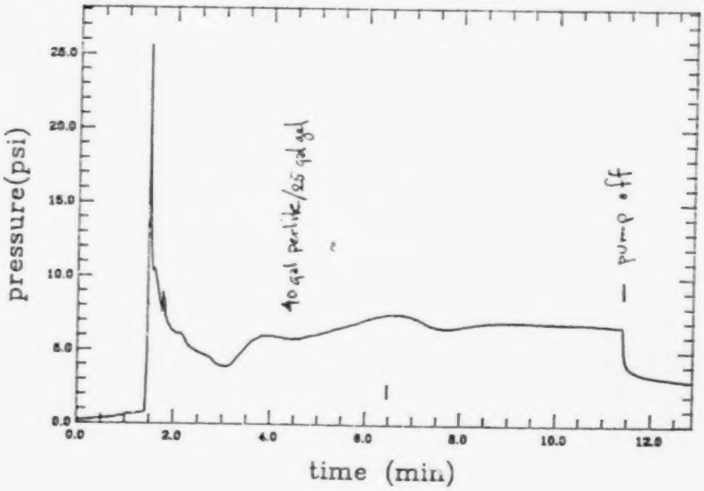

Figure 8.1, continued. Pressure records from fracturing tests during 1989.

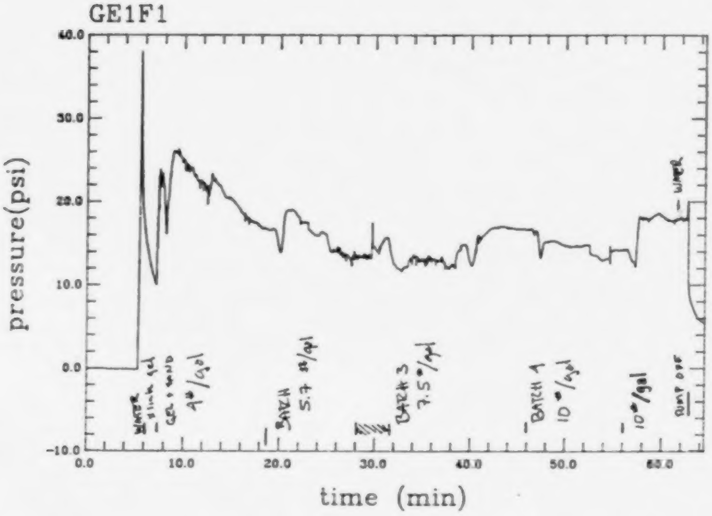

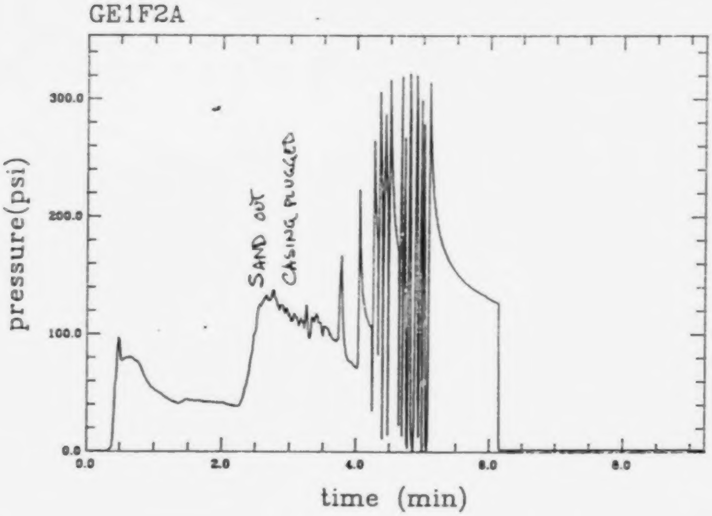

Figure 8.1, continued. Pressure records from fracturing tests during 1989.

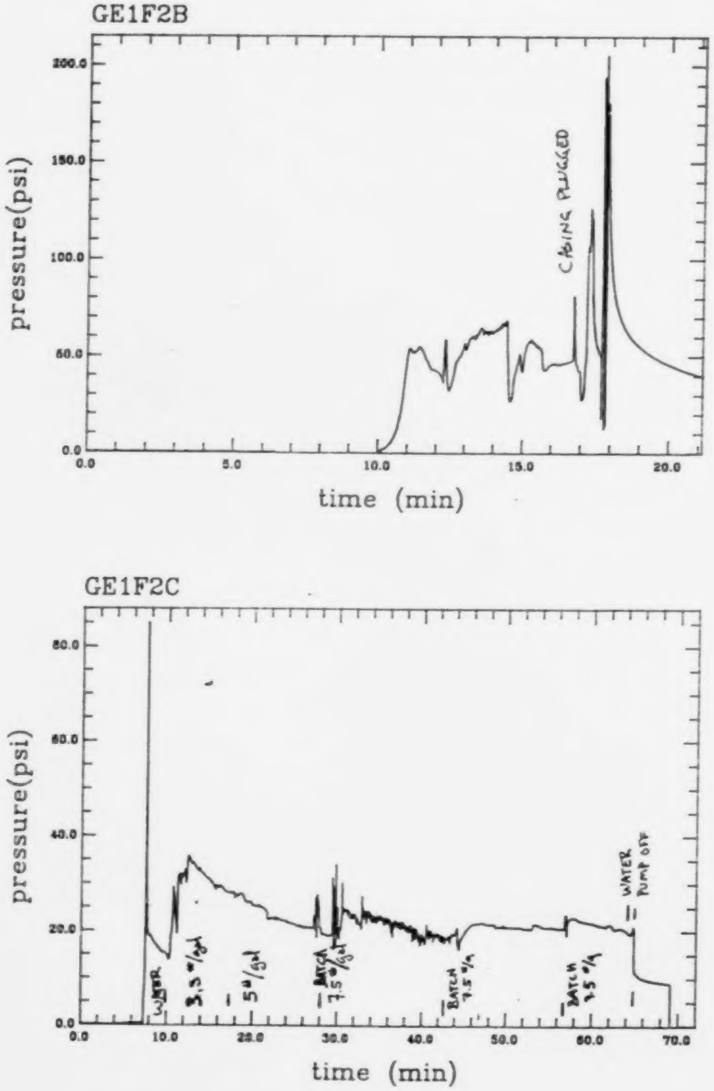

Figure 8.1, continued. Pressure records from fracturing tests during 1989.

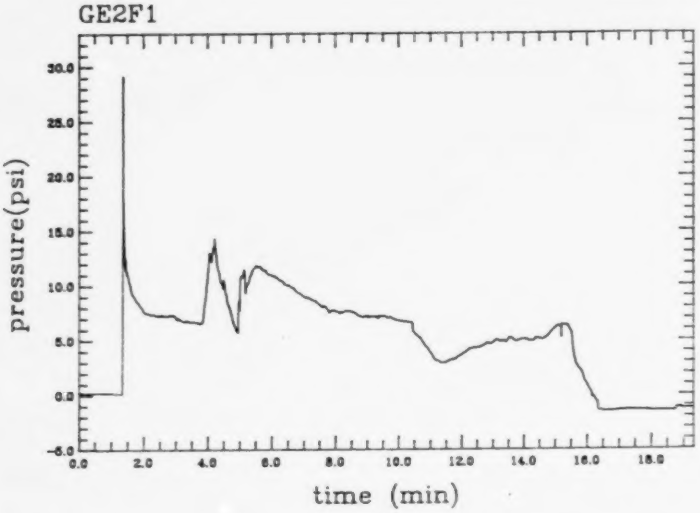

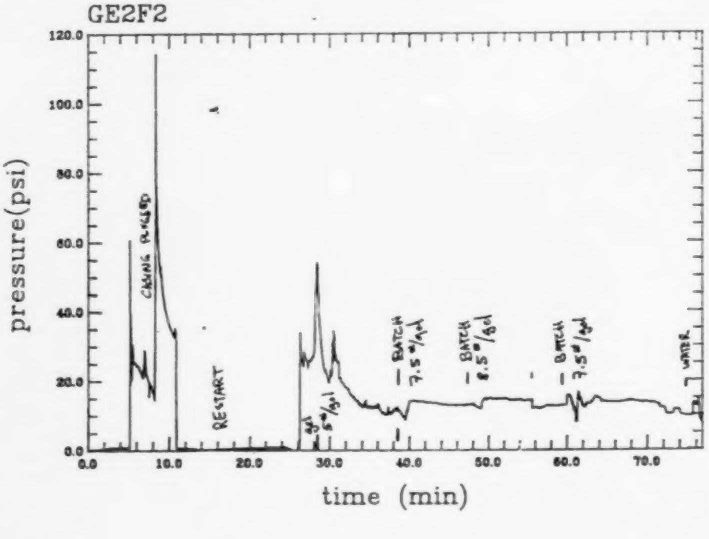

Figure 8.1, continued. Pressure records from fracturing tests during 1989.

Period I: Pressure increases rapidly for several seconds and reaches a peak between 70 and 275 kPa (10 and 40 psi)[1].

Period II: Pressure decreases over one to several minutes and reaches a minimum between 20 and 70 kPa (3 and 10 psi).

Period III: Pressure increases to between 35 and 70 kPa (5 and 10 psi), and then decreases gradually. This is the longest of the periods and lasts from several minutes to more than an hour, depending on the volume of fluid pumped into the ground.

Period IV: Pressure decreases abruptly and is followed by a gradual flattening of the slope.

The fracturing periods are associated with various events during the fracturing procedure. Typically, a change in flow rate causes an instantaneous change in pressure, whereas a change in fluid properties results in a change in pressure roughly 30 seconds later. This lag is the same length of time it took fluid to traverse the injection hose and reach the transducer.

Inflation of the pumping system prior to fracturing occurs during Period I. We infer that the abrupt decrease in pressure marking the beginning of Period II marks the onset of fracture propagation. The increase in pressure marking the beginning of Period III typically occurs roughly 30 seconds after we began to pump gel and sand, and it is due to the increase in viscosity of that fluid compared with fluid that was injected initially. As the fracture increases in size, we expect a gentle decrease in pressure and this behavior is seen during Period III of most tests. Pressure fluctuations within Period III are typically associated with changing from one batch of gel to another. Increasing the sand concentration, for example, is commonly followed by an increase in pressure within Period III (e.g. EL6F3). Other fluctuations in pressure during Period III are associated with minor adjustments in pumping rate. The decrease in pressure during the beginning of Period IV is associated with a reduction in fluid viscosity when we changed from pumping sand-laden gel to water at the end of a test. A sharp drop in pressure, marked by a nearly vertical slope on the record, corresponds to the time when the pump stopped. Pressures were not recorded after the pump was turned off, so we are unable to evaluate the methods of Nolte and Smith (1981), who use the record of pressure after shut-in to determine leakoff parameters.

The pressure record can be used to diagnose problems associated with the fracturing equipment. When the fracture is growing during Period III, a major increase in pressure (EL6F1, GE1F2A, GE1F2B) typically indicated a blockage downstream of the transducer, whereas a major decrease (e.g. EL54F4) indicates an upstream blockage. Downstream blockages were caused when plugs of sand formed at the entrance to the fracture. This problem is caused either by excessive early leakoff, or by an early concentration of sand that was too great. Therefore, when the pressure record indicated a downstream blockage, we recut the starter notch, increased the volume and viscosity of the pad, decreased the initial sand concentration and tried again to create the fracture. This strategy was successful. Unexpected pressure drops indicating upstream blockages were caused, at least during our tests, by clogging of the pump usually because of inadequate crosslinking.

---

[1] Cited pressures are for tests at the ELDA site. Pressures at the Goettle site were typically greater, as seen on the records.

Venting of the fracture to the ground surface occurred during the creation of five fractures (EL1F1, EL2F1, EL2F2, EL3F1, EL3F2), and in most cases venting has negligible effect on the form of the pressure record. One explanation is that the pressure of the injection fluid at the tip of the fracture is essentially zero, so that pressure at the tip would be unaffected by venting. All of those fractures, except EL1F1, merged with another earlier fracture, but we were unable to identify a feature of the records that indicates merging.

The form of the pressure record, after removing fluctuations due to changes in fluid properties or pumping rate, is related to the geometry of the fracture and rate of leakoff. Methods are currently available for inferring the geometry of vertical fractures from the forms of records during Period III (Nolte and Smith, 1981 and 1987). Some of those methods are applicable to shallow, flat-lying, asymmetric fractures such as the ones we created, but most of the methods of interpretation have been developed for oil-field applications where fractures are vertical.

Leakoff characteristics can be determined from pressure records made during pumping and after the pump has been shut off (Nolte, 1979; Nolte and Smith, 1987). Records made during this work were terminated too early to make reliable measurements of leakoff characteristics, however. Future work should focus on obtaining the leakoff characteristics, and using that information to anticipate tip screen-out (Smith and others, 1987; Nolte, 1984).

SURFACE TILT

The ground surface overlying a hydraulic fracture is deformed as the fracture inflates. Characteristics of the fracture can be inferred by measuring the deformation and then using various theoretical analyses. In this study, deformation was determined either by measuring changes in slope of the ground surface with tiltmeters, or by measuring changes in altitude with a leveling device. The work with tiltmeters was conducted during the 1988 tests and is described in the following section.

Method

Surface tilt was measured as a function of time using Model 722 tiltmeters rented from Applied Geomechanics Inc., Santa Cruz, California. That model is cylindrical in shape and designed to be placed below the ground surface in a boring. It is accurate to within 0.1 microradian.

The tiltmeters were installed slightly below the ground surface in vertical boreholes. Sand was placed around the tiltmeters and the orientation of their major axis was adjusted to vertical. Signals from the tiltmeters were conditioned using electronic equipment rented from Applied Geomechanics Inc. and then recorded on our data acquisition system.

A total of eight tiltmeters were installed around the cluster of boreholes 4, 5, 6, and 7 (Fig. 8.2). Three of those boreholes are at the vertices of an equilateral triangle, and the other is at the center of the triangle. Six of the tiltmeters were arranged in a hexagonal pattern around the three boreholes, and the other two tiltmeters were near the central borehole (Fig. 8.2). The arrangement placed three tiltmeters at roughly equal distances from each borehole, and placed the others at greater distances. A single layout of tiltmeters was necessary because installation required several hours and we were unable to move them on the day of the 1988 test. One of the tiltmeters, tiltmeter F, yielded erratic data and was omitted from the interpretations.

Results

Creating hydraulic fractures caused tilts of as much as 2000 microradians (Appendix A), a strong signal for the instruments we used. Tilt signals varied widely as functions of time and location (Fig. 8.3), and a meaningful interpretation of this information is only possible after data reduction. Qualitative information about the location and orientation of the fracture can be obtained by plotting tilts as vectors in plan view. Such plots can be created in real time and interpreted as the fracture is being created. This procedure was not attempted during field tests.

Tilt data can also be used to obtain quantitative estimates of fracture geometry. This procedure involves inverting the tilt measurements using a mathematical solution for surface displacement over a fracture at depth. The solution used in this work assumes that the fracture is planar and shaped like a rectangle. A total of eight parameters, which specify the size, location, aspect ratio, and aperture of the fracture, are obtained from a nonlinear inversion of that solution (Davis, 1983). Engineers at Applied Geomechanics Inc. developed the inversion technique, and analyzed the data from the tiltmeters. They estimated the geometry of each fracture at several times during its creation, and their results are compared with maps of the fractures in Figures 8.4 through 8.6.

Each of Figures 8.4 through 8.6 consists of a series of two or three contour maps illustrating the change of fracture geometry during the fracturing process. Figure 8.4 shows three stages in the development of fracture HF5 (created from borehole #5); Figure 8.5 shows three stages in the development of fracture HF6 (borehole #6); and Figure 8.6 shows two stages in the development of fracture HF7 (borehole #7).

Table 8.1 compares orientations (strikes and dips) of fractures determined from tiltmeter data to those determined from excavation of the fractures. Following the convention used by Applied Geomechanics Inc., the subcontractor responsible for tiltmeter data, the direction of fracture dip represents a clockwise, 90° rotation from the azimuth of the fracture strike. Coordinates of the center of the fracture relative to the borehole, calculated from tiltmeter data, along with fracture aperture

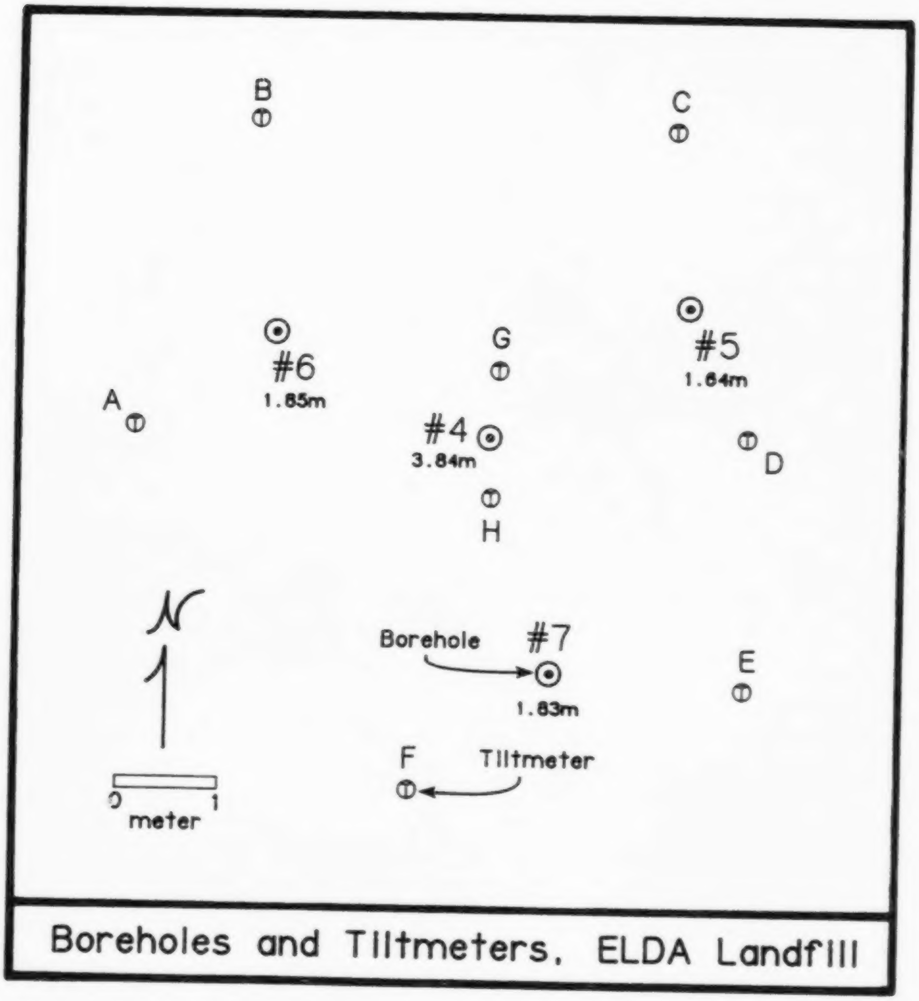
B
C
#6
1.85m
G
#5
1.64m
A
#4
3.84m
D
H
N
Borehole
#7
1.83m
E
F
Tiltmeter
0
1
meter
Boreholes and Tiltmeters, ELDA Landfill

Figure 8.2. Tiltmeter array from 1988 tests.

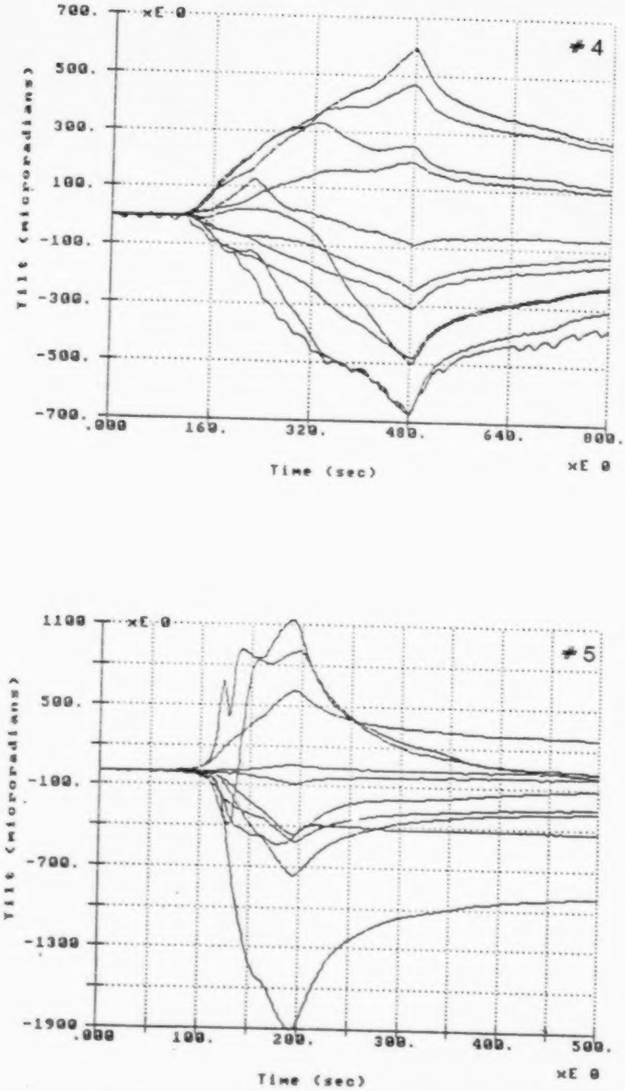

Figure 8.3. Tilt as a function of time.

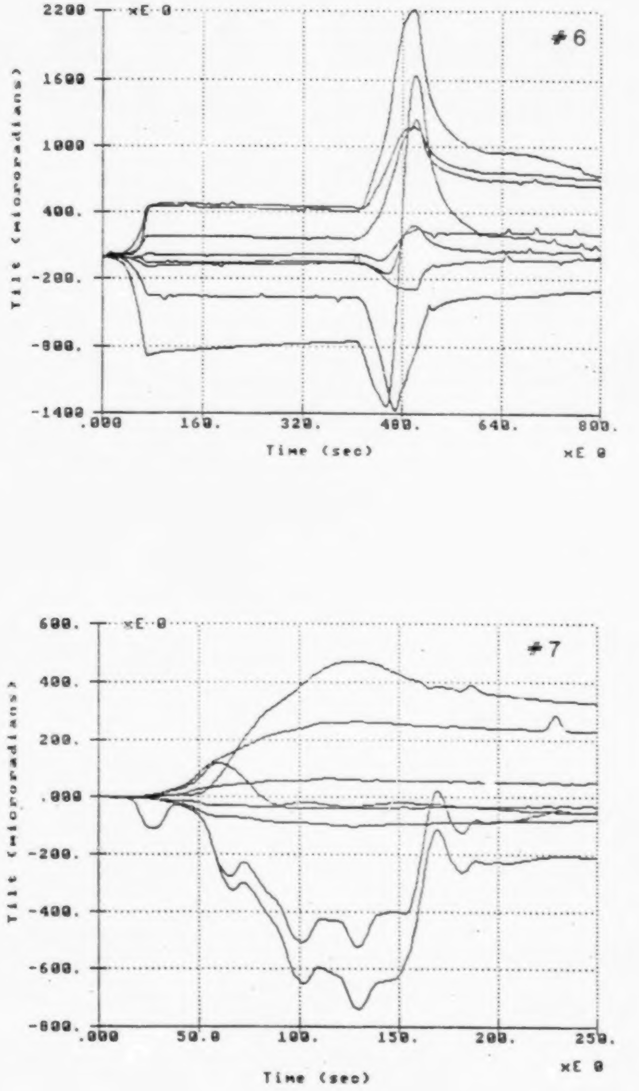

Figure 8.3, continued. Tilt as a function of time.

(thickness), are also given in Table 8.1. Coordinates are measured in ft, with the positive *x* direction pointing eastward, and the positive *y* direction pointing northward. Fracture aperture is measured in inches.

TABLE: 8.1. ACTUAL AND PREDICTED ORIENTATIONS OF FRACTURES

Frx	Actual Strike	Tilt-meter Strike	Actual Dip	Tilt-meter Dip
HF5a	80	98	22	8
HF5b	84	143	26	37
HF5c	40	359	17	37
HF6a	359	332	9	11
HF6b	359	334	9	23
HF6c	349	4	14	29
HF7a	228	242	27	1
HF7b	228	213	27	27

Borehole 5

Inversion of data from borehole 5 indicates that a very thin (0.03 cm; 0.01 in), nearly horizontal fracture, striking 98° and dipping 8° SW, formed 1 minute after fracturing commenced (Figure 8.4a). The "tiltmeter strike" is fairly close to the strike based on excavation (80°), although the "tiltmeter dip" is considerably shallower than the "excavation dip" (23°). One minute later (Figure 8.4b), tiltmeter data indicate a somewhat thicker fracture (0.03 cm; 0.01 in), with strike rotated clockwise to 143°, and dip increased to 37° SW. Although the tiltmeter strike at this stage is less consistent with the excavated strike than it was a minute earlier (Figure 8.4a), the tiltmeter dip is closer to the excavated dip. Tiltmeter data shown in Figures 8.4a and 8.4b suggest that the smaller, eastern lobe of the fracture formed during the first two minutes of fracturing. Tiltmeter data for the final phase of fracturing (Figure 8.4c), 3 minutes and 20 seconds after fracturing commenced, indicate formation of a fracture twice as thick (0.61 cm; 0.24 in) as a minute earlier, striking 359° and dipping 37° NE. Fracture propagation during this phase occurred several ft west of the borehole. The location and orientation of the fracture based on tiltmeter data strongly suggests that the larger, western lobe of the fracture (as mapped from excavation) formed late during the fracturing process (after 3 minutes).

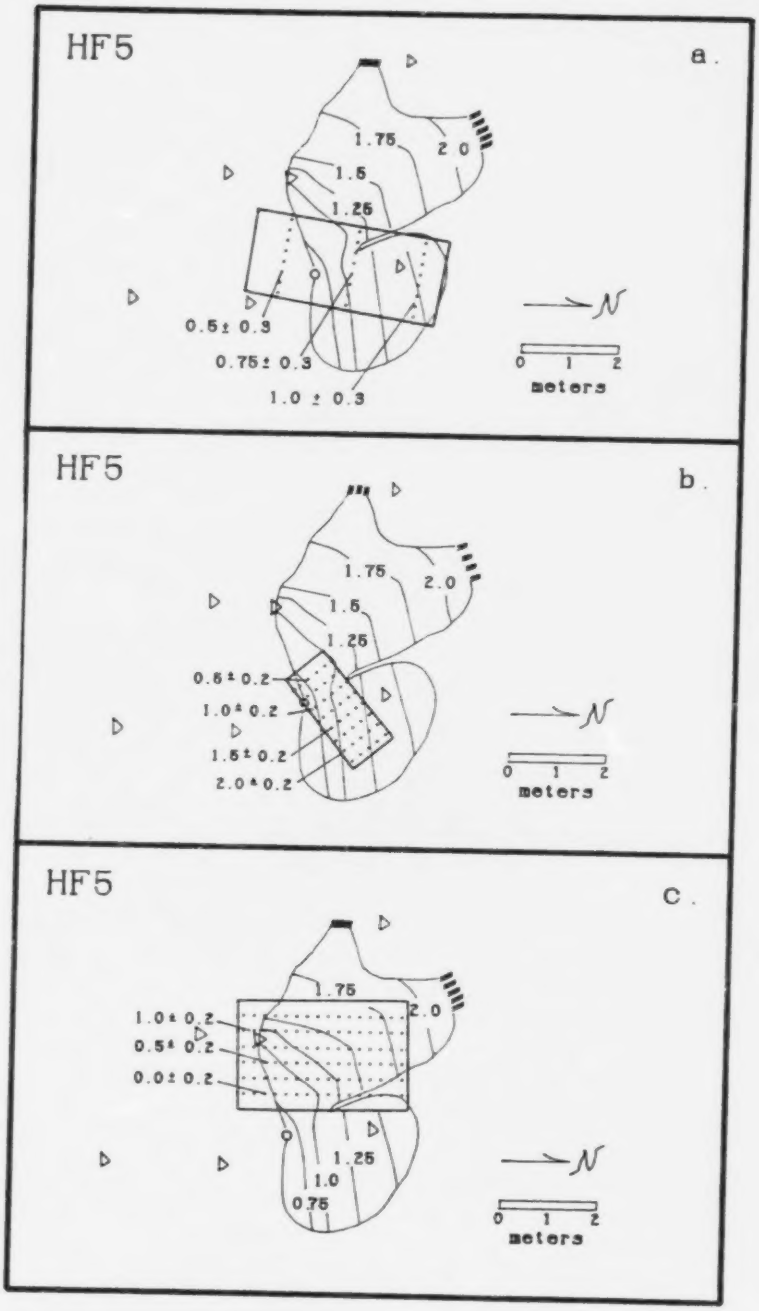
HF5
a.
1.75
2.0
1.5
1.25
0.5± 0.3
0.75± 0.3
1.0 ± 0.3
N
0 1 2
meters
HF5
b.
1.75
2.0
1.5
1.25
0.5± 0.2
1.0± 0.2
1.5± 0.2
2.0± 0.2
N
0 1 2
meters
HF5
c.
1.75
2.0
1.0± 0.2
0.5± 0.2
0.0± 0.2
1.25
1.0
0.75
N
0 1 2
meters

Figure 8.4. Hydraulic fracture HF5 and interpretation of surface tilts at three times during the test.

The fracture inferred from early tiltmeter data at borehole 5 is inconsistent with excavation data, but the later two fractures are consistent with field observations. The second frame in the interpretation indicates that the eastern lobe of HF5 formed first and was followed by growth of the western lobe. Apparently, propagation of the eastern lobe was arrested before it could vent. Continued injection resulted in growth of the western lobe, which vented in two locations west and northwest of the borehole. The tiltmeter inversion underestimates the area of the fracture, but overestimates its dip, based on excavation of the fractures.

Borehole 6

Comparison of tiltmeter inversion data with the fracture map based on excavation around borehole 6, shown in Figure 8.5, indicates that comparatively shallow-dipping (11°), NW-striking (332°) portions of the fracture, close to the borehole, formed during the first 2 minutes of fracturing (Figure 8.5a). Somewhat steeper-dipping (23°) but still NW-striking (334°) portions of the fracture formed up to 2 m away from the borehole, as late as 7 minutes and 40 seconds after fracturing commenced (Figure 8.5b). Finally, distal portions of the fracture, dipping as much as 29° SE and striking NNE (4°), formed over 8 minutes after fracturing commenced.

Tiltmeter and excavation data for fracture HF6 clearly illustrate the ability to trace the dynamic development of a fracture using tiltmeter inversion data.

Borehole 7

Development of a relatively small fracture is documented in Figure 8.6, showing tiltmeter inversion data and excavation data for fracture HF7, 2 minutes (Figure 8.6a) and 3 minutes (Figure 8.6b) after commencement of fracturing. Comparison of the first frame (Figure 8.6a) with other frames representing 2 minutes after commencement of fracturing (Figures 8.4b and 8.5a) reveals comparatively low fracture dip (1° NW). Tiltmeter-generated strike and dip of the fracture 3 minutes after commencement, shown in Figure 8.6b, is in fairly good agreement with excavation data (Table 8.1).

Discussion

Propagation direction and strike are predicted within roughly 45°, and dip is generally within 15°--mostly dip is overestimated. Sizes of fractures are generally underestimated, except in the case of HF7 where it is markedly overestimated. The general locations of the fractures is predicted with reasonable accuracy, however.

The results of the inversions of tiltmeter data are remarkably consistent with field mapping, considering that the inversion scheme must reconcile the tilt field resulting from a fracture whose geometry is much more complex than the simple rectangular model it uses. The inversions of tilt data taken during the 1989 tests, where the fracture forms were quite simple, certainly would have yielded more accurate results. Moreover, some of the error in the tilt data results from

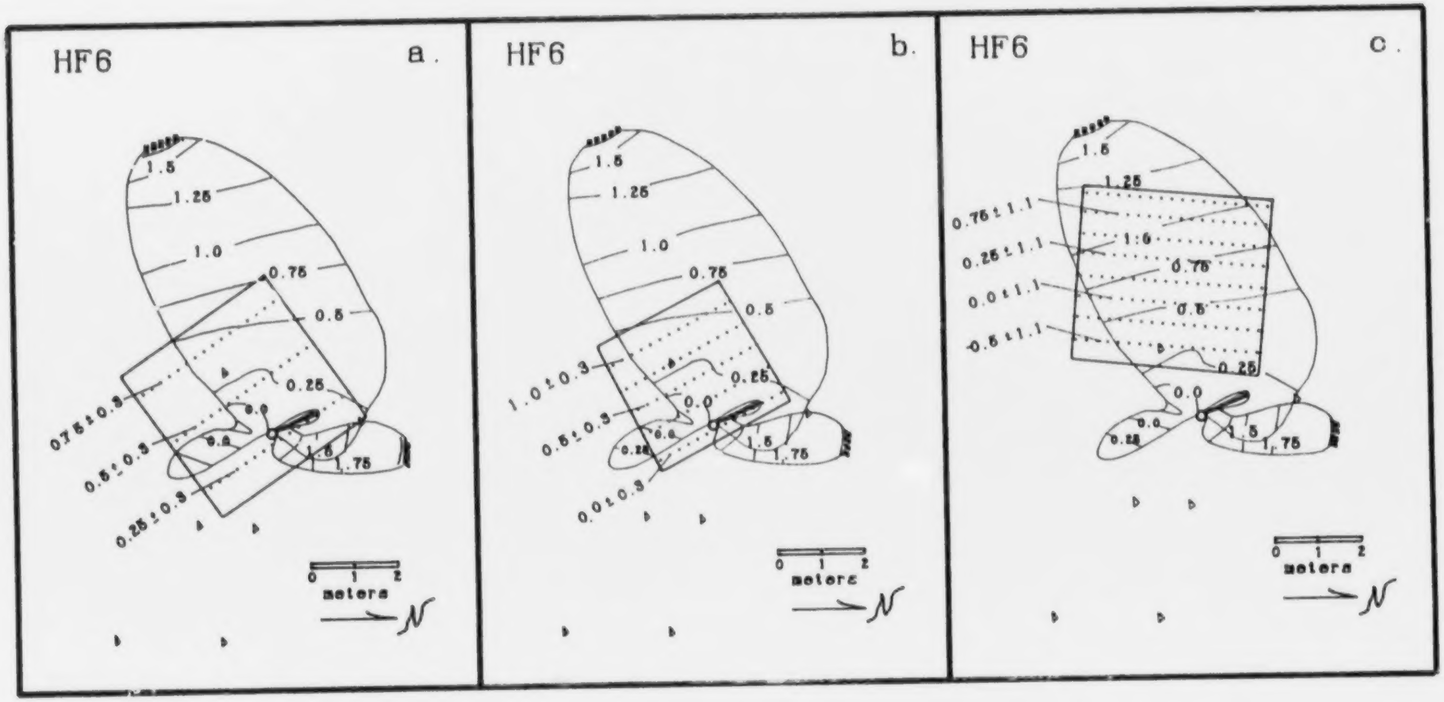

Figure 8.5. Hydraulic fracture HF6 and interpretation of surface tilts at three times during the test.

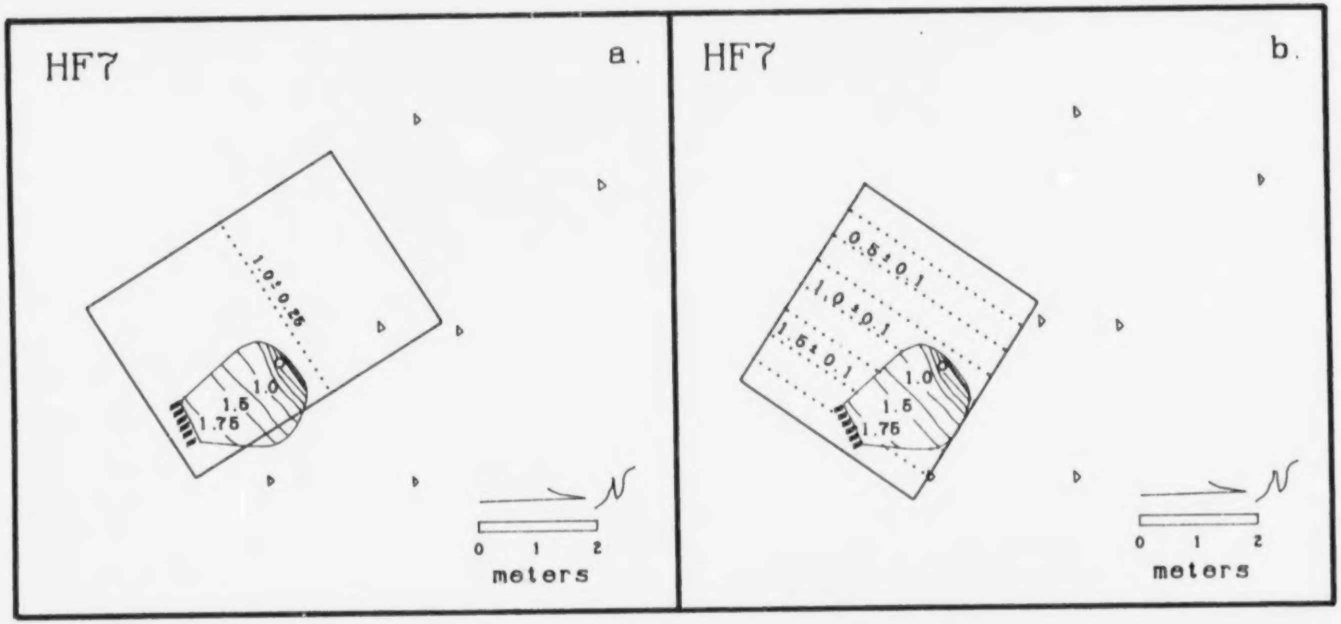
HF7
a.
1.0±0.25
1.0
1.5
1.75
N
0 1 2
meters
HF7
b.
0.5±0.1
1.0±0.1
1.5±0.1
1.0
1.5
1.75
N
0 1 2
meters

Figure 8.6. Hydraulic fracture HF7 and interpretation of surface tilts at three times during the test.

placement of the tiltmeters. For example, the inversion of data from HF7 overestimates the extent of the southern boundary of the fracture, but there are no tilt data from the southern side so the inversion must resort to extrapolation.

Inversion of tiltmeter data should provide estimates of location during propagation. Application of this technique to real-time monitoring -- inversion in the field during fracturing -- should provide a safeguard against the growth of errant fractures, and it may allow for small adjustments in the fracturing process to optimize fracture performance.

SURFACE UPLIFT

Design

Standard surveying techniques were employed to measure surface uplift incurred during fracturing. Elevations of points distributed radially around each borehole were measured before and after individual fracturing episodes. Values of the difference between elevations before and after fracturing, measured in mm at each surveying point, are contoured for several fractures in Figures 8.7 - 8.10.

Superimposed on the uplift contours are contours representing the thickness of the fracture associated with the measured uplift. Thicknesses of fractures were measured directly on trench walls exposing traces of the fractures.

Uplift contours shown in Figures 8.7 and 8.10 represent total uplift incurred during the creation of a chronological series of fractures. Accordingly, the superimposed thickness contours indicate the combined thickness of all fractures involved in the uplift.

Results

Surface uplift and fracture thickness contours combined for fractures EL6F2 and EL6F3 are shown in Figure 8.7. Contours for fractures EL7F1 and EL7F2 are shown in Figures 8.8 and 8.9, respectively. Combined contours for fractures EL5F1 through EL5F4 are shown in Figure 8.10. Fracture thickness contours are bold, and surface uplift contours are medium weight in the figures.

Several characteristic features were used to compare the uplift and thickness contours for each fracture or group of fractures. These include the strike of the major axis of the ellipse roughly defined by the contours; the ratio of major to minor axis (aspect ratio); the maximum values of uplift and thickness; the distances from the borehole to the points of maximum value (the tops of the domes defined by the contour sets); and the distances from the points of maximum value to the points of zero uplift or thickness, measured along the major axes.

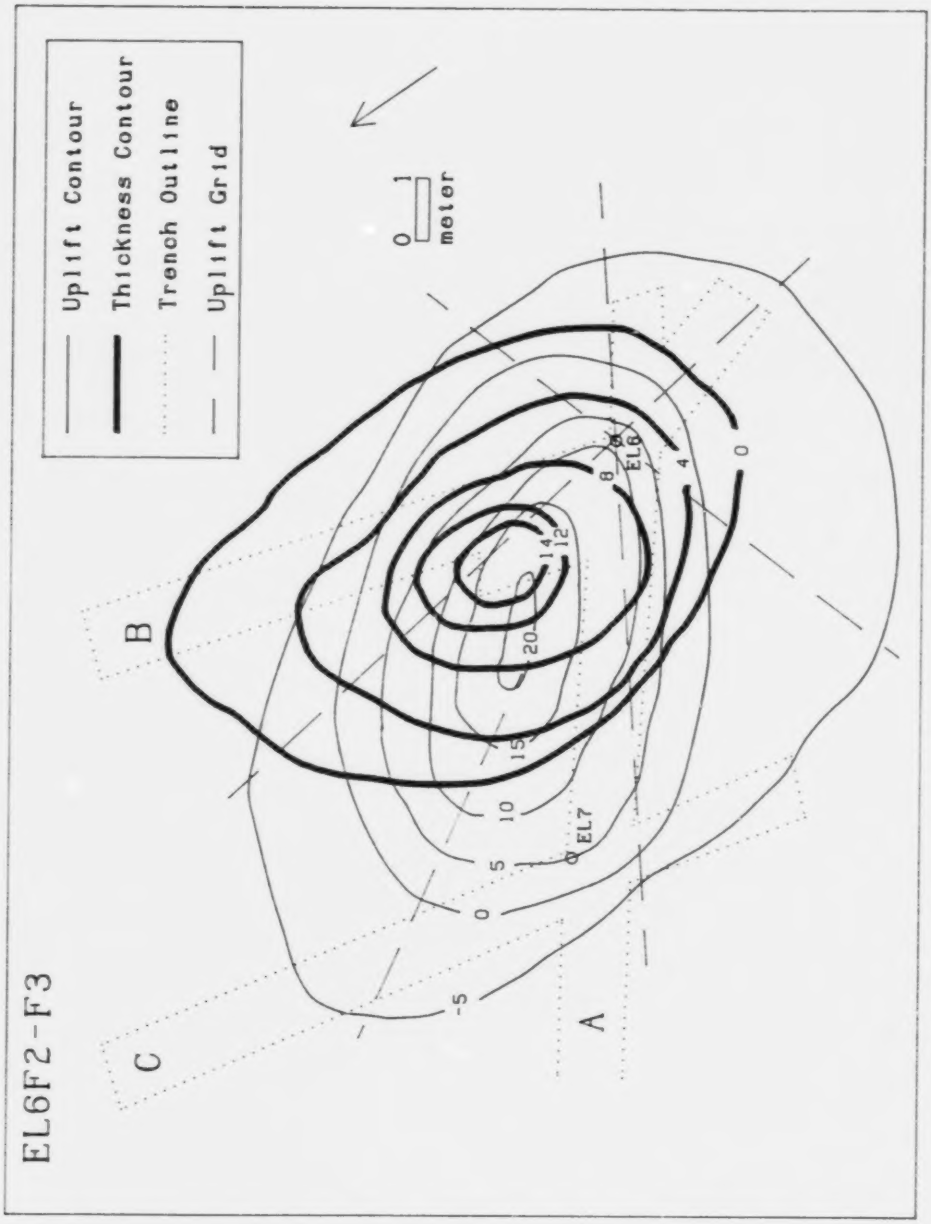
EL6F2-F3
Uplift Contour
Thickness Contour
Trench Outline
Uplift Grid
0 1
meter
B
C
A
-5
0
5
10
15
20
14
12
8
4
0
EL7
EL6

Figure 8.7. Thickness and uplift contours, combined for fractures EL6F2 and EL6F3.

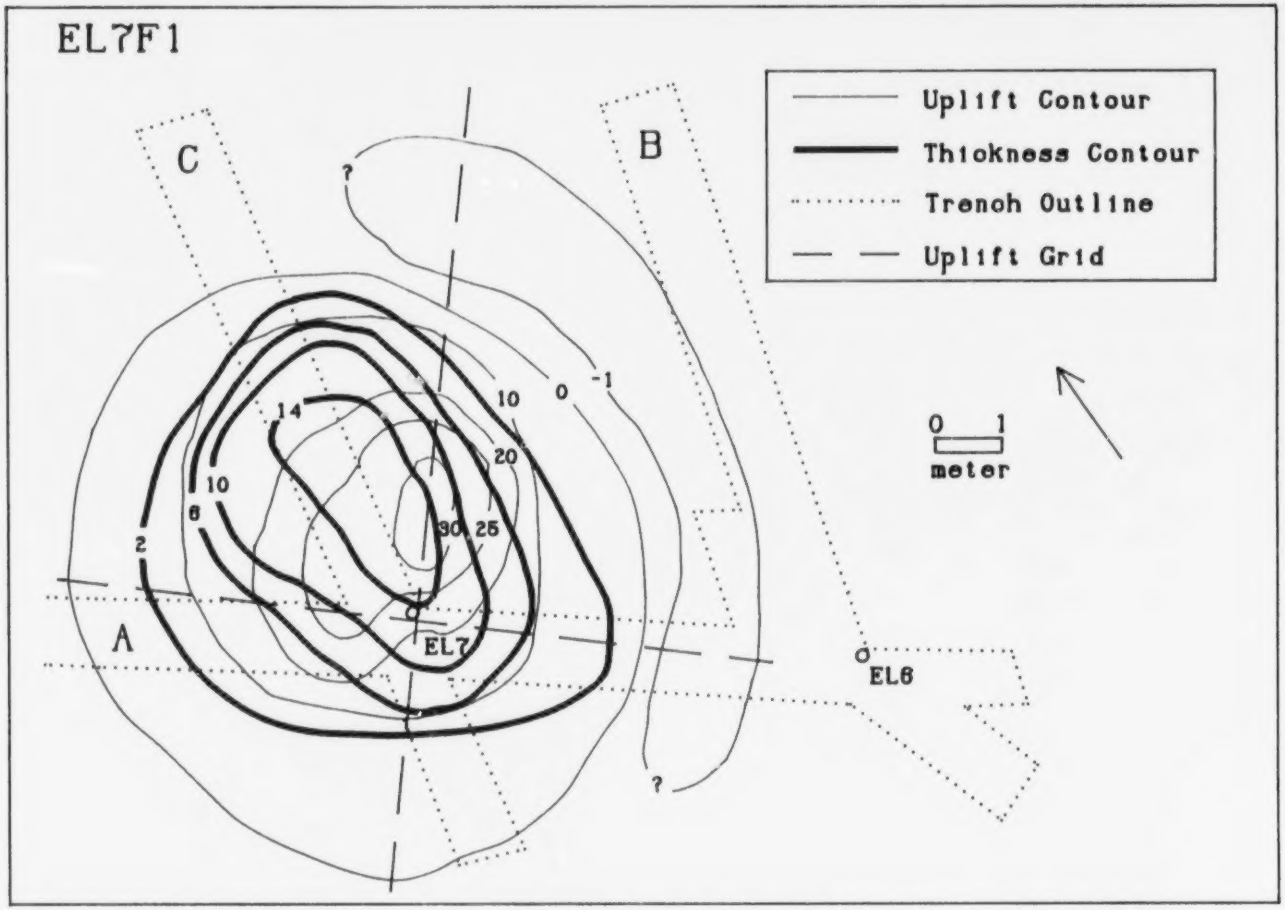

EL7F1
Uplift Contour
Thickness Contour
Trench Outline
Uplift Grid
C
B
A
?
?
14
10
6
2
10
0
-1
20
30
25
EL7
EL6
0
1
meter

Figure 8.8. Thickness and uplift contours for fracture EL7F1.

Borehole 6

Total surface uplift and total fracture thickness associated with fracturing episodes EL6F2 and EL6F3 are shown in Figure 8.7. Both contour sets are roughly elliptical in shape, with aspect ratios of about 1.5 to 1.6. The major axis of uplift contours generally trends to the northwest, whereas that of thickness contours trends roughly to the north. The distance between the maximum and zero values along the major axes is about 5 to 5.5 m in both contour sets. The distances between the borehole and the points of maximum value are 3.5 m for the uplift contours, and 2.5 m for the thickness contours. Maximum uplift is 20 mm and maximum thickness is 14 mm, indicating 30% deflation.

It appears that the general shape and size of the contour domes defined by uplift and thickness contours for fractures EL6F2 and EL6F3 are roughly equivalent, whereas the major axis trends differ by about 45°. The major axis trend for the thickness contours coincides more closely with the downslope direction than that for the uplift contours. The downslope direction is approximately parallel to the trends of trenches B and C.

A noteworthy feature of the surface deformation is the zone of subsidence beyond the zone of uplift. Subsidence appears to have occurred along or beyond the outer margins of the fractures, a result predicted by theoretical analyses (Pollard and Holzhausen, 1979).

Borehole 7

Uplift and thickness contours are plotted separately for two fractures created at borehole 7 -- EL7F1 and EL7F2. Shapes and degrees of consistency between uplift and thickness data are quite different for the two fractures.

Contours of fracture EL7F1, shown in Figure 8.8, are fairly circular, with radial distances of approximately 3.5 meters between the maximum value (center of the circle) to values of zero, in both the uplift and thickness contour sets. The maximum uplift is 30 mm, and maximum thickness is about half of maximum uplift, indicating 50% deflation. Distances from the borehole to points of maximum uplift and thickness are 1.5 m and 2 m, respectively. Subsidence was observed on two of the lines of data, but the other lines recorded only uplift (Fig. 8.8).

The two contour sets reflect good general agreement over the shape and areal extent of fracture EL7F1. Doubling of surface uplift, measured immediately after creation of the fracture, compared to fracture thickness reflects significant settling, or deflation, of the fracture and its overburden following the creation of the fracture.

The main difference between the contour sets lies in the orientations of the elliptical, inner contours of both sets. Inner contours of uplift trend northeastward, whereas those of thickness trend northward. These trends reflect bias due to the distribution of data points, which is limited to two orthogonal axes for uplift, and the trench walls for thickness.

The surface deformation over EL7F2 (Figure 8.9) is unusual; there is a zone of subsidence containing the borehole and the maximum uplift (5 mm) is located about 5 m north of the borehole. The thickest part of EL7F2 is 5 m north of the borehole, and that location is coincident with the point of maximum uplift. The basin-like zone of subsidence, however, is difficult to explain. The fracture EL7F2 dips slightly 5° to the south, and Pollard and Holzhausen (1979) show that a dipping fracture will produce an asymmetric deformation field. The sense of asymmetry predicted theoretically, however, is opposite that which is observed; it predicts a zone of subsidence centered north of the well. The zone of subsidence is difficult to explain.

Differences in the trends of major axes of the two contour sets are that same as those exhibited by contours of the overlying fracture (EL7F1). The differences are due to the distribution of data points, which was dictated by trench location for thickness contours, and by the surveying grid configuration for uplift contours. Time constraints prevented the use of more surveying data points.

Borehole 5

The clearest correlation between uplift and thickness contours is exhibited by the combined contours for fractures EL5F1, EL5F2, EL5F3, and EL5F4, shown in Figure 8.10. Both contour sets are roughly circular, with maxima (center of circle) at or near the borehole. Maximum uplift, located approximately 1 m east of the borehole, is almost 30 mm, and maximum thickness, located at the borehole, is 20 mm, so thickness is 33% less than uplift. The average distance from the maximum value to the zero contour is 4 m for uplift, and 3 m for thickness, so the area enclosed by the zero uplift contour is 33% larger than the area enclosed by the zero thickness contour.

The shapes of the uplift and thickness contour sets are similar. Both contour sets exhibit a conspicuous, localized disturbance in the northeastern hemisphere, about midway between the borehole and the periphery (zero contour). The irregularity seems to reflect a discontinuity in one of the fractures. This is not surprising, since the trace of fracture EL5F1, shown in Figure 7.18, is markedly discontinuous.

The areal distributions of the two contour sets, however, are different, as manifested by the distances from the borehole to the maxima, and by the areas enclosed within the zero contours. Compared to the area underlain by fractures, the area of surface uplift is 33% larger, and shifted approximately 2 m eastward, or downslope (see Figure 7.1 for topography).

ELECTRICAL RESISTIVITY

Electrical resistivity is another method of sensing hydraulic fractures without disturbing the subsurface. Adding an electrolyte to the fracturing fluid will result in a highly conductive fracture that is embedded in poorly conductive till. Three geophysical techniques of monitoring fracture location by sensing the conductivity contrast were employed at the ELDA site during the 1988 fracturing test. These

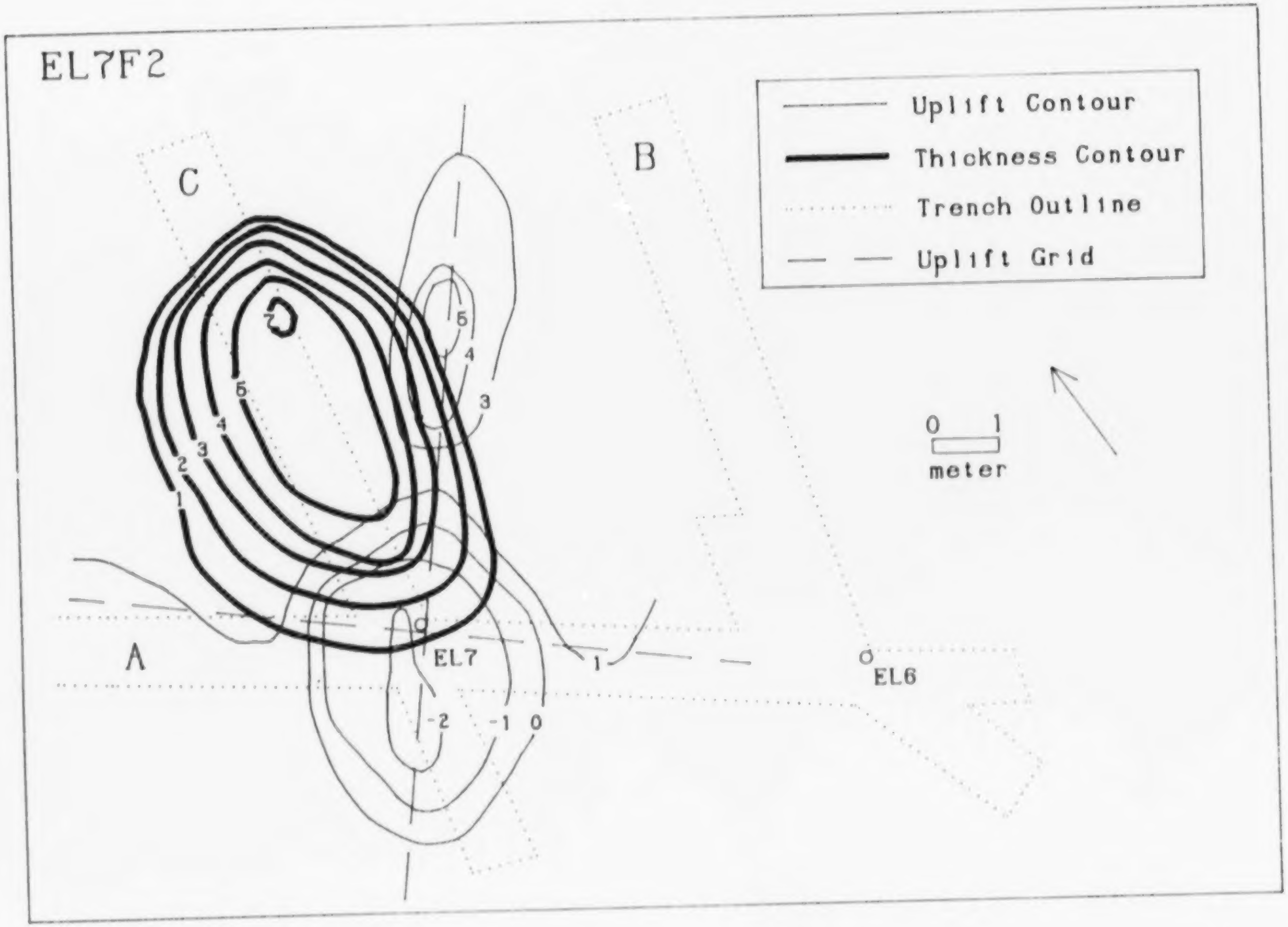
EL7F2
Uplift Contour
Thickness Contour
Trench Outline
Uplift Grid
A
B
C
0
1
meter
EL7
EL6
1
2
3
4
5
7
5
4
3
1
0
-1
-2

Figure 8.9. Thickness and uplift contours for fracture EL7F2.

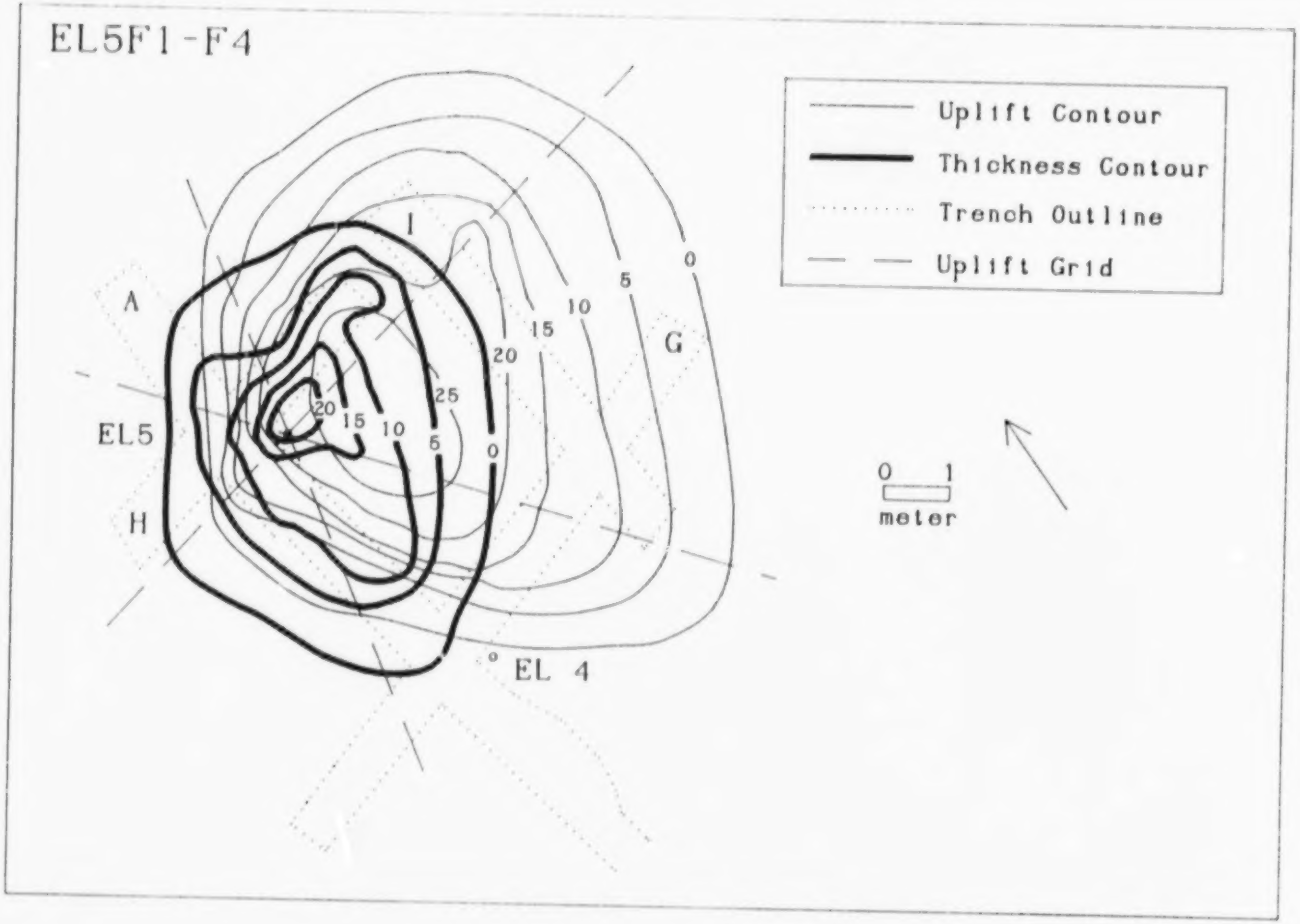
EL5F1-F4
Uplift Contour
Thickness Contour
Trench Outline
Uplift Grid
0
5
10
15
20
25
0
5
10
15
20
A
I
G
EL5
H
EL 4
0 1
meter

Figure 8.10. Thickness and uplift contours, combined for fractures EL5F1, EL5F2, EL5F3 and EL5F4.

were, the mise-a-la-masse, Wenner, and dipole-dipole methods. The mise-a-la-masse method was the most successful, yielding encouraging results for static and dynamic tests during the 1988 field test. It revealed fields of well-developed changes in apparent resistivity following fracturing. In addition, mise-a-la-masse showed abrupt changes in apparent resistivity as a function of time during a test, probably indicating the fracture had reached a critical location with respect to the sensing electrodes. The resistivity measurements were made in collaboration with Dr. Donald Stierman, who is a specialist in applying geophysical techniques to waste sites (Stierman, 1988). The following two sections are based on Stierman's findings.

Design

All resistivity measurements were made using a SoilTest R-60 resistivity system and a digital ammeter. The R-60 transmitter consists of 6 batteries wired such that output voltages can be varied between 45 and 840 volts in 6 dial-selected steps. Porous pots containing saturated copper sulfate solution as electrolyte served as electrodes. Distances were measured with a fiberglass surveyor's tape.

Slurry injected into the hydraulic fractures was spiked with about 3% KCl to ensure strong contrast between the electrical resistivities of the fluid and the formation. Samples collected were tested in the laboratory and found to exhibit electrical resistivities of about 0.3 ohm-meters at 25° C, consistent with a concentration of between 20 and 30 ppb of total dissolved solids. The fluid was about 120 to 400 times more conductive (less resistive) than the till in which the new fractures were developed.

Electromagnetic ground conductivity measurements were also made using a Geonics EM34-3XL in the horizontal dipole mode. Results were converted to apparent resistivity so that they could be compared directly with DC resistivity measurements.

The mise-a-la-masse method uses a conductive rock or soil body as one current electrode, with a second current electrode set at some distance away. A roving potential electrode maps the electrical field resulting from injecting current into the rock or soil body. If the ground is homogeneous, the current electrode acts as an electrical monopole at the center of a series of concentric circular equipotential contours. This field is distorted in the presence of subsurface conductors and the equipotentials tend to outline any buried conductive structures. This technique has been applied to mapping leaks from waste disposal lagoons (Stierman, 1988).

During the 1988 ELDA fracturing test, one current electrode was planted over 200 m to the east, effectively at infinity over the 20-m diameter array. Boreholes H4, H5, H6, or H7 served as the second current electrode. Potential was measured with respect to a porous pot planted over 200 m to the west. Colinear electrodes were planted along lines connecting boreholes. The total number of electrodes is 18.

Results

Following the creation of fracture H4, mise-a-la-masse measurements were made for boreholes 4 and 6. Results were dramatic at borehole 4, shown in Figure 8.11, which is a contour map of apparent resistivity at borehole 4 after fracture H4. Results were unimpressive at borehole 6 during creation of fracture H4. Post-fracture measurements show resistivity decreased 10 to 15% for electrodes nearest borehole 4, but increased slightly for borehole 6 (Figure 8.12). There is a strong correlation between the resistivity decrease and distance from borehole 4, with an elongation of this trend southeastward, toward borehole 5. This elongation suggests that fracture H4 propagated preferentially toward the southeast. The generally elliptical shape of the resistivity change contours suggests a largely horizontal fracture.

Boreholes 5, 6 and 7 were shallower than borehole 4, and the shallower fractures created at these boreholes were expected to obscure deeper fractures. Due to time constraints, results shown in Figure 8.13 represent the composite effect of fractures H4 and H5. Again, there is a clear correlation between a decrease in resistivity and the distance from borehole 5 for mise-a-la-masse using borehole 5 as a current electrode. Resistivity on borehole 4 following fracture 5 (Figure 8.14) shows a resistivity increase at most electrodes. The "bulls-eye" patterns of opposite polarities suggests a horizontal fracture extending some 3 to 5 m in each direction from the borehole.

Following the creation of fracture H7, mise-a-la-masse measurements on borehole 4, contoured in Figure 8.15, show complex distortion of the electrical field. Resistivity decreases at most electrodes with a maximum decrease of 13.5% on a corner of the array opposite from the fractured borehole. Resistivity increases at one of the electrodes nearest boreholes 4 and 7. This pattern suggests a single vertical fracture extending from borehole 7 nearly to borehole 6.

Changes for mise-a-la-masse measurements on borehole 7 (Figure 8.16) represent a composite of the effects of fractures H4, H5 and H7. The composite result is a decrease in resistivity of about 10%, extending north and south approximately 6 m (20 ft), with less distortion of the electrical field east or west. This suggests the fracture from borehole 7 trends north-south rather than east-west. The fracture vented into the shallow hole dug for one of the electrodes (E4). It is interesting that the change in resistivity measured by this electrode, directly in the new fracture, is less than that observed at other electrodes.

Following fracturing of borehole 6, mise-a-la-masse measurements of fracture H4 showed an increase in apparent resistivity of 6 to 10% in the vicinity of the borehole (Figure 8.17). A region of low apparent resistivity extends west from borehole 4 toward boreholes 7 and 6, suggesting that fractures have intersected. Mise-a-la-masse measurements of composite of the effects of fractures H5, H7 and H6 on borehole 6, contoured in Figure 8.18, yield a more complex pattern. It is interesting that the largest decrease in apparent resistivity for this final mise-a-la-masse measurement on borehole 6 is nearer borehole 4 than 6. Because these calculations reflect only changes after measurements made subsequent to fracture H4 (Figure 8.12), the interpretation that fractures H6, H4, and possibly H7 are interconnected must be checked against direct observations.

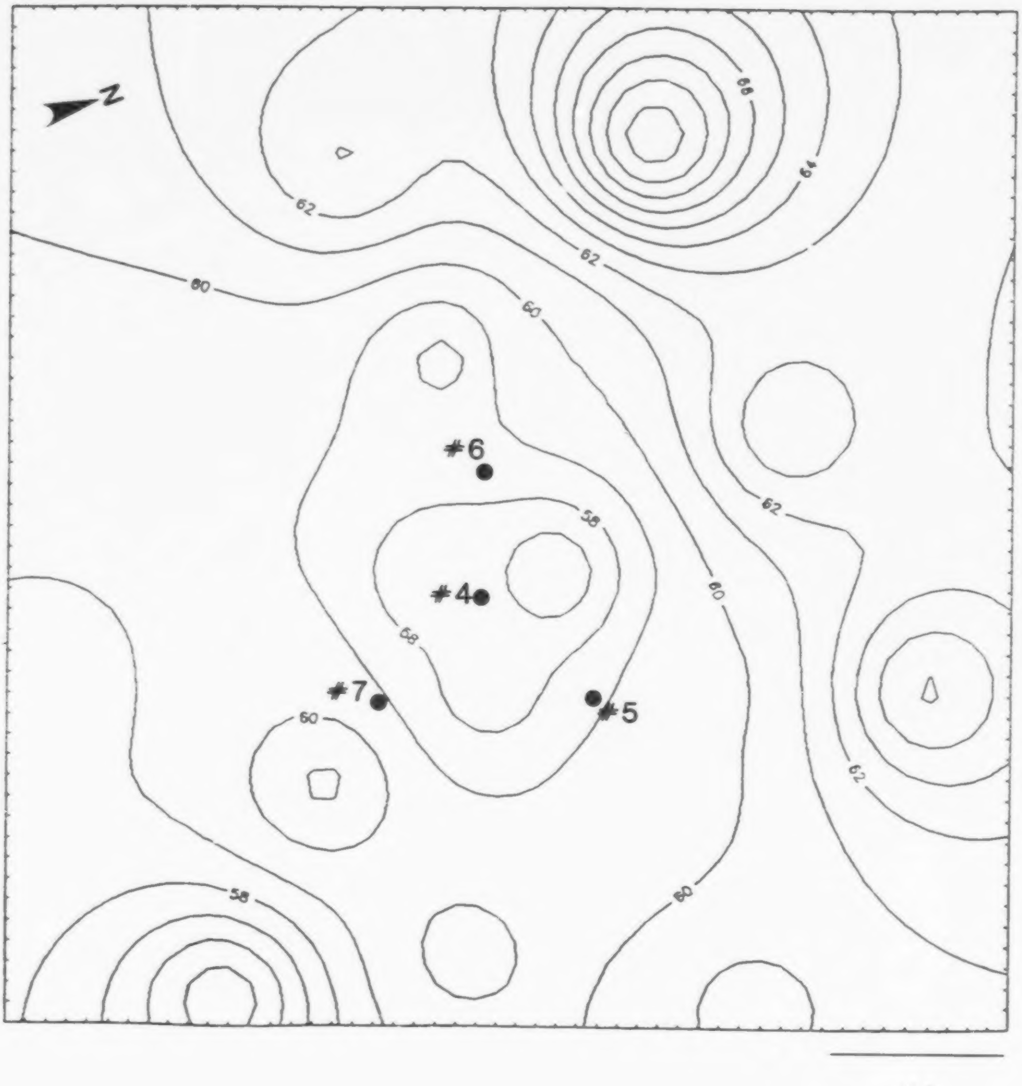
N
62
62
60
60
64
68
#6
58
#4
58
#7
#5
60
60
62
62
60
58
60
10 ft

Figure 8.11. Apparent resistivity contour map (mise-a-la-masse) on borehole 4, following fracture H4. Contour interval is 1 ohm-meter.

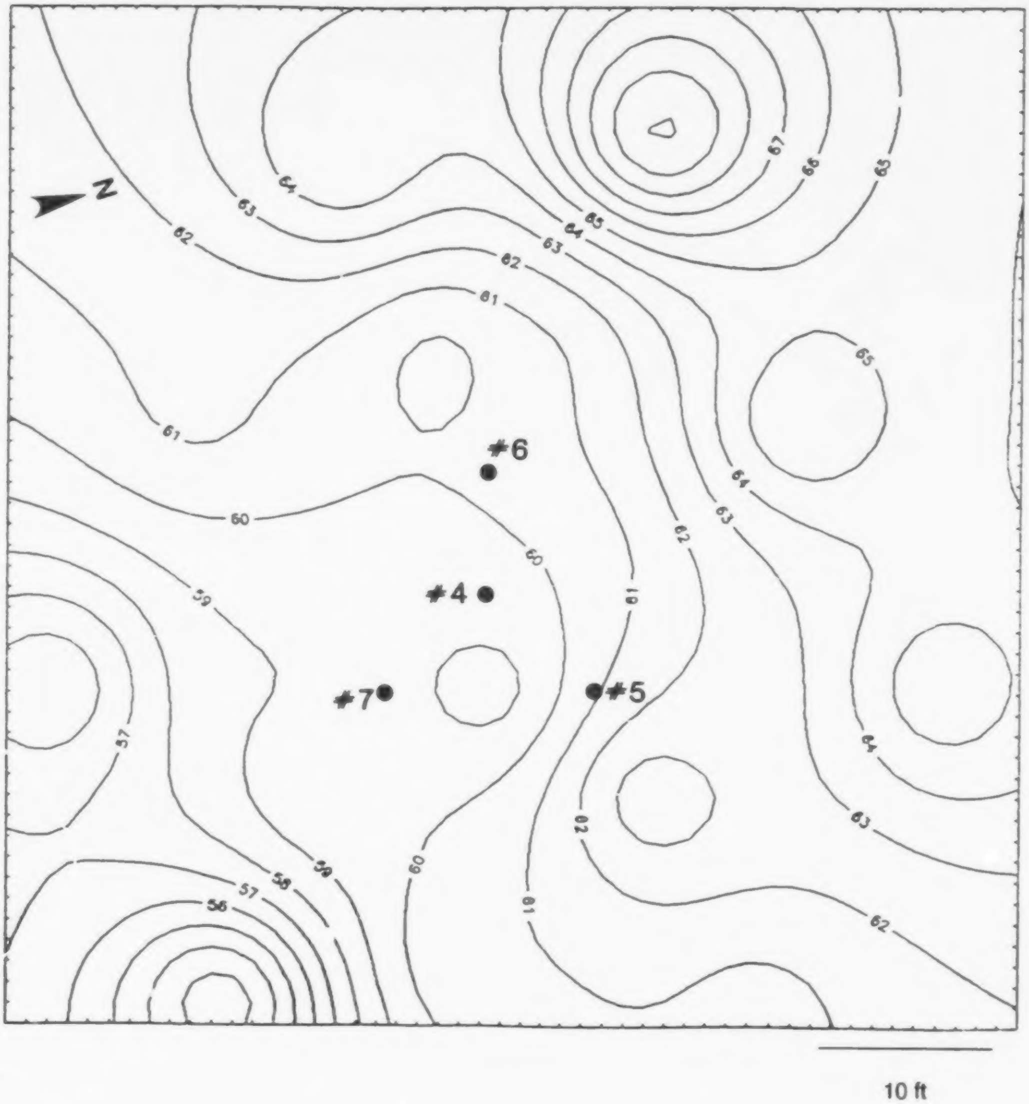
N
67
66
65
64
63
62
61
60
59
58
57
56
#6
#4
#7
#5
10 ft

Figure 8.12. Apparent resistivity contour map (mise-a-la-masse) on borehole 6, following fracture H4. Contour interval is 1 ohm-meter.

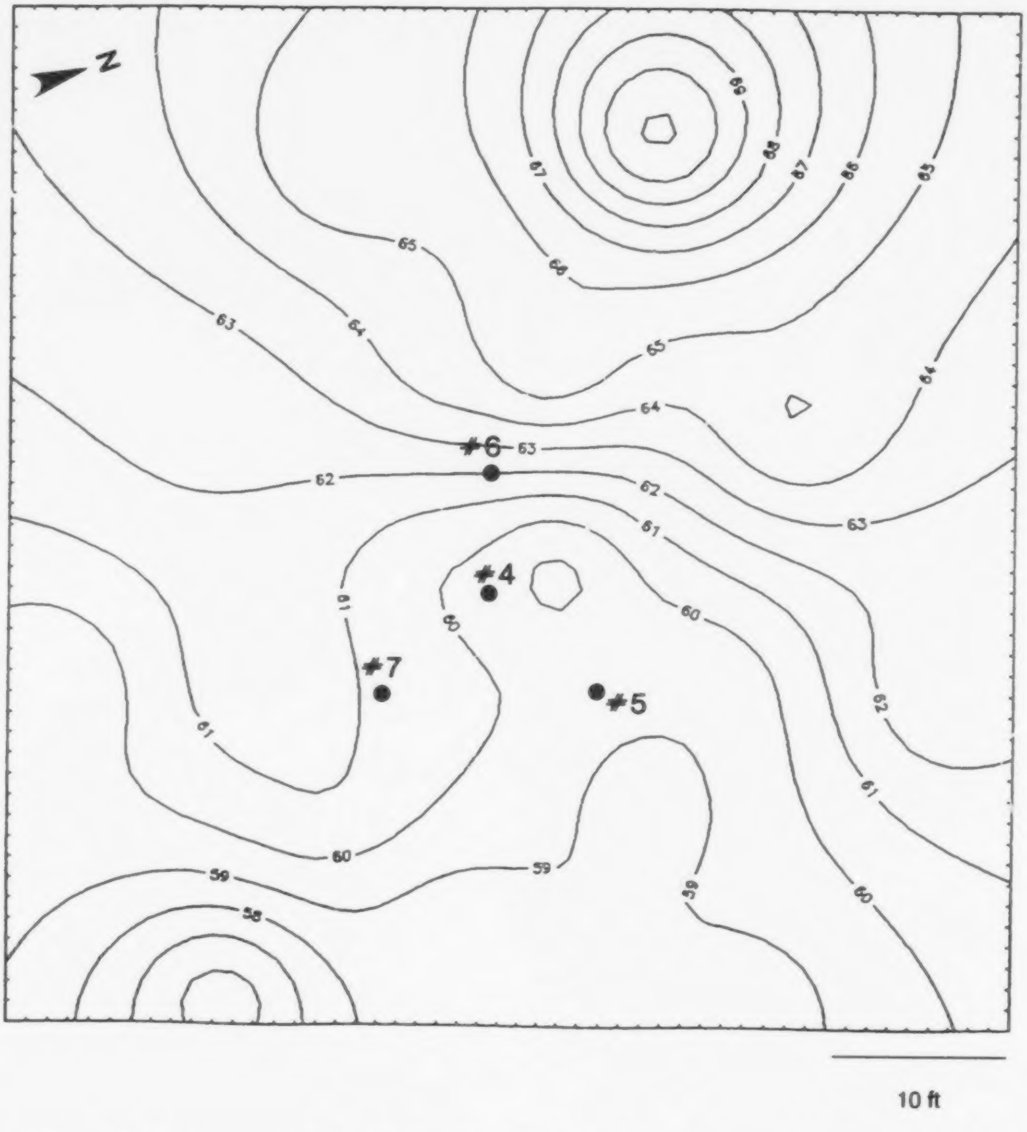
N
69
67
68
67
66
65
65
66
63
64
65
64
64
#6
63
62
62
63
61
#4
61
60
60
#7
#5
62
61
61
60
59
59
59
60
58
10 ft

Figure 8.13. Apparent resistivity contour map (mise-a-la-masse) on borehole 5, following fractures H4 and H5. Contour interval is 1 ohm-meter.

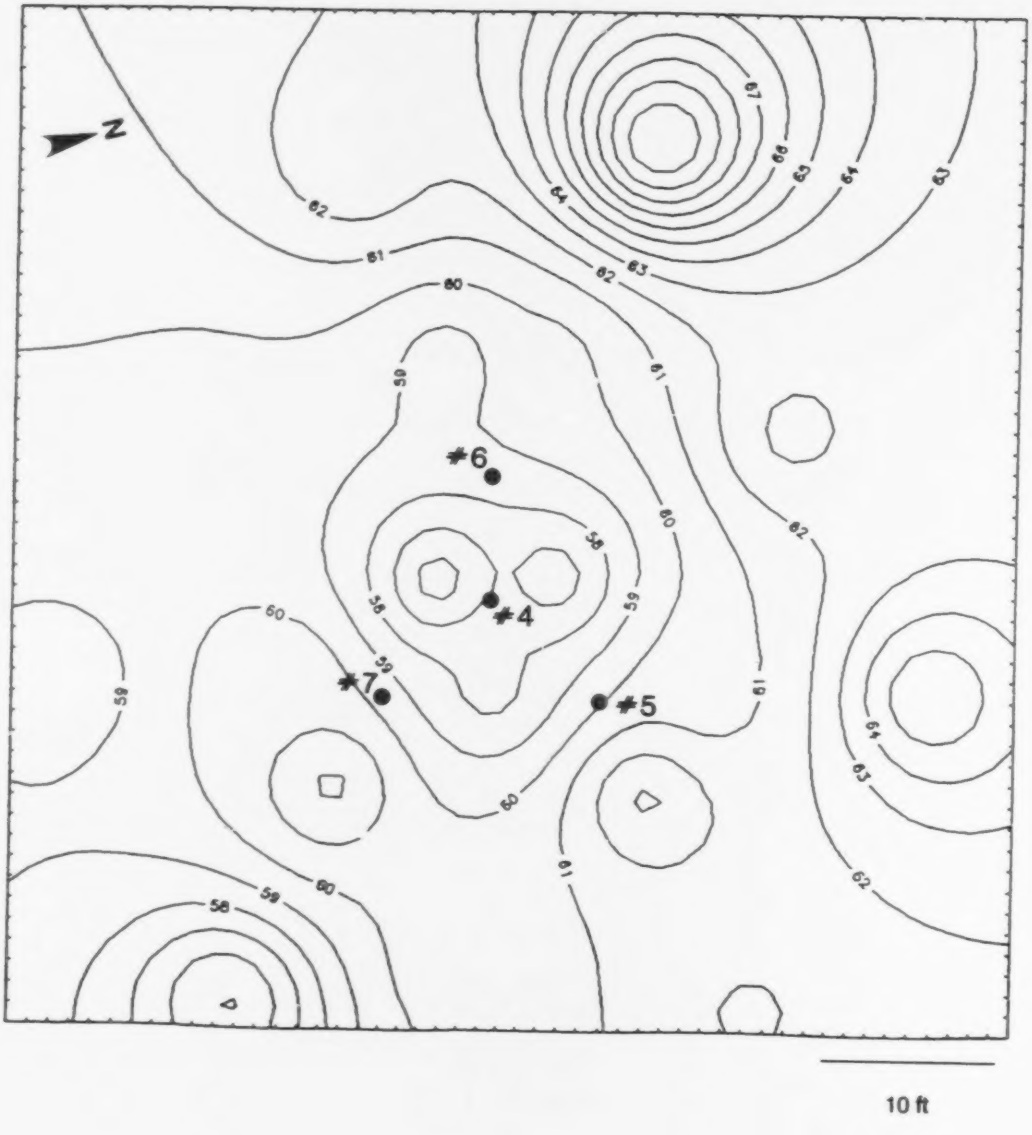
N
67
66
65
64
63
62
61
60
62
63
64
63
59
61
#6
62
60
58
59
#4
58
60
59
#7
#5
61
59
64
63
60
61
62
58
59
60
10 ft

Figure 8.14. Apparent resistivity contour map (mise-a-la-masse) on borehole 4, following fracture H5. Contour interval is 1 ohm-meter.

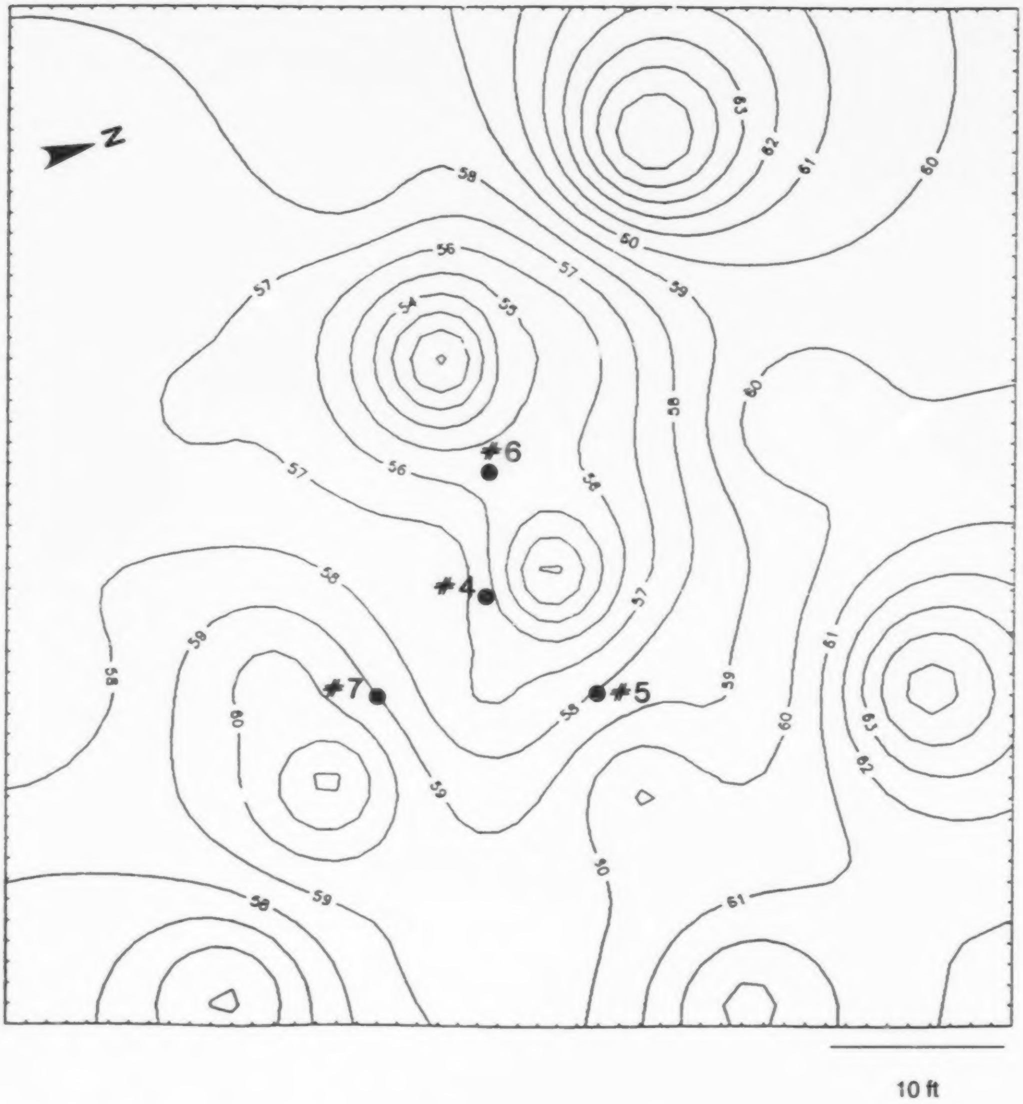
N
58
63
62
61
60
60
56
57
59
57
54
55
58
60
#6
57
56
58
58
#4
57
58
59
58
#7
#5
59
60
61
60
63
62
59
60
58
59
61
10 ft

Figure 8.15. Apparent resistivity contour map (mise-a-la-masse) on borehole 4, following fractures H4, H5 and H7. Contour interval is 1 ohm-meter.

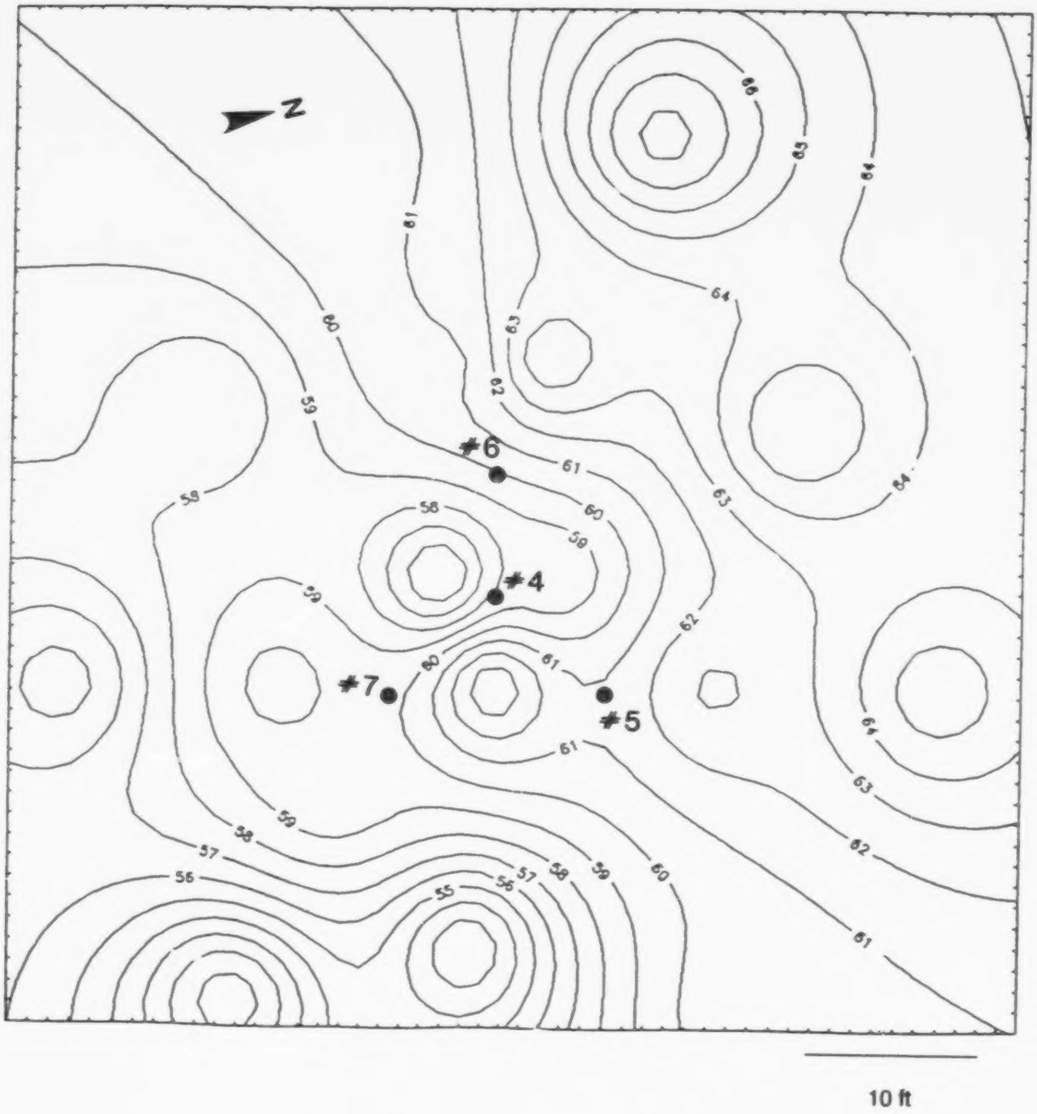
N
55
56
57
58
59
60
61
62
63
64
65
66
#4
#5
#6
#7
10 ft

Figure 8.16. Apparent resistivity contour map (mise-a-la-masse) on borehole 7, following fractures H4, H5 and H7. Contour interval is 1 ohm-meter.

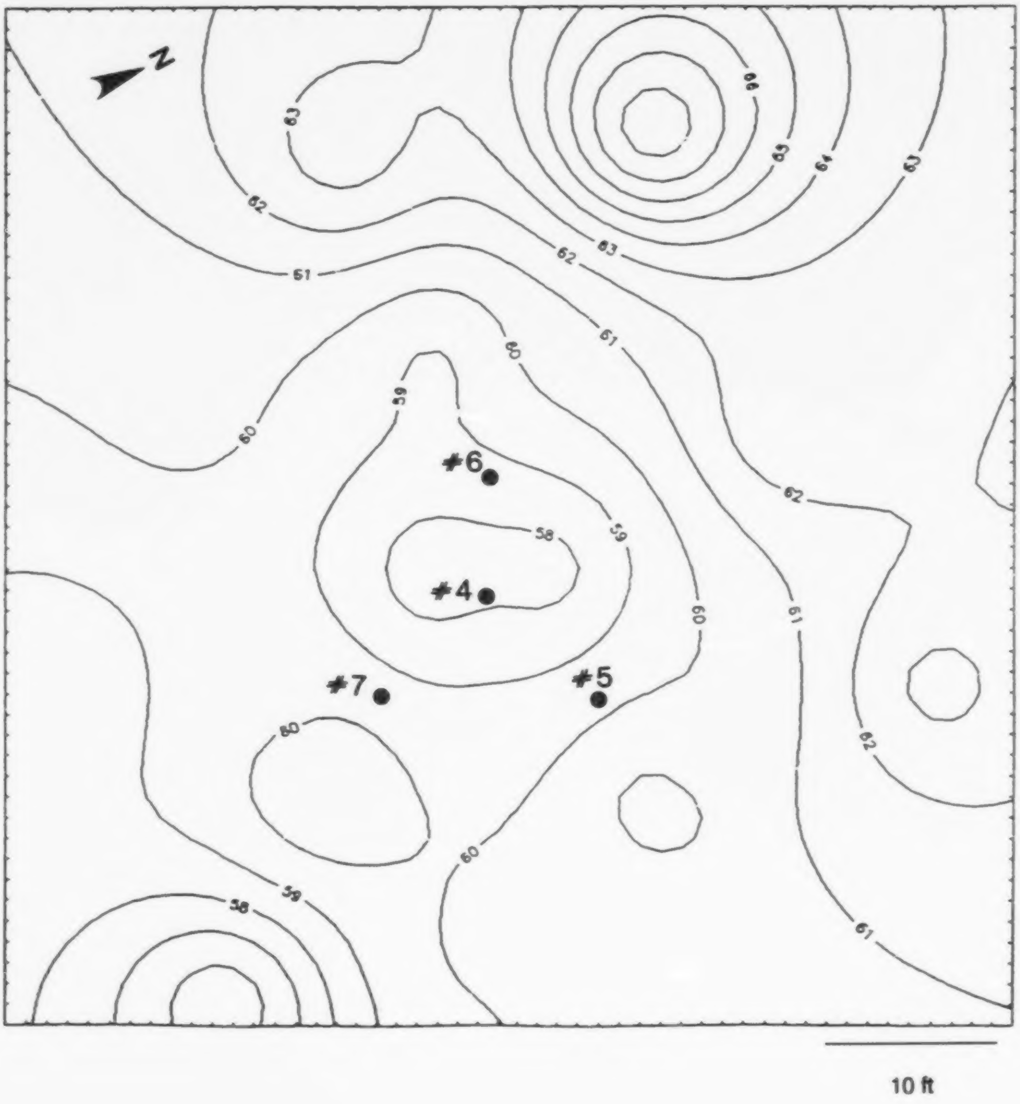
N
63
62
61
66
65
64
63
63
62
61
60
59
60
61
62
#6
58
59
#4
60
61
#7
#5
60
62
60
59
58
61
10 ft

Figure 8.17. Apparent resistivity contour map (mise-a-la-masse) on borehole 4, following fracture H6. Contour interval is 1 ohm-meter.

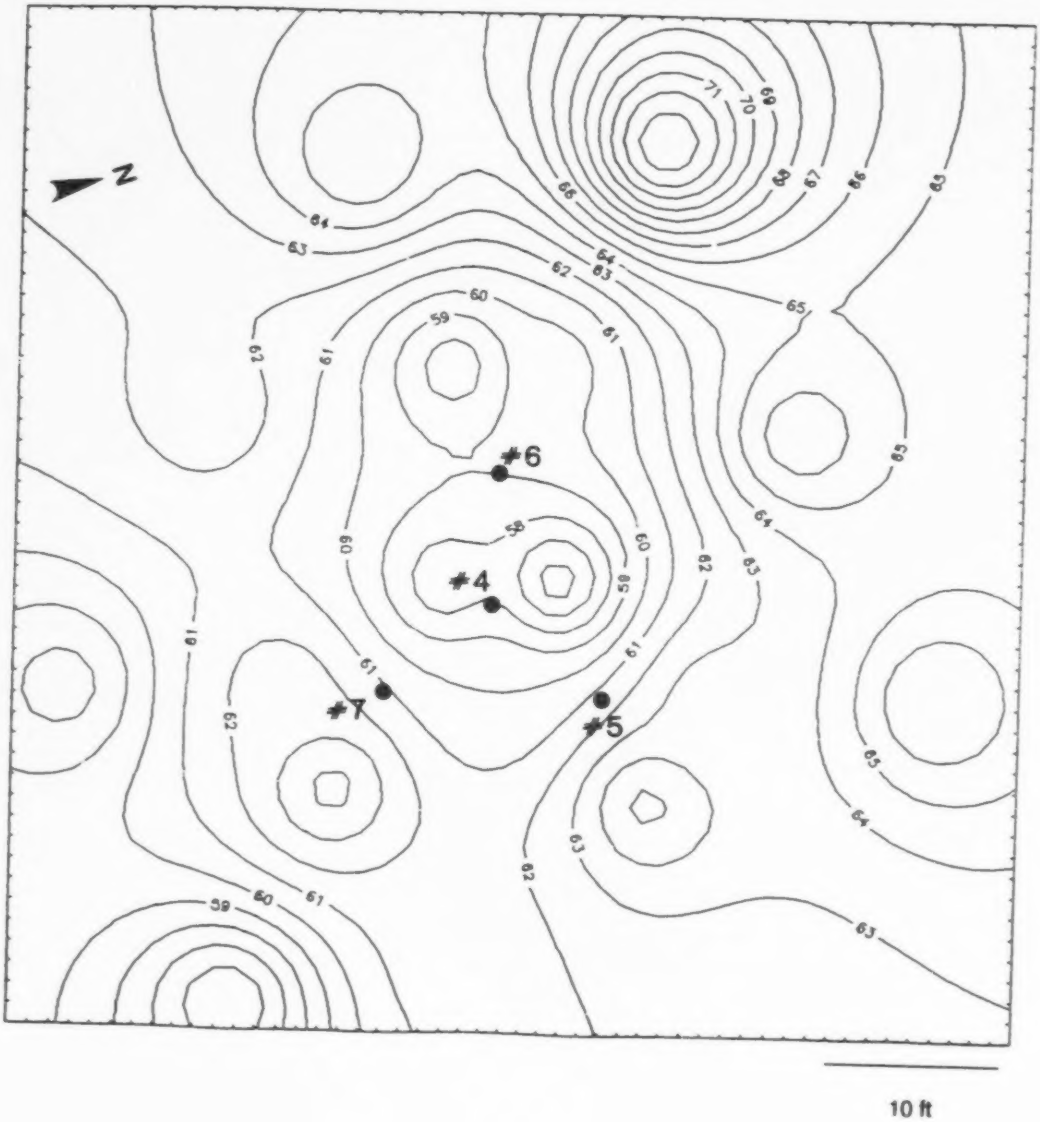
N
64
63
66
71
70
69
68
67
66
65
64
63
62
60
59
62
61
61
65
#6
58
60
60
59
62
63
64
#4
61
61
#7
62
61
#5
63
65
64
62
59
60
61
63
10 ft

Figure 8.18. Apparent resistivity contour map (mise-a-la-masse) on borehole 6, following fracture H6. Contour interval is 1 ohm-meter.

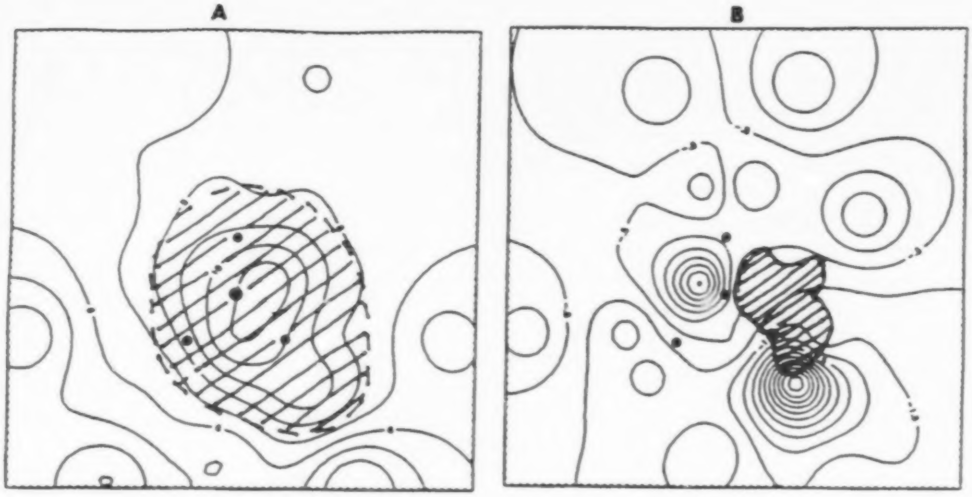

% DECREASE, FRAC 4

% DECREASE, FRAC 5

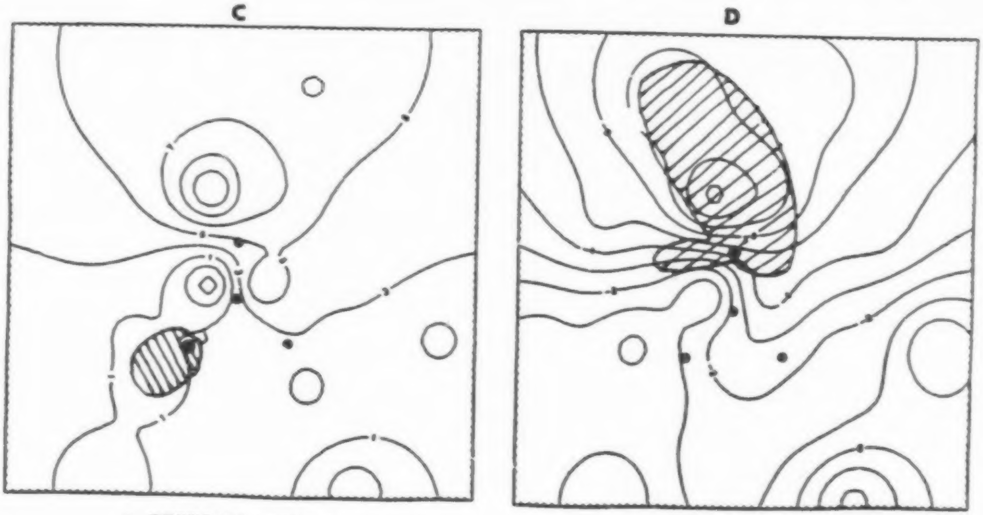

% DECREASE, FRAC 7

% DECREASE M4 FRAC 6

Figure 8.19. Summary of mise-a-la-masse apparent resistivity changes relative to borehole 4 resulting from fractures H4, H5, H6 and H7. Cross-hatching indicates locations of fractures.

borehole 7 toward borehole 6, representing a unilateral rupture, which is probably vertical. Figure 8.19d shows a decrease in apparent resistivity toward the midpoint between boreholes 6 and 7, with a decrease in apparent resistivity over much of the remaining array. This means electrical current density has decreased over most of the array, so current must have been diverted through a new conductor developed during the creation of fracture H6.

In conclusion, it is clear that hydraulic fracturing with a conductive fluid in a relatively resistive formation causes observable, but complex changes in the electrical properties of the formation. The mise-a-la-masse method yields valuable results, but further research is needed before its use could become commonplace. Specifically, measurements made as fractures are being propagated may help understand and interpret the sometimes complex results.

DISCUSSION

Pressure records, surface uplift, and surface tilt all are available methods of monitoring hydraulic fractures at shallow depths. Pressure records require simple equipment (a transducer and a data recorder), and indicate the onset of fracturing, show various fluctuations in pumping schedule and provide a rapid indicator of various problems. Methods of estimating orientation, asymmetry, and tip screenout (e.g. Nolte and Smith, 1981; Smith and others, 1987) from the pressure records of shallow fractures seems feasible.

Surface uplifts of a cm or more over hydraulic fractures were readily measured with a standard engineer's leveling telescope. Contour plots of uplift correlated with shallow hydraulic fractures, providing estimates of the leading edge and point of maximum thickness. Numerical inversion of uplift data should improve the qualitative correlations attempted in this work, providing estimates of the size, thickness, orientation and location of hydraulic fractures at depth.

During the 1988 tests, surface tilts were measured in real time with sophisticated tiltmeters and a datalogger. Inversion of those data after the tests provided estimates of how the fractures developed as a function of time. Comparison with maps indicates that the inversion provides crude simplifications of the actual fracture forms. In future applications, real time inversion of the tiltmeter data could yield estimates of fracture form as it is being created.

Electrical resistivity measurements, particularly those using the mise-a-la-masse technique, are able to sense the shallow fractures created during these tests. Methods of inverting electrical signals to obtain estimates of fracture geometry, which are currently being developed, will be required before the mise-a-la-masse method is practical for monitoring hydraulic fractures.

SECTION NINE

SUMMARY AND CONCLUSIONS

The objective of this study was to evaluate the feasibility of using hydraulic fracturing under conditions of contaminated regions. Most current applications of hydraulic fracturing are in oil reservoirs, and available techniques are designed for that application. Oil reservoirs are typically deeper and composed of different materials than contaminated regions, so the suitability of reservoir fracturing methods for contaminated soil use is unknown. Contaminants commonly occur in soils, or unlithified sediments, that are weaker and more compliant than the limestone or sandstone typical of reservoirs. Previous studies of hydraulic fracturing of soil have focused on methods of preventing fracture initiation during various geotechnical practices, so little is known about the details of the propagation of a hydraulic fracture in soil. Moreover, most contaminants occur at relatively shallow depths, so that hydraulic fractures could vent to the ground surface before they grow any appreciable distance from a well. The technique will be of limited value if venting limits fracture lengths to, say, a few well diameters.

The project consisted of studies in the laboratory and in the field, as well as an investigation of possible applications and a review of previous work. Laboratory studies were intended to reveal details of the process of hydraulic fracturing of soil, and to assess the ability of linear elastic fracture mechanics to predict the essential details. Field studies were intended to show whether fractures of useful size could be created and propped with sand at shallow depths in soil.

POTENTIAL APPLICATIONS

Most remedial systems requiring fluid flow either into or out of the subsurface could benefit from hydraulic fracturing. Pump and treat systems are obvious candidates because they employ procedures resembling those used in petroleum recovery, where the benefits of hydraulic fractures are without question. A review of data from oil wells, gas wells, and water wells that have been hydraulically fractured indicate a consistent increase in yield. Preliminary data from this research indicate that steady-state rates of inflow into unsaturated ground are greater, by factors of 3.1 to 9.0, into wells intersecting hydraulic fractures as compared with those in unfractured ground. Magnitudes of increase in observed yields, in general, are similar to magnitudes calculated using simple theoretical analyses. Based on a review of published data and simple analyses, we expect that hydraulic fracturing could increase yields of contaminant recovery wells consistently by as much as five times, commonly by as much as 10 times, and in some cases it could increase yields by factors much more than 10 times. The magnitude of the effect will depend on site conditions, the methods used to create hydraulic fractures, and the methods used to complete and develop associated wells.

Pump and treat systems are by no means the only remedial methods that might benefit from hydraulic fracturing. The yields of vapor-producing wells, such as those recovering natural gas or steam, are improved by hydraulic fracturing, so by analogy we expect that vapor extraction systems could benefit from this technology. Similarly, hydraulic fracturing could be used in conjunction with steam stripping -- a process developed to improve yields of oil wells and currently being tested under remedial conditions. Horizontal, sheet-like hydraulic fractures placed below a contaminated region could be used as gravity drains to intercept the leachate from soil flushing systems (Murdoch and others, 1987), improving the effectiveness of that remedial action.

The novel application of delivering solid material, as granules pumped into hydraulic fractures, is noteworthy. Bio-remediation systems stand to benefit in particular because either nutrients for microorganisms, or the microorganisms themselves, could potentially be delivered as fine-grained solids in hydraulic fractures. Air sparging--pumping air into the ground to encourage the growth of aerobic bacteria--could be more effective in ground containing hydraulic fractures.

LABORATORY STUDIES: SUMMARY OF RESULTS

1. Hydraulic fracturing in the Center Hill clay can be predicted and analyzed using methods of linear elastic fracture mechanics, similar to those used to predict hydraulic fracturing in rock. The large body of published papers analyzing hydraulic fracturing in rock can be used to predict field applications in soil, with appropriate modifications for boundary conditions (e.g. ground surface), material properties (e.g. elastic constants, leakoff parameters), and state of stress encountered at shallow depths.

2. Hydraulic fractures created in the laboratory consist of the following zones, which are arranged in order from the point of injection to the leading edge:

1) Starter slot This feature was created during sample preparation;

2) Parent fracture A continuous fracture surface marked by slight steps, ridges, or grooves.

3) Lobes The parent fracture twists or curves slightly, breaking into a family of discontinuous fracture lobes.

4) Unwetted tip Leading edge of the fracture is unstained by dye in the injection fluid.

Those zones were identified on almost all fracture surfaces. The only exception is that the unwetted tip zone was absent from fractures created in samples of less than 21% moisture; the entire fracture surface was stained. Published descriptions of the appearance of hydraulic fractures created in rock are similar to those produced in soil during this study.

3. Records of injection pressure as a function of time show three characteristic periods, which are interpreted as follows:

Period I: Injection pressure increases linearly with time, slope constant. Indicates inflation of the starter slot.

Period II: Slope of pressure record decreases but remains positive. Change in slope indicates onset of fracturing, positive slope indicates stable propagation.

Period III: Pressure reaches a maximum and slope becomes negative. Indicates unstable propagation.

In some samples, particularly the wetter ones, propagation begins slightly before the change in slope of the record, and the onset of propagation may have been overestimated by methods used in the study.

4. Moisture content and length of starter slot strongly affect the pressure record. As moisture content decreases, the duration of stable propagation (Period II) diminishes and the slope steepens during unstable propagation (Period III). Moreover, the pressure required to initiate fracturing increases as moisture content decreases. Similar trends occur when the length of the starter slot decrease; the duration of stable propagation diminishes and the pressure required to initiate fracturing increases.

5. The critical stress intensity factor can adequately predict the pressure required to initiate hydraulic fracturing of soil. It is independent of the length of the starter slot, for the slot lengths used in this study, and it predicts the driving pressure at the onset of fracturing to within 10 percent, on average. It was more accurate for samples wetter than the plastic limit (20% moisture by weight) and less accurate for samples drier than that value.

6. Under the confining stress used in the laboratory experiments, the size of the crack-tip process zone is estimated to increase from 0.13 to 0.47 cm as moisture decreases from 27 to 20%, according to preliminary measurements. The accuracy of the critical stress intensity method diminishes as the size of the process zone increases, which is consistent with the findings that accuracy of the laboratory tests decreased as samples became drier. Ouchterlony (1982) suggests that the starter slot should be at least 9.3 times longer than the process zone to ensure small scale yielding and maintain sufficient accuracy. Slot lengths ranged from 1.22 cm to 5.08 cm in the experiments, suggesting that the criteria of Ouchterlony are satisfied when using samples moister than the plastic limit. Those criteria are not met for the shorter slot lengths used in the drier samples, suggesting that slots at least 5 cm long should be used in samples drier than the plastic limit.

7. The value of the critical stress intensity is highly sensitive to moisture content, decreasing sharply from roughly 200 kPa cm$^{1/2}$ to 30 kPa cm$^{1/2}$ as moisture content increased by a few percent (from 20 to 22%). The sharp change in critical stress intensity corresponds to the plastic limit of the Center Hill clay.

8. Critical stress intensity goes to zero for samples of Center Hill clay greater than 32% moisture, although hydraulic fractures are readily created under those moisture conditions. Critical stress intensity fails as a predictor of moisture conditions that preclude the formation of a hydraulic fracture. Presumably, hydraulic fracturing will be impossible at extremely high moisture contents when the soil approaches a slurry in composition, but the moisture content at which this

occurs exceeds those used in this study and cannot be predicted using critical stress intensity.

9. Theoretical analyses based on linear elastic fracture mechanics and linear viscous fluid mechanics explain many of the details of the laboratory experiments, including the development of an unwetted tip, the average propagation velocity, changes in the form of the pressure record with changes in slot length or moisture content. Analyses used to predict field applications should include the effects of leakoff, which were omitted from the analyses presented here.

FIELD STUDIES: SUMMARY OF CONCLUSIONS

1. Hydraulic fractures of useful size can be created and propped with sand at shallow depths in glacial till.

2. Pumps and blenders used by the oil industry will successfully create hydraulic fractures at shallow depths. Blenders and pumps used for the 1988 test were designed for pumping rates, pressures and volumes that greatly exceed the specifications required for shallow depths. Several shortcomings, including sparse proppant density in the fractures created during the 1988 test, appear to be related to lack of control of the oversized equipment.

A blender and pump unit which is readily available for injection grouting and was used in the 1989 tests consistently resulted in hydraulic fractures propped with sand. That equipment is inexpensive and simple to operate relative to the oil-field equipment, but it too has drawbacks. The blenders were underpowered, resulting in long mixing times that limited the rate of injection. A progressive cavity pump used to inject slurry suffered excessive wear, and as a result the rotor and stator had to be replaced at the end of the project.

3. Vertical fractures nucleated at the walls of open cylindrical boreholes, even when the far-field state of stress favored horizontal fractures. Shallow horizontal notches, cut 3.75 cm into the walls of the open boreholes, failed to nucleate a horizontal fracture in most cases. The vertical fractures extend several cm to several dm away from the open borehole, and then abruptly (typically within a few cm) roll over and become flat-lying. Vertical fractures at the borehole reduced the maximum lengths fractures achieved before venting, and they may have restricted the transport of proppant.

Vertical fractures created during the 1988 test were a consequence of the borehole design because they were eliminated by decreasing the length of the cylindrical hole and increasing the size of the notch. Hydraulic fractures adjacent to boreholes in till were always horizontal when they were nucleated from notches cut 10 to 20 cm in till with a water jet, as in the 1989 tests.

4. The form of the fractures created during the 1988 test is characterized by the following four zones arranged in increasing distance from the parent borehole:

Zone 1: a sub-vertical orientation adjacent to the borehole.

Zone 2: a flat-lying orientation in the vicinity of the borehole.

Zone 3: a planar to trough-like fracture dipping gently (15° to 25°) toward the borehole. This zone extends in one direction away from the borehole and composes most of the fracture.

Zone 4: a steeply-dipping orientation that vents to the ground surface

In plan the fractures are crudely elliptical, with aspect ratios of roughly 2:3. The parent borehole is typically near one end of the major axis and the vent is at the other end.

The form of the fractures created during the 1989 test was simpler than that of the previous year; the fractures were nearly flat-lying from their parent borehole to their leading edge. Some fractures dipped gently toward the borehole, but even the steepest dip was only 5°. In plan, the fractures created during 1989 were slightly elongate (aspect of 2:3) and they were highly assymetric with respect to the borehole; in plan they are similar to the results of the previous year.

5. Fractures created during the 1988 dipped more steeply than those of the 1989 test. The dip is important because it defines how far the fracture can extend before venting. Three differences between the 1988 and 1989 tests are recognized that could have affected the average dip.

a) Rate of injection during the 1989 test was less than that of the 1988 test. Pollard and Holzhausen (1979) show that decreasing the pressure gradient within the fracture (say, by decreasing pumping rate) will inhibit growth toward the ground surface.

b) Sand concentration, and thus slurry density, was greater during the 1989 test. Increasing fluid density will decrease the static driving pressure gradient (e.g. Secor and Pollard, 1975; Abou-Sayed and others, 1984), inhibiting upward growth.

c) The topographic surface overlying fractures during the 1989 test was benched, whereas it was nearly flat over the dipping fractures created in 1988. It appears that topography may contribute to the orientation of shallow hydraulic fractures (perhaps by inducing horizontal variations in vertical stress), but mechanisms controlling this suggestion must be investigated in more detail.

6. The major axes of hydraulic fractures created during both tests extended away from parent boreholes in directions that minimize the vertical stress. During the 1988 tests, fractures either propagated away from a backhoe parked next to the borehole, or they propagated in the same direction as the overlying slope. During the 1989 tests, all fractures grew away from a steep embankment.

Those observations suggest that preferred propagation directions of horizontal fractures can be crudely predicted based on topography; they will grow in the downslope direction. This raises the possibility that the direction of propagation could be influenced by artificially loading the ground surface, which could be important at sites underlain by regions that should not be fractured. It also indicates that a horizontal hydraulic fracture created next to a building will tend to grow away from the building.

7. Fractures were created and filled with sand at depths ranging from 1 to 4 m. Dimensions of fractures created between 1 and 2 m are known in detail from excavations. They are as follows: during the 1988 tests, the maximum length, from borehole to the leading edge, ranged from 1.8 to 13.5 m and it averaged 5.8 m. Areas covered by those fractures ranged from 2.2 to 90 m^2, and averaged 25 m^2. The thickest part of a fracture created in 1988 was 9mm, and many of the fractures created that year were nearly devoid of sand.

During the 1989 tests, the maximum lengths ranged from 0.8 to 7.2 m, and averaged 4.0 m. Areas covered by the fractures ranged from 0.8 to 36.7 m^2, and they averaged 19.2 m^2. All the fractures contained sand, ranging in maximum thickness from 2 to 20 mm, and averaging 11 mm.

The fractures created in 1989 were slightly smaller in area than those of the previous year; however, the sizes of all the 1988 fractures were limited by venting, whereas most of the 1989 fractures did not vent and they could have been larger if more fluid had been pumped into them. The average thickness of sand in the 1989 fractures exceeded the maximum thickness from the previous year.

The increase in thickness of sand, from the 1988 to the 1989 tests, apparently results from changes in the above-ground mixers and pumps. The above-ground equipment used in 1988 was designed for flow rates and pressures required to create hydraulic fractures in oil wells, which are as much as several orders of magnitude more than the flow rates and pressures required for our applications. The oil-field equipment lacked the control required to mix and pump the relatively small applications that we required. This simply indicates that filling hydraulic fractures with sand will be facilitated by using above-ground equipment that is designed for the conditions of the application.

8. A method of creating fractures from a device driven into the ground was developed to facilitate the creation of multiple fractures in soil. As many as four, flat-lying hydraulic fractures were stacked at spacings of 30 cm without intersecting their neighbors. When one fracture was created 15 cm below another, the lower fracture would commonly climb upward and intersect the overlying fracture several meters from the borehole. One spacing of 7 cm was attempted; the lower fracture intersected the upper one several dm from the borehole.

It would be possible to stack flat-lying fractures at spacings between 15 and 30 cm throughout a contaminated region at the ELDA site, and similar spacings should be possible under similar site conditions.

9. Pressure records, surface uplift, and surface tilt all are available methods of monitoring hydraulic fractures at shallow depths. Pressure records require simple equipment (a transducer and a data recorder), and indicate the onset of fracturing, show various fluctations in pumping schedule and provide a rapid indicator of

various problems. Methods of estimating orientation, assymetry, and tip screenout (e.g. Nolte and Smith, 1981; Smith and others, 1987) from the pressure records of shallow fractures seems feasible.

Electric resistivity measurements, particularly those using the mise-a-la-masse technique, were able to detect the hydraulic fractures created during the 1988 tests. Methods of inverting electrical signals to obtain estimates of fractures geometry will be required, however, before this method yield quantitative estimates of fracture geometry.

Surface uplifts of a cm or more over hydraulic fractures were readily measured with a standard engineer's leveling telescope. Contour plots of uplift correlated with shallow hydraulic fractures, providing estimates of the leading edge and point of maximum thickness. Numerical inversion of uplift data should provide valuable estimates of the size, thickness and location of hydraulic fractures at depth.

During the 1988 tests, surface tilts were measured in real time with tiltmeters and a datalogger. Inversion of those data after the tests provided estimates of how the fractures developed as a function of time. Comparison with maps indicates that the inversion provides crude simplifications of the actual fracture forms. In future applications, real time inversion of the tiltmeter data could yield estimates of fracture form as it is being created.

Electrical resistivity measurements, particularly those using the mise-a-la-masse technique, are able to sense the shallow fractures created during these tests. Methods of inverting electrical signals to obtain estimates of fracture geometry, which are currently being developed, will be required before the mise-a-la-masse method is practical for monitoring hydraulic fractures.

REFERENCES CITED

Aamodt, R.L. and M. Kuriyagawa. 1982. Measurement of instantaneous shut-in pressure in crystalline rock. Proceedings of Workshop on Hydraulic Fracturing Stress Measurements. Zoback, M.D. and C. Haimson.(eds.) U.S. National Comm. for Rock Mechanics. Menlo Park, CA. 394-402.

Abe, H., T. Mura and L.M. Keer. 1976. Growth rate of a penny-shaped crack in hydraulic fracturing of rocks. J. Geop. Res. 81:5335-5340.

Abou-Sayed, A.S. 1977. Fracture toughness, K, of triaxially loaded Indiana limestone. In: Proc. 18th U.S. Sym. Rock Mech. 1-8.

Abou-Sayed, A.S., C.E. Brechtel and R.J. Clifton. 1978. In-situ stress determination by hydrofracturing: A fracture mechanics approach. J. Geop. Res. 83:2851-2862.

Abou-Sayed, A.S., K.P. Sinha and R.J. Clifton. 1984. Evaluation of the influence of in-situ reservoir conditions in the geometry of hydraulic fractures using a 3-D simulator: Part 1--Technical Approach, SPE Paper 12877. In: Proc. Uncon. Gas Rec. Sym., Pittsburg, PA.(May) 433-438.

Abramowitz, M. and I.A. Stegun. 1964. eds. Handbook of Mathematical Functions with Formulas, Graphs, and Mathematical Tables. U.S. Govt. Printing Office. Washington, DC. 1046.

Acharya, A. 1988. Hydraulic-fracture-treatment design simulation. SPE Production Engineering. 40:139-142.

Advani, S.H., H. Khattab and J.K. Lee. 1985. Hydraulic fracturing geometry, modeling, prediction and comparisons, SPE Paper 13863. In: Proc. Low Perm. Gas Res. Sym., Denver, CO.(May) 135-139.

Ahmed, U., J. Strawn, M. Wilson and J. Schatz. 1983. Effect of stress distribution on hydraulic fracture geometry: A laboratory simulation study in one meter cubic blocks, SPE Paper 11637. In: Proc. SPE Sym. Low Permeability, Denver, CO. 1-5.

Anderson, G.D. 1979. Laboratory experiments on hydraulic fracture growth near an interface. In: Proc. U.S. Sym. Rock Mech., Golden, CO. 19:333-339.

Anderson, R.A. 1974. Slurry injection of vein materials in the Coeur d'Alene district. Economic Geology. 69:414-415.

Anderson, R.W. and A.M. Phillips. 1988. Practical application of economic well-performance criteria to the optimization of fracturing treatment design. SPE Production Engineering. 40:223-228.

Babcock, R.E., C.L. Prokop and R.O. Kehle. 1967. Distribution of propping agents in vertical fractures. Prod. Monthly. 11-18.

Barenblatt, G.I. 1962. The mathematical theory of equilibrium cracks in brittle fracture. Adv. Appl. Mech. 7:55-129.

Baski, H. 1987. Hydrofracturing of water wells. Water Well J. 41:6:34-35.

Biot, M.A., L. Masse and W.L. Medlin. 1982. A two-dimensional theory of fracture propogation, SPE Paper 11067. In: Proc. Ann. SPE Fall Tech. Conf., New Orleans, LA. 1-15.

Biot, M.A., W.L. Medlin and L. Masse. 1983. Fracture penetration through an interface. Soc. Petr. Eng. J. 857-869.

Bjerrum, L. and K.H. Andersen. 1972. In-situ measurement of lateral pressures in clay. Geotechnique. 15:11-20.

Bjerrum, L., J.K.L. Nash, R.M. Kennard and R.E. Gibson. 1972. Hydraulic fracturing in field permeability testing. Geotechnique. 22:319-332.

Boone, T.J., A.R. Ingraffea and J.C. Roegiers. 1989. Visualization of hydraulically driven fracture propagation in poroelastic media using a superworkstation. J. Petr. Tech., Trans. AIME. 41:574-580.

Bouteca, M.J. 1988. Hydraulic fracturing model based on a three-dimensional closed form: Tests and analysis of fracture geometry and containment. SPE Production Engineering. 3:445-454.

Bouwer, H. 1978. Groundwater Hydrology. McGraw-Hill Book Co. New York. 480.

Briones, A.A. and G. Uehara. 1977a. Soil Elastic Constants: I. Calculations from sound velocities. Soil Sci. Soc. Am. J. 41:22-25.

Briones, A.A. and G. Uehara. 1977b. Soil Elastic Constants: II. Application to analysis of soil cracking. Soil Sci. Soc. Am. J. 41:26-29.

Brooker, E.W. and H.O. Ireland. 1965. Earth pressures at rest related to stress history. Canadian Geotech. J. 2:1-15.

Brunsing, T.P. 1987. The block displacement method field demonstration and specifications. U.S. EPA Project Summary. 600-S2-87-023:1-6.

Brunsing, T.P. and R.B. Henderson. 1984. A laboratory technique for assessing the in-situ constructability of a bottom barrier for waste isolation. In: Proc. Nat. Conf. Manag. Uncont. Haz. Wast. Sites, Washington, DC. 135-140.

Bryant, D.G. 1968. Intrusive breccias associated with ore, Warren (Bisbee) Mining District, Arizona. Economic Geology. 63:1-12.

Cinco-Ley, H., V.F. Samaniego and N.A. Dominguez. 1978. Transient pressure behavior for a well with a finite-conductivity vertical fracture. Soc. Petr. Eng. J. 253-264.

Cinco-Ley, H., V.F. Samaniego and A. Dominguez. 1981. Transient pressure analysis for fractured wells. J. Petr. Tech., Trans. AIME. 1749-1764.

Clark, J.B. 1949. A hydraulic process for increasing the productivity of wells. Petr. Trans. AIME. 2510:1-8.

Cleary, M.P. 1978a. Primary factors governing hydraulic fractures in heterogeneous stratified porous formations. In: Proc. ASME Energy Tech. Conf. & Exh., Houston, TX.(Nov.) 1-12.

Cleary, M.P. 1978b. Some deformation and fracture characteristics of oil shale. In: Proc. U.S. Sym. Rock Mech., Rapid City, SD. 72-82.

Cleary, M.P. 1980a. Analysis of mechanisms and procedures for producing favourable shapes of hydraulic fractures, SPE Paper 9260. In: Proc. 55th Ann. SPE Fall Tech. Conf. Exh., Dallas, TX. 1-12.

Cleary, M.P. 1980b. Comprehensive design formulae for hydraulic fracturing, SPE Paper 9259. In: Proc. 55th Ann. SPE Fall Tech. Conf. Exh., Dallas, TX. 1-16.

Cleary, M.P. 1988. The engineering of hydraulic fractures: State of the art and technology of the future. J. Petr. Tech., Trans. AIME. 13-21.

Cleary, M.P. and S.K. Wong. 1985. Numerical simulation of unsteady fluid flow and propagation of a circular hydraulic fracture. Int. J. Num. Anal. Meth. Geomech. 9:1-14.

Cleary, M.P., A.R. Crockett, J.I. Martinez and V.M. Narendran. 1983a. Surface integral schemes for fluid flow and induced stresses around fractures in underground reservoirs, SPE Paper 11632. In: Proc. SPE Sym. Low Permeability, Denver CO. 283-292.

Cleary, M.P., M. Kavvadas and K.Y. Lam. 1983b. Development of a fully three-dimensional simulator for analysis and design of hydraulic fracturing, SPE Paper 11631. In: Proc. SPE Sym. Low Permeability, Denver, CO. 271-278.

Clifton, R.J., E.R. Simonson, A.H. Jones and S.J. Green. 1976. Determination of the critical-stress-intensity factor K from internally pressurized thick-walled vessels. Experimental Mechanics. 233-238.

Cornet, F.H., J.M. Hosanski, F. Bernaudat and E. Ledoux. 1982. Shallow depth experimentation on the concept of energy extraction from deep hot dry rocks. Hydraulic Fracturing and Geothermal Energy. Nemat-Nasser, S., H. Abe and S. Hirakawa.(eds.) Martinus Nijhoff Pub. The Hague. 75-93.

Cotterell, B. and J.R. Rice. 1980. Slightly curved or kinked cracks. Int. J. Fracture. 16:155-169.

Crockett, A.R., R.M. Willis and M.P. Cleary. 1989. Improvement of hydraulic fracture predictions by real-time history matching on observed pressures. SPE Production Engineering. 4:408-416.

Daneshy, A.A. 1973a. Experimental investigation of hydraulic fracturing through perforations, SPE Paper 4333. In: Proc. 2nd Ann. SPE European Meeting, London, England. 1-12.

Daneshy, A.A. 1973b. On the design of verticla hydraulic fractures. J. Petr. Tech., Trans. AIME. 83-97.

Daneshy, A.A. 1973c. A study of inclined hydraulic fractures. Soc. Petr. Eng. J. 13:61-68.

Daneshy, A.A. 1973d. Three-dimensional propagation of hydraulic fractures extending from open holes. Rock Mechanics. 157-179.

Daneshy, A.A. 1976a. Hydraulic fracture propagation in layered formations. Soc. Petr. Eng. J. 33-41.

Daneshy, A.A. 1976b. Rock properties controlling hydraulic fracture propagation, SPE Paper 5752. In: Proc SPE European Spring Meeting, Amsterdam, The Netherlands.(April) 1-8.

Daneshy, A.A. 1978a. Hydraulic fracture propagation in layered formations. Soc. Petr. Eng. J. 33-41.

Daneshy, A.A. 1978b. Numerical solution of sand transport in hydraulic fracturing. J. Petr. Tech., Trans. AIME. 132-140.

Davis, P.M. 1983. Surface deformation associated with a dipping hydrofracture. J. Geop. Res. 88:5826-5834.

Dean, R.H. and S.H. Advani. 1984. An exact solution for pistonlike leak-off of compressible fluids. J. Energy Res. Tech., Trans. ASME. 106:539-542.

De Laguna, W. 1966a. Disposal of radioactive wastes by hydraulic fracturing, Part I: General concept and first field experiments. Nuclear Eng. & Design. 3:338-352.

De Laguna, W. 1966b. Disposal of radioactive wastes by hydraulic fracturing, Part II: Mechanics of fracture formation and design of observation and monitoring wells. Nuclear Eng. & Design. 3:432-438.

Detournay, E. 1979. The interaction of deformation and hydraulic conductivity in rock fracture. Improved stress determination proceedures by hydraulic fracturing. Univ. of Minn., Civil & Mineral Eng. Dept. Minneapolis. 1-42.

Dickinson, R.M. 1988. Review of consolidation grouting of rock masses and methods for evaluation. U.S. Army Corps of Eng. Final Report REMR-GT-8. 86.

Dugdale, D.S. 1960. Yielding of steel sheets containing slits. J. Mech. Phys. Solids. 8:100-104.

Dyes, A.B., C.E. Kemp and B.H. Claude. 1958. Effect of fractures on sweep-out pattern. Petr. Trans. AIME. 213:245-248.

Elbel, J.L. and P.A. Sookprasong. 1987. Use of cumulative-production type curves in fracture design. SPE Production Engineering. 2:191-198.

Ernst, P. 1980. Linking of boreholes. Meded. Rijks. Geol. Dienst. 33:35-40.

Fairhurst, C. 1964. Measurement of in-situ rock stresses, with particular reference to hydraulic fracturing. Felsmechanik. 2:129-147.

Farmin, R. 1934. Pebble dikes and associated mineralization at Tintic, Utah. Economic Geology. 29:356-370.

Farrell, D.A., E.L. Greacen and W.E. Larson. 1967. The effect of water content on axial strain in a loam soil under tension and compression. Soil Sci. Soc. Am. Proc. 31:445-450.

Geertsma, J. and F. de Klerk. 1969. A rapid method of predicting width and extent of hydraulically induced fractures. J. Petr. Tech., Trans. AIME. 1571-1581.

Geertsma, J. and R. Haafkens. 1979. A comparison of theories for predicting width and extent of vertical hydraulically induced fractures. J. Energy Res. Tech., Trans. ASME. 101:8-19.

Griffith, A.A. 1920. The phenomena of rupture and flow in solids. Phil. Trans. Roy. Soc. London. 221:163-198.

Griffith, A.A. 1924. The theory of rupture. In: Proc. 1st Int. Cong. Appl. Mech., Delft. 55-63.

Griffiths, S.K., R.H. Nilson and F.A. Morrison. 1983. Hybrid analytical/numerical computation of heat transfer in a gas driven fracture. Paper No. 83-WA/HT-35, Winter Meeting, Boston, MA. 1-9.

Gringarten, A.C. 1982. Flow-test evaluation of fractured reservoirs. Geol. Soc. Amer. Spec. Paper. 189:237-263.

Gringarten, A.C. and H.J. Ramey. 1973. The use of source and Green's functions in solving unsteady flow problems in reservoirs. Soc. Petr. Eng. J. 285-296.

Gringarten, A.C. and H.J. Ramey. 1974. Unsteady-state pressure distributions created by a well with a single horizontal fracture, partial penetration, or resticted entry. Soc. Petr. Eng. J. 413-426.

Gringarten, A.C., H.J. Ramey and R. Raghaven. 1974. Unsteady-state pressure distributions created by a well with a single infinite-conductivity vertical fracture. Soc. Petr. Eng. J. 347-360.

Gronseth, J.M. 1979. Stress determination by hydraulic fracturing. Improved stress determination procedures by hydraulic fracturing. Univ. of Minn., Civil & Mineral Eng Dept. Minneapolis. 1-114.

Haimson, B. and C. Fairhurst. 1967. Initiation and extension of hydraulic fractures in rocks. Soc. Petr. Eng. J. 7:310-318.

Haimson, B. and C. Fairhurst. 1969. Hydraulic fracturing in porous-permeable materials. J. Petr. Tech., Trans. AIME. 21:811-817.

Haimson, B. and C. Fairhurst. 1970. In-situ stress determination at great depth by means of hydraulic fracturing. (28) Rock Mechanics: Theory and Practice. Somerton, W.H.(ed.) The American Institute of Mining, Metallurgical, and Petroleum Engineers, Inc. New York. 559-584.

Haimson, B. and E.J. Stahl. 1970. Hydraulic fracturing and the extraction of minerals through wells. In: Proc. 3rd Sym. on Salt, Northern Ohio Geol. Soc., Cleveland, OH. 2:421-432.

Hanson, M.E., G.D. Anderson, R.J. Shaffer, D.N. Montan, B. Haimson and M.P. Cleary. 1978a. LLL gas stimulation program quarterly progress report January through March 1978. Lawrence Livermore Laboratories Report. No. UCRL 536-78-1-2:1-25.

Hanson, M.E., G.D. Anderson, R.J. Shaffer, D.N. Montan, L.D. Thorson, W. Lin, C. Haimson and M.P. Cleary. 1978b. LLL gas stimulation program quarterly progress report October through December 1977. Lawrence Livermore Laboratories Report. UCRL 50036-78-4:1-25.

Hanson, M.E., G.D. Anderson, R.J. Shaffer, D.F. Towse, A.G. Duba, N.R. Burkhard, W. Lin, M.P. Cleary and B.C. Haimson. 1979. LLL gas stimulation program quarterly progress report January through March 1979. Lawrence Livermore Laboratories Report. UCRL 50036-79-1:1-24.

Harrison, E., W.F. Kieschnick and W.J. McGuire. 1954. The mechanics of fracture induction and extension. Petr. Trans. AIME. 20:252-263.

Hartley, R. and M.G.R. Bosma. 1985. Fracturing in chalk completions. J. Petr. Tech., Trans. AIME. 73-79.

Hartsock, J.H. and J.E. Warren. 1961. The effect of horizontal hydraulic fracturing on well performance. J. Petr. Tech., Trans. AIME. 1050-1056.

Helmer, O. 1957. Mechanical analysis of the dike pattern of the Spanish Peak area, Colorado. Geol. Soc. Am. Bull. 68:567-576.

Holzer, T.L., T.L. Youd and T.C. Hanks. 1989. Dynamics of liquefaction during the 1987 Superstition Hills, California Earthquake. Science. 244:56-59.

Holzhausen, G.R., C.C. Card, J.M. Raisbeck and T.L. Dobecki. 1985a. Hydraulic fracture growth during steam stimulation in a single-well test, SPE Paper 13619. In: Proc. SPE Regional Meeting, Ventura, CA.

Holzhausen, G.R., C.S. Haase, S.H. Stow and G. Gazonas. 1985b. Hydraulic-fracture growth in dipping anisotropic strata as viewed through the surface deformation field. In: Proc. 26th U.S. Sym. Rock Mech., Rapid City, SD.

Horsrud, P., R. Risnes and R.K. Bratli. 1982. Fracture initiation pressures in permeable poorly consolidated sands. Int. J. Rock Mech. Min. Sci. Geomech. Abs. 19:255-266.

Howard, G.C. and C.R. Fast. 1957. Optimum fluid characteristics for fracture extension. Drilling & Prod. Prac., API. 261-270.

Howard, G.C. and C.R. Fast. 1970. Hydraulic Fracturing. Society of Petroleum Engineers AIME. New York. 198.

Hubbert, M.K. and D.G. Willis. 1957. Mechanics of hydraulic fracturing. Petr. Trans. AIME. 210:153-168.

Huck, P.J., M.J. Waller and S.L. Shimondle. 1980. Innovative geotechnical approaches to the remedial in-situ treatment of hazardous materials disposal sites. In: Proc. Nat. Conf. Control Haz. Mater. Spills, Louisville, KY. 421-426.

Hurlburt, S. 1989. Moving ahead with hydrofracing. Water Well J.(Feb.) 37-40.

Inglis, C.E. 1957. Stresses in a plate due to the presence of cracks and sharp corners. Inst. Naval. Architects, Trans., London. 55:1.

Irwin, G.R. 1957. Analysis of stresses and strains near the end of a crack traversing a plate. J. Appl. Mech., Trans. ASME. 361-364.

Jaworski, G.W., J.M. Duncan and H.B. Seed. 1979. An experimental study of hydraulic fracturing, Report UCB/GT/79-02. U.S. Bur. Reclam.(Oct.) 234.

Jaworski, G.W., J.M. Duncan and H.B. Seed. 1981. Laboratory study of hydraulic fracturing. J. Geotech. Eng. GT6:713-732.

Johnson, A.M. 1970. Physical Processes in Geology. Freeman Cooper and Company. San Fransisco. 577.

Kaufman, J.G. and F.G. Nelson. 1974. More on specimen size effects in fracture toughness testing. Fracture Toughness and Slow-Stable Cracking, ASTM STP 559. Irwin, G.R.(ed.) Amer. Soc. for Testing & Materials. Baltimore. 74-85.

Keck, R.G., M.P. Cleary and A. Crockett. 1984. A lumped numerical model for the design of hydraulic fractures, SPE Paper 12884. In: Proc. SPE Unconventional Gas Recovery Sym., Pittsburgh, PA. 507-514.

Kehle, R.O. 1964. The determination of tectonic stresses through analysis of hydraulic well fracturing. J. Geop. Res. 69:259-273.

Kerr, R.A. 1987. Hot dry rocks: Problems, Promise. Science. 238:1226-1228.

Kesler, S.E., N. Russell, M. Seaward, M. Rivera, K. McCurdy, G.L. Cumming and J.F. Sutter. 1981. Geology and geochemistry of sulfide mineralization underlying the Pueblo Viejo gold-silver oxide deposit, Dominican Republic. Economic Geology. 76:1096-1117.

Khristianovic, S.A. and Y.P. Zheltov. 1955. Formation of vertical fractures by means of highly viscous liquid. In: Proc. 4th World Petroleum Congress, Rome. 2:579-586.

Kirkham, D., M.F. De Boodt and L. De Leenheer. 1959. Modulus of rupture determination on undisturbed soil core samples. Soil Science. 87:141-144.

Klepaczko, J.R., M.N. Bassim and T.R. Hsu. 1984. Fracture toughness of coal under quasi-static and impact loading. Eng. Frac. Mech. 19:305-316.

Knauss, W.G. 1976. Fracture of solids possessing deformation rate sensitive material properties. In: Proc. ASME Winter Ann. Meeting, New York. AMD-19:70-103.

Koenig, L. 1960. Survey and analysis of well stimulation performance. J. Am. Water Works Assoc. 52:333-350.

Lam, K.Y. and M.P. Cleary. 1984. Slippage and re-initiation of hydraulic fractures at frictional interfaces. Int. J. Num. Anal. Meth. Geomech. 8:589-604.

Lambe, T.W. and R.V. Whitman. 1969. Soil Mechanics. John Wiley and Sons. New York. 553.

Landrum, B.L. and P.B. Crawford. 1961. Horizontal fractures do affect ultimate recovery. The Petroleum Engineer. 80-98.

Lawn, B.R. and T.R. Wilshaw. 1975. Fracture of Brittle Solids. Cambridge University Press. Cambridge.

Leach, R.E. 1977. Hydraulic fracturing of soils: A literature review. Misc. Paper S-77-6 U.S. Army Waterway Experiment Station.(Mar.) 1-25.

Luiskutty, C.T., L. Tomusta and I.D. Palmer. 1989. A three-dimensional semianalytical model of hydraulic fracture growth through weak barriers. SPE Production Engineering. 4:226-232.

Macaulay, D. 1987. Hydrofracturing the hard rock well. Ground Water Age. 21:22-25,28,30.

Massarch, K.R., R.D. Holtz, B.G. Holm and A. Fredriksson. 1975. Measurement of horizontal in-situ stresses. In: Proc. ASCE-GED Spec. Conf. In-situ Meas. Soil Prop., Raleigh, NC. 1:266-286.

Massarsch, K.R. 1978. New aspects of soil fracturing in clay. J. Geotech. Eng. Div. GT8:1109-1123.

McGuire, W.J. and V.J. Sikora. 1960. The effect of vertical fractures on well productivity. Petr. Trans. AIME. 219:401-403.

McLennan, J.D. and J.C. Roegiers. 1982. Do instantaneous shut-in pressures accurately represent the minimum principal stress? Proceedings of Workshop on Hydraulic Fracturing Stress Measurements. Zoback, M.D. and B.C. Haimson.(eds.) U.S. National Comm. for Rock Mechanics. Menlo Park, CA. 181-207.

Medlin, W.L. and L. Masse. 1979. Laboratory investigation of fracture initiation pressure and orientation. Soc. Petr. Eng. J. 129-144.

Medlin, W.L. and L. Masse. 1982. Plasticity effects in hydraulic fracturing, SPE Paper 11068. In: Proc. Ann. SPE Fall Tech. Conf., New Orleans, LA. 1-14.

Medlin, W.L. and L. Masse. 1984. Laboratory experiements in fracture propagation. Soc. Petr. Eng. J. 256-268.

Mendelsohn, D.A. 1984. A review of hydraulic fracture modeling, Part I: General concepts, 2D models, motivation for 3D modeling. J. Energy Res. Tech., Trans. ASME. 106:369-376.

Meyer, B.R. 1989. Heat transfer in hydraulic fracturing. SPE Production Engineering. 4:423-429.

Mony, P.M. 1989. Hydro-frac: One Man's Opinion. Water Well J.(Feb.) 48-50.

Morgenstern, N.R. and P.R. Vaughan. 1963. Some observations on allowable grouting pressures. In: Proc. Conf. Grouts and Drill. Muds, Instit. Civ. Eng., London. 36-42.

Mori, A. and M. Tamura. 1987. Hydrofracturing pressure of cohesive soils. Soils and Foundations. 27:14-22.

Morita, N., D.L. Whitfill and H.A. Wahl. 1988. Stress-intensity factor and fracture cross-sectional shape predictions from a three-dimensional model for hydraulically induced fractures. SPE Production Engineering. 40:1329-1342.

Morrisson, T.E. and J.H. Henderson. 1960. Gravity drainage of oil into large horizontal fractures. Petr. Trans. AIME. 219:7-15.

Murdoch, L.C., G. Holzhausen, J.C. Roegiers and B.K. Naceur. 1987. Innovative delivery and recovery systems: Hydraulic fracturing. EPA Center Hill Research Facility Interim Report. 46.

Murphy, H. 1982. Hot dry rock reservoir development and testing in the USA. Hydraulic Fracturing and Geothermal Energy. Nemat-Nasser, S., H. Abe and S. Hirakawa.(eds.) Martinus Nijhoff Pub. The Hague. 33-58.

Muskat, M. 1937. Use of data on build-up of bottom hole pressures. Trans. AIME. 123:44-48.

Nakatsuka, K., H. Takahashi and M. Takanohashi. 1982. Hydraulic fracturing experiment at Nigorikawa and fracture mechanics evaluation. Hydraulic Fracturing and Geothermal Energy. Nemat-Nasser, S., H. Abe and S. Hirakawa.(eds.) Martinus Nijhoff Pub. The Hague. 95-111.

Narendran, V.M. and M.P. Cleary. 1983. Analysis of growth and interaction of multiple hydraulic fractures, SPE Paper 12272. In: Proc. SPE Sym. Res. Sim., San Francisco, CA. 389-397.

Narendran, V.M. and M.P. Cleary. 1984. Elastostatic interaction of multiple arbitrarily shaped cracks in plane inhomogeneous regions. Eng. Frac. Mech. 19:481-506.

NAVFAC. 1982. Soil Mechanics Design Manual 7.1. Dept. of Navy, Navy Facilities Eng. Command. Alexandria. 348.

Nilson, R.H. 1981. Gas-driven fracture propagation. J. Appl. Mech., Trans. ASME. 48:757-762.

Nilson, R.H. 1986. An integral method for predicting hydraulic fracture propagation driven by gases or liquids. Int. J. Num. Anal. Meth. Geomech. 10:191-211.

Nilson, R.H. and S.K. Griffiths. 1986. Similarity analysis of energy transport in gas-driven fractures. Int. J. Fracture. 30:115-134.

Nilson, R.H., W.J. Proffer and R.E. Duff. 1985. Modelling of gas-driven fractures induced by propellant combustion within a borehole. Int. J. Rock Mech. Min. Sci. Geomech. Abs. 22:3-19.

Nolte, K.G. 1979. Determination of fracture parameters from fracturing pressure decline, SPE Paper 8341. In: Proc. 54th Ann. SPE Fall Tech. Conf. Exh., Las Vegas, NV. 1-16.

Nolte, K.G. 1982. Fracture design considerations based on pressure analysis, SPE Paper 10911. In: Proc. SPE Cotton Valley Sym., Tyler, TX.

Nolte, K.G. 1984. Determination of proppant and fluid schedules from fracturing pressure decline, SPE Paper 13278. In: Proc. 59th SPE Ann. Tech. Conf. & Exh., Houston, TX.

Nolte, K.G. 1988a. Application of fracture design based on pressure analysis. SPE Production Engineering. 3:31-42.

Nolte, K.G. 1988b. Principles for fracture design based on pressure analysis. SPE Production Engineering. 3:22-30.

Nolte, K.G. and M.B. Smith. 1981. Interpretation of fracturing pressures. J. Petr. Tech., Trans. AIME. 1767-1775.

Nolte, K.G. and M.B. Smith. 1987. Hydraulic Fracturing Pressure Analysis. 1st. NSI Technologies, Inc. Tulsa. 96.

Nordgren, R.P. 1972. Propagation of a vertical hydraulic fracture. Soc. Petr. Eng. J. 306-314.

Northrop, D.A., N.R. Warpinski, R.A. Schmidt and C.W. Smith. 1978. Stimulation and mineback experiment project: The direct observation of hydraulic and explosive fracturing tests. In: Proc. Sym. Enhanced Oil & Gas Recovery & Improved Drilling Meth., Tulsa, OK. 1-14.

Novotny, E.J. 1977. Proppant transport, SPE Paper 6813. In: Proc. SPE Ann. Tech. Meeting & Exh., Denver, CO.

Ode, H. 1957. Mechanical analysis of the dike pattern of the Spanish Peak area, Colorado. Geol. Soc. Am. Bull. 68:567-576.

Ouchterlony, F. 1982. Review of frature toughness testing of rock. SM Archives. 7:131-211.

Paillet, F.L. 1985. Problems in fractured-reservoir evaluation and possible routes to their solution. The Log Analyst. 26:26-41.

Palmer, I.D. and C.T. Luiskutty. 1986. Comparison of hydraulic fracture models for highly elongated fractures of variable height. J. Energy Res. Tech., Trans. ASME. 108:107-115.

Papadoloulos, J.M., V.M. Narendran and M.P. Cleary. 1983. Laboratory simulations of hydraulic fracturing, SPE Paper 11618. In: Proc. SPE Sym. Low Permeability, Denver, CO. 161-168.

Pascal, H. 1986. Rheological behavior effects of non-newtonian fracturing fluids on propagation of vertical hydraulic fracture. Int. J. Num. Anal. Meth. Geomech. 10:443-448.

Perkins, T.K. and L.R. Kern. 1961. Widths of hydraulic fractures. J. Petr. Tech., Trans. AIME. 937-949.

Phillips, W.J. 1972. Hydraulic fracturing and mineralization. J. Geol. Soc. London. 128:337-359.

Phillips, W.J. 1973. Mechanical effects of retrograde boiling and its probable importance in the formation of some porphyry ore deposits. Instit. Mining Metallurgy Trans. 82:B90-B98.

Pollard, D.D. 1973. Derivation and evaluation of a mechanical model for sheet intrusions. Tectonophysics. 19:233-269.

Pollard, D.D. 1978. Forms of hydraulic fractures as deduced from field studies of sheet intrusions. United States Symposium of Rock Mechanics. Kim, Y.S.(ed.) University of Nevada. Reno. 1-9.

Pollard, D.D. and G. Holzhausen. 1979. On the mechanical interaction between a fluid-filled fracture and the earth's surface. Tectonophysics. 53:27-57.

Pollard, D.D., O.H. Muller and D.R. Dockstader. 1975. The form and growth of fingered sheet intrusions. Geol. Soc. Am. Bull. 86:351-363.

Pollard, D.D., P. Segall and P.T. Delaney. 1982. Formation and interpretation of dilatant echelon cracks. Geol. Soc. Am. Bull. 93:1291-1303.

Pouios, H.G. and E.H. Davis. 1974. Elastic Solutions for Soil and Rock Mechanics. John Wiley & Sons, Inc. New York. 411.

Prats, M. 1961. Effect of vertical fractures on reservoir behavior--incompressible fluid case. Soc. Petr. Eng. J. 105-118.

Prats, M. 1981. Effect of burial history on the subsurface horizontal stresses of formations having different material properties. Soc. Petr. Eng. J. 21:658-662.

Ramey, H.J. 1967. Application of the line source solution to flow in porous media: A review. Producers Monthly. 4-27.

Rice, J.R. 1968. A path independent integral and the approximate analysis of strain concentration by notches and cracks. J. Appl. Mech., Trans. ASME. 379-386.

Rice, J.R. 1979. The mechanics of quasi-static crack growth. In: Proc. 8th U.S. Nat. Cong. Applied Mechanics. 191-216.

Robinson, B.M., S.A. Holditch and W.S. Whitehead. 1988. Minimizing damage to a propped fracture by controlled flowback procedures. SPE Production Engineering. 40:753-759.

Roegiers, J.C., J.D. McLennan and D.L. Murphy. 1982. Influence of preexisting discontinuities on the hydraulic fracturing propagation process. Hydraulic Fracturing and Geothermal Energy. Nemat-Nasser, S., H. Abe and S. Hirakawa.(eds.) Martinus Nijhoff Pub. The Hague. 413-430.

Rogowski, A.S., W.C. Moldenhauer and D. Kirkham. 1968. Rupture parameters of soil aggregates. Soil Sci. Soc. Am. Proc. 32:720-724.

Ruina, A. 1978. Influence of coupled deformation-diffusion effects on the retardation of hydraulic fracture. In: Proc. U.S. Sym. Rock Mech., Rapid City, SD. 19:274-282.

Rummel, F. and O. Kappelmeyer. 1982. The Falkenberg geothermal frac-project: Concepts and experimental results. Hydraulic Fracturing and Geothermal Energy. Nemat-Nasser, S., H. Abe and S. Hirakawa.(eds.) Martinus Nijhoff Pub. The Hague. 59-74.

Scheidegger, A.E. 1960. On the connection between tectonic stresses and well fracturing data. Geofisica Pura e Applicata. 46:66-76.

Scheidegger, A.E. 1965. Discussion of paper by P.E. Gretener, "Can the state of stress be determined from hydraulic fracturing data?". J. Geop. Res. 70:6213.

Schlichting, H. 1960. Boundary Layer Theory. McGraw Hill. New York. 647.

Schmidt, R.A. 1977. Fracture mechanics of oil shale: Unconfined fracture toughness, stress corrosion cracking, and tension test results. In: Proc. 18th U.S. Sym. Rock Mech. 1-6.

Scott, P.P., W.G. Bearden and G.C. Howard. 1953. Rock rupture as affected by fluid properties. Petr. Trans. AIME. 198:111-124.

Secor, D.T. and D.D. Pollard. 1975. On the stability of open hydraulic fractures in the earth's crust. Geophysical Research Letters. 2:510-513.

Settari, A. 1980. Simulation of hydraulic fracturing processes. Soc. Petr. Eng. J. 487-500.

Settari, A. 1983. A new general model of fluid loss in hydraulic fracturing, SPE Paper 11625. In: Proc. SPE Sym. Low Permeability, Denver, CO. 219-228.

Settari, A. 1985. Quantitative analysis of factors influencing vertical and lateral fracture growth, SPE Paper 13862. In: Proc. Low Perm. Gas Res. Sym., Denver, CO.(May) 117-128.

Settari, A. 1988. Quantitative analysis of factors influencing vertical and lateral fracture growth. SPE Production Engineering. 3:310-322.

Settari, A. and M.P. Cleary. 1982a. Development and testing of a pseudo-three-dimensional model of hydraulic fracture geometry, SPE Paper 10505. In: Proc. 6th SPE Sym. Res. Sim., New Orleans, LA. 187-215.

Settari, A. and M.P. Cleary. 1982b. Three-dimensional simulation of hydraulic fracturing, SPE Paper 10504. In: Proc. 6th SPE Sym. Res. Sim., New Orleans, LA. 159-186.

Settari, A. and M.P. Cleary. 1984. Three-dimensional simulation of hydraulic fracturing. J. Petr. Tech., Trans. AIME. 1177-1190.

Settari, A. and M.P. Cleary. 1986. Development and testing of a pseudo-three-dimensional model of hydraulic fracture geometry. SPE Production Engineering. 449-466.

Settari, A. and H.S. Price. 1984. Simulation of hydraulic fracturing in low permeability reservoirs. Soc. Petr. Eng. J. 24:141-150.

Sherard, J.L. 1973. Embankment dam cracking. Embankment Dam Engineering. Hirschfeld, R.C. and S.J. Poulos.(eds.) John Wiley & Sons. New York. 271-353.

Shockey, D.A., K.C. Dao and R.L. Jones. 1979. Effect of grain size on the static and dynamic fracture behavior of titanium. Mechanisms of Deformation and Fracture. Easterling, K.E.(ed.) Permagon Press. Oxford. 77-85.

Shoji, T. and S. Takenouchi. 1982. Hydraulic fracturing in geological processes: A review. Hydraulic Fracturing and Geothermal Energy. Nemat-Nasser, S., H. Abe and S. Hirakawa.(eds.) Martinus Nijhoff Pub. The Hague. 175-190.

Smart, P. and J.W. Dickson. 1979. Deformation and shear of normally consolidated flocculated kaolin. Mechanisms of Deformation and Fracture. Easterling, K.E.(ed.) Permagon Press. Oxford. 129-136.

Smith, E. 1981. Some observations on the viability of crack tip opening angle as a characterising parameter for plane strain crack growth in ductile materials. Int. J. Fracture. 17:443-448.

Smith, M.B., W.K. Miller, and J. Haga. 1987. Tip screenout fracturing: A technique for soft unstable formations. SPE Production Engineering. 2:95-103.

Smith, S. 1989. Rock fracturing methods: Their development and use. Water Well J.(Feb.) 41-47.

Sneddon, I.N. 1946. The distribution of stress in the neighborhood of a crack in an elastic solid. Proc. Royal Soc. London. 187:229-260.

Snyder, V.A. 1980. Theoretical Aspects and Measurement of Tensile Strength in Unsaturated Soils. Ph.D. Cornell University. 94.

Snyder, V.A. and R.D. Miller. 1985. Tensile strength of unsaturated soils. Soil Sci. Soc. Am. J. 49:58-65.

Spence, D.A. and D.L. Turcotte. 1985. Magma-driven propagation of cracks. J. Geop. Res. 90:575-580.

Stewart, G.W. 1974. Hydraulic fracturing of crystalline rock stimulates yield of two test wells drilled in New Hampshire. Ground Water. 12:46-47.

Stewart, G.W. 1978. Hydraulic fracturing of drilled water wells in crystalline rocks of New Hampshire. New Hampshire Dept. of Resources and Econ. Devel., and Water Resources Research Center. New Hampshire. 161.

Stierman, D.J. 1988. Geophysical monitoring of shallow hydraulic fractures, Unpublished draft report. Univ. of Toledo, Geology Dept.

Stow, S.H., S. Haase and H.O. Weeren. 1985. Waste disposal by hydrofracture and application of the technology to the management of hazardous wastes. In: Proc. Int. Conf. New Frontiers Haz. Waste Manag. EPA/600/9-85/025:138-144.

Streeter, V.L. 1971. Fluid Mechanics. 5th McGraw-Hill Book Co. New York. 755.

Strickland, F.G. 1985. Reasons for production decline in the diatomite, Belridge Oil Field: A rock mechanics view. J. Petr. Tech., Trans. AIME. 521-526.

Strubhar, M.K., W.L. Medlin, S.M. Nabi and F.S. Andreani. 1984. Fracturing results in diatomaceous earth formations, South Belridge Field, California. J. Petr. Tech., Trans. AIME. 495-502.

Sun, Y. and C. Ting. 1988. Introduction to a new apparatus for hydraulic fracturing tests. Geotech. Test. J. 11:288-292.

Tada, H., P.C. Paris and G.R. Irwin. 1985. The Stress Analysis of Cracks Handbook. 2nd Paris Productions Inc. St. Louis. 475.

Tavenas, F.A., G. Blanchette, S. Laroueil, M. Roy and P. La Rochelle. 1975. Difficulties in the in-situ determination of Ko in soft sensitive clays. In: Proc. ASCE-GED Spec. Conf. In-situ Meas. Soil Prop., Raleigh, NC. 1:450-476.

Telelman, A.S. and A.J. McEvily. 1967. Fracture of Structural Materials. John Wiley & Sons, Inc. New York. 697.

Thiem, A. 1906. Hydrologische Methoden. Gebhardt. Leipzig. 56.

Thiercelin, M., R.G. Jeffrey and K.B. Naceur. 1989. Influences of fracture toughness on the geometry of hydraulic fractures. SPE Production Engineering. 4:435-442.

Tyler, L.D. and W.C. Vollendorf. 1975. Physical observations and mapping of cracks resulting from hydraulic fracturing in situ stress measurements, SPE Paper 5542. In: Proc. 50th Ann. Fall Meeting SPE-AIME, Dallas, TX. 1-16.

Vandamme, L., R.G. Jeffrey and J.H. Curran. 1988. Pressure distribution in three-dimensional hydraulic fractures. SPE Production Engineering. 3:181-186.

van Eekelen, H.A. 1980. Hydraulic fracture geometry--Fracture containment in layered formations, SPE Paper 9261. In: Proc. 55th Ann. SPE Fall Tech. Conf. Exh., Dallas, TX. 1-9.

van Poolen, H.K., J.M. Tinsley and C.D. Saunders. 1958. Hydraulic fracturing: Fracture flow capacity vs. well productivity. Petr. Trans. AIME. 213:91-95.

Veatch, R.W. 1983a. Overview of current hydraulic fracturing design and treatment technology--Part 1. J. Petr. Tech., Trans. AIME. 677-687.

Veatch, R.W. 1983b. Overview of current hydraulic fracturing design and treatment technology--Part 2. J. Petr. Tech., Trans. AIME. 853-863.

Vomocil, J.A. and W.J. Chancellor. 1967. Compressive and tensile failure strengths of three agricultural soils. Trans. ASAE. 771-774, 779.

Waltz, J. and T.L. Decker. 1981. Hydro-fracturing offers many benefits. Johnson Driller's Journal. 53:4-9.

Waltz, J.P. 1988. Hydro-frac Basics. Ground Water Age. 22:26-29.

Warpinski, N.R. 1983. Investigation of the accuracy and reliability of in-situ stress measurements using hydraulic fracturing in perforated cased holes. In: Proc. 24th U.S. Sym. Rock Mech., Golden, CO. 773-786.

Warpinski, N.R. and P.T. Branagan. 1989. Altered-stress fracturing. J. Petr. Tech., Trans. AIME. 41:990-997.

Warpinski, N.R., J.A. Clark, R.A. Schmidt and C.W. Huddle. 1982. Laboratory investigation on the effect of in-situ stresses on hydraulic fracture containment. Soc. Petr. Eng. J. 333-340.

Weertman, J. 1980. The stopping of a rising, liquid-filled crack in the earth's crust by a freely slipping horizontal joint. J. Geop. Res. 85:967-976.

Weidmann, G.W. and W. Doell. 1979. Crazes and the fracture of glassy thermoplastics. Mechanisms of Deformation and Fracture. Easterling, K.E.(ed.) Permagon Press. Oxford. 385-391.

Williams, B.B. 1970. Fluid loss from hydraulically induced fractures. J. Petr. Tech., Trans. AIME. 882-888.

Williams, J.G. 1984. Fracture Mechanics of Polymers. John Wiley and Sons. New York. 302.

Williamson, W.H. and D.R. Woolley. 1980. Hydraulic fracturing to improve the yield of bores in fractured rock. Australian Water Resources Council Technical Paper. 55:1-76.

Wolff, R.G., J.D. Bredehoeft, W.S. Keys and E. Shuter. 1975. Stress determination by hydraulic fracturing in subsurface waste injection. Water Tech. Res., J. AWWA. 519-523.

Wong, H.Y. and I.W. Farmer. 1973. Hydrofracture mechanisms in rock during pressure grouting. Rock Mechanics. 5:21-41.

Yuster, S.T. and J.C. Calhoun. 1945. Pressure parting of formations in water flood operations. The Oil Weekly.

Zhang, Z.M. 1989. Application of hydrofracture principals to grouting in deep foundation. Pile Buck. 1-12.

Zoback, M.D. and D.D. Pollard. 1978. Hydraulic fracture propagation and the interpretation of pressure-time records for in-situ stress determinations. U.S. Symposium of Rock Mechanics. Kim, Y.S.(ed.) Univesity of Nevada. Reno. 14-22.

Zoback, M.D., F. Rummel, R. Jung and C.B. Raleigh. 1977. Laboratory hydraulic fracturing experiments in intact and pre-fractured rock. Int. J. Rock Mech. Min. Sci. Geomech. Abs. 14:49-58.

APPENDIX

RECORDS OF PRESSURE, INJECTED VOLUME, SURFACE UPLIFT AND SURFACE TILT AS FUNCTIONS OF TIME.

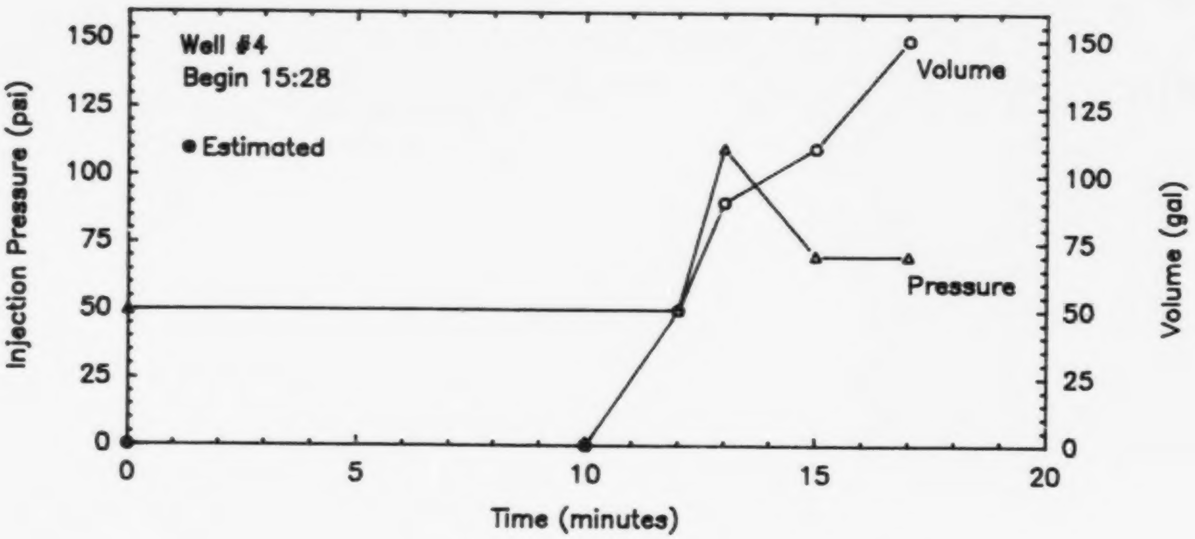
Well #4
Begin 15:28
● Estimated
Volume
Pressure
Injection Pressure (psi)
Volume (gal)
Time (minutes)
0
25
50
75
100
125
150
0
5
10
15
20

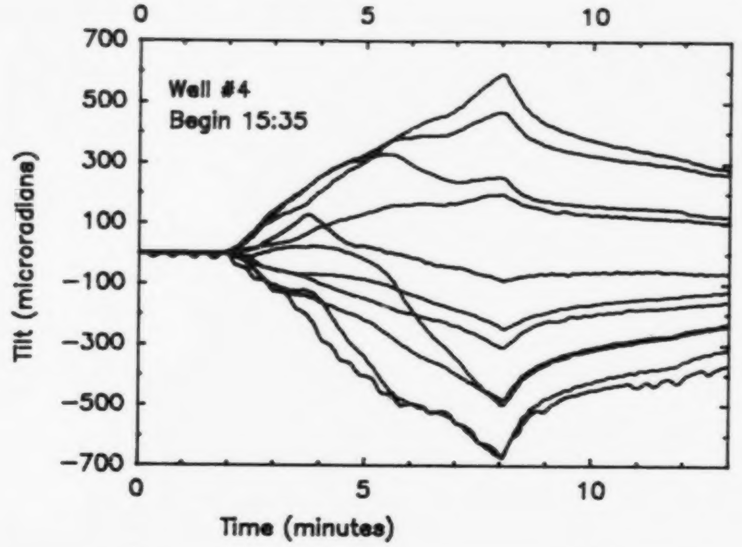
Well #4
Begin 15:35
Tilt (microradians)
Time (minutes)
700
500
300
100
−100
−300
−500
−700
0
5
10

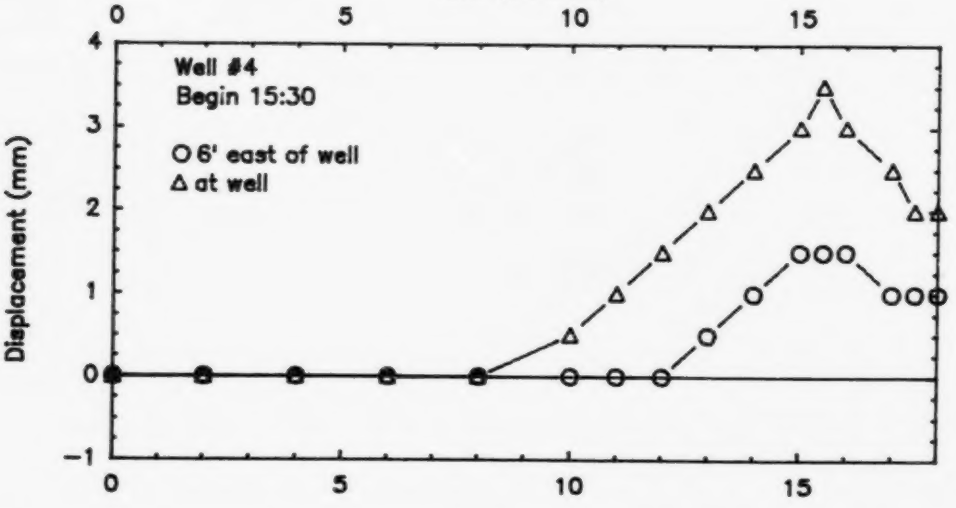
Well #4
Begin 15:30
○ 6' east of well
△ at well
Displacement (mm)
4
3
2
1
0
−1
0
5
10
15

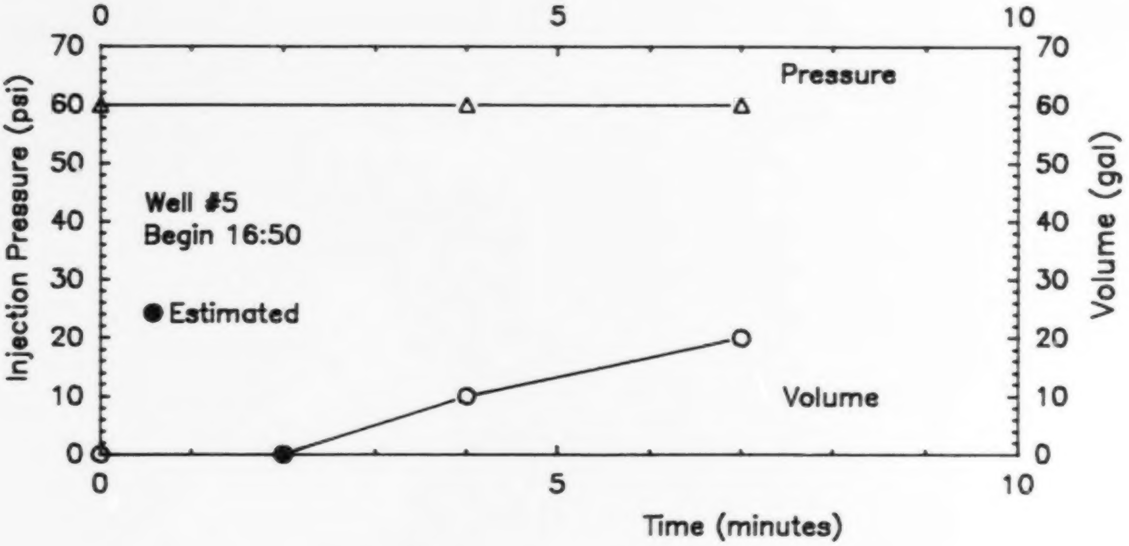
Injection Pressure (psi)
Volume (gal)
Time (minutes)
Pressure
Volume
Well #5
Begin 16:50
● Estimated
0
5
10
70
60
50
40
30
20
10
0

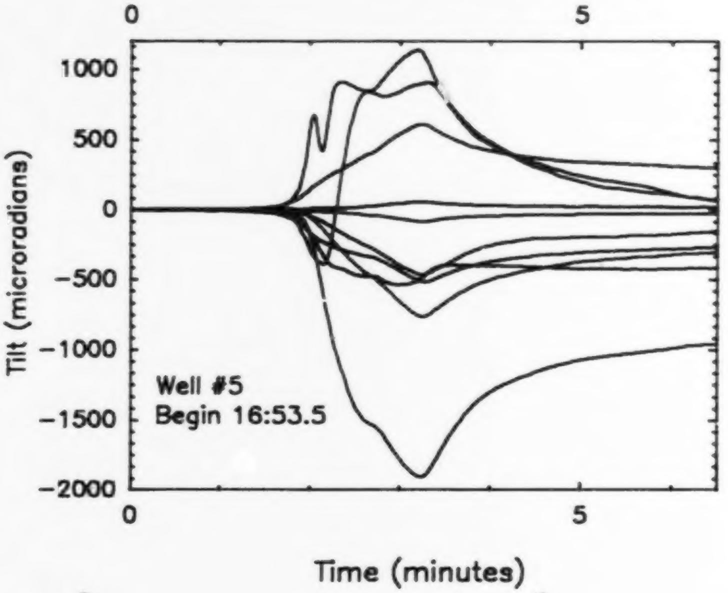
Tilt (microradians)
Time (minutes)
Well #5
Begin 16:53.5
0
5
1000
500
0
−500
−1000
−1500
−2000

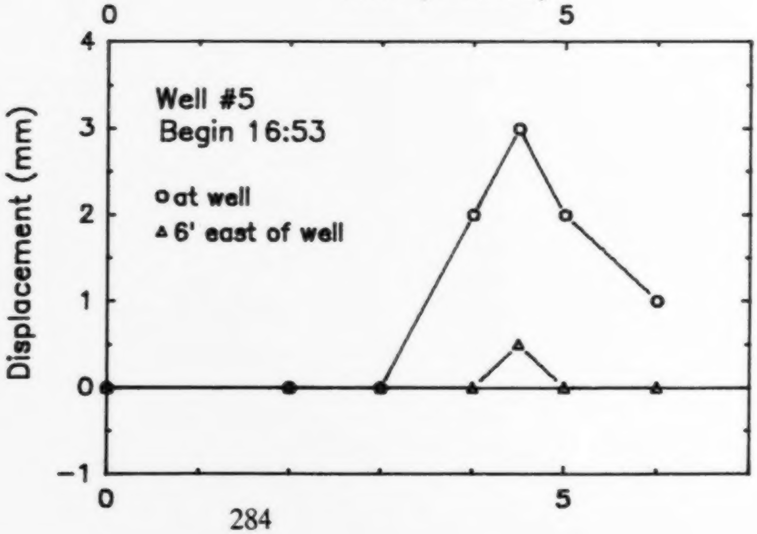
Displacement (mm)
Well #5
Begin 16:53
o at well
▵ 6' east of well
0
5
4
3
2
1
0
−1

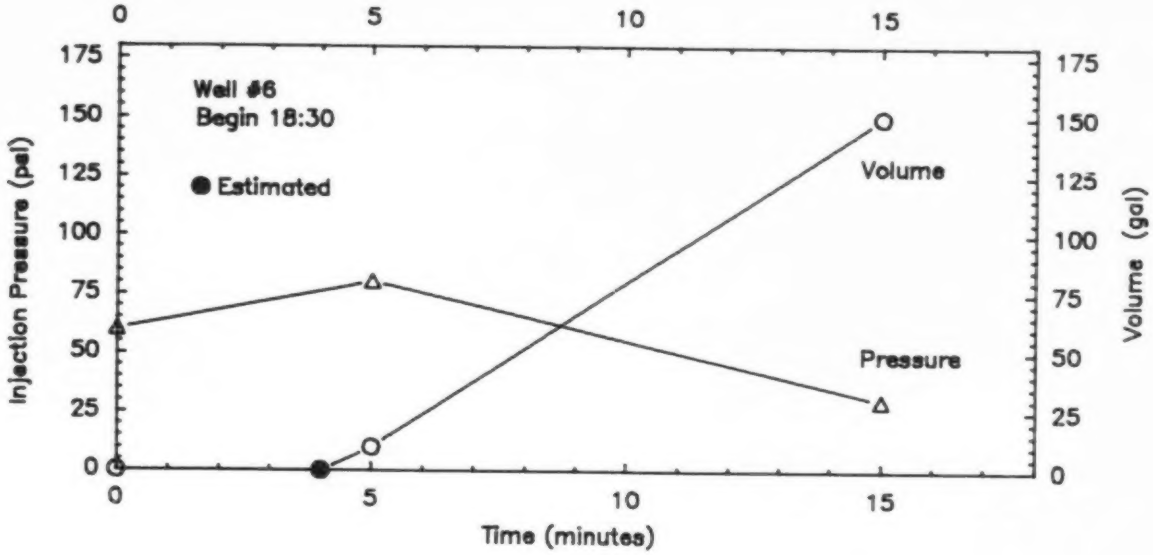
Well #6
Begin 18:30
● Estimated
Volume
Pressure
Injection Pressure (psi)
Volume (gal)
Time (minutes)
0
5
10
15
0
25
50
75
100
125
150
175

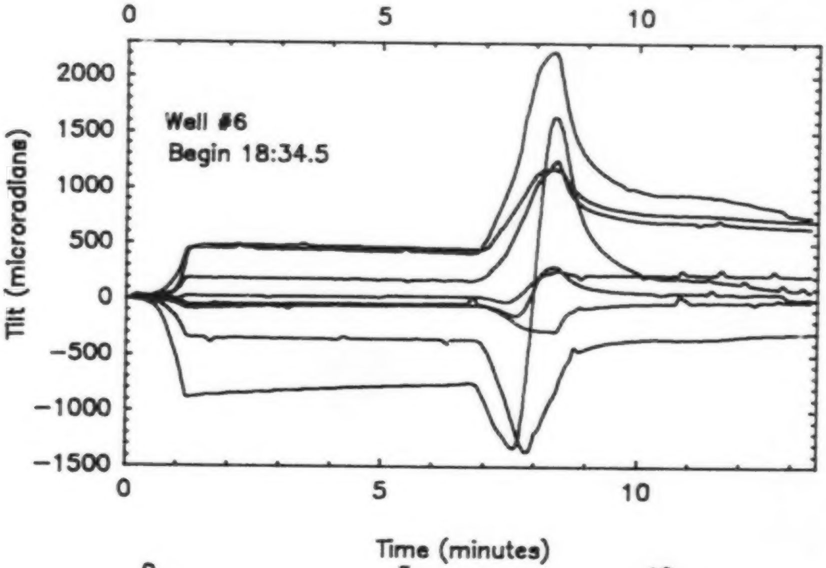
Well #6
Begin 18:34.5
Tilt (microradians)
Time (minutes)
2000
1500
1000
500
0
−500
−1000
−1500
0
5
10

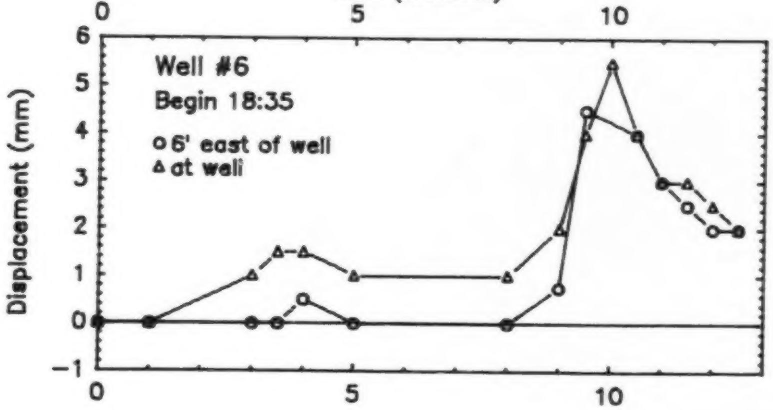
Well #6
Begin 18:35
○ 6' east of well
△ at well
Displacement (mm)
6
5
4
3
2
1
0
−1
0
5
10

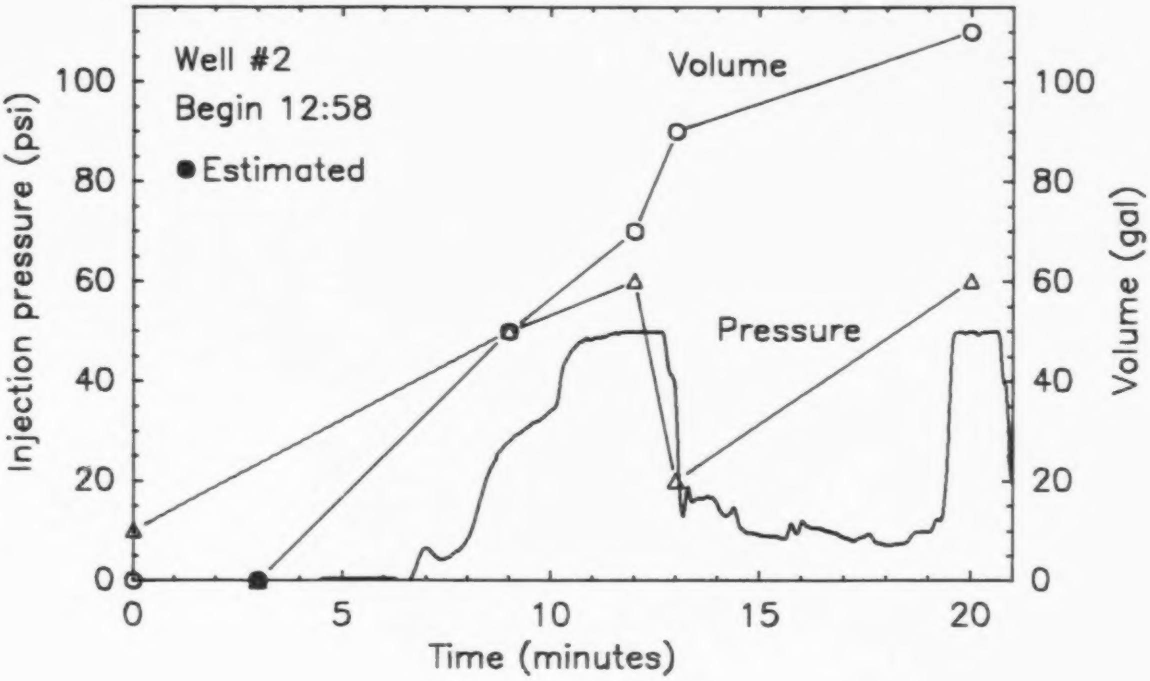
Well #2
Begin 12:58
● Estimated
Volume
Pressure
Injection pressure (psi)
Volume (gal)
Time (minutes)
0
20
40
60
80
100
0
5
10
15
20

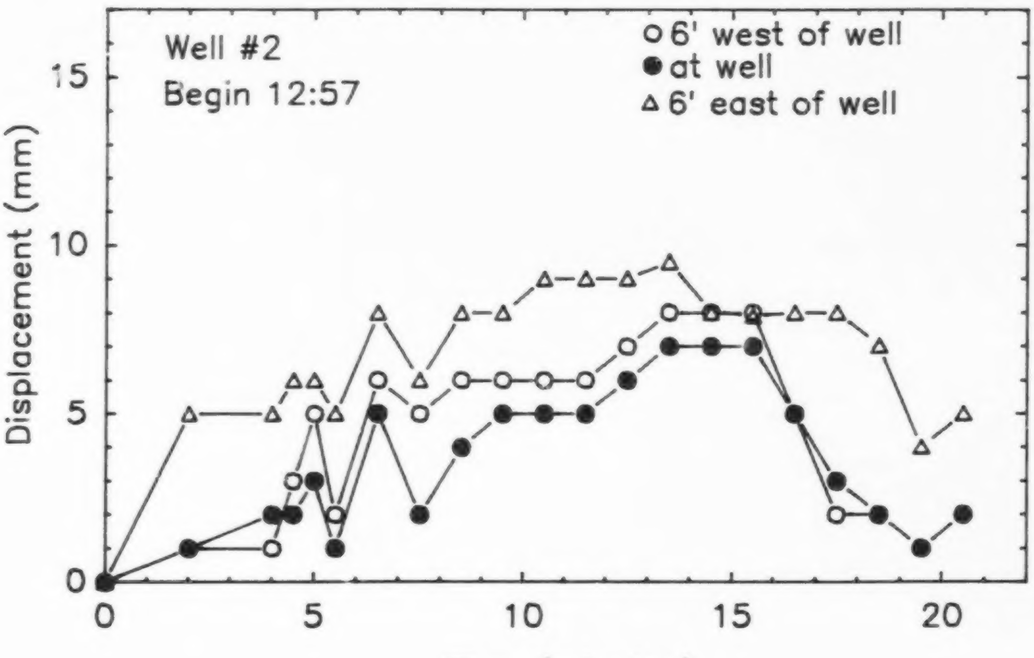
Well #2
Begin 12:57
○ 6' west of well
● at well
△ 6' east of well
Displacement (mm)
Time (minutes)
0
5
10
15
20

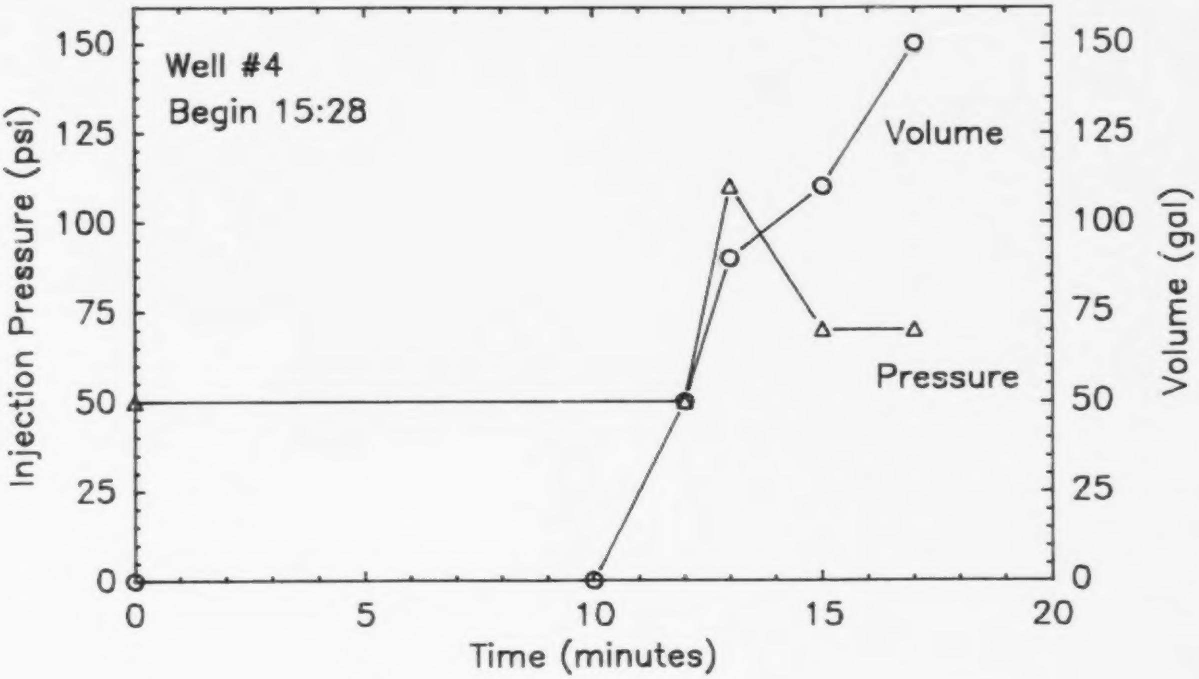

Well #4
Begin 15:28
Volume
Pressure
Injection Pressure (psi)
Volume (gal)
Time (minutes)
0
25
50
75
100
125
150
0
5
10
15
20

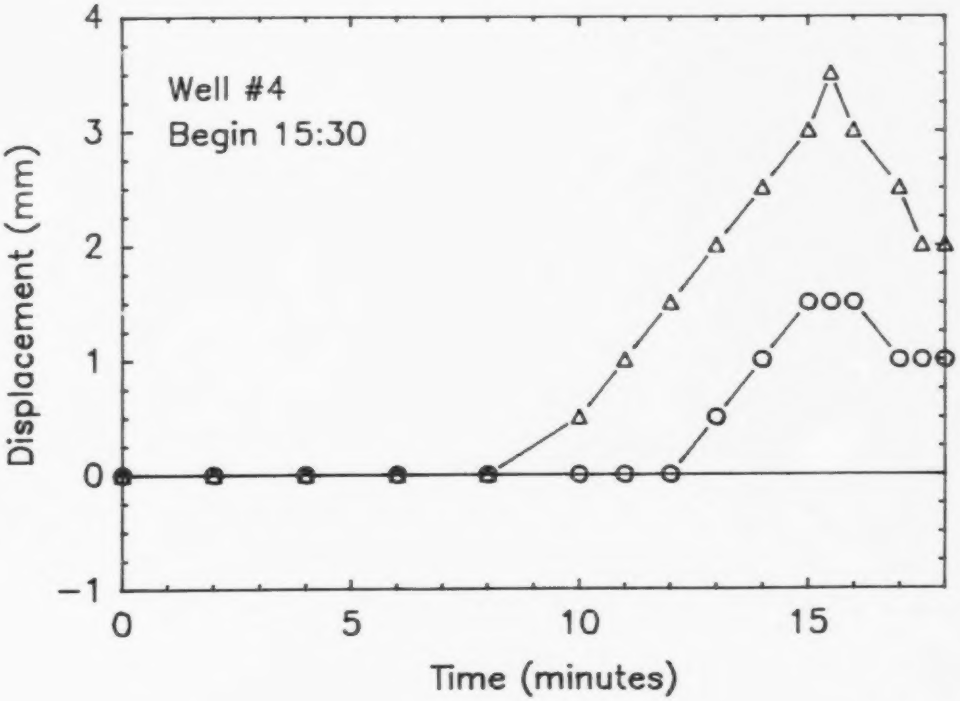

Well #4
Begin 15:30
Displacement (mm)
Time (minutes)
−1
0
1
2
3
4
0
5
10
15

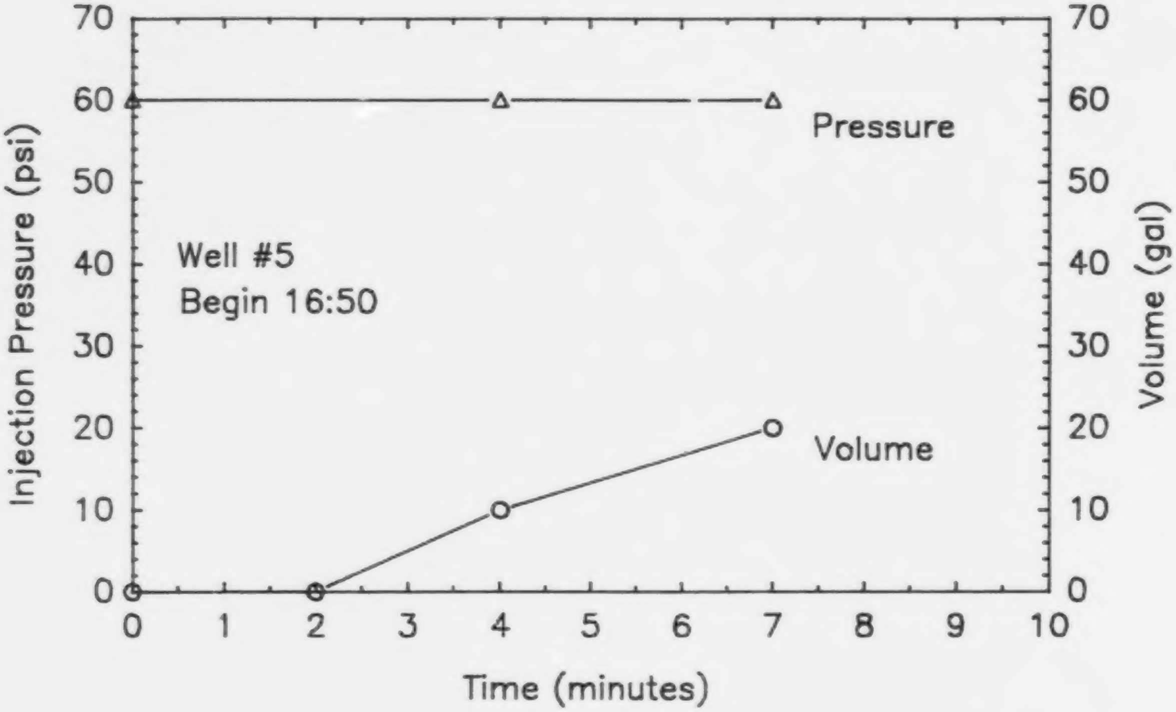

Injection Pressure (psi)
Volume (gal)
Time (minutes)
Well #5
Begin 16:50
Pressure
Volume
0
10
20
30
40
50
60
70
0
1
2
3
4
5
6
7
8
9
10

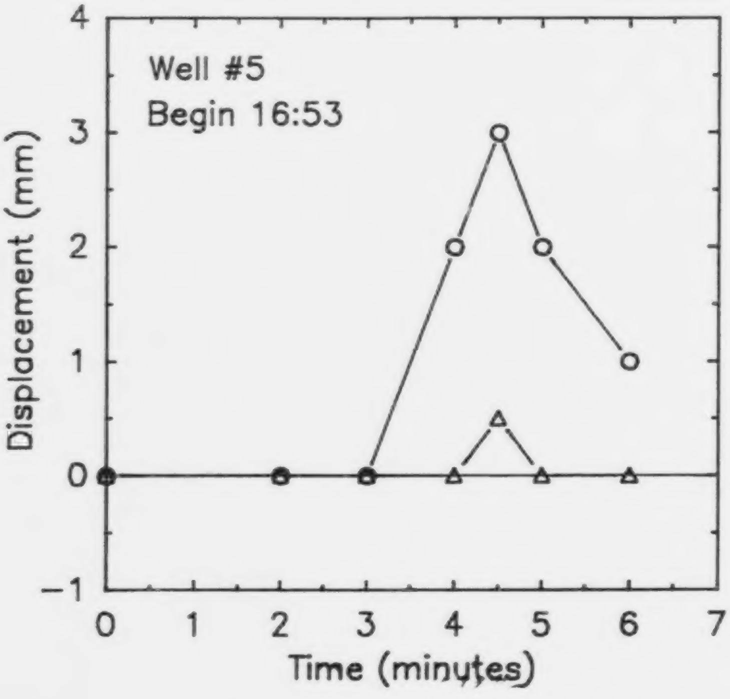

Displacement (mm)
Time (minutes)
Well #5
Begin 16:53
-1
0
1
2
3
4
0
1
2
3
4
5
6
7

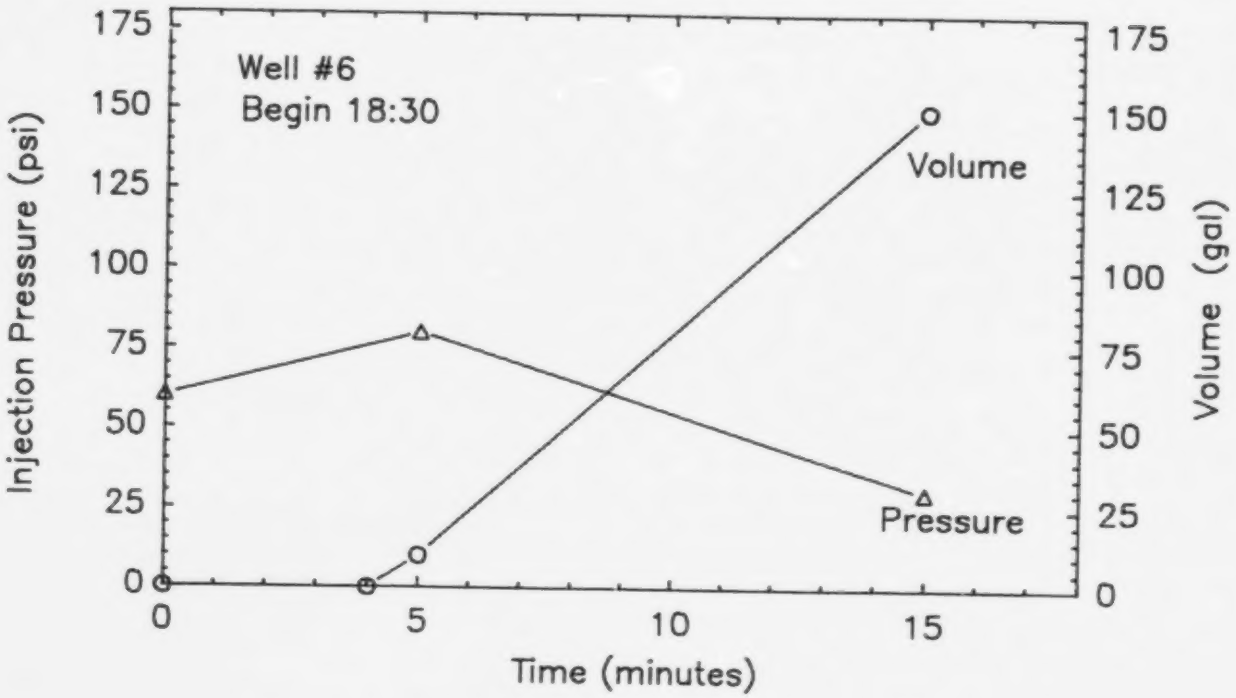
Well #6
Begin 18:30
Volume
Pressure
Injection Pressure (psi)
Volume (gal)
Time (minutes)
0
25
50
75
100
125
150
175
0
5
10
15

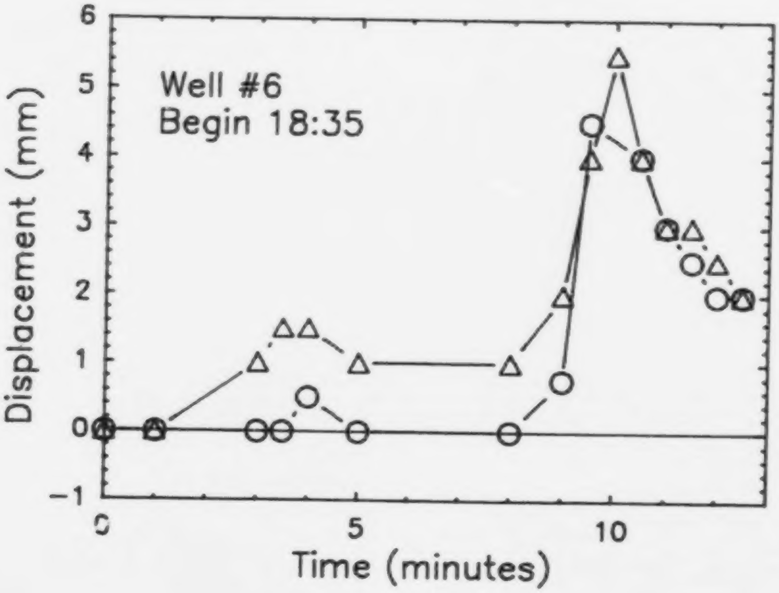
Well #6
Begin 18:35
Displacement (mm)
Time (minutes)
-1
0
1
2
3
4
5
6
0
5
10

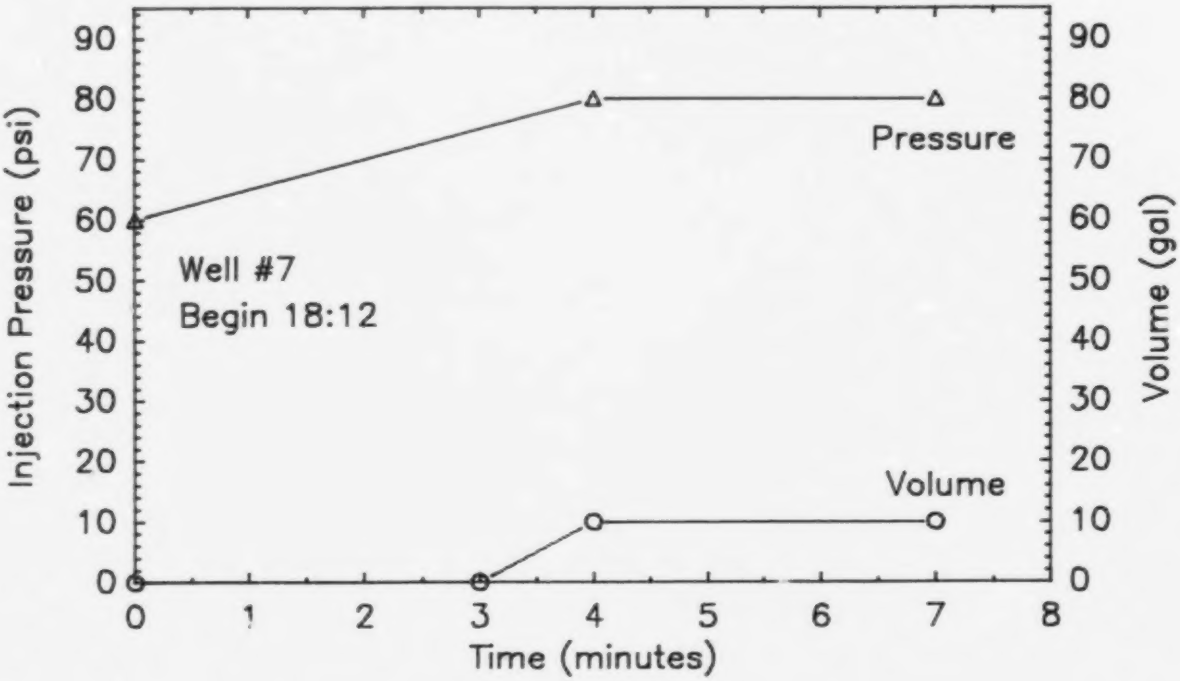
Injection Pressure (psi)
Volume (gal)
Time (minutes)
Pressure
Volume
Well #7
Begin 18:12
0
10
20
30
40
50
60
70
80
90
0
1
2
3
4
5
6
7
8

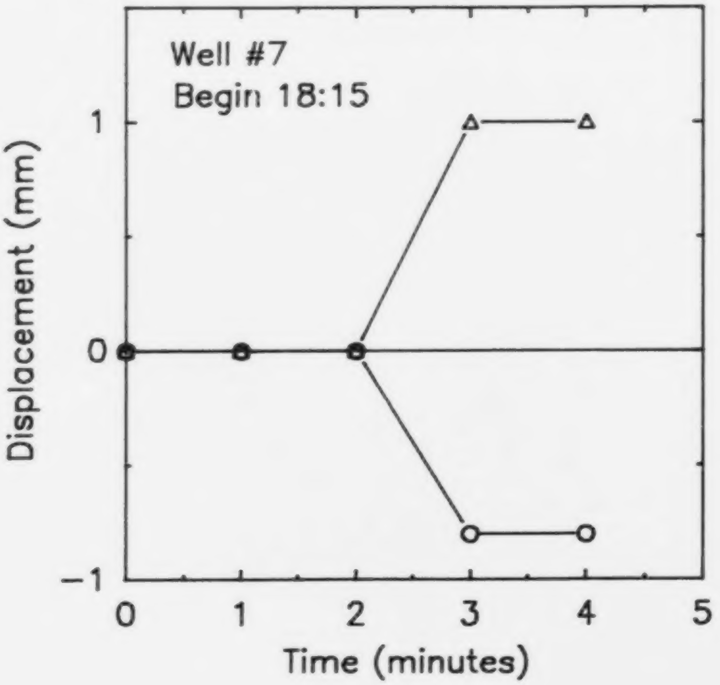
Displacement (mm)
Time (minutes)
Well #7
Begin 18:15
1
0
−1
0
1
2
3
4
5

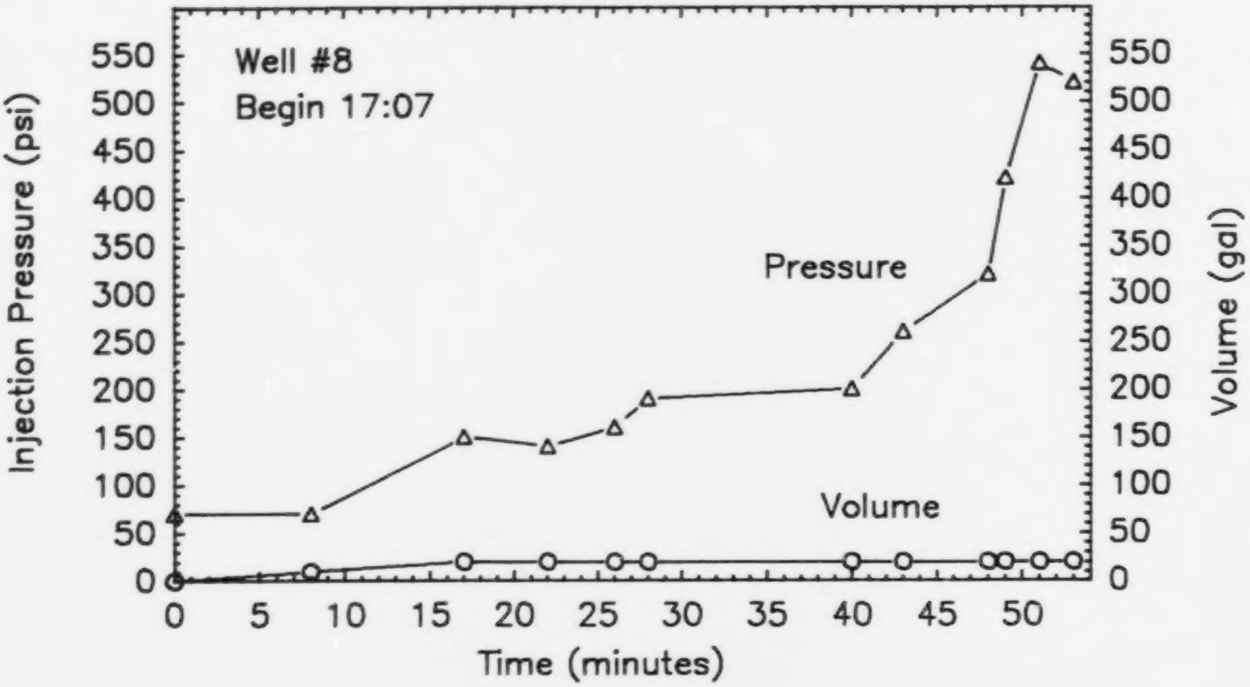
Well #8
Begin 17:07
Pressure
Volume
Injection Pressure (psi)
Volume (gal)
Time (minutes)
0
50
100
150
200
250
300
350
400
450
500
550
0
5
10
15
20
25
30
35
40
45
50

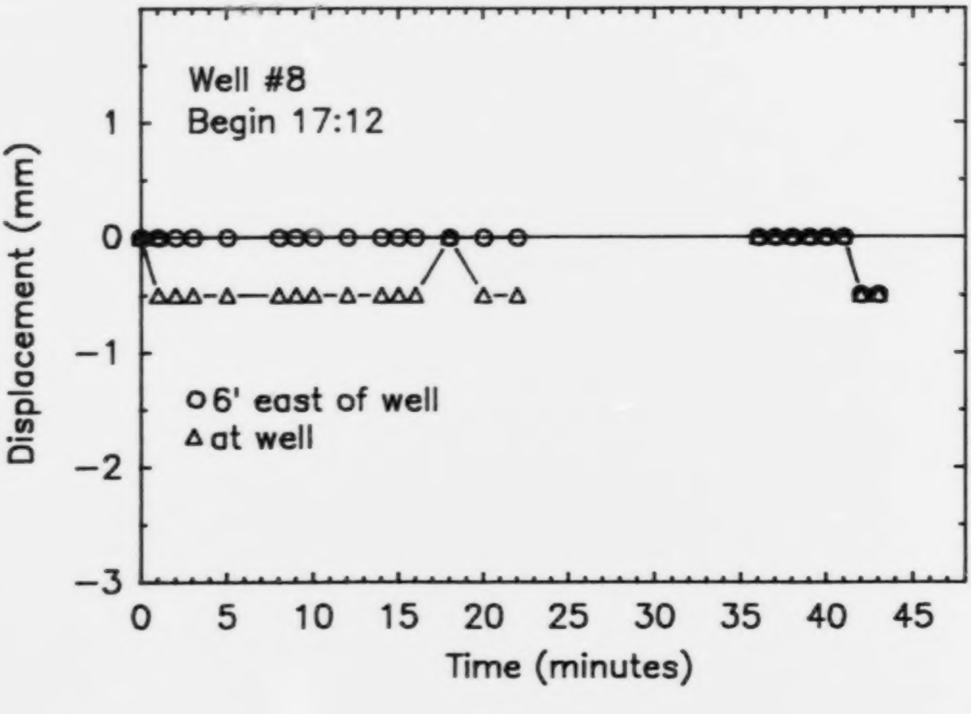
Well #8
Begin 17:12
○ 6' east of well
△ at well
Displacement (mm)
Time (minutes)
1
0
−1
−2
−3
0
5
10
15
20
25
30
35
40
45

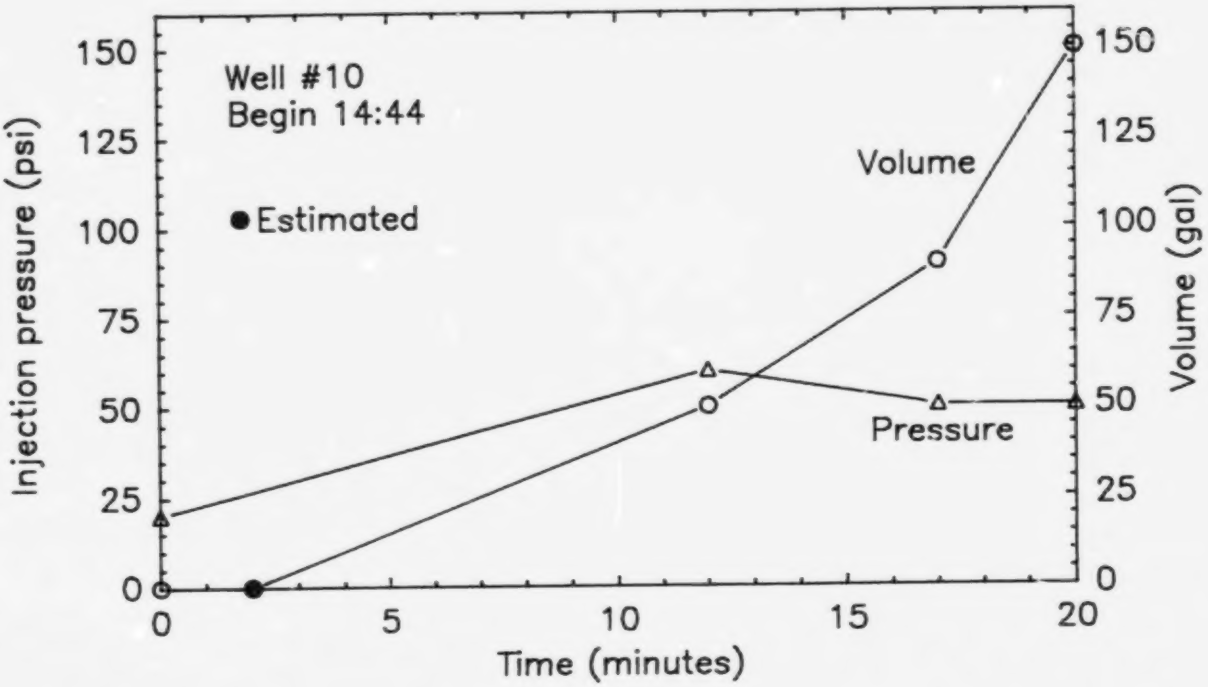
Well #10
Begin 14:44
● Estimated
Volume
Pressure
Injection pressure (psi)
Volume (gal)
Time (minutes)
0
25
50
75
100
125
150
0
5
10
15
20

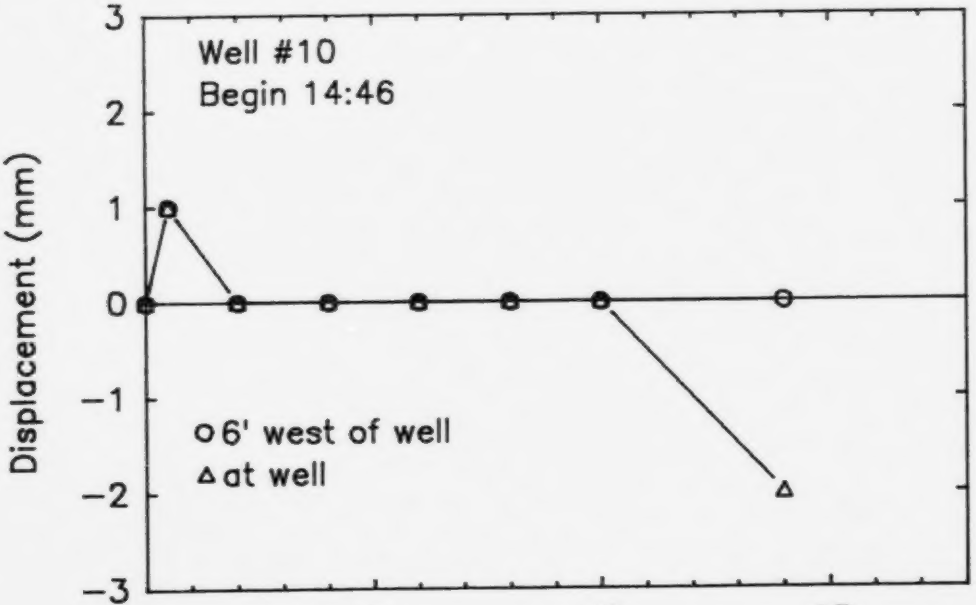
Well #10
Begin 14:46
○ 6' west of well
△ at well
Displacement (mm)
Time (minutes)
3
2
1
0
−1
−2
−3
0
5
10
15

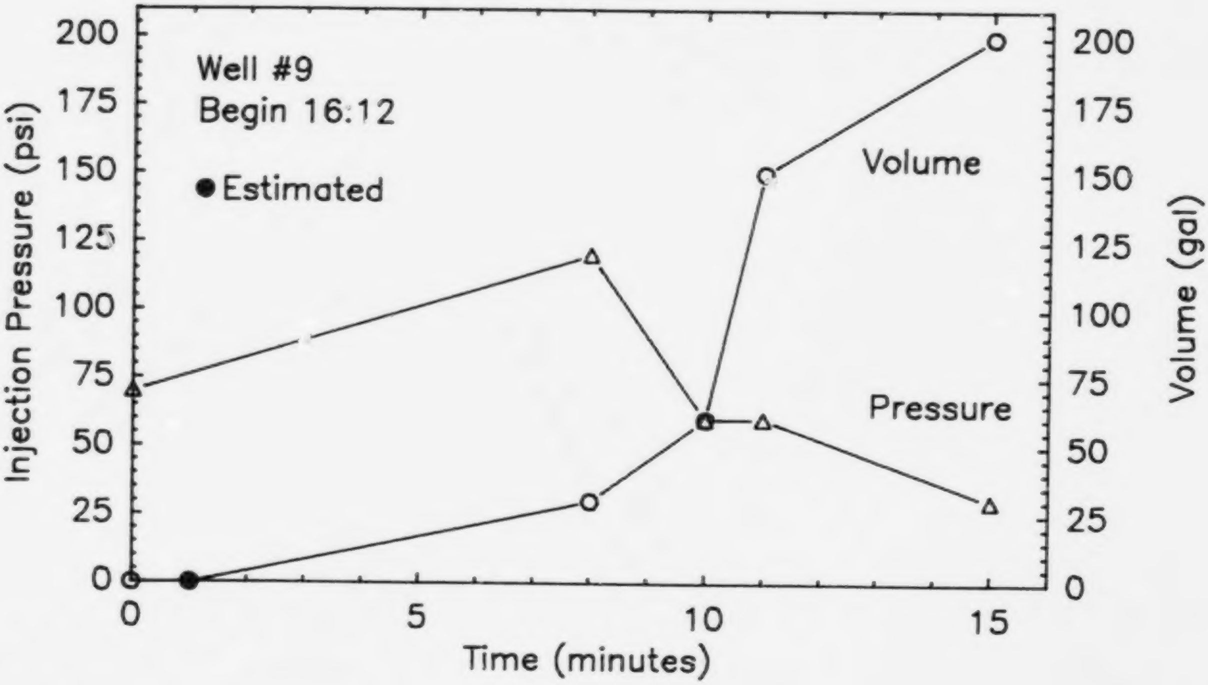
Well #9
Begin 16:12
● Estimated
Volume
Pressure
Injection Pressure (psi)
Volume (gal)
Time (minutes)
0
25
50
75
100
125
150
175
200
0
5
10
15

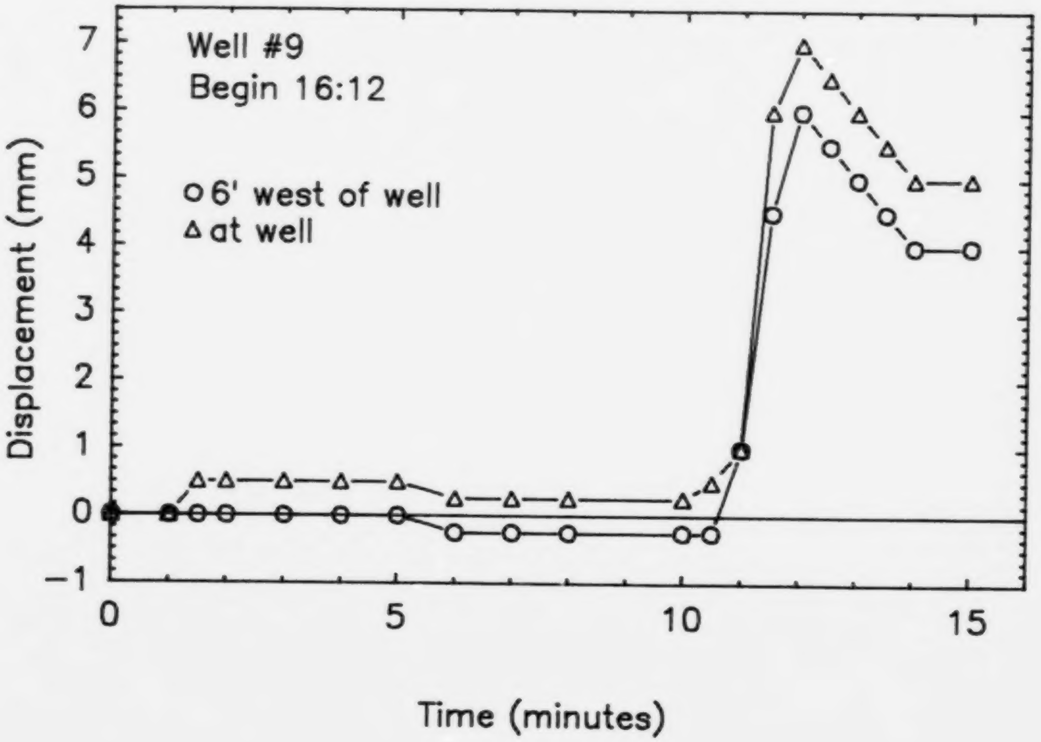
Well #9
Begin 16:12
○ 6' west of well
△ at well
Displacement (mm)
Time (minutes)
−1
0
1
2
3
4
5
6
7
0
5
10
15

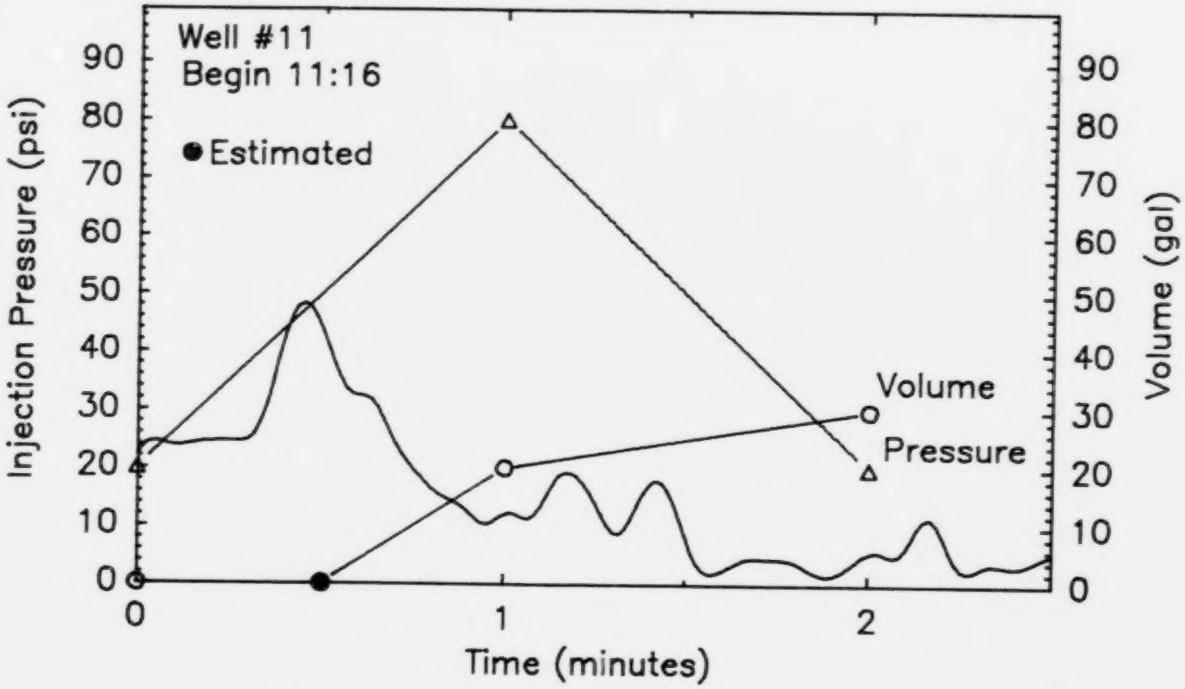
Well #11
Begin 11:16
● Estimated
Injection Pressure (psi)
Volume (gal)
Time (minutes)
Volume
Pressure
0
10
20
30
40
50
60
70
80
90
0
1
2

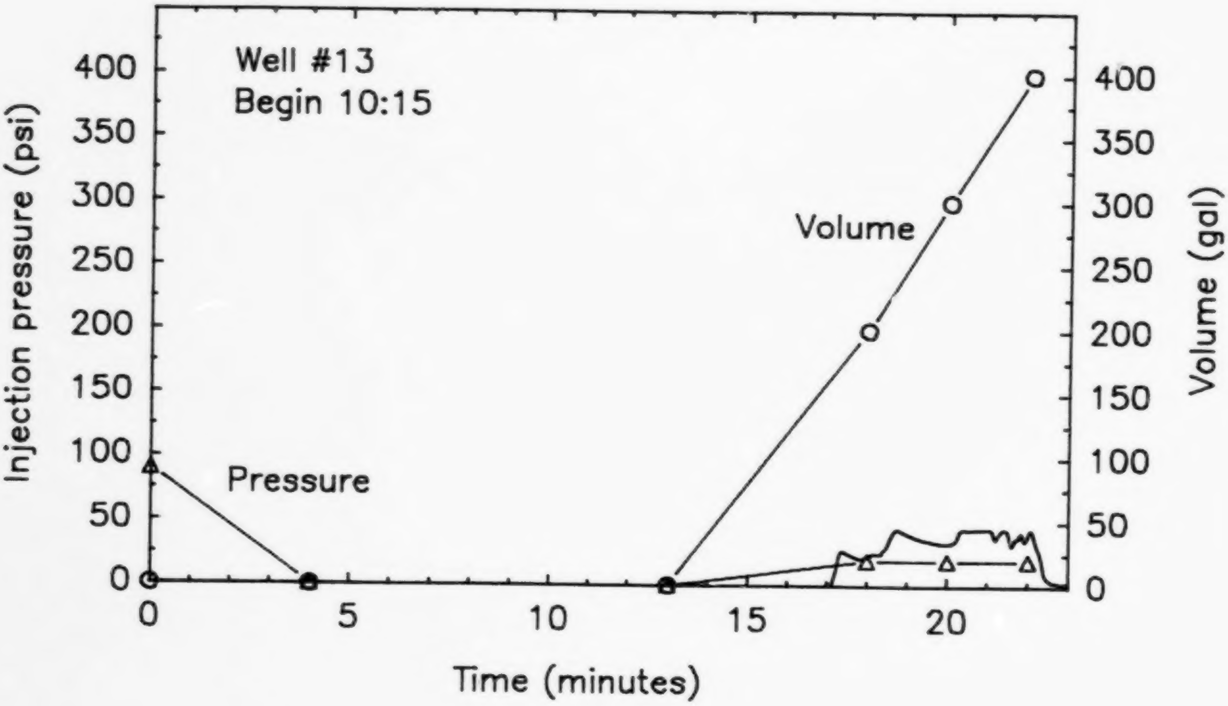
Well #13
Begin 10:15
Injection pressure (psi)
Volume (gal)
Volume
Pressure
Time (minutes)
0
50
100
150
200
250
300
350
400
0
5
10
15
20

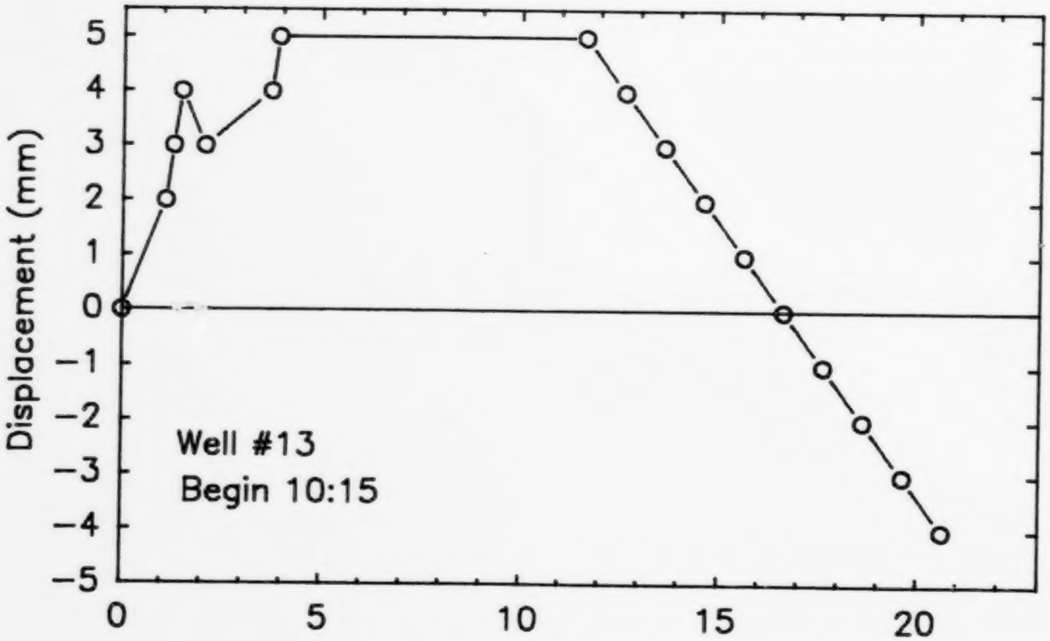
Well #13
Begin 10:15
Displacement (mm)
Time (minutes)
5
4
3
2
1
0
−1
−2
−3
−4
−5
0
5
10
15
20